

# **A Grid Reactor with Low Ion Bombardment Energy for Large Area PECVD of Thin Film Silicon Solar Cells**

THÈSE N° 5686 (2013)

PRÉSENTÉE LE 5 AVRIL 2013  
À LA FACULTÉ DES SCIENCES DE BASE  
CRPP - PROCÉDÉS PLASMAS  
PROGRAMME DOCTORAL EN PHYSIQUE

ÉCOLE POLYTECHNIQUE FÉDÉRALE DE LAUSANNE

POUR L'OBTENTION DU GRADE DE DOCTEUR ÈS SCIENCES

PAR

**Michaël CHESAUX**

acceptée sur proposition du jury:

Prof. R. Houdré, président du jury  
Dr C. Hollenstein, Dr A. Howling, directeurs de thèse  
Prof. U. Czarnetzki, rapporteur  
Dr I. Furno, rapporteur  
Dr U. Kroll, rapporteur



ÉCOLE POLYTECHNIQUE  
FÉDÉRALE DE LAUSANNE

Suisse  
2013





EARN FROM YESTERDAY

live for today, hope for tomorrow.

The important thing is to not stop questioning.

Albert Einstein (\*1879 – †1955)

in *Relativity: The Special and the General Theory* (1916)





## Abstract

This thesis presents the development and study of a plasma processing radio frequency (RF) reactor design using intense localized plasmas in a grid. The aim is to reduce the ion bombardment energy inherent in RF capacitively-coupled parallel-plate reactors used to deposit large area thin film silicon solar cells. High ion bombardment energy can cause defects in silicon layers and deteriorate electrical interfaces, therefore, by reducing the ion bombardment energy, lower defect density might be obtained.

The approach followed in this study was to insert a grounded grid inside a symmetric parallel-plate reactor. The reactor and grid were designed to form a uniform array of intense localized plasmas in the grid holes. The grid then divides the symmetric parallel-plate reactor into two connected volumes: a parallel-plate RF plasma source above, and a grounded chamber below. The plasma fills both volumes by conducting the plasma potential via the plasma in the grid holes. In this way, the grounded chamber increases the effective area of the grounded electrode, thereby creating a novel asymmetric-area reactor whilst maintaining a uniform plasma across the substrate. The low ion bombardment energy in this grid reactor is a consequence of the negative DC self-bias caused by this strong electrode asymmetry.

In addition to the self-bias, the time evolution of plasma light emission and plasma potential RF waveform are also affected by the grid, thereby further reducing the time-averaged plasma potential and ion bombardment energy.

The analysis of these phenomena was supported by a wide range of complementary plasma diagnostics (i.e. retarding field energy analyser, phase-resolved optical emission spectroscopy, capacitive probe and Langmuir probes). The measurements were complemented by a numerical fluid simulation which reproduced the observed physics.

In parallel to the plasma diagnostics, silicon thin films were deposited using a semi-industrial version of the grid reactor. The analysis showed that the layer defect densities and the best solar cells obtained with this grid reactor are approaching the quality of the reference cells obtained with other low energy ion bombardment reactors.

**Keywords:** Plasma enhanced chemical vapor deposition, capacitively coupled, grid reactor, low ion bombardment energy, plasmoid, retarding field energy analyser,

phase resolved optical emission spectroscopy, capacitive probe, fluid simulation, thin film, photovoltaic solar cell.

## Résumé

Cette thèse présente le développement et l'étude d'un design de réacteur plasma Radio Fréquence (RF). Ce design utilise d'intenses plasmas localisés dans une grille. Il a pour but de réduire l'énergie du bombardement ionique inhérent aux réacteurs RF à configuration plaques parallèles et couplage capacitif. Ces réacteurs sont communément utilisés pour le dépôt, sur des grandes surfaces, de cellules solaires de type couches minces à base de silicium. Le bombardement par des ions de haute énergie peut être néfaste et causer des défauts dans les couches de silicium ainsi qu'endommager les interfaces électriques. Dès lors, il est possible qu'en réduisant l'énergie de ce bombardement ionique, la densité de défauts dans les couches soit réduite.

L'approche suivie dans cette étude a été d'insérer une grille, dont le potentiel est mis à la terre, à l'intérieur d'un réacteur à configuration plaques parallèles. Le réacteur ainsi que la grille ont été conçus pour former une matrice uniforme d'intenses plasmas localisés dans les trous de la grille. Cette grille divise le réacteur en deux volumes connectés : une source plasma de type plaques parallèles au dessus de la grille et une chambre dont les parois sont mises à la terre en dessous de la grille. Le plasma remplit ces deux volumes en conduisant son potentiel à travers le plasma présent dans les trous de la grille. Dès lors, la chambre au dessous de la grille augmente l'aire effective des surfaces mises à la terre et en contact avec le plasma. Cette transmission a pour conséquence que les surfaces de ce nouveau design de réacteur sont asymétriques, bien que l'uniformité du plasma d'un côté à l'autre du substrat soit préservée. Le faible bombardement ionique dans ce réacteur découle, en partie, de l'auto-polarisation négative de l'électrode RF créé par cette forte asymétrie des surfaces.

En addition de l'auto-polarisation, l'évolution temporelle de l'émission optique du plasma, ainsi que la forme d'onde du potentiel plasma, sont tous deux aussi affectées par la présence de la grille. Cela a pour conséquence de réduire encore plus la moyenne temporelle du potentiel plasma et donc de réduire l'énergie du bombardement ionique.

L'analyse de ces phénomènes est soutenue par un large panel de diagnostics plasmas complémentaires (i.e. analyseur d'énergie à champs retardants, spectroscopie

d'émission optique résolue en phase, sonde capacitive et sonde Langmuir). Les mesures sont complémentées par une simulation numérique basée sur un modèle fluide. Cette simulation reproduit la physique observée expérimentalement.

En parallèle de l'analyse des paramètres plasmas, des couches minces de silicium ont été déposées à l'aide d'une version industrielle du réacteur à grille. L'analyse a montré que la densité de défauts dans les couche ainsi que les performances des meilleures cellules solaires obtenues avec ce réacteur s'approchent de la qualité des cellules de référence déposées avec d'autres réacteurs ayant un bombardement ionique de faible énergie.

**Mots-clés :** Dépôt chimique en phase vapeur assisté par plasma, couplage capacitif, réacteur à grille, bombardement ionique de faible énergie, plasmöide, analyseur d'énergie à champs retardants, spectroscopie d'émission optique résolue en phase, sonde capacitive, simulation fluidique, couche mince, cellule solaire photovoltaïque.

# Contents

<b>1</b>	<b>Introduction</b>	<b>1</b>
<b>2</b>	<b>Key phenomena</b>	<b>5</b>
2.1	Plasma sheath and potential . . . . .	5
2.1.1	Self-bias potential . . . . .	12
2.2	Ion bombardment . . . . .	13
2.3	Plasma simulation . . . . .	17
2.3.1	Simulation domains and boundaries . . . . .	19
2.4	Plasma breakdown . . . . .	21
<b>3</b>	<b>Experimental setup</b>	<b>25</b>
3.1	Reactor design . . . . .	25
3.1.1	Setup for special reactor geometries . . . . .	30
3.2	Plasma breakdown and reactor impedance . . . . .	30
3.2.1	Plasma breakdown . . . . .	30
3.2.2	Reactor impedance and matching . . . . .	31
<b>4</b>	<b>Diagnostics</b>	<b>35</b>
4.1	Voltage probe . . . . .	35
4.2	Langmuir probes . . . . .	36
4.3	Optical emission . . . . .	37
4.4	Retarding Field Energy Analyser . . . . .	40
4.4.1	Consideration on collisions within the RFEA . . . . .	47
4.4.2	Particles flows inside the RFEA . . . . .	49
4.4.3	RFEA resolution . . . . .	52
4.5	Capacitive probe . . . . .	57
<b>5</b>	<b>Low ion energy in the grid reactor and the associated plasma phenomena</b>	<b>63</b>

5.1	Optical emission intensity and plasma density . . . . .	64
5.2	Self-bias and conduction of RF currents through holes . . . . .	68
5.2.1	Plasmoid and RF current transmission . . . . .	70
5.3	Influence of the self-bias potential on the ion bombardment energy . .	84
5.4	Influence of plasma evolution on the ion bombardment . . . . .	87
5.5	Parameter study of the grid reactor geometry . . . . .	98
5.5.1	Sensitivity to grid geometry . . . . .	98
5.5.2	Partially floating substrate and DC biasing . . . . .	101
5.6	Conclusion on ion bombardment energy . . . . .	105
<b>6</b>	<b>Numerical fluid simulation results</b>	<b>107</b>
6.1	Simulated geometry . . . . .	107
6.2	Time-averaged plasma densities . . . . .	108
6.3	Self-bias, plasma potential and time evolution . . . . .	113
6.4	Conclusion . . . . .	122
<b>7</b>	<b>Layer deposition and solar cell quality</b>	<b>125</b>
7.1	Deposition rates . . . . .	126
7.2	Raman crystallinity . . . . .	128
7.3	Fourier transform infrared absorption spectroscopy . . . . .	130
7.4	Defect density . . . . .	131
7.5	Cell efficiency . . . . .	133
7.6	Conclusion . . . . .	137
<b>8</b>	<b>Final conclusions and outlook</b>	<b>141</b>
<b>A</b>	<b>Appendix: Derivation of the momentum conservations</b>	<b>145</b>
<b>B</b>	<b>Appendix: Conformal transformation</b>	<b>147</b>
	<b>Bibliography</b>	<b>151</b>
	<b>Acknowledgements</b>	<b>163</b>
	<b>Curriculum vitæ</b>	<b>165</b>

# Chapter 1

## Introduction

The early descriptions of plasmas were done by Crookes [1], Langmuir [2] and others at the beginning of the last century. Since then, many industrial products have been developed with the use of plasmas. Common examples are the utilisation of plasma as a light emitting device (i.e. neon tubes, plasma flat panel display, spectroscopic lamps), as a hot flame to cut metal pieces in the automotive industry, or as a tool to deposit thin films. The latter utilisation has many applications which can be split into two categories. The technique of Physical Vapour Deposition (PVD) in which the plasma is used as a source of energetic ions bombarding a target and sputtering its atoms. These atoms will then form a thin layer on an exposed substrate. The other technique is called Plasma Enhanced Chemical Vapour Deposition (PECVD). There, energetic electrons within the plasma are used to produce chemical reactions inside the gas. This technique is relatively close to another technique called Chemical Vapour Deposition (CVD) in which heat, typically a hot surface, is used to produce the desired chemical reactions. The great advantage of PECVD is that the surface to be coated and the gas can remain relatively cold while still having high-energy chemical reactions taking place due to the energetic electrons of the plasma.

PECVD is widely used to deposit thin film silicon layers both for the display and solar industry (photovoltaic industry). In the display industry, these layers are used as a matrix of thin film transistors to control each pixel of a flat panel displays. In the photovoltaic industry, the thin film silicon layer is used to absorb incoming light and produce current. The thin film silicon solar cell technology is in competition with several other technologies: the monocrystalline silicon solar cell, with which most of the solar cells are currently produced; the heterojunction cell which is a combination of monocrystalline and thin film silicon cells; and technologies based on other semiconductors (i.e. cadmium telluride, gallium arsenide and copper indium gallium

selenide). The main advantages of thin film silicon solar cells are the relatively low production costs and the large abundance of silicon. However, the efficiency of thin film silicon solar cells is lower than those obtained with the other technologies listed previously. The thin film silicon cells are therefore targeted to a market where large areas can be covered with relatively inexpensive cells, thus compensating the lower efficiency of the cells by using larger areas. However, to stay competitive, thin film silicon technology is required to decrease its production costs and increase the cell efficiency. Among the efforts to reach that goal are requirements to improve the production rate by increasing the silicon deposition rate and increase the efficiency by reducing the defect density of the thin films.

The thin film silicon layers are usually deposited at low pressure with Radio Frequency Capacitively-Coupled Plasmas (RF CCP) in parallel-plate reactors. In these reactors, the substrate is in contact with the plasma and it is bombarded by ions from the plasma. A difficulty with this technology is that high energy bombarding ions can cause defects in silicon layers and deteriorate electrical interfaces. The bombarding energy of these ions varies with the injected RF power and therefore this bombardment prevents the use of high RF power. However, high RF power is required as it also strongly influences the deposition rate. Several techniques have been proposed to reduce the ion bombardment. Very High Frequencies (VHF, 30 MHz and above) [3, 4] can be used to reduce the potential drop through the plasma sheath and therefore lower the ion bombarding energy. However, with VHF, the RF wavelength becomes significant compared to the reactor dimensions. Therefore, standing wave non-uniformities [5–7] must be corrected [8] to maintain a good layer uniformity necessary for solar cell deposition. Another approach to reduce the ion bombardment energy is to increase the gas pressure [9, 10]. The ions then lose energy via collisions within the gas as they travel through the sheath. However, increased gas pressure promotes undesired powder formation. This powder is trapped within the plasma and can alter the plasma properties or potentially damage the deposition. In recent years Czarnetzki et al. [11, 12] have proposed another method to reduce the ion bombardment. They suggested tailoring the waveform of the RF excitation frequency in a parallel-plate reactor. This method (electrical asymmetry effect) causes a self-bias voltage and thus can be used to tune the ion bombardment energy. Finally, it has also been suggested to change the reactor design/type in order to reduce the ion bombardment. Examples of low ion bombardment reactor types are Inductively Coupled Plasmas (ICP) reactors, cascaded arc reactors and hot wire reactors. However, these reactors have difficulties producing large area



homogeneous layers.

In this study, the approach of producing low ion bombardment by modifying the reactor geometry is followed. To keep the large area plasma uniformity of parallel-plate reactors, it was proposed to modify these reactors by adding a grid electrode close to the RF electrode. The grid reactor developed in this study partly resembles the grid or triode reactors which have been studied extensively in the literature. In these studies, grounded grids have been inserted into parallel-plate DC [13, 14] or RF [15–18] reactors to shield or screen the substrate from the plasma by confining the plasma to the other side of the grid. For the same purpose, the grid has also been biased [19–24], acting as a third electrode (hence “triode reactor”) which could also be combined with a substrate bias [25, 26]. One drawback of this grid approach is that many radicals are lost by drift and diffusion to the grid surface [27].

In contrast, the grid reactor in this work has two different functions: Firstly, the reactor dimensions (RF-grid spacing, grid thickness, hole diameter) are chosen to give a uniform array of intense localized plasma in the grid holes, where each localized plasma is a strong source of radicals. Secondly, the grounded grid divides the symmetric parallel-plate reactor into two connected volumes: a parallel-plate RF plasma source above, and a grounded chamber below. The plasma fills both volumes by conducting the plasma potential via the plasma in the grid holes. In this way, the grounded chamber leads to an increase of the effective area of the grounded electrode, thereby creating an asymmetric-area reactor whilst maintaining a uniform plasma across the substrate. The resulting negative DC self-bias on the capacitively-coupled RF electrode lowers the plasma potential and hence reduces the ion bombardment energy on the substrate.

This work is organised as follows: First, a few key phenomena are presented. Then, the designs of the parallel-plate reactor and the grid used in this study are presented. Additional engineering difficulties found in the grid reactor are discussed. Then the different diagnostics and their methods are presented with emphasis on the retarding field energy analyser and its energy resolution. The results discussion starts by comparing the optical emission and the plasma density profiles in both reactors. It continues with a discussion of the transmission of RF current through the grid and its influence on the self-bias potential in the grid reactor. This leads to the study of the RF current transmission through holes of various diameters and the impact of this transmission on reactor designs. Afterwards, the influence of the self-bias and the time-evolutions of the plasma potential on the ion bombardment energy is discussed. A section on numerical simulation highlights the agreement between

a simple two fluid model and the phenomena observed experimentally. Finally, a section is dedicated to the influence of this grid geometry on the deposition of silicon layers and cells before concluding.

# Chapter 2

## Key phenomena

### 2.1 Plasma sheath and potential

In plasmas, the density of ions and electrons are nearly equal and the plasmas are said to be quasi-neutral. The excess of one type of charge creates an electric field within the plasma which tends to bring the plasma back to a quasi-neutral condition. In the low temperature non-equilibrium plasmas as used in this study, the electrons temperature ( $T_e$ ) is higher than the ions temperature and since the electron mass is smaller than that of ions, the electron thermal velocity  $(T_e/m_e)^{\frac{1}{2}}$  is two to three orders of magnitude higher than that of ions. Here  $T_e$  is in electron volts,  $m_e$  is the electron mass and  $M_i$  the ion mass. Thus, when these plasmas are in contact with a wall, in the absence of electric field, the electrons would rapidly be lost to the wall. Instead, the loss of electrons close to the wall creates a region (called a sheath) where the ion density is higher than the electron density, as shown in figure 2.1. This local positive density within the sheath leads to a potential profile which is positive within the plasma and falls sharply to zero at a grounded wall. The resulting electric field repels the electrons travelling towards the wall back into the plasma and attracts the ions entering the sheath toward the wall so that the ion flux and electron flux are equal. The ions are accelerated toward the sheath in a region called the pre-sheath and they enter the sheath with a velocity  $u_B = (T_e/M_i)^{\frac{1}{2}}$  (Bohm velocity).

Outside the sheath region, in the bulk of the plasma, the quasi-neutrality implies that the potential is constant to a first approximation. This potential with respect to a grounded wall is the plasma potential ( $V_{pla}$ ) shown in figure 2.1. Due to the higher electron thermal speed, the plasma potential is almost always more positive than all surfaces in contact with the plasma.

In industrial reactors, some walls (electrodes) in contact with the plasma are electri-

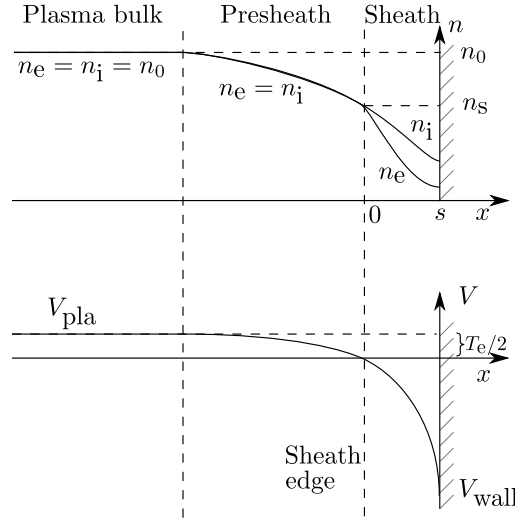


**Figure 2.1:** (a) Ion and electron density ( $n_i, n_e$ ) in the plasma bulk, presheath and sheath.  $n_s$  is the density at the sheath edge and  $s$  is the sheath width. (b) Plasma potential ( $V_{\text{pla}}$ ) in the plasma bulk, the presheath and the sheath.  $V_{\text{wall}}$  is the wall potential,  $T_e$  is the electron temperature and  $T_e/2e$  is the voltage drop through the presheath. Figure taken from [28].

cally biased whereas others are usually grounded. In Radio Frequency Capacitively-Coupled Plasmas (RF CCP), one electrode (the RF electrode) is biased with a sinusoidal potential oscillating at typically 13.56 MHz. The potential on this RF electrode imposes RF oscillations to the plasma potential as the sheaths adapt to retain the electrons inside the plasma. The response of the plasma potential to this RF electrode potential depends on the magnitude of the different currents through the sheath. These currents are the ion current density ( $J_i$ ), the electron current density ( $J_e$ ) and the displacement current density ( $J_d$ ) caused by the time variation of the potential through the sheath. This displacement current in the sheath can be approximated to the current in a vacuum capacitor with two parallel plates (the wall and the sheath edge). Assuming a Boltzmann distribution for the electrons, these current densities are given by [28]:

$$J_i = en_i \alpha u_B = J_{\text{isat}} \quad (2.1.1)$$

$$J_e = \frac{1}{4} en_e \left( \frac{8T_e}{\pi m_e} \right)^{\frac{1}{2}} e^{\frac{-eV_s}{T_e}} = J_{\text{esat}} \cdot e^{\frac{-eV_s}{T_e}} \quad (2.1.2)$$

$$J_d = \epsilon_0 \frac{\partial E}{\partial t}, \quad (2.1.3)$$

where  $\alpha \sim 0.61$  is the ratio between the ion density in bulk and at the sheath edge,  $n_i$  is the ion density,  $n_e$  is the electron density,  $V_s$  is the voltage drop through the sheath and  $E$  is the electric field within the sheath. At high frequencies (13.56 MHz and above), the displacement current usually dominates the conduction currents in

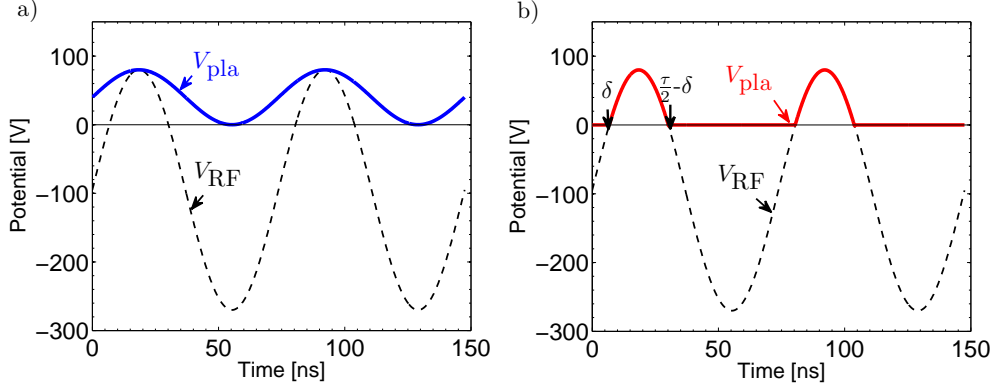


**Figure 2.2:** Potential on the RF electrode ( $V_{\text{RF}}$ ) and plasma potential ( $V_{\text{pla}}$ ) for a plasma with (a) capacitive sheaths and (b) resistive sheaths.  $\delta$  and  $\tau/2 - \delta$  are the first zeros of  $V_{\text{RF}}$  and  $\tau$  is the RF period. In this graphical representation, it is assumed that  $V_{\text{pla}} \gg V_f$  the floating sheath potential and therefore  $V_f$  is neglected.

the sheaths. In these plasmas, the current in the sheaths is therefore similar to the one in a capacitor and the sheaths are said to be capacitive. In this condition, the plasma potential oscillation is sinusoidal as shown in figure 2.2(a).

However, the displacement current is not always dominant. The amplitude of the displacement current in a RF plasma is given by [28]:

$$|J_d| \approx \frac{w\epsilon_0 |V_s|}{s}, \quad (2.1.4)$$

where  $w$  is the angular frequency of the plasma potential and  $|V_s|$  is the RF voltage oscillation amplitude of the sheath potential (half of the peak-to-peak voltage). The ratio between the amplitude of the displacement and conduction currents is [28]:

$$\frac{J_d}{J_i} = \frac{3\pi\omega |V_s|}{4\omega_i \bar{V}_s}, \quad (2.1.5)$$

where  $\omega_i = \frac{2\pi}{\tau_i}$  and  $\tau_i = 3s \left( \frac{M_i}{2eV_s} \right)^{\frac{1}{2}}$  is the ion transit time across the sheath,  $\bar{V}_s$  is the time-averaged voltage across the sheath and  $s$  the sheath width. In equation 2.1.5, the Child Law of space-charge-limited current was used [28]:

$$J_i = \frac{4}{9}\epsilon_0 \left( \frac{2e}{M_i} \right)^{\frac{1}{2}} \frac{V_s^{\frac{3}{2}}}{s^2}. \quad (2.1.6)$$

For a high voltage sheath ( $|V_s| \gg V_f$ , the floating sheath potential), then  $\bar{V}_s \sim |V_s|$ . The equation 2.1.5 simplifies, showing that the transition from a dominant displacement current to dominant conduction current occurs when the frequency becomes smaller ( $\sim 100$  kHz [29]) or when the density is high ( $\omega_i \propto n_i^{\frac{1}{2}}$ ). When the conduction current dominates, the capacitive aspect of the sheaths becomes

negligible and the sheaths are said to be resistive. In that condition, the plasma potential waveform follows more closely the evolution of the most positive surface in contact with it as shown in figure 2.2(b).

In RF plasmas, to a first approximation, the ions are too heavy to follow the oscillations of the plasma potential and their motion is instead governed by the time-averaged plasma potential ( $\bar{V}_{\text{pla}}$ ).  $\bar{V}_{\text{pla}}$  is therefore an important parameter to determine the energy of ions hitting a wall.  $\bar{V}_{\text{pla}}$  for different plasmas can be determined, for different wall and plasma conditions.

The simplest condition is for an electrically floating plasma with respect to a grounded wall. The grounded wall potential  $\bar{V}_{\text{wall}} = 0$  and the current density to the wall ( $J_{\text{wall}}$ ) must be zero since the plasma is floating:

$$J_{\text{wall}} = 0 = J_i - J_e + \underbrace{J_d}_{=0}, \quad (2.1.7)$$

where  $J_d = 0$  since  $\partial E / \partial t = 0$  here. Therefore, using equation 2.1.2:

$$J_{\text{isat}} = J_{\text{esat}} \cdot e^{\frac{-e\bar{V}_{\text{pla}}}{T_e}}, \quad (2.1.8)$$

where  $V_s$  is replaced by  $V_{\text{pla}}$  in equation 2.1.2 since  $V_s = V_{\text{pla}}$  for a sheath to a grounded wall. Hence, using equations 2.1.1 and 2.1.2 into 2.1.8, the plasma potential is:

$$\bar{V}_{\text{pla}} = \frac{T_e}{2e} \ln \left[ \frac{M_i}{3.7m_e} \right] = V_f. \quad (2.1.9)$$

In the case of a RF capacitively-coupled plasma with respect to a grounded wall, the plasma potential ( $V_{\text{pla}}(t) = \bar{V}_{\text{pla}} + \tilde{V}_{\text{pla}}(t)$ ) where  $\tilde{V}_{\text{pla}}$  is the oscillating component of the plasma potential. If the RF electrode is coupled through a DC blocking capacitor, as is often the case in capacitively-coupled plasmas, the time-averaged current to the grounded walls is zero. Using equations 2.1.1, 2.1.2 and 2.1.3:

$$\bar{J}_{\text{wall}} = 0 = J_{\text{isat}} - \frac{1}{\tau} \int_0^\tau J_{\text{esat}} e^{\frac{-\tilde{V}_{\text{pla}}(t) + \bar{V}_{\text{pla}}}{T_e/e}} dt - \frac{1}{\tau} \int_0^\tau \underbrace{\epsilon_0 \frac{\partial E}{\partial t}}_{=0} dt \quad (2.1.10)$$

where again,  $V_s = V_{\text{pla}}$  in equation 2.1.2 since the wall is grounded. The integral of the displacement current is zero due to its periodicity. Therefore

$$\frac{J_{\text{isat}}}{J_{\text{esat}}} = e^{\frac{-e\bar{V}_{\text{pla}}}{T_e}} \frac{1}{\tau} \int_0^\tau e^{\frac{-e\tilde{V}_{\text{pla}}(t)}{T_e}} dt \quad (2.1.11)$$

and the time-averaged plasma potential is [4, 29, 30]:

$$\bar{V}_{\text{pla}} = \underbrace{\frac{T_e}{e} \ln \left( \frac{J_{\text{esat}}}{J_{\text{isat}}} \right)}_{=V_f} + \frac{T_e}{e} \ln \left[ \frac{1}{\tau} \int_0^\tau e^{\frac{-e\tilde{V}_{\text{pla}}(t)}{T_e}} dt \right]. \quad (2.1.12)$$

If the plasma has capacitive sheaths, then  $\tilde{V}_{\text{pla}}(t) = \hat{V}_{\text{pla}} \sin(\omega t)$  and

$$\frac{1}{\tau} \int_0^\tau e^{\frac{-e\hat{V}_{\text{pla}} \sin(\omega t)}{T_e}} dt = I_0 \left( \frac{e\hat{V}_{\text{pla}}}{T_e} \right) \quad (2.1.13)$$

where  $I_0$  is the modified Bessel function [4], therefore:

$$\bar{V}_{\text{pla}} = V_f + \frac{T_e}{e} \ln \left[ I_0 \left( \frac{e\hat{V}_{\text{pla}}}{T_e} \right) \right]. \quad (2.1.14)$$

If  $e\hat{V}_{\text{pla}} \gg T_e$ , the asymptotic expansion of  $I_0$  to the first order is:

$$\lim_{z \rightarrow \infty} I_0(z) \sim \frac{e^z}{(2\pi z)^{\frac{1}{2}}} (1 - O(z^{-1})). \quad (2.1.15)$$

Inserting equation 2.1.15 into equation 2.1.14 gives

$$\bar{V}_{\text{pla}} = V_f + \hat{V}_{\text{pla}} - \frac{T_e}{2e} \ln \left[ 2\pi \frac{e\hat{V}_{\text{pla}}}{T_e} \right] \quad (2.1.16)$$

and if  $e\hat{V}_{\text{pla}} \gg T_e$ , equation 2.1.16 becomes

$$\bar{V}_{\text{pla}} \sim \hat{V}_{\text{pla}}, \quad (2.1.17)$$

i.e. the time-averaged plasma potential is nearly equal to the amplitude of the plasma potential. The plasma potential in this cold, capacitive model is shown in figure 2.3. There it is seen that the plasma potential amplitude is  $\hat{V}_{\text{pla}} = \frac{1}{2} \left( \frac{V_{\text{pp}}}{2} + V_{\text{sb}} \right)$ , where  $V_{\text{pp}}$  is the peak-to-peak potential and  $V_{\text{sb}}$  the self-bias potential on the RF electrode ( $V_{\text{RF}}(t) = \frac{1}{2} V_{\text{pp}} \sin(\omega t) + V_{\text{sb}}$ ).  $V_{\text{pp}}$  is imposed by the RF generator driving the RF electrode whereas  $V_{\text{sb}}$  is a potential generated by the plasma and it will be discussed in the next section (Sec. 2.1.1). The time-averaged plasma potential is therefore:

$$\bar{V}_{\text{pla}} \sim \hat{V}_{\text{pla}} = \frac{1}{2} \left( \frac{V_{\text{pp}}}{2} + V_{\text{sb}} \right) = \bar{V}_{\text{cap}}. \quad (2.1.18)$$

Equation 2.1.18 is a standard approximation for  $\bar{V}_{\text{pla}}$  in cold plasmas with capacitive sheaths. This time averaged plasma potential for a plasma with capacitive sheath

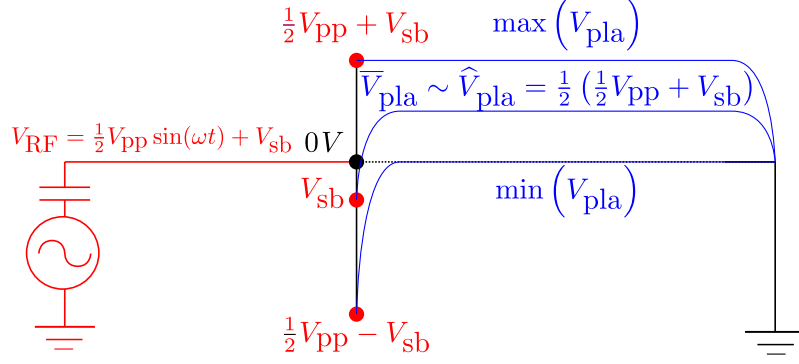


**Figure 2.3:** Cold capacitive model of the plasma potential, i.e.  $e\tilde{V}_{pla} \gg T_e$  and  $\tilde{V}_{pla}(t) = \hat{V}_{pla} \sin(\omega t)$ .  $V_{RF}$  is the potential on the RF electrode,  $V_{pp}$  is the peak-to-peak potential and  $V_{sb}$  the self-bias potential. The amplitude of the plasma potential is:  $\hat{V}_{pla} = \frac{1}{2} (\max(V_{pla}) + \min(V_{pla})) = \frac{1}{2} (\frac{1}{2} V_{pp} + V_{sb} + 0)$ .

is labelled  $\bar{V}_{cap}$  for later comparison with non capacitive sheaths plasmas. This result can also be calculated using the time-averaged value of the plasma potential. Using this model, the maximum value for the potential is  $V_{pp}/2 + V_{sb}$  whereas the lower potential value is the ground potential. Since the plasma potential is sinusoidal as shown in figure 2.2, the  $\bar{V}_{pla}$  is simply half of its amplitude as shown in equation 2.1.18.

If the plasma has resistive sheaths,  $\tilde{V}_{pla} = \hat{V}_1 \sin(\omega t) + \hat{V}_2 \sin(2\omega t) + \dots$  and the calculation becomes difficult. However, using the approximation that  $e\hat{V}_1 \gg T_e$ , the time-averaged plasma potential can be calculated by averaging the plasma potential over one RF cycle. With this cold plasma approximation, the plasma potential, shown in figure 2.2(b), is equal to zero except between  $0 + \delta$  and  $\frac{\tau}{2} - \delta$  where it is equal to  $V_{RF}(t)$ . The phase of  $\delta$  is given by the solution of:

$$\delta = \frac{1}{\omega} \arcsin\left(\frac{-2V_{sb}}{V_{pp}}\right), \quad (2.1.19)$$

and the time-averaged plasma potential is [29, 31]:

$$\begin{aligned} \bar{V}_{pla} &= \frac{1}{2\pi} \int_{0+\delta}^{\frac{\tau}{2}-\delta} \left( \frac{V_{pp}}{2} \sin(\omega t) + V_{sb} \right) dt \\ \bar{V}_{pla} &= \frac{V_{pp}}{2\pi} \left( 1 - \left( \frac{2V_{sb}}{V_{pp}} \right)^2 \right)^{\frac{1}{2}} + \frac{V_{sb}}{2\pi} \left[ \arccos\left(\frac{-V_{sb}}{V_{pp}}\right) \right] = \bar{V}_{res}. \end{aligned} \quad (2.1.20)$$

The time-averaged plasma with resistive sheath is labelled  $\bar{V}_{res}$  for comparison with plasma with non resistive sheaths.

Following the same reasoning, the time-averaged potential drop to a “floating” probe/wall ( $V_{wall}$ ) in contact with the plasma can be calculated.  $V_{wall}$  depends



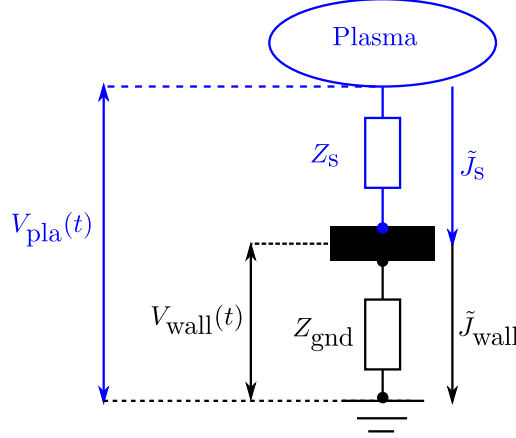


**Figure 2.4:** Diagram of a probe/wall coupled to a plasma through the sheath impedance  $Z_s$  and coupled to ground through the wall impedance  $Z_{\text{gnd}}$ .  $V_{\text{wall}}$  is the wall potential and  $\tilde{J}_s$  and  $\tilde{J}_{\text{wall}}$  are respectively the current density through the sheath and through the probe impedance.

strongly on the coupling to ground ( $Z_{\text{probe}}$ ) of the probe/wall. If  $Z_{\text{gnd}} \rightarrow \infty$ , then the wall is truly floating, otherwise it is labelled as “partially floating” (or “grounded” if  $Z_{\text{gnd}} = 0$ ). A schematic of the potentials and impedances is shown in figure 2.4. Using the current continuity:

$$\tilde{J}_s = \frac{\tilde{V}_{\text{pla}}}{Z_s + Z_{\text{gnd}}} = \frac{\tilde{V}_{\text{wall}}}{Z_{\text{gnd}}} = \tilde{J}_{\text{wall}}, \quad (2.1.21)$$

Where  $\tilde{V}_{\text{wall}}$  is the oscillating wall potential. Therefore:

$$\tilde{V}_{\text{wall}} = \tilde{V}_{\text{pla}} \frac{Z_{\text{gnd}}}{Z_s + Z_{\text{gnd}}}. \quad (2.1.22)$$

Imposing that the time-averaged current is zero for simplicity and replacing  $V_{\text{pla}}$  by  $V_{\text{pla}} - V_{\text{wall}}$  in equation 2.1.11 since now the wall potential is not zero, gives:

$$0 = 1 - \frac{J_{\text{esat}}}{J_{\text{isat}}} \frac{1}{\tau} \int_0^\tau e^{\frac{\tilde{V}_{\text{wall}}(t) + \bar{V}_{\text{wall}} - \tilde{V}_{\text{pla}}(t) - \bar{V}_{\text{pla}}}{T_e/e}} dt. \quad (2.1.23)$$

Using equation 2.1.22 into equation 2.1.23, the time-averaged potential between the plasma and the partially floating wall is:

$$\bar{V}_{\text{pla}} - \bar{V}_{\text{wall}} = V_f + \frac{T_e}{e} \ln \left[ \frac{1}{\tau} \int_0^\tau e^{\frac{\tilde{V}_{\text{pla}}(t) \left( \frac{Z_{\text{gnd}}}{Z_s + Z_{\text{gnd}}} - 1 \right)}{T_e/e}} dt \right]. \quad (2.1.24)$$

If  $Z_{\text{gnd}} \rightarrow \infty$  (perfectly floating wall), equation 2.1.24 gives  $\bar{V}_{\text{pla}} - \bar{V}_{\text{wall}} = V_f$  as would be expected. If however  $Z_{\text{gnd}} < \infty$ , equation 2.1.24 shows how the potential drop between the plasma potential and a partially floating wall deviates from the floating potential. Using this equation, it is possible to estimates which impedance  $Z_{\text{gnd}}$  is

required to consider, with reasonable error, that a wall/probe is “floating”. This is particularly important for RF coupling where the impedances of stray capacitances can be small compared to the sheath impedance. It can also be seen that for  $Z_{\text{gnd}} = 0$  (grounded wall), equation 2.1.24 is equal to the equation for a grounded wall discussed previously (Eq. 2.1.12).

### 2.1.1 Self-bias potential

In capacitively-coupled plasma reactors, the RF electrode is often connected through a DC blocking capacitor and therefore no DC current can flow from the RF electrode. Consequently, if the RF and grounded surfaces in contact with the plasma are not identical (asymmetric electrodes) as shown in figure 2.5, a self-bias potential ( $V_{\text{sb}}$ ) builds up on the RF electrode. This effect can be described by looking at the time-averaged potential drop through the RF sheath (labelled “a”) and the ground sheath (labelled “b”) [28]:

$$V_{\text{sb}} = -(\bar{V}_{\text{a}} - \bar{V}_{\text{b}}). \quad (2.1.25)$$

Since the voltage drop across the sheaths are, to a first approximation, inversely proportional to the sheath capacitances, the sheath with the smaller area has a smaller capacitance hence a larger voltage drop [31]. In the standard case shown in figure 2.5,  $\bar{V}_{\text{a}} > \bar{V}_{\text{b}}$  and therefore  $V_{\text{sb}}$  is negative.

However, the variation of the sheath potential with the area ratio is more complicated as the sheath width varies with the sheath potential. Using the Child’s Law (Eq. 2.1.6) to relate these two parameters, the total RF current in both sheaths can be expressed as [28]:

$$I_{\text{a}} \propto \bar{V}_{\text{a}}^{\frac{1}{4}} \int_{A_{\text{a}}} n_{\text{a}}^{\frac{1}{2}}(x) d^2x \quad (2.1.26)$$

$$I_{\text{b}} \propto \bar{V}_{\text{b}}^{\frac{1}{4}} \int_{A_{\text{b}}} n_{\text{b}}^{\frac{1}{2}}(x) d^2x \quad (2.1.27)$$

where  $n_{\text{a}}$  and  $n_{\text{b}}$  are the plasma densities at the sheath edges and  $A$  is the surface in contact with the plasma. The RF current continuity imposes that  $I_{\text{a}} = I_{\text{b}}$  and, if  $n_{\text{a}} = n_{\text{b}}$ , both independent of  $x$  for simplicity, the ratio of the time-averaged voltages through both sheaths is:

$$\frac{\bar{V}_{\text{a}}}{\bar{V}_{\text{b}}} = \left( \frac{A_{\text{b}}}{A_{\text{a}}} \right)^4. \quad (2.1.28)$$

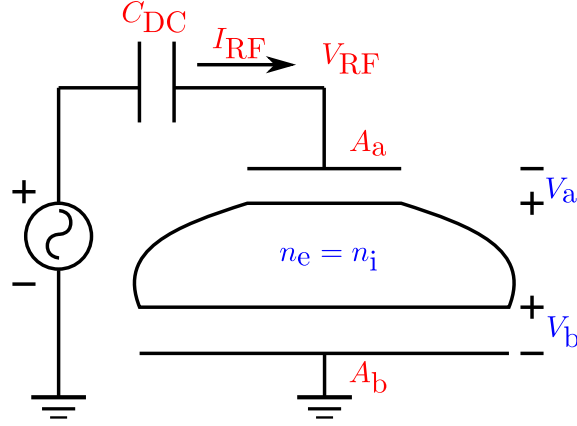


**Figure 2.5:** Asymmetric low frequency capacitive discharge. Figure taken from [28].

Therefore, since  $V_{sb} = \bar{V}_{RF} = -(\bar{V}_a - \bar{V}_b)$ , it is proportional to the ratio of electrodes area in contact with the plasma:

$$V_{sb} = -\bar{V}_b \left( 1 - \left( \frac{A_a}{A_b} \right)^4 \right). \quad (2.1.29)$$

The exponent of the area ratio varies with the model used to relate the sheath time-average potential drop to its density and thickness (i.e. Child's Law, constant  $\lambda_i$  law). Experimentally, this factor is  $\lesssim 2.5$  [28].

Equation 2.1.28 was obtained by assuming equal densities at both sheath edges ( $n_a = n_b$ ). If for some reason  $n_b = \alpha n_a$ , still independent of  $x$ , then:

$$\frac{\bar{V}_a}{\bar{V}_b} = \left( \frac{n_b}{n_a} \right)^{\frac{q}{2}} \left( \frac{A_b}{A_a} \right)^q = \alpha^{\frac{q}{2}} \left( \frac{A_b}{A_a} \right)^q. \quad (2.1.30)$$

This shows that, for a case where the densities are not equal, the area ratio determining  $V_{sb}$  is weighed by the ratio of densities at the sheath edges. In complex geometries, this effect could have a significant impact on the self-bias.

## 2.2 Ion bombardment

It was discussed in the previous section that the ions are accelerated toward the walls by the electric field inside the sheaths. In a collisionless plasma, the ions reach a wall with the energy equal to the potential through the sheath (times the electric charge). It was said that, due to their inertia and, to a first approximation, the ions motion is dominated by the time-averaged potential of the sheath and those potentials were calculated for several plasma and wall conditions in section 2.1. The influence of the potential oscillations on the ion bombardment energy is more complicated as

it depends of the ratio between ion transit time through the sheath ( $\tau_i$ ) to the RF period ( $\tau_{\text{RF}}$ ). Indeed, depending on the phase at which the ions enter the sheath, the potential driving them is different. The amplitude of this phase-related spread of the ion velocity becomes small for large ratios of  $\tau_i/\tau_{\text{RF}}$  [28]. In a collisionless sheath,  $\tau_i$  can be estimated by  $\tau_i = 3s(\frac{M_i}{2eV_s})^{\frac{1}{2}}$  where  $s$  is the sheath width and  $\bar{V}_s$  is the time-average voltage through the sheath. With the typical experimental conditions here ( $s = 8$  mm: (see table:5.2) and  $\bar{V}_s = 40$  V), the transit times are: 270, 390 and 480 ns for  $\text{H}^+$ ,  $\text{H}_2^+$  and  $\text{H}_3^+$  respectively and 1700 ns and 1750 ns for  $\text{Ar}^+$  and  $\text{ArH}^+$ . The RF period at 13.56 MHz is 74 ns. Therefore, in argon, the transit time is  $\sim 23$  times the RF period. In hydrogen, the dominant ion is  $\text{H}_3^+$  [32–34] and its transit time in a collisionless sheath is 6.4 times the RF period. However, at 50 Pa or more, collisions become important and  $\tau_i$  increases. Therefore, in both gases,  $\tau_i/\tau_{\text{RF}}$  is large and the phase-related spread of the ion velocity distribution is expected to be smaller or similar to the RFEA energy resolution. Hence only the time-averaged energy is measured here.

In a collisional sheath, the ions lose energy by collisions with the gas. In argon, two collisional process are involved: elastic and resonant charge exchange collisions. Resonant charge exchange can occur when ions move in their parent gas and it is an interchange of roles between ion and neutral by the resonant transfer of an electron [35]. Therefore, in argon, only  $\text{Ar}^+$  has resonant charge exchange collisions with Ar whereas  $\text{ArH}^+$  does not. Resonant charge exchange collisions are of particular importance for the ion bombardment energy as they represent the dominant loss of ion energy in this gas [36–38]. Therefore, at pressures where elastic collisions have no significant effect on the ion energy, the  $\text{ArH}^+$  reach grounded walls with an energy equal to  $\bar{V}_{\text{pla}}$ .

In a sheath composed only of  $\text{Ar}^+$  ions originating from the bulk (no ionisation inside the sheath), assuming the charge exchange cross-section is independent of the ion energy, the theoretical ion energy distribution in the presence of charge exchange collisions can be calculated with the following argument [36]: The number of charge exchange collisions between  $z$  and  $z + dz$  is  $n_0 \frac{dz}{\lambda_{\text{cx}}}$  where  $n_0$  is the number of ions entering the sheath,  $\lambda_{\text{cx}}$  is the charge-exchange mean free path and  $z$  is the distance to the wall. The probability that these ions will not have another charge exchange collision until the wall is  $e^{-\frac{z}{\lambda_{\text{cx}}}}$ . Therefore, the number of ions reaching the wall with the energy  $eV_z$  is:  $\frac{n_0}{\lambda_{\text{cx}}} e^{-\frac{z}{\lambda_{\text{cx}}}} dz$ . Assuming a quadratic evolution of the potential [39, 40] in the sheath, then  $\left( z = s \left[ 1 - \left( 1 - \frac{V_z}{V_s} \right)^{\frac{1}{2}} \right] \right)$  where  $V_s$  is the

voltage drop through the sheath. Finally, the ion energy distribution is obtained [36]:

$$\frac{dN}{dV} = \frac{n_0}{V_s} \frac{s}{2\lambda_{cx}} \left(1 - \frac{V_z}{V_s}\right)^{-\frac{1}{2}} e^{\frac{-s}{\lambda_{cx}} \left[1 - \left(1 - \frac{V_z}{V_s}\right)^{\frac{1}{2}}\right]}. \quad (2.2.1)$$

It has to be noted that the ions that do not suffer any collision but arrive at the wall with energy equal to the time-averaged sheath potential have not been included so far. Their relative number is given by  $n_0 e^{-\frac{s}{\lambda_{cx}}}$ . Theoretically, these collisionless particles all have the same energy and therefore their energy distribution is  $n_0$  times a Dirac function. Experimentally, the shape of this high-energy peak, as well as for the rest of the energy distribution, will of course depend on the instrumental resolution [36]. Therefore, to compare the theoretical distribution with the measurements (Sec. 4.4, Fig 4.8), the theoretical distribution, including the collisionless ions, is convolved with a Gaussian function having a full width at half maximum similar to the measurement resolution.

In a plasma such as hydrogen, the chemistry in the sheath is more complex since there are three different ions ( $H^+$ ,  $H_2^+$  and  $H_3^+$ ) which undergo a complicated chemistry. The collisions with the background gas can convert one ion species into another (i.e.  $H_2^+$  into  $H_3^+$ ). To illustrate the complexity, the different relevant cross-sections are shown in figure 2.6. Using this set of reactions, the main reactions in the plasma and the sheath were discussed by [34]. Outside the sheath, as the ion velocity is small, the  $H_2^+$  are likely to have an exothermic reaction with  $H_2$  and create  $H_3^+$ . Therefore, the majority of ions entering the sheath are  $H_3^+$ . At low energy, these ions have only momentum transfer collisions whose cross-section quickly decreases with the ion energy. Starting at 10 eV, Collision-Induced (CID) dissociative and asymmetric charge exchange collisions also becomes possible and quickly dominates the collisions. At this point,  $H_3^+$  ions are either continuing in free fall or are reacting to form  $H^+$  or  $H_2^+$  ions.  $H^+$  ions have a similar behaviour as  $H_3^+$  with an asymmetric charge exchange collisions starting at 2 eV whereas  $H_2^+$  ions tend to create again  $H_3^+$  or have charge exchange with  $H_2$ . To add to this complexity, some ions can be created inside the sheath by energetic secondary electrons or when electrons are accelerated into the sheath during field reversal (see Sec. 4.3). Therefore, due to the complexity of this chemistry, there is no simple analytical calculation of the ion energy distribution in hydrogen [34].

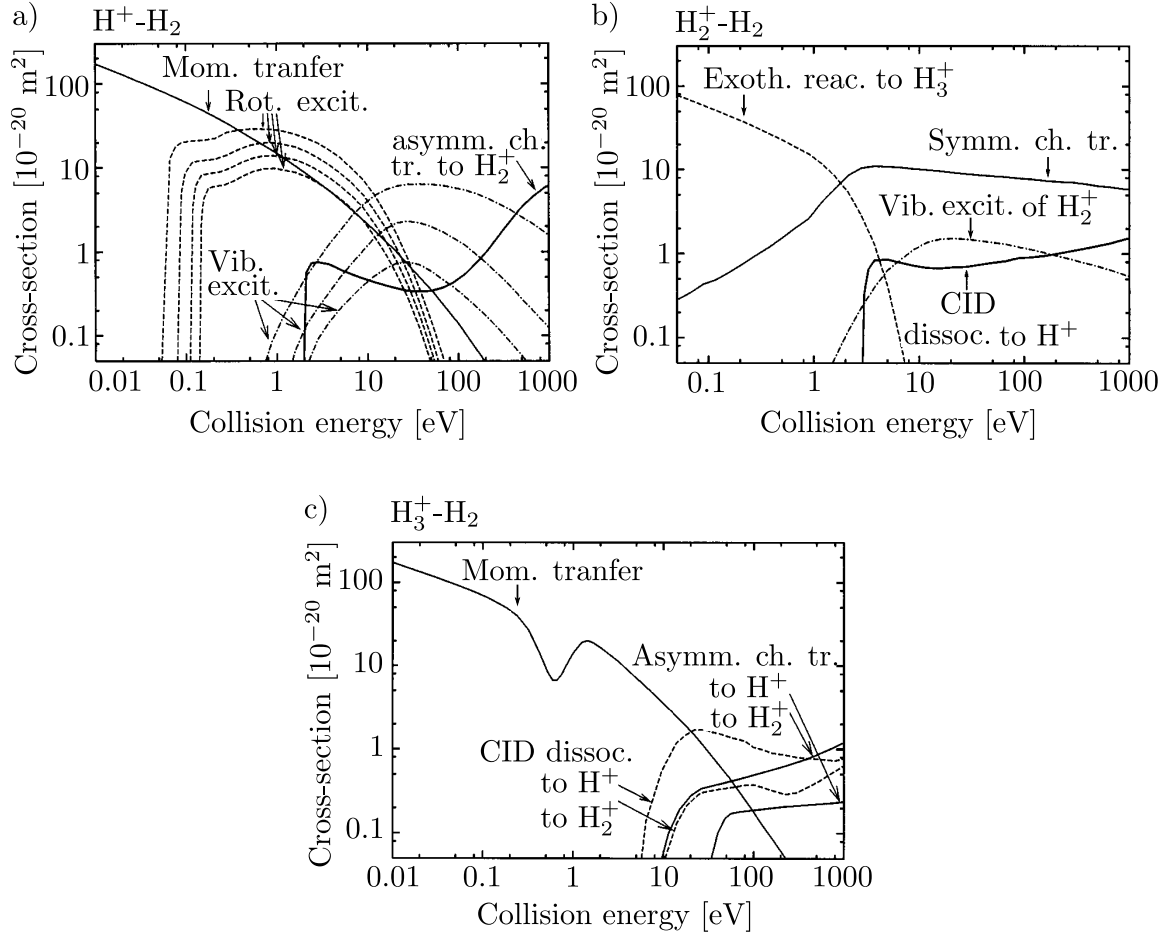


**Figure 2.6:** Cross-sections for (a) the  $\text{H}^+$ , (b) the  $\text{H}_2^+$  and (c) the  $\text{H}_3^+$  collisions in  $\text{H}_2$ , taken from [41]. The cross-sections include momentum transfer, rotational and vibrational excitation, asymmetric and symmetric charge transfer, exothermic reaction and Collision Induced (CID) dissociation.

## 2.3 Plasma simulation

The plasma was simulated using a two dimensional, two fluid model with the commercial finite element solver COMSOL [42]. The particles and momentum conservations are briefly derived in appendix A by integrating the moments of the Boltzmann equation [28, 43]. The particle conservation is:

$$\frac{\partial}{\partial t}n_\alpha + \nabla \cdot n_\alpha v_\alpha = S - L, \quad (2.3.1)$$

where  $\alpha = i, e$  represents the particle type (ion or electron),  $v_\alpha$  is mean velocity,  $S$  and  $L$  are the particles source and loss rates. The momentum conservation is:

$$m_\alpha n_\alpha \left[ \frac{\partial}{\partial t}v_\alpha + v_\alpha \cdot \nabla v_\alpha \right] = q_\alpha n_\alpha E - \nabla P_\alpha - m_\alpha n_\alpha \nu_{m,\alpha} v_\alpha, \quad (2.3.2)$$

where  $q_\alpha$  is the electric charge, the external forces are caused by an electric field  $E$  and  $P_\alpha$  is the partial pressure of particles  $\alpha$ . The collisions with the background gas is given by  $m_\alpha n_\alpha \nu_{m,\alpha} v_\alpha$  where  $\nu_{m,\alpha}$  is the momentum transfer frequency. In these equations,  $P_\alpha$  is the partial pressure and not the total pressure because the pressure is calculated by the second momentum from the one particle distribution (see App. A, Eq. A.0.4).

The different moment of the Boltzmann equation form a non closed set of equation as each moment depends on a higher order moment. To close this infinite progression of momentum equations, this state equation  $P = n_\alpha k_B T_\alpha = n_\alpha T_\alpha$  was selected (see App. A). Here  $T_\alpha$  is in kelvins and  $T_\alpha$  in electron volts. This closure choice is common in fluid models [43] and is usually associated with the assumption that the system is isothermal [44]. Here however,  $\nabla P_\alpha = (n_e \nabla T_e + T_e \nabla n_e)$  since the normalised electron temperature gradient ( $\nabla T_e / T_e$ ) is non-negligible compared to the normalised density gradient ( $\nabla n_e / n_e$ ) (see the gradient around the grid hole of a grid reactor in section 6.2). This term was also kept by other studies [45, 46]. This temperature gradient term is neglected for ions since their temperature is in equilibrium with the gas and is therefore isothermal to a good approximation.

Equation 2.3.2 can be simplified in RF plasmas at 13.56 MHz and 50 Pa. The acceleration term ( $\frac{\partial}{\partial t}v$ ) is neglected for slow time variation and the adiabatic ( $v \cdot \nabla v$ ) term is neglected with regard to the influence of collisions at high pressure (50 Pa) [28, 44]. Using these approximations and multiplying equation 2.3.2 by  $n_\alpha$  gives the particle flux:

$$\Gamma_\alpha = n_\alpha v_\alpha = q_\alpha \mu_\alpha n_\alpha E - D_\alpha \nabla n_\alpha - n_\alpha \mu_\alpha \nabla T_\alpha, \quad (2.3.3)$$

where  $\mu_\alpha = \frac{1}{m_\alpha \nu_{m,\alpha}}$  is the mobility constant and  $D_\alpha = \frac{T_\alpha}{m_\alpha \nu_{m,\alpha}}$  the diffusion constant. Substituting equation 2.3.3 into equation 2.3.1 gives the electron and ion continuity equations:

$$\frac{\partial}{\partial t} n_e + \nabla \cdot \Gamma_e = k_{\text{ion}}(T_e) n_e n_n \quad (2.3.4)$$

$$\begin{aligned} \Gamma_e &= -\mu_e n_e E - D_e(T_e) \nabla n_e - n_e \mu_e \nabla T_e \\ \frac{\partial}{\partial t} n_i + \nabla \cdot \Gamma_i &= k_{\text{ion}}(T_e) n_e n_n \quad (2.3.5) \\ \Gamma_i &= +\mu_i n_i E - D_i \nabla n_i, \end{aligned}$$

where  $n_n$  is the neutral gas density. The source of particles is given by the electron impact ionisation of the background gas ( $S = k_{\text{ion}}(T_e) n_e n_n$ ) where  $k_{\text{ion}}(T_e)$  is the ionisation rate and the particle loss term ( $L$ ) in equation 2.3.1 is neglected inside the plasma. To calculate the electron temperature required to determine the ionisation rate and the temperature gradient, the electron energy continuity is calculated from the second moment of the Boltzmann equation:

$$\frac{\partial}{\partial t} n_e \epsilon + \nabla \cdot \Gamma_w = -e \Gamma_e \cdot E - k_{\text{loss}}(T_e) n_e n_n \quad (2.3.6)$$

$$\begin{aligned} \Gamma_w &= -\frac{5}{3} \mu_e (n_e \epsilon) E - \frac{5}{3} D_e \nabla (n_e \epsilon) - \frac{5}{3} n_e \mu_e \nabla T_e \\ k_{\text{loss}} &= \sum_l \epsilon_j k_j(T_e) \end{aligned} \quad (2.3.7)$$

where  $n_e \epsilon$  is the electron energy density,  $k_j(T_e)$  are the excitation and ionisation reaction rates and  $\epsilon_j$  is the energy loss per excitation and ionisation. The electron temperature is calculated from the ratio of electron energy density and electron density :

$$T_e = \frac{2}{3} \frac{n_e \epsilon}{n_e}. \quad (2.3.8)$$

Finally, the electric field is calculated using the Poisson equation:

$$\nabla^2 V = -\frac{e}{\epsilon_0} (n_i - n_e), \quad (2.3.9)$$

With this set of equations, numerical instabilities could appear in the sheaths. These instabilities are due to a numerical error in the calculation of  $n_e$  inside the sheaths, close to the wall. There  $n_e$  abruptly drops by a few orders of magnitude and could, at one mesh point, be zero or even slightly negative. This effect is known, and to prevent it, it was suggested to use the logarithm of the densities in the model [47]. However, this formulation also renders the model unstable close to the walls [47].



Therefore, here, it was decided to stabilise the model by using an arbitrary pedestal for the electron temperature  $\left(T_e = \frac{2}{3} \frac{n_e \epsilon + \max(n_e/100)}{n_e + \max(n_e/100)}\right)$  whose influence was negligible outside the sheath. Furthermore, the absolute values of the densities were used in equation 2.3.9  $\left(\nabla^2 V = -\frac{e}{\epsilon_0} (|n_i| - |n_e|)\right)$ . It was verified that this stabilisation method had no significant influence as the obtained results are similar to those of D. Passchier [44].

### 2.3.1 Simulation domains and boundaries

The system boundary conditions are important parameters for the simulation. The simulation domains and boundaries in the parallel-plate and the grid reactors (see Ch. 3.1) are shown in figure 2.7. The boundaries are divided into two distinct groups: the surfaces (“wall”) and the symmetry planes (“symmetry”). At the latter boundaries, the fluxes are set to zero ( $\Gamma_\alpha \cdot \hat{n} = 0$ ), where  $\hat{n}$  is the normal to the boundary and the electric field is perpendicular to the surface ( $\hat{n} \cdot \epsilon_0 E = 0$ ). The wall boundaries (“wall”) act as particle sinks. Therefore, in this model, the ions and electrons are created by ionisation in the volume and lost by recombination on the walls. The electron, ion and electron energy fluxes to the walls are given by [48]:

$$\Gamma_{e,\text{wall}} = \frac{1}{4} n_e v_{\text{the}} \quad (2.3.10)$$

$$\Gamma_{i,\text{wall}} = \mu_i n_i E \quad (2.3.11)$$

$$\Gamma_{ee,\text{wall}} = \frac{1}{3} n_e e v_{\text{the}}, \quad (2.3.12)$$

where  $v_{\text{the}} = (8T_e/\pi m_e)^{\frac{1}{2}}$  is the electron thermal velocity. The electrons and electron energy fluxes to the walls are dominated by the thermal velocity. Inside an isothermal plasma, the thermal fluxes do not contribute to the fluid particle fluxes. This is because, since the fluxes are isotropic, the total thermal flux of particles in one direction is balanced by an identical flux of particles flowing in the opposite direction. However, next to a wall, the thermal flux toward the wall is not compensated by a thermal flux coming from the wall since the wall is not emitting particles in this model. For the ion flux toward the walls (Eq. 2.3.11), the diffusive term ( $D_i \nabla n_i$ ) was neglected with respect to the drift term ( $\mu_i n_i E$ ) inside the sheath.

The Electrical boundaries at the walls are:

$$V_{\text{RF electrode}} = \frac{V_{\text{pp}}}{2} \sin(\omega t) + V_{\text{sb}} \quad (2.3.13)$$

$$V_{\text{Gnd}} = 0, \quad (2.3.14)$$

where equation 2.3.13 is for the RF electrode and equation 2.3.14 for the grounded grid and the grounded electrode. In this simulation,  $V_{\text{sb}}$  was calculated by an ordinary

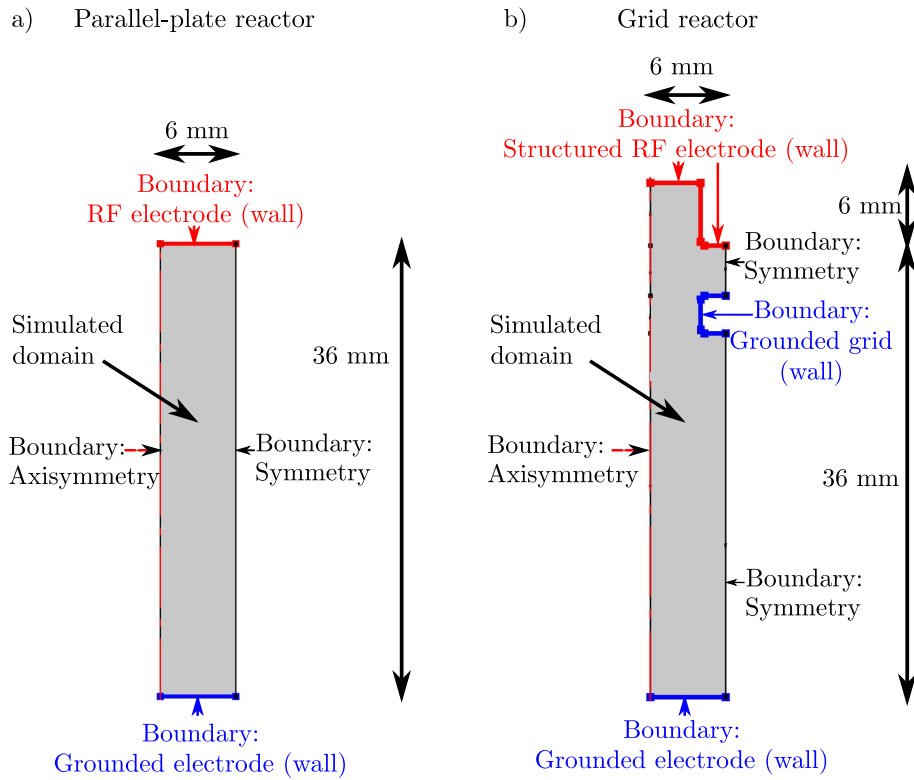


**Figure 2.7:** Simulation domains and boundaries in (a) the parallel-plate reactor and (b) the grid reactor. The 6 mm deep cylindrical structure in the grid reactor RF electrode is shown. The simulation domains in the parallel-plate reactor is covered with  $\sim 3300$  mesh points and with  $\sim 7000$  mesh points in the grid reactor. The mesh density is higher close to the wall boundaries.

differential equation, integrating the current reaching the RF electrode [49]:

$$\frac{\partial V_{\text{sb}}}{\partial t} = (\Gamma_{\text{i,wall}} - \Gamma_{\text{e,wall}})A/C_{\text{DC}}, \quad (2.3.15)$$

where  $A$  is the RF electrode area and  $C_{\text{DC}}$  is the DC blocking capacitor connected to the RF electrode.

It was decided to make this model simple but not simpler. Therefore, in argon and hydrogen, only a few dominant chemical reactions were chosen to reproduce the general plasma behaviour and only one ion species for each gas ( $\text{Ar}^+$  and  $\text{H}_2^+$ ).

In this study, the chosen cross-sections in argon are: ionisation and one excitation. In this gas, the threshold energy of these two reactions are similar. In hydrogen, three cross-sections are kept: one ionisation, one high energy excitation and one molecular low energy (rovibrational) excitation. As in argon, the ionisation and high energy excitation reactions have similar threshold energies, however the low energy excitation has a lower threshold energy.

The reaction rate constants in both gases were calculated with Boltzmann equation solver Bolsig<sup>+</sup> [50] using the cross-section databases therein. The reaction rates in both gases are shown in figure 2.8 and the chosen ones are listed in table 2.1. In the same table are listed the mobilities and ion diffusion constants.

The choice to make this model simple but not simpler reduced both the model complexity and the calculation time. Nonetheless, this model gives a reasonable description of the relevant physical phenomena as shown in chapter 6. More complex models can include several chemical reactions, several ions (i.e.  $\text{H}^+$ ,  $\text{H}_2^+$ ,  $\text{H}_3^+$  and  $\text{H}^-$ ), metastable states, elastic collisions [32,33]

## 2.4 Plasma breakdown

This section briefly discusses some concepts regarding the plasma breakdown. These concepts will be useful to understand the underlying phenomena behind the measured breakdown voltages in the two reactors used in this study.

Before breakdown occurs, the density of free electrons and ions inside the gas are too low to have a significant influence on the electric field created by the electrodes. The electrons are accelerated in this electric field, they gain energy, have collisions with the gas and thereby produce ionisation reactions. The electrons are lost by two different channels: they recombine on the walls; volumetric collisions becomes a possible non-negligible source of recombination for electrons in certain gases at pressures above a few hundreds Pa. If the production rate exceeds the loss rate, then

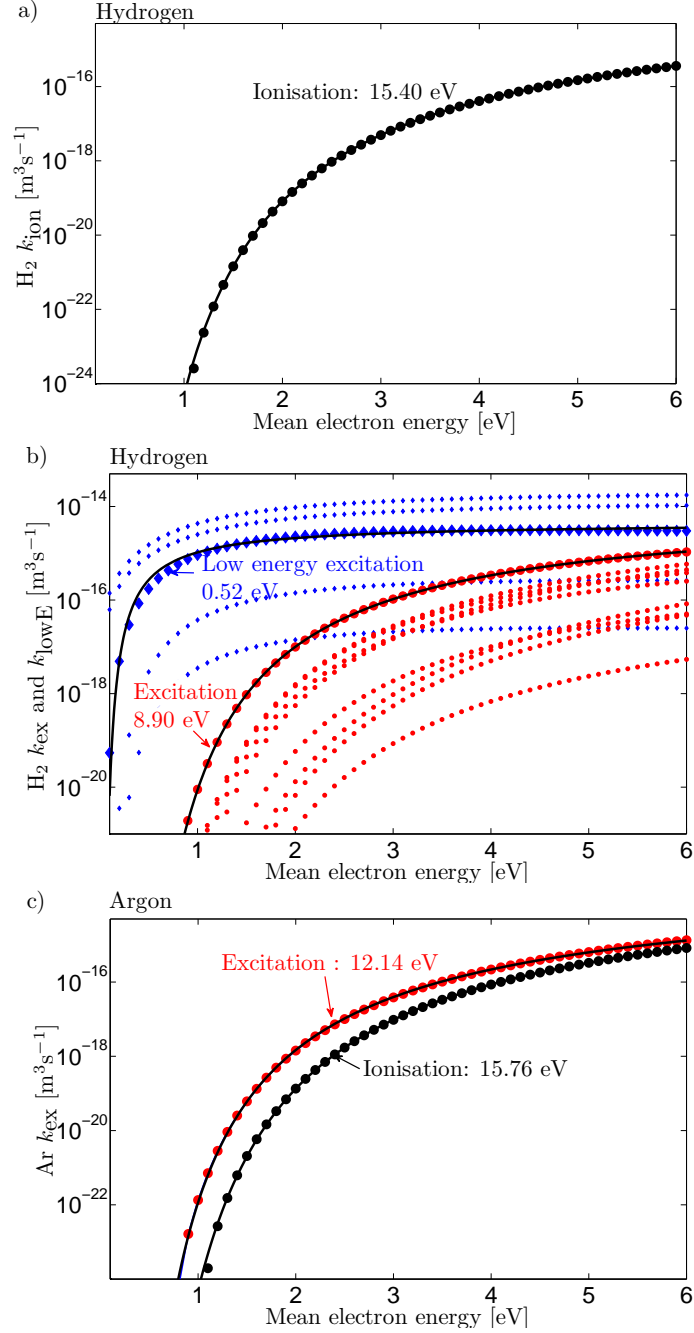


**Figure 2.8:** (a) Ionisation rate constant ( $k_{ion}$ ) in hydrogen, (b) excitation ( $k_{ex}$ ) and low energy molecular excitation ( $k_{lowE}$ ) rate constants in hydrogen. (c) Ionisation ( $k_{ion}$ ) and excitation ( $k_{ex}$ ) rate constants in argon. The dominant excitation rate constants for hydrogen were chosen regarding their contribution to  $k_{loss}$  and they are indicated by a thicker line. In (b), the other rate constants are shown for reference. The dots are the calculated rate constants and the black lines are the interpolated functions used in the model.

	Argon		Hydrogen	
$\mu_e [\text{Torr m}^2 \text{V}^{-1} \text{s}^{-1}]$	30	[48]	40	[50]
$\mu_i [\text{Torr m}^2 \text{V}^{-1} \text{s}^{-1}]$	$1.53 \cdot 10^{-1}$	[51, 52]	$9.8 \cdot 10^{-1}$	[51, 52]
$D_i [\text{Torr m}^2 \text{s}^{-1}]$	$4.2 \cdot 10^{-3}$	[51, 52]	$2.7 \cdot 10^{-2}$	[51, 52]
$k_{\text{ion}} [\text{m}^3 \text{s}^{-1}]$	$2.0 \cdot 10^{-14} \cdot T_e^{0.62} \cdot e^{\frac{-16}{T_e}}$	[28]	$7.3 \cdot 10^{-15} \cdot T_e^{0.61} \cdot e^{\frac{-15}{T_e}}$	[50]
$k_{\text{ex}} [\text{m}^3 \text{s}^{-1}]$	$9.1 \cdot 10^{-15} \cdot T_e^{0.75} \cdot e^{\frac{-12}{T_e}}$	[28]	$1.2 \cdot 10^{-14} \cdot T_e^{-0.01} \cdot e^{\frac{-9}{T_e}}$	[50]
$k_{\text{lowE}} [\text{m}^3 \text{s}^{-1}]$			$4.0 \cdot 10^{-15} \cdot T_e^{0.06} \cdot e^{\frac{-0.9}{T_e}}$	[50]
$k_{\text{loss}} [\text{eVm}^3 \text{s}^{-1}]$	$15.8k_{\text{ion}} + 12.1k_{\text{ex}}$	[28]	$15.4k_{\text{ion}} + 8.9k_{\text{ex}} + \dots$ $+0.5K_{\text{lowE}}$	[50]

**Table 2.1:** Mobilities, diffusivity, rate constants and energy loss rate in both gases. The ion mobilities are calculated using the polarisability in [51] and the low field Langevin equation in [52]. The simulation is done at 50 Pa and 350  $V_{\text{pp}}$  in both gases.

the densities sharply increase and the plasma forms (breakdown). The voltage at which the breakdown occurs (breakdown voltage) is influenced by several factors (i.e. distance between the electrodes, electric field, gas composition, gas pressure) [53].

A typical measured breakdown curve in a parallel-plate reactor in hydrogen at 13.56 MHz is shown in figure 2.9. In this curve (Paschen curve), the breakdown voltage is shown as a function of the gas pressure ( $P$ ) and the distance between the electrodes ( $d$ ). The breakdown curve is separated into three different regions. In the first region (I), the breakdown voltage slowly decreases as the pressure decreases. This is due to the fact that, as the pressure goes down, the electrons lose less energy by collisions. They can travel a greater distance in the electric field and have a greater chance of ionizing the gas [53]. In region II, the breakdown voltage is relatively flat. In this region the electron loss to the walls increases due to their higher oscillation amplitude in the electric field [53]. Here the exact range of region II is only approximative since there is only two measurement points in the vicinity of this region. In region III, the breakdown voltage increases sharply. At the transition from the region II to the region III, the electron oscillation amplitude is of the order of  $d/2$  and therefore the electron loss to the wall increases strongly. In the region III, due to the higher fluxes of energetic electrons hitting the wall, the emission of secondary electrons and other surface effects become important. The breakdown voltage is represented as a function of  $P \cdot d$  because this factor is part of a similarity law [54]. According to this law, two reactors having the same similarity parameters have similar Paschen curves. Therefore, a reactor with a smaller distance  $d$  will have a similar Paschen curve as shown here but the observed features will occur at

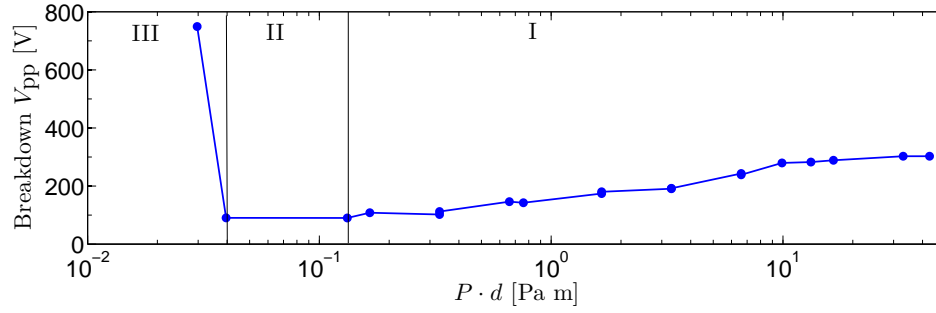


**Figure 2.9:** Typical measured breakdown voltage in a parallel-plate reactor in argon at 13.56 MHz. In this reactor,  $d = 36$  mm. The sections I-III are described in the text.

higher pressures. The variations of breakdown voltage are more complicated when the reactors are not simple parallel plates but instead have holes or protrusions [55]. However, to a certain extent, the breakdown curve of a reactor will be shifted to lower pressures if the distance between the electrodes is increased. This concept will be used in section 3.2.1 to reduce the breakdown voltage of the reactor developed in this study.

# Chapter 3

## Experimental setup

### 3.1 Reactor design

The reactors used in this study are shown in figure 3.1. On the left of this figure is the design of the parallel-plate reactor used in this study. On the right is a schematic of a grid used to convert this parallel-plate reactor into a so called grid reactor. A photograph of a typical grid is shown in figure 3.2. This grid is inserted between the RF and grounded electrodes as shown in figure 3.1 and in [56]. The grid edges are held by the reactor grounded sidewalls between the reactor top and grounded reactor box. This fixes the ground potential of the grid. As the grid is only held on its sides, the grid tends to bend under its own weight, especially when the reactor is heated to  $\sim 200^\circ\text{C}$  during deposition. The distance between the RF electrode and the ground electrode is kept identical in both reactors by adjusting the height from the sidewalls to compensate for the thickness of the grid.

The reactor is installed in a vacuum chamber which can be kept at a lower pressure than the reactor to reduce contamination by potential air leaks inside the vacuum chamber. The gases used in this study are pure argon and hydrogen for the study of plasma properties and a mixture of silane and hydrogen for the depositions done at Oerlikon Solar-Lab. The argon and hydrogen gas flows are controlled with mass flows controllers (Tylan FC-2900V, range: 500 sccm for Ar and 1000 sccm for  $\text{H}_2$ ) and the typical flows are 200 sccm for argon and 150 sccm for hydrogen. The continuous injection of gas and pumping avoids any increasing contamination of the gas inside the reactor from wall degassing and potential air leaks.

The gases are injected into the top of the reactor where they are channelled to a volume between the RF electrode and the reactor top. There, a grid kept at floating potential prevents plasma break-down. The gas flows to the reactor chamber through

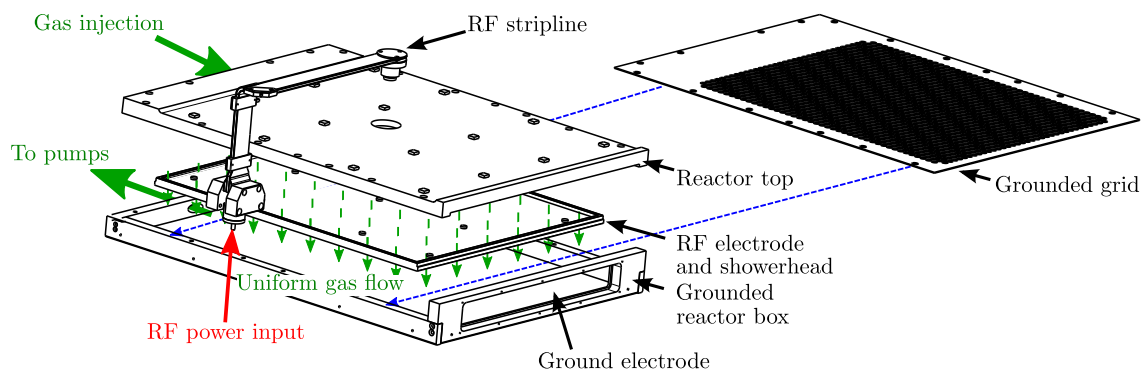


**Figure 3.1:** Parallel-plate reactor schematic with gas injection, exhaust and RF feeding system. The grounded grid on the right hand side shows an example of grid and of where it is inserted in the parallel-plate reactor. Reactor dimensions: width: 47 cm, length: 57 cm, electrode area:  $0.25 \text{ m}^2$ , inter electrode distance is 36 mm. Standard grid dimensions: distance to RF electrode: 4 mm, holes diameter: 8 mm, grid thickness: 3 mm.

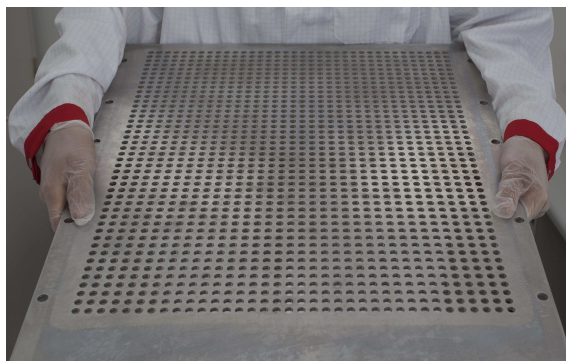


**Figure 3.2:** Photograph of a the grounded grid composed of an array of  $36 \times 44$  holes with a diameter of 8 mm. The ion bombardment energy in this grid reactor was found to be relatively insensitive to variations of the grid geometry as long as the plasma was present inside the grid holes (see Sec. 5.5.1).

uniformly spaced tiny holes built into the RF electrode. The gas exhaust is placed in the rear reactor wall. This gas injection system when coupled with a symmetric double side or single side pumping ensures homogeneous lateral distribution of gas and radicals species into the reactor [57].

The gas pressure is measured with a Baratron gauge just outside the reactor, at the beginning of the gas exhaust line. The typical base pressure of the system is 0.1 Pa or lower and the typical working pressure is 50 Pa. No significant pressure drop from the reactor chamber to the Baratron gauge is expected. The pressure is regulated by a butterfly valve (MKS type 653-B) placed after the Baratron gauge and controlled by the Baratron gauge controller. The exhaust pumps are a roots pump (Pfeiffer WKP500,  $500 \text{ m}^3 \cdot \text{hour}^{-1}$ ) assisted by a dry pump (Edwards QDP40,



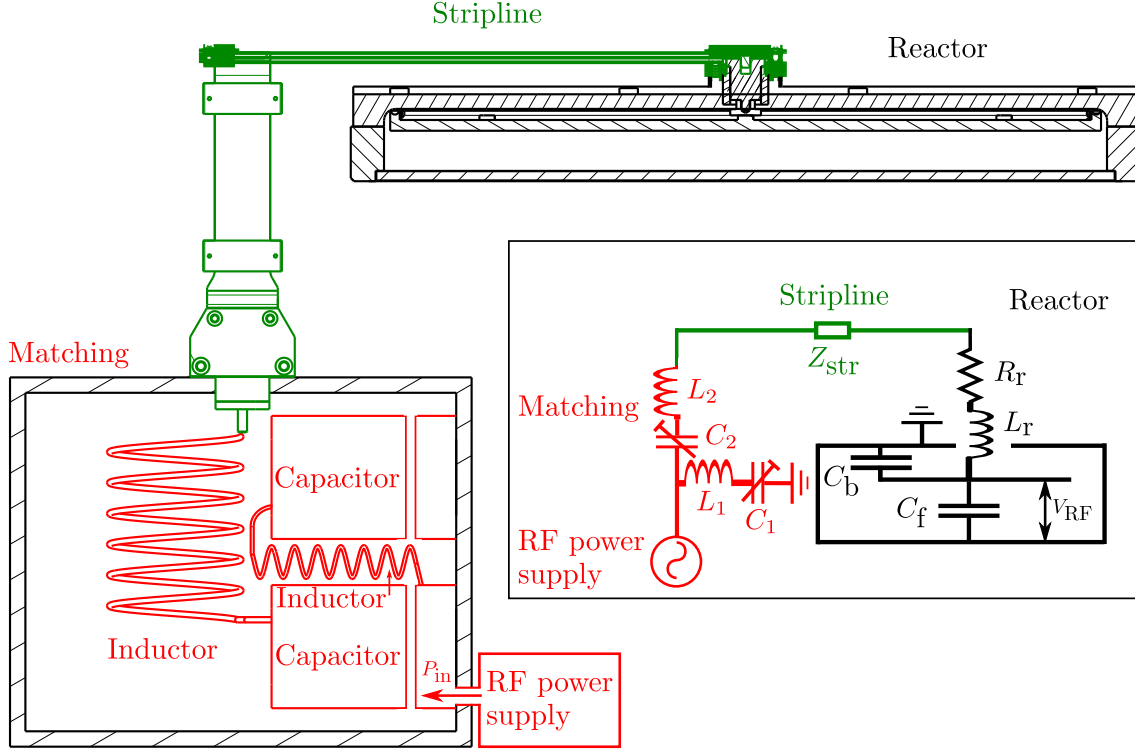


**Figure 3.3:** Side view of a parallel-plate reactor with the RF conducting stripline and the match-box.  $P_{in}$  is the injected RF power. Inset: Equivalent circuit with the matching elements ( $C_{1,2}$  and  $L_{1,2}$ ) and the stripline impedance ( $Z_{str}$ ). The reactor impedance is decomposed into :  $R_r$  the reactor resistance ( $\sim 0.2 \Omega$ );  $L_r$  the inductance and the capacitance from the back of the RF electrode to grounded box ( $C_b$ ) and from the front of the RF electrode to the grounded electrode and sidewalls ( $C_f$ ).  $V_{RF}$  is the potential on the RF electrode. Changing to the grid reactor increases  $C_f$ .

$44 \text{ m}^3 \cdot \text{hour}^{-1}$ ).

The plasma measurements were done at 13.56 MHz using a RF generator (Hüttinger PFG5000RF). The RF power is measured by a power meter (Bird model 4421 with sensor model 4024) placed between the RF generator and matchbox. To maximise RF power transmission from the generator to the reactor, a conventional L matching circuit is installed as shown in figure 3.3. The impedance matching is done using two variable capacitors and fixed inductances. In the vacuum chamber, the RF power is conducted to the RF electrode via a stripline. This stripline was specially designed to avoid parasitic plasmas by keeping the distance between RF and grounded parts smaller than 2 mm and by filling all empty volumes with insulator (PTFE).

The parallel-plate reactor and grid reactor with plasmas are shown schematically in figure 3.4. In the parallel-plate reactor, the plasma occupies most of the volume between the electrodes whereas, in the grid reactor, the plasma is confined by the grid. The grid hole size and the distance between the RF electrode and the grid were

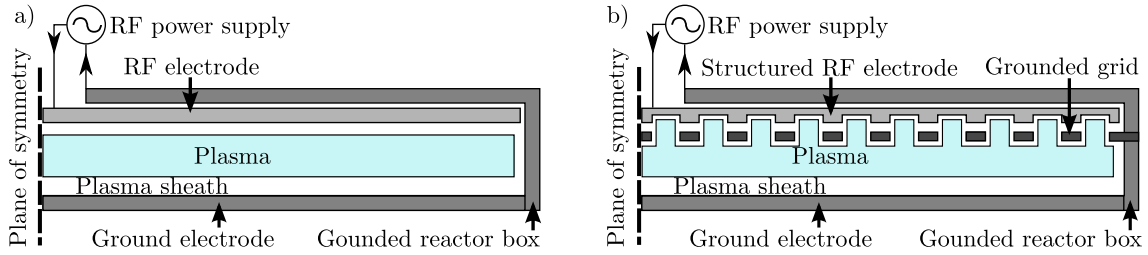


**Figure 3.4:** Representation of (a) a parallel-plate reactor and (b) a grid reactor [56]. In the grid reactor, the grid holes and RF electrode structures are aligned cylindrical holes of 8 mm diameter. The grid is made of aluminium and is 3 mm thick.

chosen so that a dense plasma forms inside the grid holes as shown in figure 3.5. The grounded grid divides the symmetric parallel-plate reactor into two connected volumes: a parallel-plate RF plasma source above, and a grounded chamber below. The plasma fills both volumes by conducting the plasma potential via the dense plasma in the grid holes as shown in figure 3.4(b).

The grid reactor developed here is different from the grid or triode reactors which have been studied extensively in the literature. In those, the grounded meshes/grids have been inserted into parallel-plate reactors to shield or screen the substrate from the plasma by confining the plasma to the other side of the mesh. There was no plasma in the grid hole and therefore the plasma potential was not conducted via the dense plasma in the grid holes. These studies were done with DC [13, 14] or RF [15–18] parallel-plate reactors. For the same purpose, the grid has also been biased [19–24], acting as a third electrode (hence “triode reactor”), also in combination with a substrate bias [25, 26].

It will be shown in chapter 5 that the presence of the dense plasma inside the grid holes and the conduction of potential through the grid are central to the reduction of ion bombardment energy in the grid reactor developed in this study.

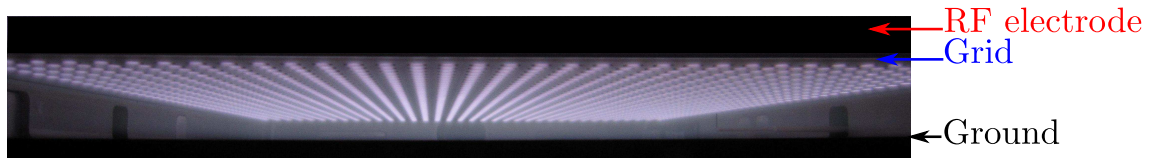


**Figure 3.5:** Photograph of a plasma inside the grid reactor seen from below the grid.

A photograph of hydrogen plasma in a grid reactor for two different distances between the RF electrode and the grid is shown in figure 3.6. This figure shows that, for a distance between the grid and RF electrode of 4 mm, the plasma is confined above the grid and expands well below the grid, as shown in figure 3.4(b). At a distance of 7 mm (Fig. 3.6(b)), the plasma expands more laterally above the grid, it

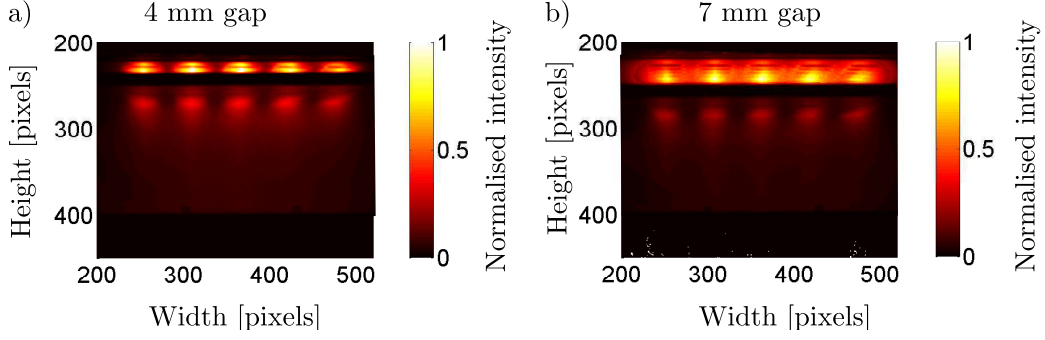


**Figure 3.6:** Photograph of a plasma in the “Test reactor” (Sec. 3.1.1) in hydrogen at 50 Pa in grid reactors with (a) 4 mm gap (standard gap) and (b) 7 mm gap. With a gap of 4 mm, the plasma in each hole is separated by a clear darker region whereas, at 7 mm, the distinction between each dense plasma is less pronounced.

starts to cover the electrode more uniformly and it is less intense below the grid. If this distance is increased further, the plasma does not fill the volume below the grid and the reactor becomes similar to a parallel-plate reactor where the grounded grid acts as a grounded electrode. Therefore, to keep the benefits from the influence of the reactor geometry on the ion bombardment energy (see Ch. 5), the grid reactor should be used with a relatively short distance between the electrode and the grid so that the plasma fills the volume below the grid. This distance between the RF electrode and the grid is a central point of the reactor design as it has a strong influence on the plasma properties, on the breakdown voltage and on the reactor impedance discussed in the following section.

The aim of the grid reactor is that the low ion bombardment energy is a consequence of the particular reactor geometry (see Ch. 5). To benefit from this, the standard working pressure should be kept relatively low (50 Pa here). At higher pressures, the collisions in the sheath would reduce the ion bombardment energy and there would be no real gain in reduced ion bombardment energy with this grid geometry compared to a parallel-plate reactor at similar pressure. Furthermore, working at low gas pressure prevents the undesired formation of powder with silane plasmas. Aside from these considerations, when the gas pressure is increased in the grid reactor, the plasma shrinks into the volume between the grid and RF electrode and stops expanding below the grid. A similar effect is observed by increasing the gap between grid and RF electrode and was discussed above. At 200 Pa or more, the plasma is nearly only present above the grid and the measured self-bias potential is nearly zero. Therefore, to benefit from the influence of the reactor geometry on the ion bombardment energy, the grid reactor is used at pressure of approximately 50 Pa.

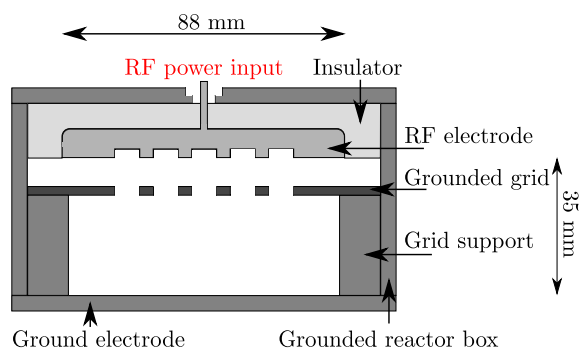


**Figure 3.7:** Schematic of the test reactor with a grounded grid. RF electrode dimensions:  $8.8 \times 8.8$  cm<sup>2</sup> (area:  $7.7 \cdot 10^{-3}$  m<sup>2</sup>), inter-electrode distance: 35 mm. Ceramic (Macor) was used as insulator around the RF electrode.

### 3.1.1 Setup for special reactor geometries

The vast majority of measurements were done in the semi-industrial reactor shown in figure 3.1. However, testing particular reactor geometries was more convenient with a smaller reactor (“test reactor”) having a more flexible setup. In this test reactor shown in figure 3.7, the area above the RF electrode is filled by a dielectric (PTFE), thus the gas flows inside the reactor through leaks at the periphery of the two glass sidewalls. This test reactor shares the same mass flow controllers and vacuum pumps as the semi-industrial reactor presented above. The grounded grid in figure 3.7 can be replaced by a metal plate with a diaphragm as shown later in chapter 5 (Fig. 5.8) or by a thin mesh as discussed in section 5.2.1.

## 3.2 Plasma breakdown and reactor impedance

### 3.2.1 Plasma breakdown

An initial difficulty with the development of this grid reactor design was to ignite the plasma. The reactor design had to be adapted, otherwise ignition required such high electric fields that it could potentially damage the equipment. The reactor RF stripline (see Fig. 3.1) had to be redesigned to prevent spurious plasma ignition within.

The conditions for plasma breakdown in the grid reactor differ strongly from the parallel-plate reactor due to the presence of the grounded grid. As discussed in section 2.4, the voltage at which breakdown occurs depends on the distance between the RF and grounded walls between which oscillating RF fields are present. In the parallel-plate reactor, the RF fields extend to the ground electrodes as shown in

figure 3.8(a). Therefore the electrons can oscillate in the RF fields within the whole distance between the electrodes. However, in the grid reactor, the electric potential is screened by the grounded grid and does not penetrate below the grid as shown in figure 3.8(b). Therefore, in the grid reactor, the plasma breakdown can only take place in this small volume. Due to this reduced distance in which the electrons oscillates, the electron loss to the walls is strongly increased resulting in a higher breakdown voltage ( $V_{BD}$ ) (see Sec. 2.4). Measured Paschen curves for the parallel-plate reactor and grid reactor are shown in figure 3.9. In this figure, one grid reactor has a flat RF electrode whereas the other reactor has a structured RF electrode as shown in figure 3.4(b). This figure shows that the breakdown voltages in the grid reactors for pressures below 200 Pa are higher than for the parallel-plate reactor. Furthermore, the breakdown voltages in the two grid reactors quickly increase at lower pressures. In this figure, the breakdown voltages in two different grid reactors are shown. The difference between the breakdown voltages of these two grid reactors shows how the RF electrode structure reduces  $V_{BD}$  since it allows for larger electron oscillations in the RF fields before the electrons collide with the walls. The effect of electrode structures on the breakdown has been discussed in [55]. Another method to reduce the breakdown voltage is to increase the distance between the grid and RF electrode. However, increasing this distance above 4 mm up to 11 mm had no significant influence on  $V_{BD}$  in the grid reactor. Furthermore, past a certain distance, the plasma shrinks out of the volume below the grid toward the volume between the grid and the RF electrode. At 50 Pa, this transition begins at distances above 4 mm as shown in figure 3.6 and the plasma is only present above the grid at distances above 11 mm. Therefore, it was decided to work with a distance of 4 mm with a RF electrode structure made with blind cylindrical cavities, a few millimeters deep and with the same radius as the grid holes.

### 3.2.2 Reactor impedance and matching

Inserting the grid not only increased the breakdown voltage as discussed in the previous section, it also reduced the reactor impedance. This reduced impedance increases the RF power required to reach the breakdown voltage. The impedances of both the parallel-plate reactor and the grid reactor can be represented by a simple equivalent circuit model shown in figure 3.3. The relevant RF voltage for the breakdown and for the plasma itself is the voltage drop across the combined capacitances  $C_{tot} = C_b + C_f$  as shown in figure 3.3. To calculate  $C_{tot}$  in both reactors, the reactor impedances at different frequencies were measured at the connection

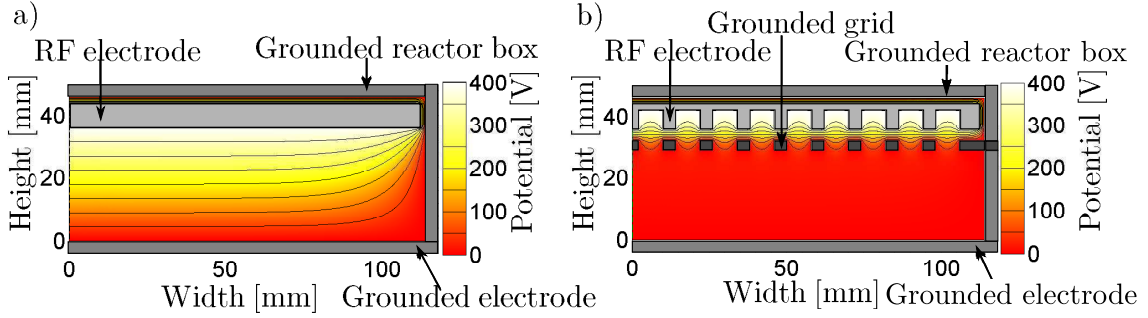


**Figure 3.8:** Electric potential (a) in the parallel-plate reactor and (b) in the grid reactor, in vacuum. The electric potential is calculated with an electrostatic model using COMSOL [42].

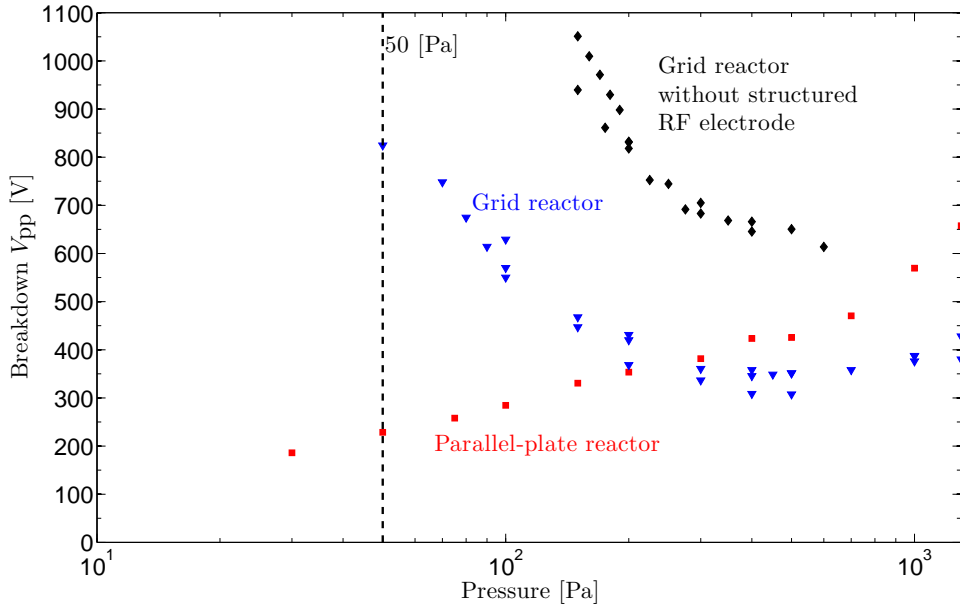


**Figure 3.9:** Breakdown voltage in hydrogen in the parallel-plate reactor, the standard grid reactor with its structured electrode and a grid reactor without structured electrode. The breakdown voltage is plotted as a function of the pressure  $P$  instead of  $P \cdot d$  since the interest here is to compare breakdown voltages at equivalent pressures.

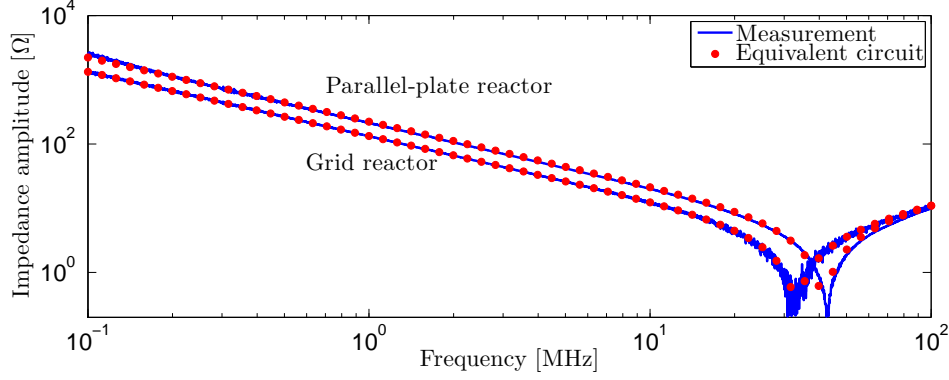


**Figure 3.10:** Reactor impedance magnitude as a function of frequency, measured by a network analyser in the parallel-plate reactor and the grid reactor. The capacitances, inductances and impedances at 13.56 MHz are 0.7 nF, 21 nH and  $0.2 - 13.8 i \Omega$  for the parallel-plate reactor, and 1.2 nF, 19 nH and  $0.2 - 8.3 i \Omega$  for the grid reactor.

between the reactor and stripline with a network analyser (Rohde & Schwarz ZVL). Typical impedance measurements are shown in figure 3.10. The values of the reactor inductance and capacitance are then calculated by interpolating the measured impedances with a combination of inductor and capacitor as shown in the equivalent circuit model. This measurement showed that  $C_{\text{tot}}$  is larger in the grid reactor due to the vicinity of the grounded grid and that the inductances are nearly equal in both reactors. The RF power required for the breakdown is increased because high voltage in a large capacitor implies strong RF currents flowing in the vacuum circuit (i.e. the inside matching, stripline and reactor) and therefore higher ohmic losses. The strong capacitance value is a drawback from the present design and is a common difficulty for capacitively coupled reactors. This capacitance increases further as the reactor area increases for deposition over larger areas. This capacitance could be reduced by increasing the distance from the RF electrode to the grounded box, thereby reducing  $C_b$ . However, special care must be taken to prevent plasma breakdown above the RF electrode.

The peak-to-peak voltage measured on the RF electrode as a function of power density in the two reactors is shown in figure 3.11. The steeper increase of  $V_{\text{pp}}$  in vacuum in the parallel-plate reactor is a direct consequence of the lower capacitance in this reactor. Using this figure, it is possible to estimate the RF power injected into the plasma using the subtraction method described in [28]. At 350 V<sub>pp</sub>, the power dissipated in the vacuum circuit in the parallel-plate reactor is 0.01 W/cm<sup>2</sup> whereas it is 0.02 W/cm<sup>2</sup> in the grid reactor. To maintain 350 V<sub>pp</sub> with a plasma, 0.04 W/cm<sup>2</sup> are necessary in the parallel-plate reactor, of which 0.03 W/cm<sup>2</sup> goes into the plasma since 0.01 W/cm<sup>2</sup> is dissipated into the vacuum circuit. In the grid

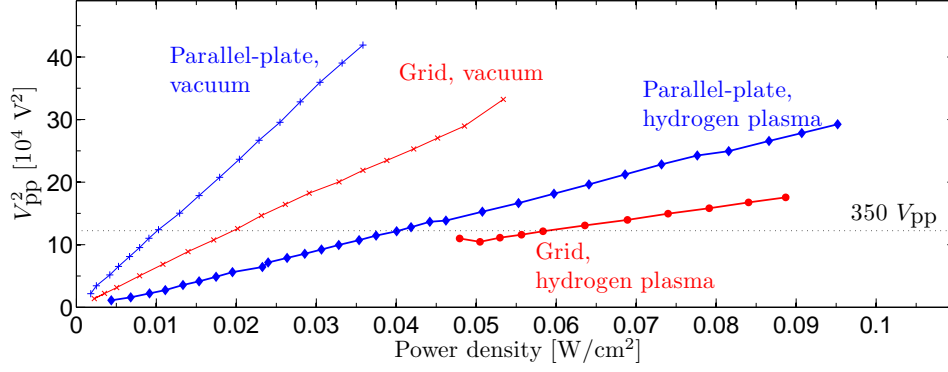


**Figure 3.11:** Peak-to-peak voltage as a function of the RF power density in vacuum and with a hydrogen plasma at 50 Pa in the grid reactor and in the parallel-plate reactor.

reactor,  $0.06 \text{ W/cm}^2$  is necessary to maintain  $350 V_{pp}$  with plasma and therefore only  $0.04 \text{ W/cm}^2$  goes into the plasma. This shows how the RF power required to maintain a given  $V_{pp}$  increases in both reactors and the resulting heating of the vacuum circuit. This subtraction method assumes that the plasma does not change the effective capacitance of the vacuum circuit which may not be true for these large area plasma reactors. Hence these injected RF powers are only an indication of the real powers. In this study, it is preferred to use the  $V_{pp}$  as a direct measure of the RF excitation amplitude on the RF electrode itself rather than the indirect measurement of RF power injected into the circuit.

Finally, the grid reactor has another complication compared to the parallel-plate reactor. In a parallel-plate reactor, once breakdown has occurred, the plasma directly fills most of the volume between the electrodes. However, in a grid reactor, the plasma usually ignites only in a few grid holes. The RF power must be increased so that the plasma is present in all holes. Once this occurs, the power can be reduced and the plasma remains in all holes over a broad power range. If the RF power becomes too small the plasma shrinks, leaving some grid holes without plasma. If the power is further reduced, the whole plasma shuts down. Nonetheless, in the grid reactor, the plasma could be maintained for hours without adjustment with a stable, complete and uniform array of intense plasmas, thus fulfilling the requirements for a robust industrial plasma process reactor.



# Chapter 4

## Diagnostics

In this section, the diagnostics used in this work will be presented. Special care is given to the Retarding Field Energy Analyser (RFEA) developed in the frame of this thesis and its energy resolution.

### 4.1 Voltage probe

To measure the potential on the RF electrode, a voltage probe was mounted directly onto the RF electrode. This probe, shown in figure 4.1, was designed prior to this thesis by Sansonnens et al. [58]. The probe is composed of two sections: First a capacitive and resistive voltage divider fixed directly on the electrode; then a voltage follower made with an operational amplifier driving the coaxial line to the  $50\ \Omega$  load of the oscilloscope (Lecroy WavePro 735Zi). The impedances of the voltage probe were adjusted to draw a very small RF current so that the voltage divisions between the RF electrode potential and the probe output potential are respectively 1/500 in DC, 1/530 at 13.56 MHz and 1/500 at 40.68 MHz. These division factors were measured by comparing the output of the voltage probe with the output from a calibrated commercial probe (Lecroy PP006, 1/10 division) having a measuring range up to 500 MHz. These measurements are done at atmospheric pressure where the RF electrode is accessible for the commercial probe. To ensure reliable RF voltage measurements, the voltage probe measurement head should be installed as closely as possible to the RF electrode. If the distance is too great, the measured voltage will be different from the RF electrode due to the voltage drop across the impedance of the connecting pieces. Also, the finite RF wavelength in the connecting pieces could also affect the measured voltage. However, here, the connector is a 1 cm long cylinder which is much smaller than the RF wavelength at 13.56 MHz ( $\sim 22\text{ m}$ )

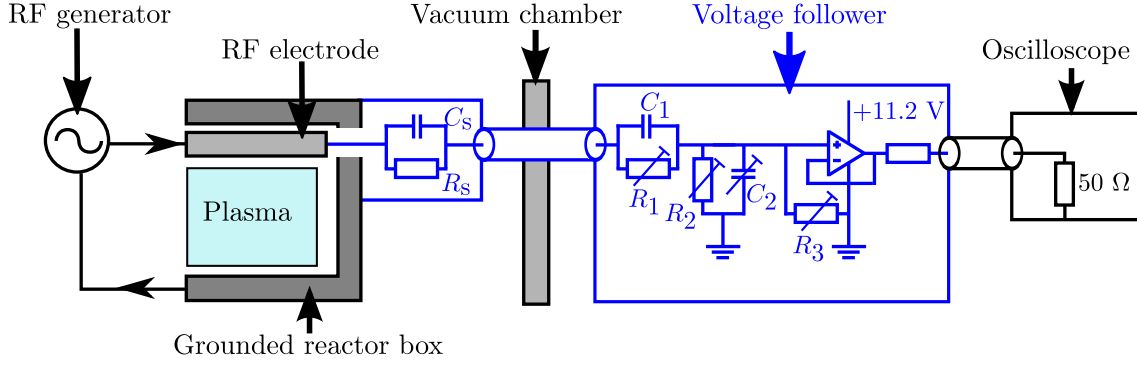


**Figure 4.1:** Scheme of the voltage probe mounted directly on the RF electrode.

and this cylinder impedance is negligible compared to the impedances inside the measurement head. Therefore, here, both effects are negligible. Nonetheless, probe calibration was made with great care to ensure errors below 5 %.

Measuring the peak-to-peak voltage ( $V_{pp}$ ) and self-bias potential ( $V_{sb}$ ) on the RF electrode allowed the estimation of the time-averaged plasma potential ( $\bar{V}_{pla}$ ) as will be explained in detail in section 4.5.

## 4.2 Langmuir probes

The plasma density profiles were measured with uncompensated Langmuir probes. Due to the oscillating potential drop between the probes and the plasma, the probes are used in the ion saturation regime. There, the current collected by a probe is the ion saturation current ( $I_{isat}$ ) which does not significantly vary with the oscillations of the plasma potential [28]. The ion density ( $n_i$ ) is calculated with a simple model which assumes a collisionless sheath and neglects the orbital motion of the ions attracted to a probe [28]:

$$n_i = \frac{I_{isat}}{0.61eAu_b} \quad (4.2.1)$$

where  $u_b = (T_e/m_i)^{\frac{1}{2}}$  is the ion velocity (Bohm velocity) as they enter the sheath around the tip of the probe,  $T_e$  is the electron temperature in eV. The factor 0.61 accounts for the ion density drop through the presheath and  $A$  is the probe collection area. In CCP plasmas,  $T_e$  is usually comprised between 1-5 eV [28] and since the ion density depends only on  $T_e^{\frac{1}{2}}$ , the error made by fixing  $T_e = 3$  eV is small compared to the ion density resolution of the probe. The probe bias is  $-27$  V delivered by batteries and protected from potential RF coupling by an inductor.

The probes schematics are shown in figure 4.2. The density profile along the electrodes was measured with a single Langmuir probe with a 4 mm long and 1 mm

diameter tip. The density profiles between the electrodes were measured with four vertical probes with smaller tips (2 mm long and 0.6 mm in diameter) to reduce their perturbations on the plasma. These vertical probes are aligned with the axis of grid holes. The vertical ion density profile is constructed by taking the mean density of the four vertical probes to reduce the probe alignment errors.

In this study, the interest is to measure ion density profiles and to roughly estimate the absolute ion densities in the different reactors. Therefore to increase the spatial resolution to the detriment of the absolute ion density resolution, probes with small tips have been used. The collection area depends on the estimation of the time-averaged sheath width surrounding the probe. This systematic error in estimating the collection area can affect the calculated absolute density by a factor of 5. However, it has no influence on the measured density profiles or when comparing the measured densities in different reactor geometries. To reduce the influence of this error, the densities measured by the vertical probes are adjusted to the density measured by the horizontal probe as the latter has a larger tip and is thus less sensitive to estimations of the probe collection areas.

Aside from its influence on the calculated density, the probe collection area also locally perturbs the plasma. This perturbation is usually small compared to the plasma volume such that it can be neglected. However, this is not the case when the plasma is confined in a small volume as in the grid holes of the grid reactor. There, the perturbation of the collection area prevents the measurement. Finally, the probe shaft blocks collection from below the probe, hence the collection region expands above the tip but not below it as shown by the  $\cap$  shaped collection area in figure 4.2. This shape can cause a small vertical shift of the measured density profile as observed later in figure 5.3.

## 4.3 Optical emission

Optical Emission Spectroscopy (OES) and Phase Resolved Optical Emission Spectroscopy (PROES) of the plasma were performed with a fast camera (PI-Max 1K), two optical band pass filters and a low jitter triggering system ( $< 1$  ns) as shown in figure 4.3. The pictures were taken with an exposure time of 2 ns hence the RF cycle evolution is segmented into 37 images at 13.56 MHz (RF period is 74 ns). The optical filter used in hydrogen is a tunable bandpass filter (VariSpec Vis from Cambridge Research & Instrumentations) centred on the  $H_\alpha$  emission line (656.3 nm) with a bandwidth of 20 nm. In argon plasmas, a fixed bandpass filter (Thorlabs)

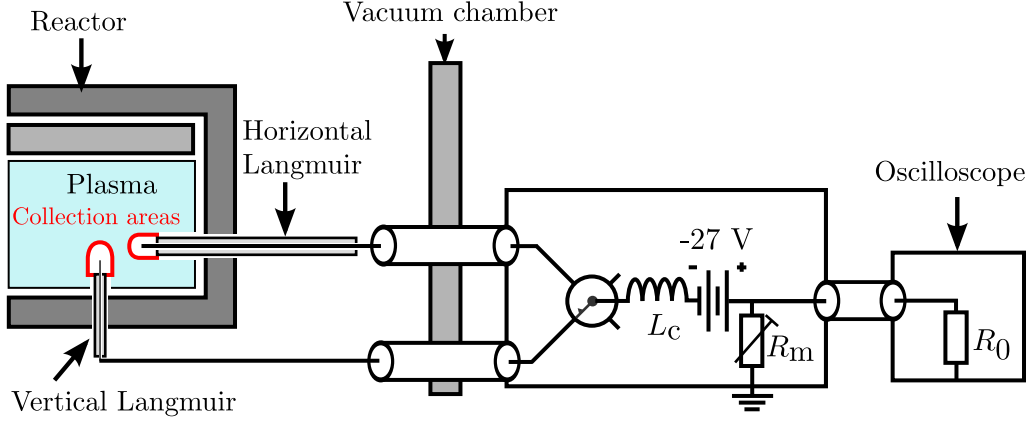


**Figure 4.2:** Scheme of the horizontal and one of the vertical Langmuir probes in a parallel-plate reactor. The horizontal probe is 7 mm above the bottom of the reactor box (ground electrode). The plasma perturbation due to the collection area of each probe is represented by a red line around the probe ( $\cap$ ).  $L_c$  prevents RF current from reaching the batteries and scope.  $R_m = 10^4 - 10^5 \, \Omega$ ,  $L_c = 1 \text{ mH}$  and  $R_0 = 10^6 \, \Omega$ .

was used instead. It was centred on 750 nm on two argon emission lines (at 750.4 and 751.5 nm) and had a bandwidth of 10 nm. These emissions lines have been chosen both for their intensity and for their respective short lifetimes ( $H_\alpha$  :  $<2.5 \text{ ns}$  and  $\text{Ar}$ :  $<21 \text{ ns}$  and  $<23 \text{ ns}$  [59]). These short lifetimes improve the time resolution in PROES measurements.

The precise trigger was generated from the potential on the RF electrode as shown in figure 4.3. This RF signal had to be converted to a 50 kHz triggering signal for the camera electronics. The measurement delay was adjusted by the camera controller (Princeton Instruments ST-133). This adjusted delay allowed the measurement at different phases of the RF cycle.

Finally, to compare optical emission intensity with RF potential measurements, the phase delays of each measurement (electronics and cables) had to be taken into account. These delays were measured with two identical commercial voltage divider probes (Lecroy PP006). For the optical emission measurement, one probe was connected to the RF electrode and the other probe was connected to the trigger input of the camera. The internal delay of the camera and the delay associated to the time required for the emitted light to reach the camera were also taken into account. For the phase delays in RF potential measurements (voltage probe and capacitive probe), the same procedure was applied except that the second probe was then connected to the measured signal at the oscilloscope input.

To compensate for the low emission intensity collected during the exposure of 2 ns, the exposure was repeated  $0.5 - 12 \cdot 10^6$  times before reading the camera sensor

(CCD). The total exposition time was used to calculate the optical intensity in counts per microsecond.

Using the emission intensity at the 37 phases of a RF cycle, a spatially resolved time-averaged OES spectra was calculated by averaging these emission intensities. This time-averaged emission intensity was used to identify the regions in the plasma with higher electron energy and higher electron density, thereby localising where ionisation rates were higher. This identification can be justified using a simple excitation model in which the optical emission intensity of an optical line such as  $H_\alpha$  and Ar (750 nm) are given by [60]:

$$\bar{I}_{H_\alpha} \propto n_e [n_{H_2} \bar{k}_{\text{diss}}(T_e) + n_H \bar{k}_{\text{dir}}(T_e)] \quad (4.3.1)$$

$$\bar{I}_{Ar} \propto n_e [n_{Ar} \bar{k}_{\text{dir}}(T_e)] \quad (4.3.2)$$

where  $n_e$  is the electron density,  $n_{H_2}$ ,  $n_H$  and  $n_{Ar}$  are respectively the density of  $H_2$ , H and Ar. The  $k(T_e)$  are the excitation rate constants for the dissociative excitation and direct excitations. The rate constants are non linear and increase rapidly at  $T_e < 5$  eV as shown in figure 2.8. Consequently, strong gradients in emission intensities are most likely related to variations of  $T_e$  or  $n_e$ . Therefore, these intensity gradients are good indications for changes in electron density and temperature. The ionisation rates ( $S_{n_e} = n_e n_n X_{\text{ion}}(T_e)$ ) shown in figure 2.8 vary in a similar fashion with  $n_e$  and  $T_e$ . Therefore, variations of optical emission intensities are a good indicator of the variations of the ionisation rates.

Using the emission intensity at different phases, the phase evolution of the emission (PROES) was studied. Only the vertical profile of the emission intensity was taken from each image as shown in figure 4.4. These profiles were centred on a grid hole axis. Assembling them side by side gave an evolution of the vertical optical emission versus time (or versus phase). In figure 4.4, emission patterns could be identified and their underlying physical phenomena has been studied in parallel-plate reactors [61–63]. The patterns  $I_{\text{RF}}$  and  $I_{\text{Gnd}}$  are caused by a field reversal accelerating electrons in the sheath toward the electrodes. As the sheath quickly collapses to follow the RF potential, a high electron current must quickly flow inside the sheath to compensate the RF cycle-integrated ion flux. This high current density at low electron mobility can only be realized in the sheath by an electric field which attracts electrons to the electrodes, this creates a field inversion around the sheath edge which accelerates the electrons inside the sheath [61, 62]. The field reversal occurs in the RF sheath when  $V_{\text{RF}}$  is nearly maximum and at the ground sheath when  $V_{\text{RF}}$  is nearly minimum. The patterns  $II_{\text{RF}}$  and  $II_{\text{Gnd}}$  are caused by the electron



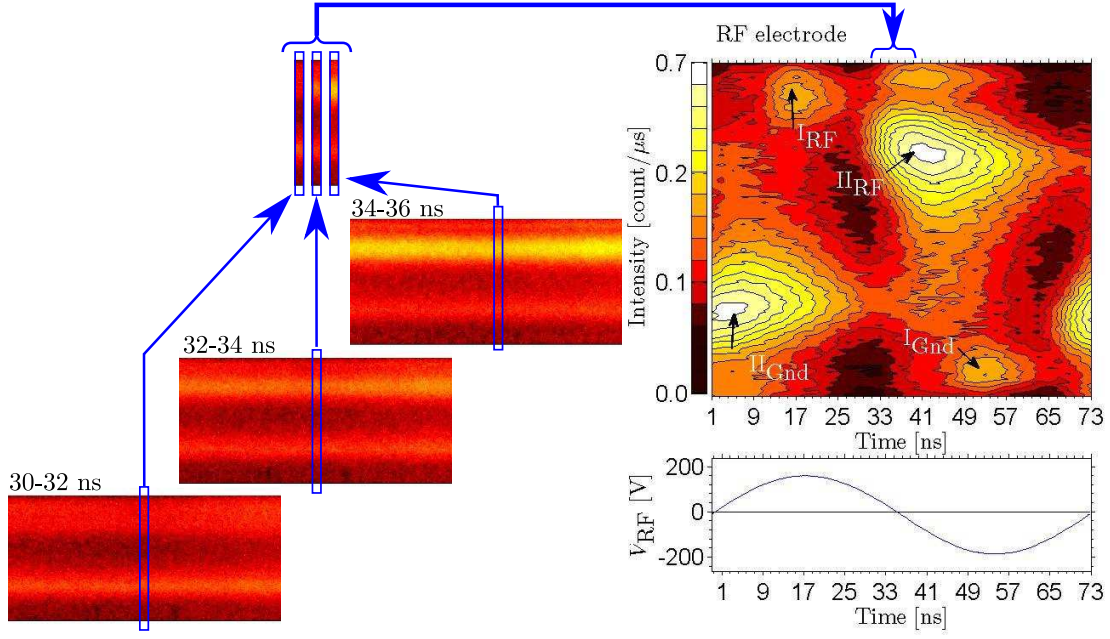


**Figure 4.4:** Construction of the PROES image with the different steps: Images at different phases; Vertical profiles; Assembling the vertical profiles. The images are taken in a parallel-plate reactor in hydrogen at 50 Pa and 350  $V_{pp}$ . Below the PROES image, the potential on the RF electrode ( $V_{RF}$ ) versus time is shown for reference.

substrate would receive. The electronics for the RFEA is shown in figure 4.6. The potential on the selector grid could be inverted to sweep with negative potentials. This provided a useful in-situ check of the grids potential based on the measured features which are shown later in figure 4.11. The voltage difference between collector and secondary electron repeller grid could also be inverted although this was not used in this study. The electronics were constructed so that the grid potentials were referenced to the metal case of the RFEA itself. This allowed the installation of the RFEA in the grounded or floating electrode and measured the ion bombardment energy on this electrode. In the case of floating measurements, a resonant RF filter was also added close to the RFEA. This filter reduced the RF coupling to ground and also protected the RFEA electronics from the RF.

The working principle of a RFEA in a simple case where collisions inside the RFEA can be neglected is illustrated in figure 4.7(a). Ions and electrons enter the RFEA through the aperture after having been accelerated through the sheath. The vast majority of electrons entering the RFEA are repelled toward the aperture by the -55 V on the plasma electron repeller grid. The entering ions pass through this grid before being decelerated by the selector grid. Only ions whose energies are higher than the selector potential can traverse it and eventually be collected on the collector

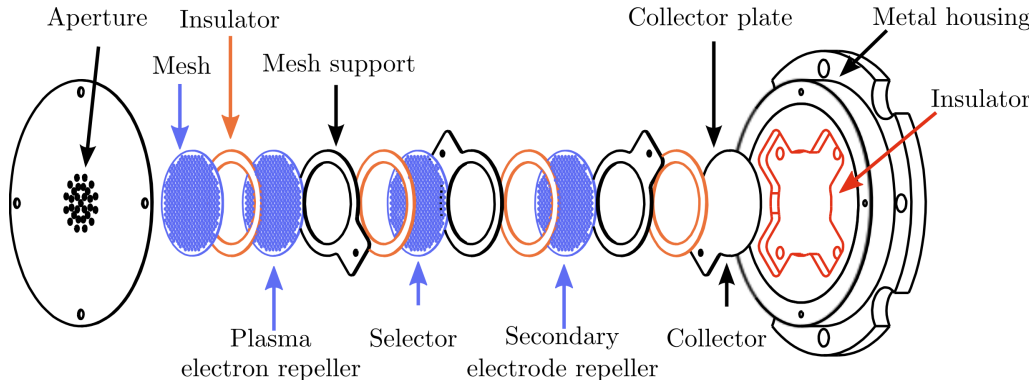


**Figure 4.5:** Schematic of the RFEA. This modular design was inspired from the work of Baloniak et al. [37]. The RFEA can be installed in different reactors by adapting the metal housing.

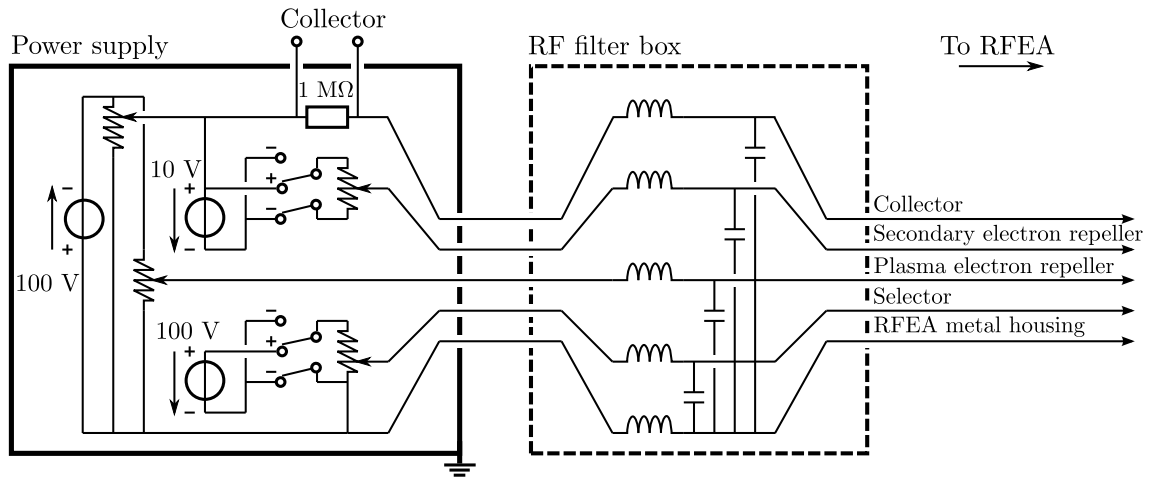


**Figure 4.6:** Schematic of the RFEA electronic with the RF filter box used to protect the RFEA electronic and insulate the RFEA in section 5.5.2. The grid bias is made using floating DC to DC power supplies, hence the grid potential reference is defined by the RFEA metal housing. The current from the collector is measured through the load shown on the collector line.



plate. The last grid (secondary electron repeller) is used to repel secondary electrons emitted on the collector plate. By increasing the positive voltage on the selector grid ( $V_{\text{sel}}$ ), the ion current on the collector grid is reduced as more and more ions are repelled. The current reaches zero when the selector potential is higher than the energy of the fastest ions. The ion velocity distribution is derived from the collected current-selector voltage characteristic as follows [64]. The total ion density is given by:

$$\int_0^{+\infty} f(v)dv = n, \quad (4.4.1)$$

where  $f(v)$  is the one-dimensional velocity distribution. By definition  $f(v)dv = g(\epsilon_i)d\epsilon_i$ , where  $g(\epsilon_i)$  is the ion energy distribution. Since  $d\epsilon_i = M_i v dv$ , then  $f(v) = M_i v g(\epsilon_i)$ . The total ion current density in the entrance plane of the analyser ( $I_i$ ) is defined in this special, one-dimensional, one-directional case as:

$$I_i(\epsilon_i) = e \int_0^{\epsilon_i} v f(v)dv = \frac{e}{M_i} \int_0^{\epsilon_i} f(v)d\epsilon_i = \frac{e}{M_i} \int_0^{\epsilon_i} f \left[ \left( \frac{2\xi}{M_i} \right)^{\frac{1}{2}} \right] d\xi, \quad (4.4.2)$$

where  $0 < \epsilon_i < \infty$ . The differentiation yields:

$$d[I_i(\epsilon_i)] = \frac{e}{M_i} f(v)d\epsilon_i. \quad (4.4.3)$$

In the case of the ion-current measurement, the collected current is:

$$I_m(\epsilon_i) = \frac{e}{M_i} \int_{\epsilon_i}^{\infty} f \left[ \left( \frac{2\xi}{M_i} \right)^{\frac{1}{2}} \right] d\xi \quad (4.4.4)$$

since only the ions whose energy  $\epsilon_i$  is higher than  $V_{\text{sel}}$  are collected. With the relation  $I_i(\epsilon_i) = I(V_{\text{sel}} = 0) - I_m(\epsilon_i)$ , the ion velocity distribution can be derived from:

$$f(v) = \frac{M_i}{e} \left( -\frac{dI_m(\epsilon_i)}{d\epsilon_i} \right) = \frac{M_i}{e^2} \left( -\frac{dI_m(V_{\text{sel}})}{dV_{\text{sel}}} \right), \quad (4.4.5)$$

where  $\epsilon_i$  has been substituted by the product  $e \cdot V_{\text{sel}}$ . In RFEA measurements,  $f(v)$  are represented as a function of the energy  $\epsilon_i$  instead of the velocity  $v$ . Though it might be argued about, this choice is a tradition in RFEA measurements. A representation of  $f(v)$  as a function of  $v$  could be obtained by rescaling the abscissa using  $v = (2\epsilon_i/M_i)^{1/2}$  [64].

However, the ions entering the RFEA have a certain probability of not being collected, even if they had enough energy to overcome the potential barrier of the selector. The total probability of an ion entering the RFEA to be collected  $P_{\text{tot}}$  is the sum of the probability that the ion has no collision with a grid ( $P_{\text{grid}}$ ) and

the probability that the ion has no collision with the gas, producing an ion at rest energy (such as charge exchange collision), in certain region of the RFEA ( $P_{c.x.}$ ), as discussed below. Therefore the relation  $I_i(\epsilon_i) = I(V_{sel} = 0) - I_m(\epsilon_i)$  should include the probability for an ion to be collected as the ion current is not conserved.  $I_i$  would then be rewritten as  $P_{tot} \cdot I_i(\epsilon_i) = I(V_{sel} = 0) - I_m(\epsilon_i)$  [37]. The probability of collision with each single grid is given by the ratio of a grid open area to metal area (grid transparency), here is 0.38. Therefore a simple estimation of the probability for a ion to pass through the four grids is  $P_{grid} = (1 - 0.38)^4 = 0.15$ . The real probability is however more complex as it depend on the precise alignment of the grid holes [37].  $P_{c.x.}$  can be estimated in argon (see Eq. 4.4.6), however,  $P_{c.x.}$  is not known in hydrogen due to the complex chemistry in this gas. Therefore the RFEA measurement were not corrected for  $P_{tot}$  in this study.

At very low pressure, the influence of collisions on ion energy is negligible and therefore all ions have the same energy (Sec. 2.2). However, in all the measurements done in this study, the measured current densities were influenced by collisions with the gas. Consequently, the ions have a more complex energy distribution. Measurements done at the low end of the pressure range in argon are shown in figure 4.8. There, even at 1 Pa, the current density decreases slowly between 0 and 65 eV due to the collisions with the gas. Between 65 eV and the maximum ion bombardment energy ( $E_i = 80$  eV), the measured current density decreases sharply, hence most ions have energies between 65-80 eV. The resulting velocity distribution ( $f(v)$ ) is peaked between the energies 65 eV and  $E_i$ . The width of this peak is influenced by the RFEA resolution. Figure 4.8 shows that the velocity distribution at 50 Pa is dominated by collisions, the majority of ions having low energies with a small quantity of ions having energies close to the maximum. These measured distributions at 1 and 50 Pa are in good agreement with the theoretical energy distributions in argon (see Sec. 2.2 and Eq. 2.2). At both pressures, the decrease of current density between -20 and 0 V is not fully understood. It could be attributed to one of the phenomena responsible for degrading the RFEA resolution discussed below.

The current density and velocity distribution in hydrogen are shown in figure 4.9. There, even at 1 Pa, the ion distribution is not peaked around at the maximum ion energy. The velocity distributions are different from those measured in argon due to the different and more complex chemistry of the hydrogen sheath as discussed in section 2.2. The two measurements at 160  $V_{pp}$  show that, in hydrogen,  $E_i$  is significantly lower at 50 Pa than at 1 Pa due to the collisions in the sheath. The

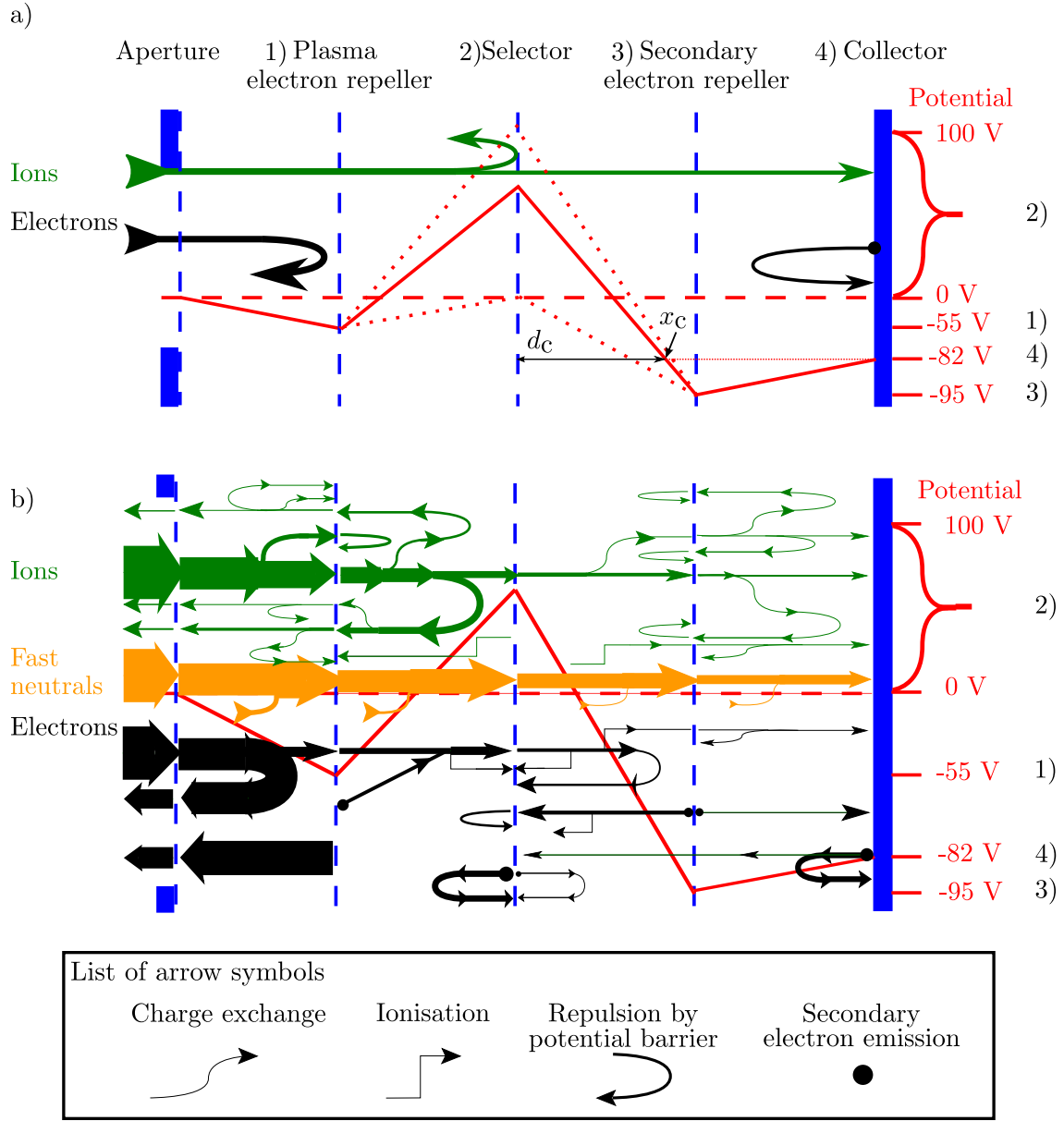


**Figure 4.7:** (a) Potential and schematic of particles collisionless trajectories inside the RFEA. The potentials on the grids were chosen following the work of Böhm et al. [64]. The potential of the secondary electron repeller grid ( $-95 \pm 10\text{V}$ ) is adjusted so that the secondary electron current is zero. The point  $x_c$  indicates where the potential between the selector and secondary electron repeller grid is equal to the potential on the collector plate. (b) Potential and schematic of particle flows inside the RFEA including charge exchange collisions, fast neutrals, ionisation and secondary electron emission. The arrow widths are proportional to the relative number of particles, for each type of particles.

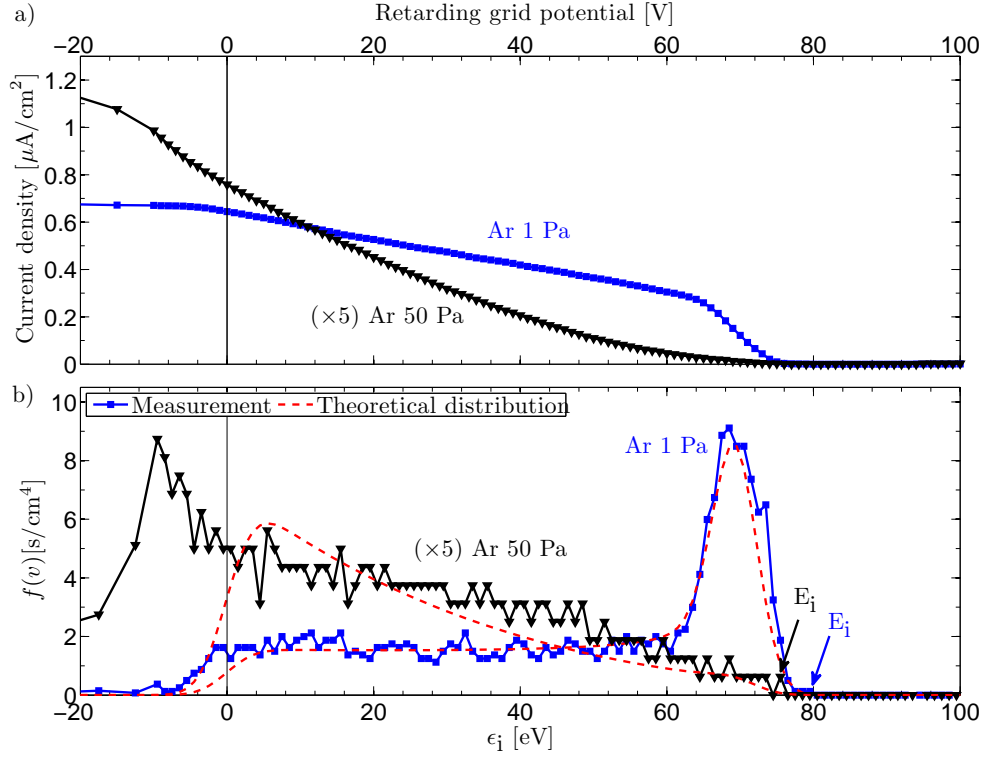


**Figure 4.8:** (a) Typical current density as a function of the retarding grid potential and (b) ion velocity distribution ( $f(v)$ ) as a function of the ion bombardment energy ( $\epsilon_i$ ) in a parallel-plate reactor in argon. The theoretical velocity distribution is calculated using equation 2.2 convolved with a Gaussian function ( $\sigma = 3$  eV) to emulate the measurement error and it is interpolated to the measurements using  $\lambda_{c.x.}$  from [38]. The maximum ion bombardment energy ( $E_i$ ) are respectively 80 and 76 eV for the 1 and 50 Pa measurements.

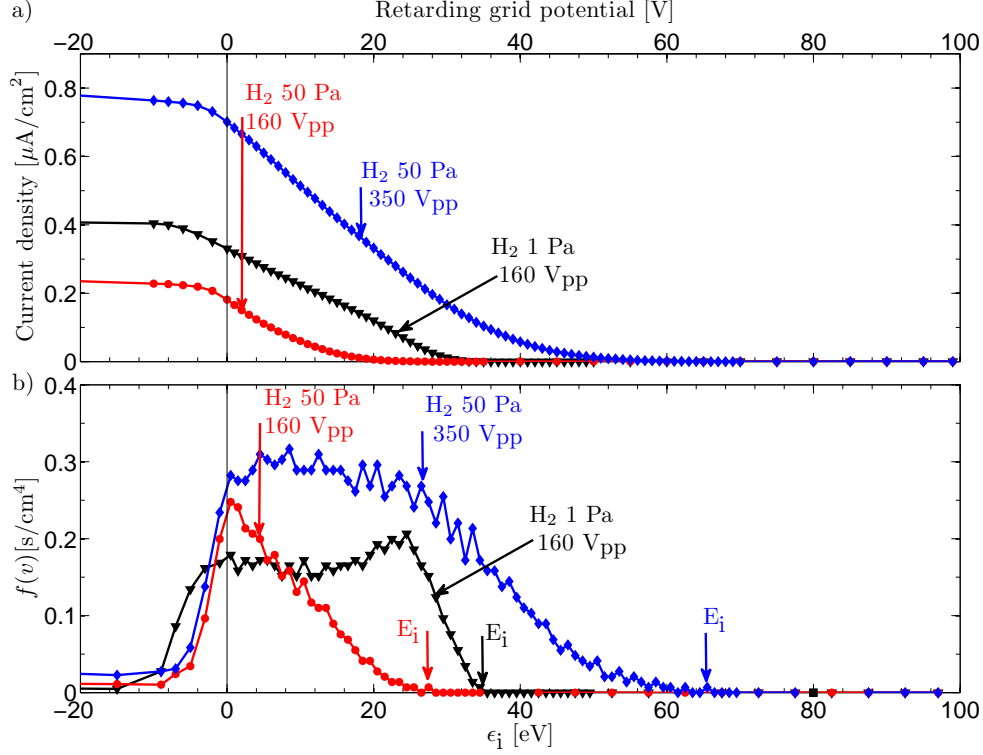


**Figure 4.9:** (a) Typical current density as a function of the retarding grid potential and (b) ion velocity distribution ( $f(v)$ ) as a function of the ion bombardment energy ( $\epsilon_i$ ) in a parallel-plate reactor in hydrogen. The maximum ion bombardment energy ( $E_i$ ) are respectively 28 and 35 eV for 1 and 50 Pa at 160 V<sub>pp</sub> and 66 eV at 50 Pa and 350 V<sub>pp</sub>.

two measurements at 50 Pa illustrate how  $E_i$  varies with  $V_{pp}$  in hydrogen.

#### 4.4.1 Consideration on collisions within the RFEA

After entering the RFEA, the ion travel 1.6 mm inside the RFEA before reaching the collector. This distance is of the same order of magnitude as the sheath thickness (1-10 mm). Therefore, at pressures where collisions in the sheath have a strong influence on the ion velocity distribution, the influence of collisions inside the RFEA on the measured distributions has to be considered. After a charge exchange collision, the resulting ion is at rest and drifts with the electric field inside the RFEA toward lower potentials. Looking at the figure 4.7(a), the ions produced by charge exchange collisions before the selector are either trapped in the potential-well around the plasma electron repeller grid or they exit the RFEA through the aperture. Any ion having a charge exchange collision after the selector can only reach the collector if the collision took place between the selector grid and  $x_c$  since they start from a potential higher than the collector potential (Fig. 4.7). Otherwise, they are trapped

around the secondary electron repeller potential-well and collected on that grid. Therefore, most ions having a charge exchange collision inside the RFEA are not measured on the collector and all the ions reaching the collector had enough energy to pass through the selector grid beforehand. Thus, to a good approximation, the charge exchange only affects the ion velocity distribution by reducing the number of collected ions by a factor [36,37]:

$$P_{c.x.} = e^{-(1.6-d_c)/\lambda_{c.ex.}}. \quad (4.4.6)$$

$P_{c.x.}$  is not constant as it depends of  $d_c$  which increases with the potential of the selector grid. However, this variation is small ( $0.35 \rightarrow 0.375$  mm) and can be neglected in comparison to the 1.6 mm thickness of the RFEA. In conclusion, the charge exchange only reduces the collected signal and does not affect the shape of the energy distribution.

Charge exchange is not the only ion-neutral collision. In argon, elastic collisions can also slow the ion. However charge exchange is usually considered to be the dominant collisional ion momentum loss [37]. This could be verified in this study by comparing the calculated time-averaged plasma potential to the measured maximum ion bombardment energy. Even at 50 Pa in argon, they are equal showing that no significant energy was lost by elastic collisions (Fig 4.8).

In hydrogen however, the sheath chemistry is complex as discussed in section 2.2. As discussed previously, collisions inside the RFEA producing an ion at rest (i.e. charge exchange [37], proton abstraction [65]) do not alter the shape of the measured ion velocity distribution but reduce the measured ion flux. However elastic collisions and other collisions shown in figure 2.6 could also play a significant role in hydrogen. Therefore a proper estimation of the influence of collisions inside the RFEA would require a simulation, probably using a particle in cell model. However the aim here is to compare the effect of the two reactor configurations by measuring the maximum ion bombardment energy in both reactors, not to fully resolve the velocity distribution.

Hence, it was decided to do a crude approximation of the possible systematic error on the maximum ion bombardment energy in hydrogen due to all collisions. This estimation is done using the following argument: The ions loose energy during their travel through the sheath (measured thickness of  $\sim 8$  mm, see Tab. 5.2) and through the RFEA until the selector grid (0.8 mm). Collisions after the selector would not modify the shape of the velocity distribution. If the ion energy loss rate is assumed constant with energies, the ion energy loss is proportional to the travelled

distance. The distance travelled through the RFEA only accounts for  $\sim 10\%$  of the total travelled distance. Hence an ion at the selector grid of the RFEA has lost  $\sim 10\%$  more energy due to collisions inside the RFEA compared to ions reaching the grounded electrode (the entrance of the RFEA). Experimentally, in hydrogen at 50 Pa, ions starting from a plasma potential of 40 V are measured with a maximal energy of 24 eV (Fig. 5.27). The measured energy lost by collisions is 16 eV hence the real ion energy at the grounded surface is probably underestimated by  $\sim 2$  eV (26 eV instead of the measured 24 eV). This estimation is a worst case scenario as it does not consider that any collisions occurring inside the RFEA and which leaves an ion at rest does not affect the resolution. Furthermore, this potential systematic underestimation of 2 eV has no influence on the conclusions drawn from the RFEA measurements as they are all direct comparisons between measurements in different reactor geometries using the same RFEA and at the same gas pressure.

The ( $P_{c.x.}$ ) and, more generally the influence of collisions inside the RFEA, is the principal reason for reducing RFEA thickness since the measured currents quickly become small as the pressure is increased ( $\sim 1$ -100 nA at 50 Pa and above). However, reducing the RFEA thickness brings engineering difficulties as the thickness of pieces inside the RFEA become sub-millimetric. Furthermore, as will be discussed later, both the resulting grid misalignment and the short distance between the grids hinder the measurement resolution.

#### 4.4.2 Particles flows inside the RFEA

To ensure that the current measured on the collector plate is solely due to ions with desired energy, the flow of ions, electrons and also of secondary electrons and fast neutrals is studied. The particle flow inside the RFEA, when the selector potential is positive, is shown in figure 4.7(b). This figure shows that the electrons coming from the plasma which are not repelled by the plasma electron repeller grid are accelerated toward the selector to energies of  $\sim 100$  eV. At these energies they can ionise the gas after the selector. In doing so, these electrons produce ions which are likely to reach the collector plate. These ions would be mistaken for plasma ions having energy higher than the selector potential. This ion current would even increase with the selector potential as the electrons gain more energy as shown in figure 4.10. The increase in measured current density above  $\sim 45$  eV is due to ionisation from electrons accelerated toward the selector. This supplementary source of ions prevents proper measurement of the maximum ion bombardment energy  $E_i$ . Figure 4.7(b) also shows that secondary electrons are emitted from the collector.

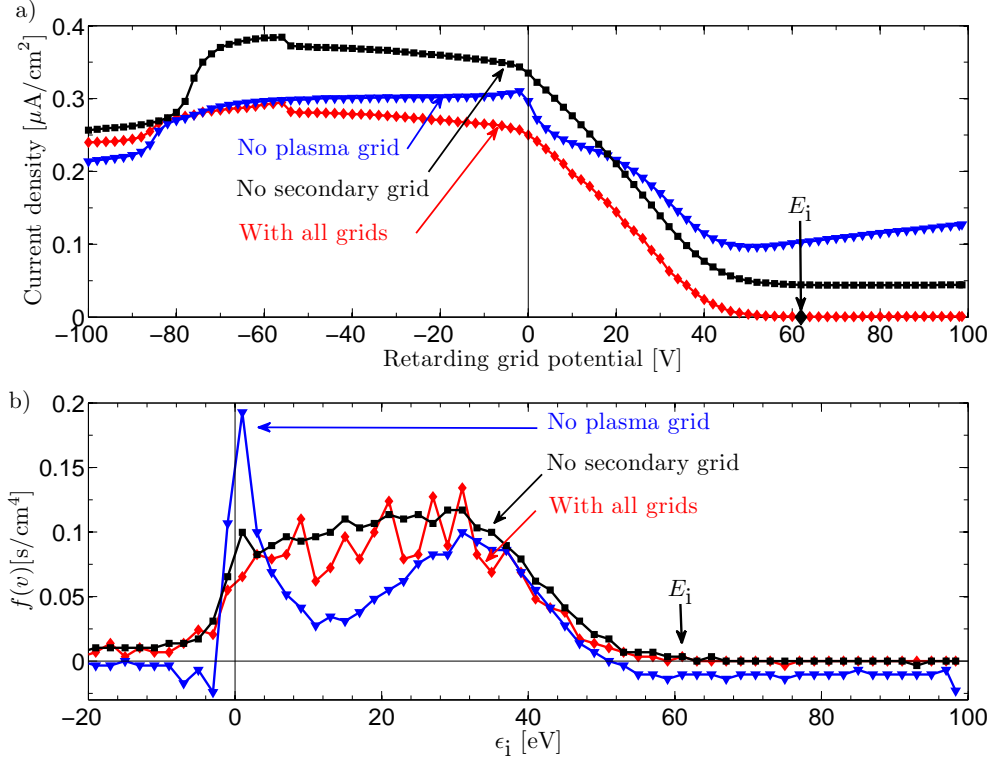


**Figure 4.10:** (a) Current density as a function of the retarding grid potential (selector) and (b) ion velocity distribution ( $f(v)$ ) as a function of the ion bombardment energy in three conditions: with all grids; without the plasma electron repeller grid; without the secondary electron repeller grid. Measurements are done in a parallel-plate reactor in hydrogen at 50 Pa. The electron repelling effect from the plasma electron repeller grid was stopped by setting this grid potential to 0 V. The electron repelling effect from electron repeller grid was stopped by setting this grid potential to -85 V (the collector potential).



The loss of these electrons from the collector plate creates a positive current and the current on the collector plate then never reaches zero. To avoid this effect, the electrons are repelled toward the collector by the secondary electron repeller grid. The measured current density without repelling the secondary electrons is shown in figure 4.10. Since these secondary electrons are produced by fast neutrals but also by ions colliding on the collector, the amount of secondary electrons varies with the selector potential. Thus, the measured energy distribution can be slightly perturbed if the secondary electrons are not repelled. However, this perturbation can hardly be observed on the ion distribution in this figure. Nonetheless, the secondary electron repeller grid was used to prevent possible distortion in further measurements. Therefore, to measure an undistorted ion velocity distribution, a plasma electron repeller grid and secondary electron repeller grid are necessary even if, by adding these two grids, the measured current density is decreased due to the grid transparencies  $P_{\text{grid}}$ . A similar discussion on the influence of these two grids can be found in [64].

To further study the influence on the different particle flows shown in figure 4.7(b) on the measured current density, the current on each grid of the RFEA is studied and shown in figure 4.11. The curve of the current density versus the selector potential can be split into four different regions with transitions from each region. In the region A, the selector grid potential is the lowest potential inside the RFEA, therefore all charge exchanged ions will drift toward it and all secondary electrons emitted from the selector will either drift toward the plasma electron repeller or toward the collector. Once the selector potential is higher than the secondary electron repeller potential (region B), this grid becomes the lowest potential and some charge exchange ions will drift toward it and toward the collector instead of being collected on the selector. This agrees with the drop in selector current and simultaneous increase of secondary electron repeller and collector current. As the selector potential is higher than the plasma electron repeller (transition to region C), the field between these two grids is inverted. Therefore charge exchange ions between the aperture and the selector now drift toward the plasma electron repeller grid and secondary electrons from the plasma electron repeller and from selector are attracted to the selector. Thus the current on the plasma electron repeller significantly increases and the current on the three other grids decreases. In region C, the current to the selector and following grids continue to decrease as the selector potential increases toward 0 V. This variation is caused by the increasing region between the aperture and the plasma electron repeller grid which is at a potential lower than that of the

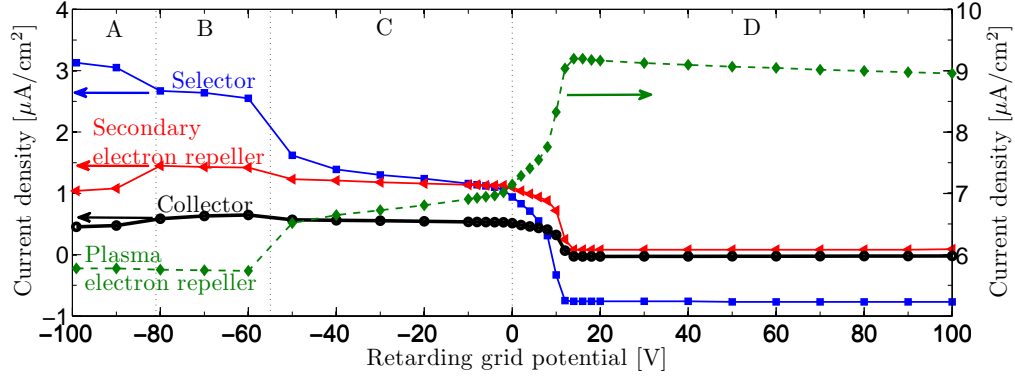


**Figure 4.11:** Current on each of the grids of the RFEA at different retarding grid (selector) potentials. Measurements taken in argon at 50 Pa in the parallel-plate reactor for a time-averaged plasma potential  $\bar{V}_{\text{pla}} \simeq 12$  V.

selector. Ions having a charge exchange in this lower potential region will not reach the selector. Finally, in region D, the ions are repelled according to their energy by the selector. Therefore the current on the selector and following grids drops whereas the plasma electron repeller current increases. For selector potentials higher than the maximum ion energy, the negative current on the selector is due to the secondary electrons flowing toward the selector. The positive current on the secondary electron repeller grid is then due to the flow of secondary electron leaving this grid toward the selector.

Understanding the particle flows inside the RFEA and their influence on the current on each grid was necessary to ensure that the measured current is indeed due to the ions bombarding the substrate. This discussion showed that, using the four grids, an undistorted ion velocity distribution can be measured in argon and that, in hydrogen, small deviations could be present due to the complex chemistry.

#### 4.4.3 RFEA resolution

In this section, the different factors affecting the energy resolution of the RFEA are discussed. In the RFEA, the ions are repelled according to their perpendicular speed with respect to the equipotential surfaces inside the RFEA instead of the ion total energy. This explains the one dimensional velocity distribution used to derive equation 4.4.5. Therefore, ions arriving with a non perpendicular angle behave as if they had less energy. Hence this angle is an important factor for the energy resolution. Another factor associated with the shape of the equipotential is the potential gradient between the wires of each grid, especially the selector. Potential variations there have a direct influence on the ion energy selection as the potential

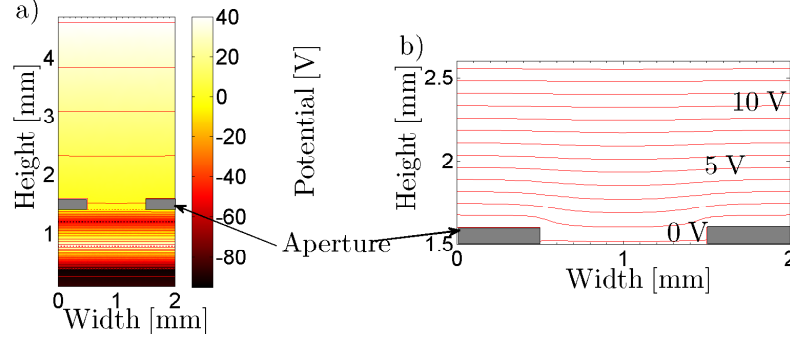


**Figure 4.12:** (a) Potential in a section of the RFEA centered on one of the aperture holes. The plasma potential and the selector grid are 40 V. (b) Bending of the equipotential lines close to the aperture.

barrier repelling the ions depends on the distance between the ion trajectory and the mesh wires.

To study the equipotential lines inside the RFEA, the potential was calculated both analytically and numerically. The numerical calculation is done with an electrostatic model solved with a commercial finite element solver COMSOL and the result is shown in figure 4.12. The simulated domain extends over the width of one aperture hole (see Fig.4.5) to allow for a dense meshing. To simulate the influence of the plasma potential onto the potential in the aperture, a potential of 40 V is imposed outside the RFEA, 3 mm away from the aperture. The real potential in the sheath is more complex but this simple approach already permits an estimation of the penetration of the plasma potential inside the aperture and thus the bending of the equipotential lines as will be discussed later. For the analytical approach, a model based on the method of conformal transformations [66] is used. This model works in two steps. First the potential is calculated in a simple geometry. Then, a coordinate transformation (conformal transformation) permits the transformation of the calculated potential from the simple into the more complex geometry, here the RFEA geometry. In this study, the simple coordinate system  $\mathcal{Z}(\rho, \theta)$ , is a circle as shown in figure 4.13. Each grid is represented by a single wire aligned on the  $\theta = 0$  axis including a small circle centred on the origin. The outer circle acts as the grounded aperture. In this coordinate system, the voltage anywhere in the circle is a simple addition of the contribution from each wire in the form of

$$V(\rho, \theta, q_{\text{col}}, q_{\text{sec}}, q_{\text{sel}}, q_p) = \sum_j -\frac{q_j}{2\pi\epsilon_0} \ln(l_i) + C \quad (4.4.7)$$

where the  $q_j$  is the charge on each grid wire. Then, using a conformal transformation  $\mathcal{W}(x, y) = \frac{2\pi}{a} \ln(\mathcal{Z})$ , the coordinate system is transformed into a planar system

where the grid wires are periodically repeated due to the  $2\pi$  symmetry of  $\theta$  in the  $\mathcal{Z}$  coordinates. Determining the integration constant  $C$  and linking the charges  $q_j$  to the potentials on each grid  $V_j$  is done by imposing the potential at the border of each grid/plate as boundary condition ( $V(x=0, y=rm) = V_{\text{sec}}$ , Fig. 4.13). The development is detailed in appendix B and the results are shown in figure 4.14(a). It is seen that the potential between each wire of a mesh is different from the potential on the mesh itself. This potential gradient in the plane of the mesh is due to the influence from the potential of the other meshes. This equipotential gradient between the grid wires affects the potential barrier repelling the ions and also affects the angle at which the ions approach the potential barrier. This gradient tends to deflect the ions from their original trajectory. Figure 4.14(b) shows the potential barrier faced by a ion travelling on a straight line through the RFEA and passing at various distances from the grid wires. It is seen that if the ions cross exactly in the middle between two wires, the positive selector potential repelling the ion is 34.2 V instead of the potential of 40 V on the selector mesh. Therefore ions with energy smaller than the selector potential can be collected hence the ion maximum energy could be overestimated. This equipotential bending effect is worsened if the grid wires are further apart (larger  $a$ ) or if the distance between the grids is reduced ( $d$ ). This effect limits the possibility of reducing the RFEA thickness without hindering the energy resolution. Figure 4.14(b) also shows that the potential calculated with the conformal transformation is in good agreement with the one calculated with the numerical simulation (Fig. 4.12). Close to the grid, some divergences between the two methods are observed. They are probably caused by the approximation of round mesh wires used in the conformal transformation instead of the more real rectangular mesh wires used in COMSOL.

Similar to the influence of the equipotential gradient inside the RFEA, part of the potential from the plasma enters the aperture if the aperture diameter is too large. This would cause the ion trajectory to be bent out of their original perpendicular trajectory by the shape of the equipotential lines inside the aperture [64]. This effect was mitigated by using several small aperture holes (1 mm in diameter) and by adding a grid on the RFEA side of the aperture. This grid also prevents the potential from the plasma electron repeller grid to distort the equipotential lines inside the aperture. Figure 4.12(b) shows that the equipotential lines at the entrance of the RFEA are indeed slightly distorted close to the sides of the aperture but this deviation is small and will therefore have only a limited effect on the resolution.

These bending of ion trajectories (lensing effects), are worsened by the non perfect

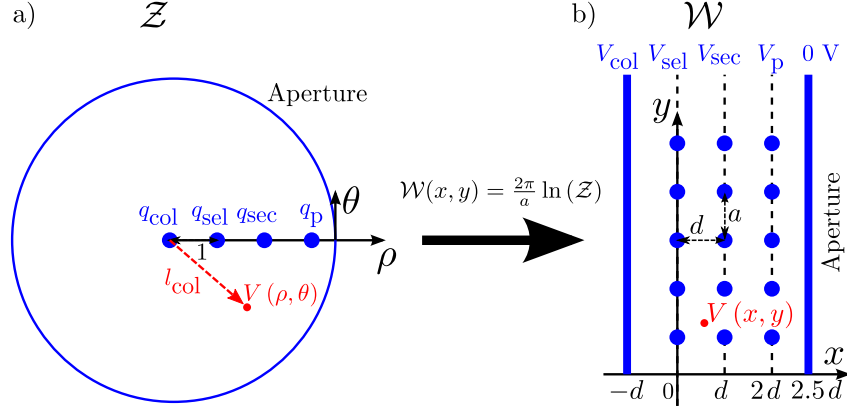


**Figure 4.13:** Potential in (a) the simple  $\mathcal{Z}$  system and (b) the  $\mathcal{W}$  system (the RFEA).  $q_j$  and  $V_j$  are the charge and potential on each grid,  $a$  is the distance between the wires in the grid,  $d$  the distance between each grid. In the RFEA,  $a \ll d$ .

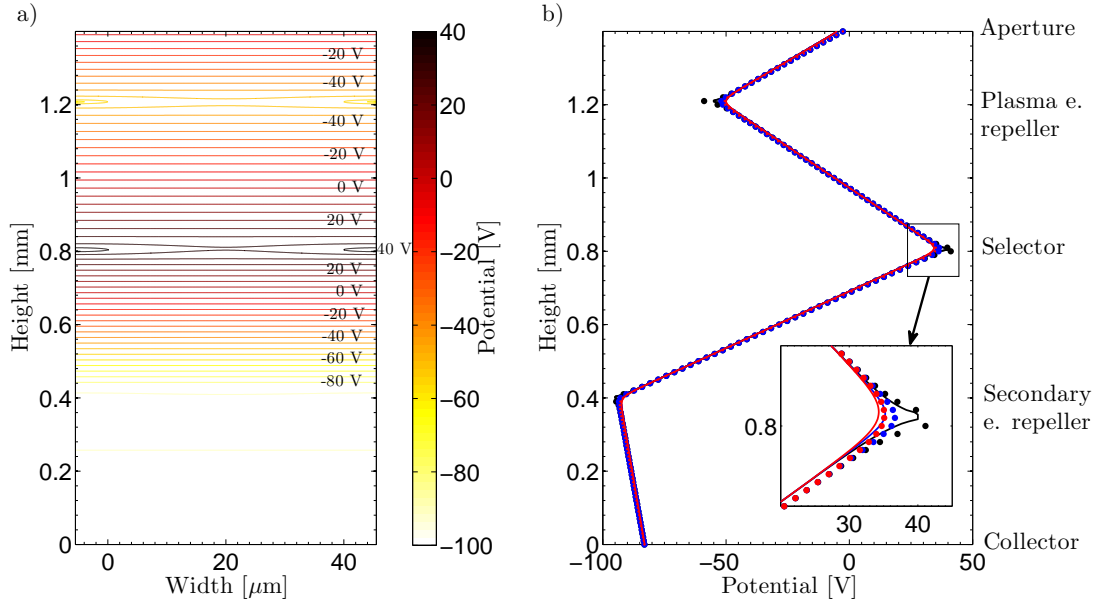


**Figure 4.14:** (a) Analytical calculation of the electric potential inside a four grid RFEA using the conformal transformation method. (b) Potential variation from aperture to collector plate at different distances from the grid wires from the numerical simulation (lines) (Fig. 4.12) and calculated with the conformal transformation method (dots). Inset : Zoom on the potential variation between the wires of the selector plate. The three positions are: (black) at the wire edge; (blue) 10  $\mu\text{m}$  from the wire; (red) at the centre between two wires. The grids are supposed to be perfectly aligned here and the selector voltage is 40 V.

parallel alignment of the grids themselves. They are 4  $\mu\text{m}$  thick and are only supported on their edges on a support ring with a diameter of 1.5 cm. Therefore, the grids bend under their own weight and any inward lateral tension causes the grids to bulge, worsening the grid alignment. During the RFEA assembling, special care is taken to align the grids, however all the RFEA pieces are narrow to minimize the ion travel distance inside the RFEA. Therefore, some error due to grid non-parallelism could not be prevented and may vary with each RFEA assembling.

Before discussing the RFEA energy resolution, a final effect was considered. As the ions approach the selector grid, they are slowed down. There is therefore a positive charge accumulation in front of the selector. If this charge accumulation is dense enough, the resulting electric field acts as a virtual grid which distorts the measurement if the potential between the grid becomes higher than the one on the selector [67]. However, with the plasma density and RFEA dimensions used in this study, the charge accumulation is too small to have such an effect.

In conclusion, the two major factors influencing the resolution are the lensing effect and the grid bending. However, to quantify the impact of these effects on the RFEA energy resolution would require a statistical analysis similar to the one done by T. Baloniak et al. [37]. Instead, two methods are proposed to estimate this resolution both experimentally and numerically.

Experimentally, this energy resolution could be measured by using a mono energetic ion beam. The resolution would then be given by the width of the measured velocity distribution. In this study, no collisionless particle beam was available. However, the high energy ions at low gas pressure in argon shown in figure 4.8 could be assimilated to a mono energetic ion beam. There, the beam spread is  $\sim 10$  eV and therefore the resolution can be estimated to be  $\pm 5$  eV.

The numerical estimation of the energy resolution is done with the calculated potential inside the RFEA. The potential distribution between the wires of the selector grid were calculated numerically for different selector potentials as shown in figure 4.15(a). The energy resolution is then determined by the necessary grid potential so that the majority of a mono energetic ion beam is reflected by the grid. The fraction of a 40 eV monoenergetic ion beam crossing the grid (the grid transparency) for various grid potentials is shown in figure 4.15(b). This figure shows that 70 % of the ions were repelled when the potential is at 45 V, thus  $\sim 5$  V above the ion energy. The particle energy in a real measurement could therefore be overestimated by  $\sim 5$  eV, in good agreement with the experimentally estimated resolution.

In conclusion the systematic error on the ion energy is  $\pm 5$  eV. On top of this system-

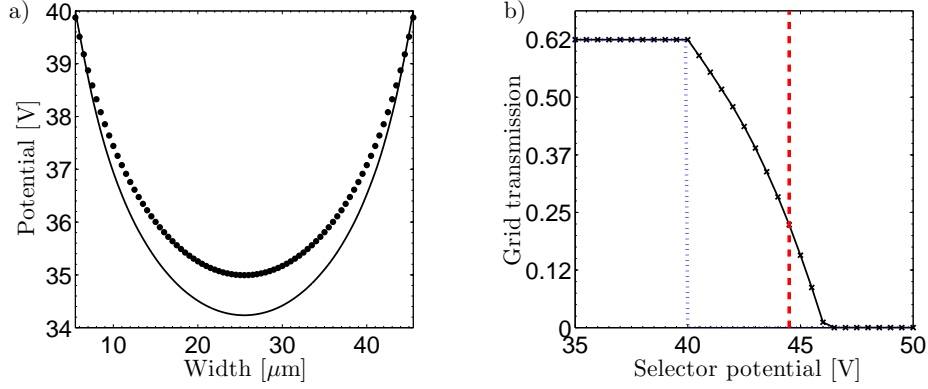


**Figure 4.15:** (a) Potential variation between the wires of the selector grid calculated with the numerical simulation (lines) (Fig. 4.12) and with the conformal transformation method (dots) for a selector potential of 40 V. (b) Grid transmission for a 40 eV monoenergetic and uniformly spatially distributed ion beam versus the selector potential, calculated with the numerical simulation. The transparency for a perfect RFEA is shown in (blue dots). The potential at which 70 % of the particles are repelled is delimited by the (red dashed) line.

atic error, in hydrogen, the maximum bombardment energy could be underestimated by  $\sim 2$  eV due to the collisions inside the RFEA. This systematic error could be improved by lowering the amplitudes of the negative voltages on the grids as it would improve the flatness of the equipotential lines between the grid wires. However it would also increase the possibility of high energy plasma electrons entering the RFEA and distorting the results. Therefore, it was decided to be more conservative, keeping the low voltages on the grid to the detriment of the energy resolution. This systematic error will not alter later discussions in which the ion energy in different reactor geometries are compared. However, these comparisons are still subject to random error due to possible alteration of the RFEA between measurement series and random errors in the potential and current measurements close to the maximum ion energy where the latter tend to zero. This random error, including variation in plasma conditions can be estimated experimentally to  $\pm 2$  eV.

## 4.5 Capacitive probe

A capacitive probe was used to measure the time evolution of the plasma potential ( $V_{\text{pla}}(t)$ ). The probe is shown in figure 4.16(a). It has a shielded extrusion into the plasma to avoid RF coupling to the potential of the ground sheath. At the end of this extrusion, a cylindrical probe tip is capacitively coupled to the plasma and therefore its RF potential is proportional to the plasma potential. Inside the capacitive probe, the probe tip is biased at 5 V DC through two 10 M $\Omega$  load. The

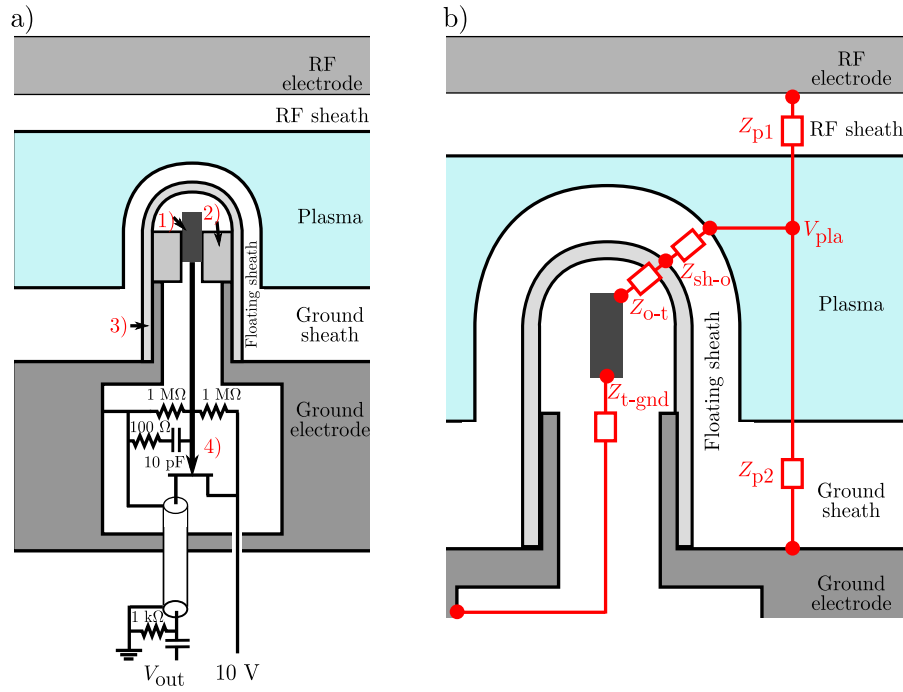


**Figure 4.16:** (a) Capacitive probe schematics. The metal tip is a cylinder with a diameter of 2 mm and 5 mm long (1) centred with a Teflon ring (2) and insulated from the ground sheath with a protrusion from the ground electrode. A 23 mm long ceramic (3) insulates the tip from a direct contact with the plasma. The voltage follower circuit in (4) was produced by the electronic workshop of Mr. Marmillod and collaborators. (b) Equivalent circuit model of a capacitive probe inside a plasma.  $V_{pla}$  is the plasma potential,  $Z_{p1}$  is the impedance between the RF electrode and the plasma region to which the capacitive probe is coupled,  $Z_{p2}$  the impedance from this coupling region to the ground.  $Z_{sh-o}$  is the impedance of the floating sheath around the probe,  $Z_{o-t}$  is the impedance between the outer surface of the probe to the probe tip and  $Z_{t-gnd}$  is the impedance from the probe tip to ground.



JFET (BF862) converts the tip potential into current which flows through the 1 k $\Omega$  load. The resulting potential drop ( $V_{\text{out}}$ ) is AC coupled to the internal 50  $\Omega$  load of an oscilloscope (Lecroy WavePro 735Zi). To avoid the saturation of the JFET, a capacitance (10 pF) to ground was inserted the region 4). This capacitance also reduces the influence of parasitic capacitance between the probe tip and ground. The resistance (100 ohm) connected in series with the capacitance prevents the system from oscillating on its own at a frequency of a few GHz.

The ratio between the plasma potential and the voltage measured by the oscilloscope (the probe gain) depends on the gain from the JFET and also on the amplitudes of the impedances ( $Z_{\text{t-gnd}}$ ), ( $Z_{\text{o-t}}$ ) and ( $Z_{\text{sh-o}}$ ) shown and described in figure 4.16(b). In a RF plasma, ( $Z_{\text{sh-o}}(t)$ ) varies with the RF phase, consequently, the probe gain changes with the RF phase. This variation of gain distorts the measured plasma potential waveform. To minimize this effect, the probe is constructed so that  $Z_{\text{t-gnd}} + Z_{\text{o-t}} \gg Z_{\text{sh-o}}$  hence the voltage drop through the sheath is minimised [68–70]. In this case, the sheath between the plasma and the probe is a RF floating sheath through which the potential ( $V_f(T_e)$ ) has only small variations compared to the tens or hundred volts oscillation amplitude of the RF and ground sheaths. To increase  $Z_{\text{t-gnd}}$ , the JFET was placed close to the tip to limit the parasitic capacitance of the probe to ground. Furthermore,  $Z_{\text{o-t}}$  was increased by introducing a ceramic surrounding the probe, thereby increasing the distance between the tip and the plasma sheath. Finally, the dimension of probe tip was reduced to increase  $Z_{\text{o-t}}$ . To ensure that the probe impedance was sufficient, measurements were performed with different tip dimensions, in a parallel-plate plasma in hydrogen and they are shown in figure 4.17. The waveforms of the measured signal at 2 and 4 mm diameter are similar and are nearly purely sinusoidal. The amplitude of the second harmonic is negligible and probably self-generated by the plasma [28] instead of coming from a probe distortion. At 8 mm, the observed distortion is probably due to the saturation of the JFET current rather than potential variation in the plasma sheath. In conclusion, the probe impedance is large enough to prevent distortions and the following measurements were done with a 2 mm diameter tip.

To ensure that potential harmonics are properly resolved by the capacitive probe, its frequency response was measured by surrounding the tip of the probe with a metallic cylinder biased at different frequencies. The results are shown in figure 4.18, showing that the probe gain was constant up to 81.36 MHz (6<sup>th</sup> harmonic) which was sufficient to accurately measure the waveform of the plasma potential at 13.56 MHz. To measure the oscillations of the plasma potential ( $\tilde{V}_{\text{pla}}$ ) with this capacitive probe,

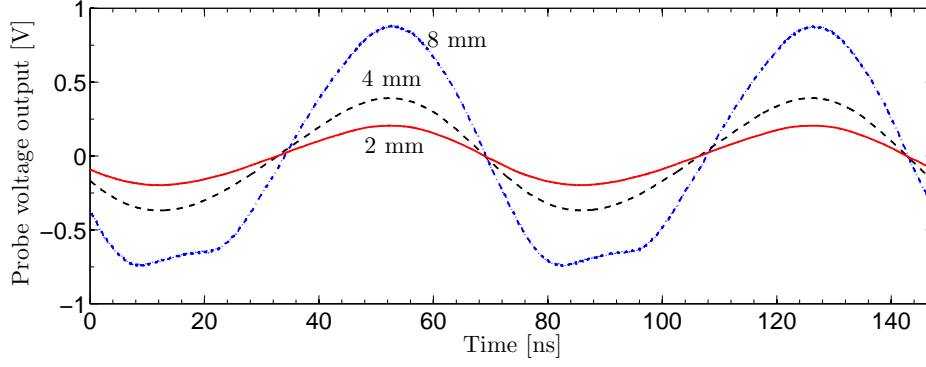


**Figure 4.17:** Capacitive probe output versus time for different probe tip diameters in a parallel-plate reactor in hydrogen.

the probe gain must be calibrated. Godyak et al. [68] have suggested to do this calibration by measuring the impedance of the sheath surrounding the probe ( $Z_{\text{sh-o}}$ ) with a special probe design. However, this was not possible with the capacitive probe used in this study. Instead, the calibration was done using the RF voltage probe and the following argument: Due to the high electron mobility, the plasma potential is more positive than all surfaces in contact with it (Sec. 2.1, [28]). During the RF cycle, the most positive surface in contact with the plasma is alternately the RF electrode when its potential is positive and the ground electrode when the RF electrode potential is negative as shown in figure 4.19. Therefore, the extrema of the positive surfaces in contact with the plasma are respectively the maximum voltage on the RF electrode ( $\max(V_{\text{RF}})$ ) and the ground electrode potential (0 V). Therefore, to a reasonable approximation, the oscillation amplitude of the plasma potential is equal to  $\max(V_{\text{RF}})$ . Therefore, the output voltage of the capacitive probe is normalised to  $\max(V_{\text{RF}})$  to obtain  $(\tilde{V}_{\text{pla}})$  as shown in figure 4.19. In this figure,  $(\tilde{V}_{\text{pla}})$  is also shifted vertically above zero to help the reader see the relation between the plasma oscillations and the positive surfaces in contact with the plasma. The phase of  $\tilde{V}_{\text{pla}}$  was adjusted so that its maximum coincided with the maximum of  $V_{\text{RF}}$ . This phase shift is due to a constant signal delay due to the circuit and cable length of the diagnostic but it also varies with the plasma impedance. From the equivalent circuit diagram in figure 4.16(b), the phase ( $\phi$ ) between the potential on the RF electrode and the plasma potential seen by the probe is given by:

$$V_{\text{pla}} = \frac{Z_{\text{p2}}}{Z_{\text{p1}} + Z_{\text{p2}}} V_{\text{RF}} = |Z| \cdot |V_{\text{RF}}| e^{i \cos(\omega t + \phi)}. \quad (4.5.1)$$

Measurements have shown that this phase shift varies for different plasma conditions and reactor geometries. Potential phase shifts are also observed in the numerical

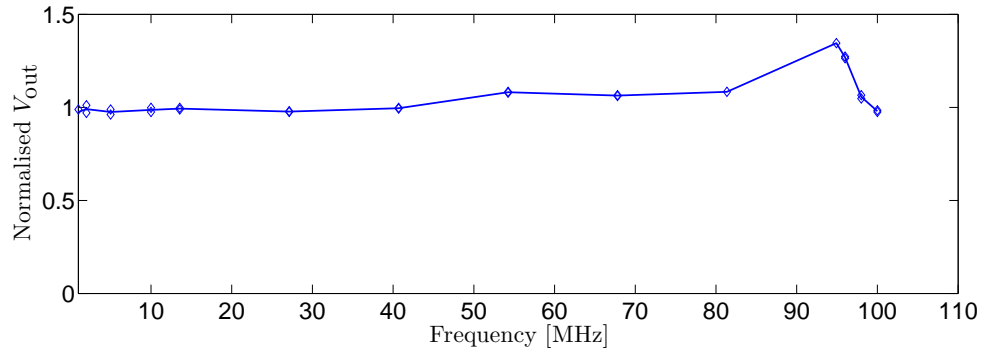


**Figure 4.18:** Normalised amplitude of the capacitive probe output voltage ( $V_{out}$ ) for a reference sinusoidal signal at various frequencies.

simulation in section 6.3.

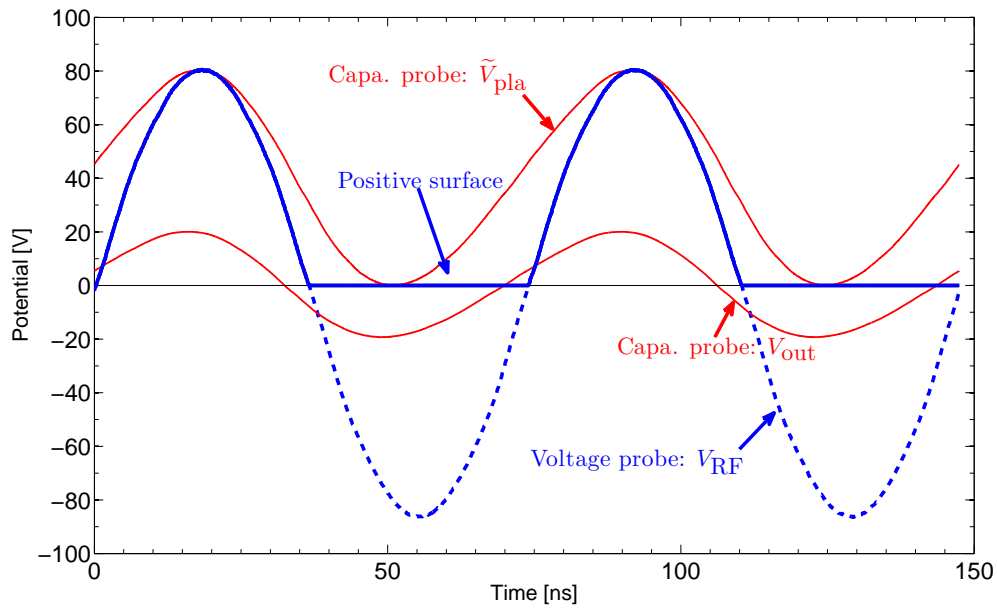


**Figure 4.19:** Potential on the RF electrode ( $V_{\text{RF}}$ ), capacitive probe output voltage ( $V_{\text{out}}$ ), oscillation of the plasma potential ( $\tilde{V}_{\text{pla}}$ ) and highest positive surface in contact with the plasma as a function of time.  $\tilde{V}_{\text{pla}}$  is shifted vertically so its extrema coincide with 0 V and  $\max(V_{\text{RF}})$ . Typical measurement taken in a parallel-plate reactor in hydrogen at 50 Pa and 170  $V_{\text{pp}}$ .

# Chapter 5

## Low ion energy in the grid reactor and the associated plasma phenomena

In order to compare measurements taken with the parallel-plate reactor and with the grid reactor, it is important that the experimental parameters (i.e. gas type, pressure and RF power) are similar in both reactors. Although it is simple to know the gas type and pressure, it is less clear which parameter should be used as reference for the RF plasma power. One possibility is to use the RF power injected into the reactor. However, it can be difficult to properly separate the RF power injected into the plasma from the RF power dissipated in the reactor vacuum circuit as discussed in section 3.2.2. Therefore, in this study, the peak-to-peak voltage ( $V_{pp}$ ) is used instead as it is independent from the ohmic losses in the matching and the reactor (see Fig. 3.3) and  $V_{pp}$  is measured directly on the RF electrode by the voltage probe. However, the range of  $V_{pp}$  at which the plasma is stable is different in both reactors (see Sec. 3.2.2). Therefore, taking measurements at the same  $V_{pp}$  in both reactors implies that the measurements in the parallel-plate reactor are taken in a regime close to the upper stability limit whereas the measurements are taken close to the lower stability limit of the grid reactor. This limits the overlapping range of  $V_{pp}$  in both reactors.

The results on ion energy presented in this section are summarised in [71]. They are structured as following: In the first section, the plasma density gradients and the optical emission intensities are compared in the two reactor designs. In the second section, the transmission of RF currents through holes in a grounded plate and its implication on self-bias potential are discussed. An extensive discussion is

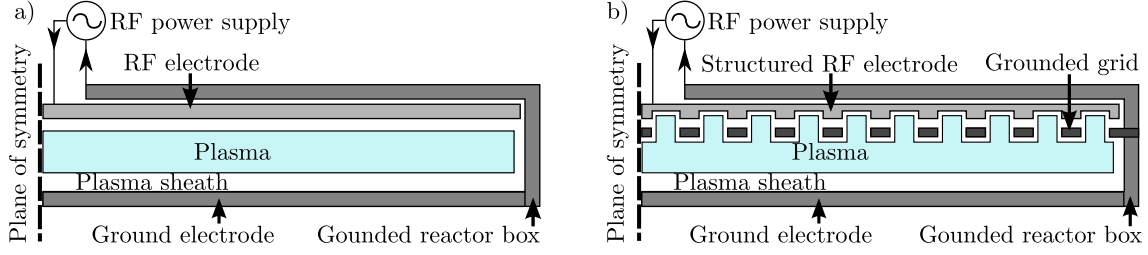


**Figure 5.1:** Representation of (a) the parallel-plate reactor and (b) the grid reactor.

made on the transmission of RF current through the plasma in the small hole of a grounded plate. In the third section, the ion velocity distribution is measured in both the parallel-plate reactor and the grid reactor. Then, the influence of the self-bias potential on the maximum ion energy is discussed. In the final section, the time evolution of the plasma in both reactors is studied in two steps. First, phase resolved optical emission spectroscopy shows that the time evolution of the ground sheath light emission differ in both reactors. In a second step, the time evolution (i.e. the waveform) of the plasma potential is measured in both reactors with the capacitive probe. The influence of the plasma potential waveform on the time-averaged plasma potential, hence on the maximum ion bombardment energy, is discussed. The section concludes by showing a good correlation between the measured ion bombardment energy and calculated time-averaged plasma potentials in both reactors and by showing the reduced ion bombardment energy in the grid reactor in a broad range of RF voltages.

## 5.1 Optical emission intensity and plasma density

Before discussing optical emission intensity measurements in both reactors, a reminder of the reactor geometries and their plasmas is shown in figure 5.1.

The optical emission intensity in the parallel-plate reactor in hydrogen is shown in figure. 5.2(a). The intensity is maximum near the sheath edge and is symmetric on both sheaths. The emission intensity is proportional to the ionisation rate (see Sec. 4.3) and therefore, this shows that the ionisation rate in the parallel-plate reactor is maximum around the sheath edges. This is expected as it is there that the convolution of sheath electric field and electron density profile is strongest such as during field reversal and electron expulsions from the sheath (see Sec. 5.4 and 6.3). This stronger ionisation rate at the sheath edges reflects in the measured ion density profile shown in figure 5.2(b). This profile is slightly different from a purely diffusive profile where the ion density profile has a cosine shape [28]. The deviation from this

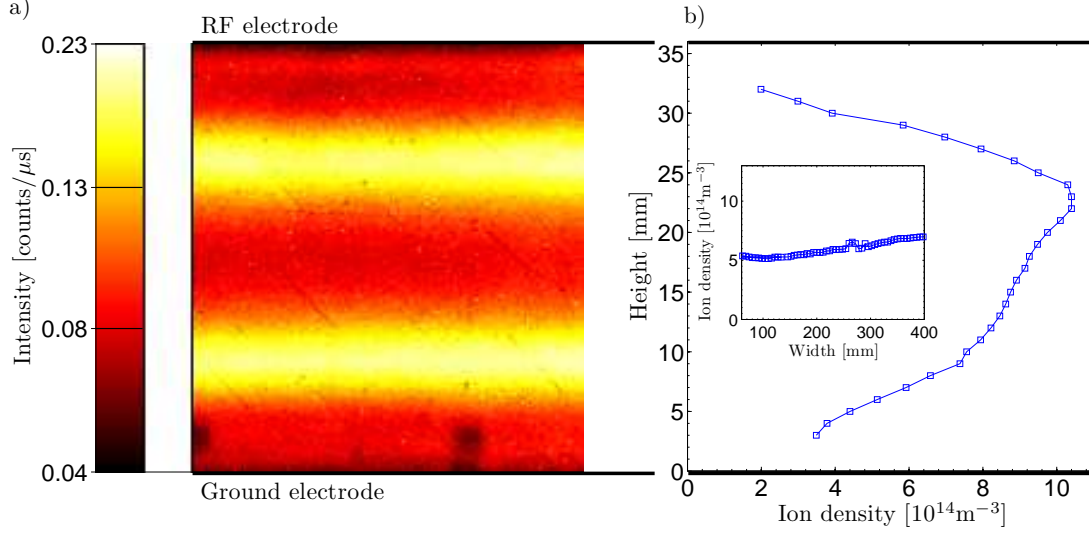


**Figure 5.2:** (a) Time-averaged  $H_\alpha$  emission intensity between the electrodes and (b) vertical ion density profile in a parallel-plate reactor in hydrogen at 350  $V_{pp}$ . Inset in (b) : Ion density profile along the electrodes, 7 mm above the ground electrode. The two low spots of emission intensity close to the ground electrode are due to the fixation screws from the RFEA. The color scale is logarithmic to highlight gradients at low and high intensities.

diffusive profile is probably due to the higher ionisation rate at the sheath edges and also due to the non-zero self-bias potential in the parallel-plate reactor. At lower  $V_{pp}$ , both the self-bias and the influence of the sheaths ionisation are weaker and the measured profile, shown in figure 5.3, is closer to the diffusive profile. In figure 5.3, the measured density is slightly higher close to the ground electrode than to the RF electrode. This effect could be a consequence of the influence on the probe shaft on the Langmuir probe collection area as discussed in section 4.2.

The ion density profile along the electrodes in figure 5.2(b) is higher on the right hand side. This is due to a denser plasma which forms around an opening in the right reactor sidewall. This opening is necessary for the insertion of the Langmuir probe scanning along the electrodes. This dense localised plasma only forms at high  $V_{pp}$  and no signs of this dense plasma is visible at lower  $V_{pp}$  as shown in figure 5.3. At this  $V_{pp}$ , the horizontal density is nearly constant as expected in such a reactor. To prevent this dense plasma in the reactor side from occurring during measurements other than Langmuir probe scans, the insertion hole is filled when any other measurement is used.

The results in argon are shown in figure 5.4. They are qualitatively similar to the results in hydrogen discussed previously. Here the emission intensity is slightly higher at the ground sheath and this reflects in a higher ion density close to the ground sheath. The horizontal ion density profile shows an even stronger perturbation

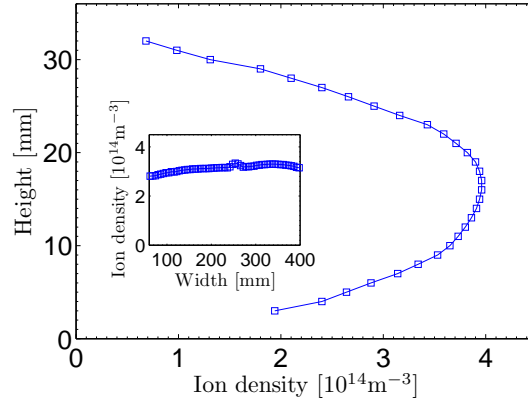


**Figure 5.3:** Ion density vertical profile in a parallel-plate reactor in hydrogen at 170  $V_{pp}$ . Inset: Ion density profile along the electrodes, 7 mm above the ground electrode.

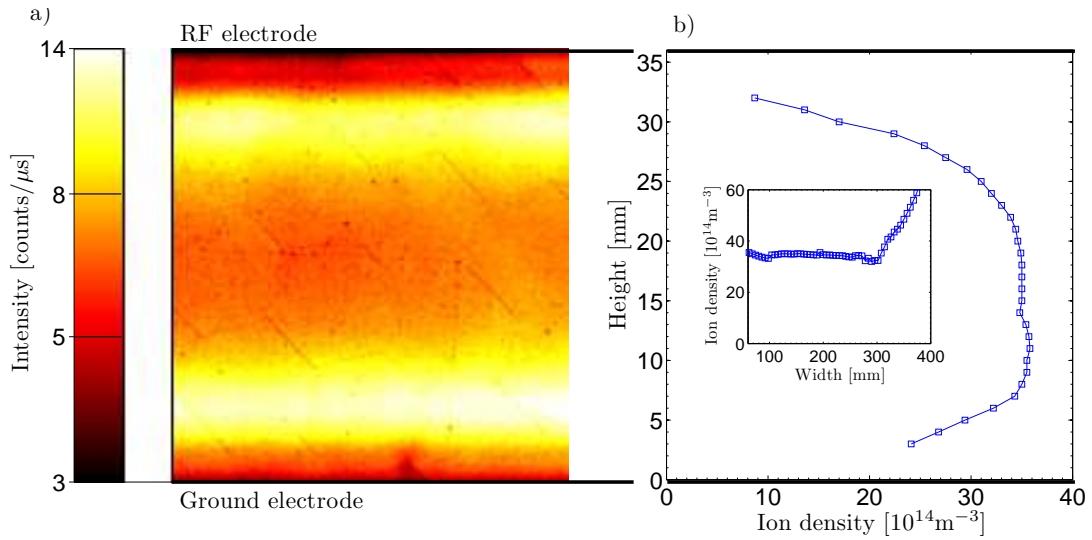


**Figure 5.4:** (a) Time-averaged Ar (750.4 and 751.5 nm) emission intensity between the electrodes and (b) vertical ion density profile in a parallel-plate reactor in argon at 350  $V_{pp}$ . Inset in (b) : Ion density profile along the electrodes, 7 mm above the ground electrode. The color scale is logarithmic to highlight gradients at low and high intensities.



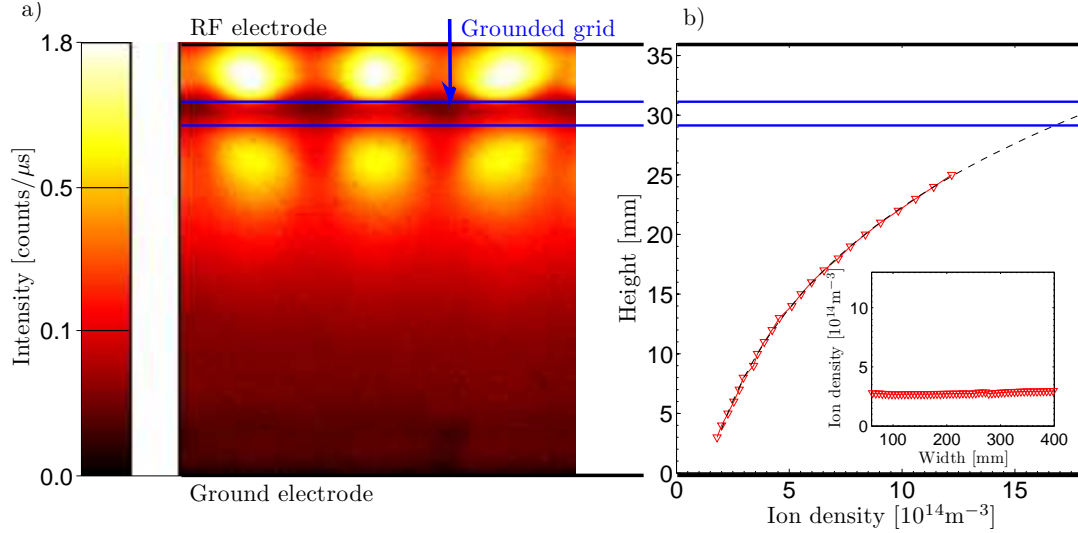


**Figure 5.5:** (a) Time-averaged  $H_\alpha$  emission intensity between the electrodes and (b) vertical ion density profile in a grid reactor in hydrogen at 350  $V_{pp}$ . The vertical profile of ion density is aligned with the axis of a grid hole. Inset in (b) : Ion density profile along the electrodes, 7 mm above the ground electrode. The color scale is logarithmic to highlight gradients at low and high intensities.

caused by the dense plasma in the right hand side probe insertion hole.

The emission intensity profile in the grid reactor in hydrogen is shown in figure 5.5. There, the intensity is strong above the grid holes and dim close to the grounded electrode. Hence, the ionisation rate is maximum above the grid. However, the ion loss rate above the grid is high due to the proximity of the RF electrode and grounded grid. Thus only a small fraction of the ions produced above the grid will travel through the grid toward the ground electrode. This effect is reflected in the vertical density profile which is peaked toward the grid. However, the horizontal ion density profile is even across the electrodes. Therefore, although the majority of the plasma density below the grid comes from the dense localised plasmas in the grid holes, each separated by 12 mm, the influence of each single hole does not influence the uniformity along the electrodes 7 mm above the substrate (22 mm away from the grid). This good uniformity across the substrate is a necessity for large area thin film deposition. Furthermore, this figure shows no sign of the denser plasma in the right sidewall which was observed in some parallel-plate measurements.

The emission intensity profile in argon is shown in figure 5.6. With this gas, the emission intensity is also brighter above the grid, but here the emission intensity is still visible close to the grounded electrode. This higher optical emission intensity close to the ground sheath is reflected in the vertical ion density profile which is still maximum close to the grid but now has a second maximum close to the grounded electrode. The mechanism responsible for the difference in ion density

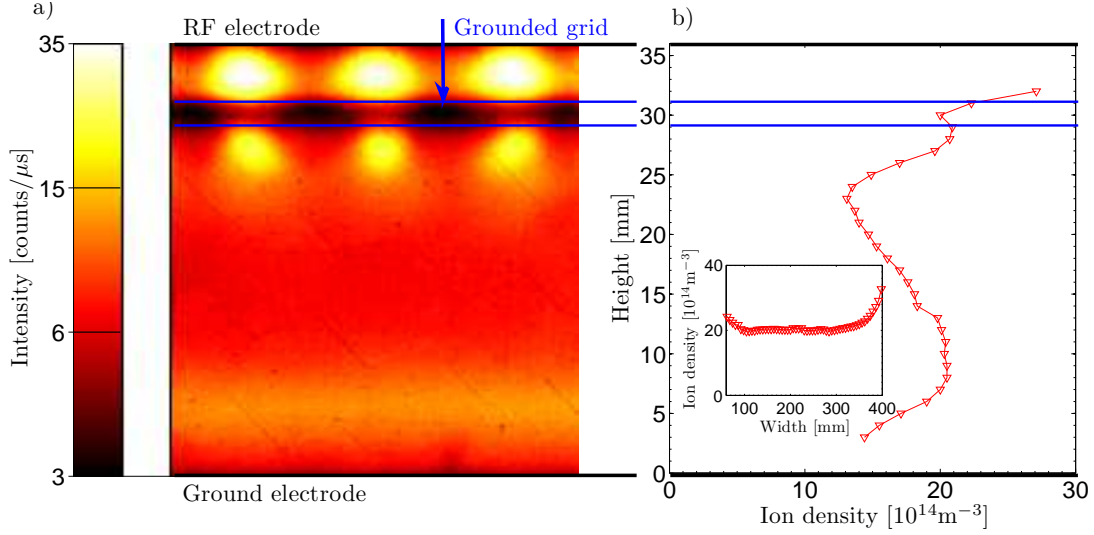


**Figure 5.6:** (a) Time-averaged Ar (750.4 and 751.5 nm) emission intensity between the electrodes and (b) ion density vertical profile in a grid reactor in argon at 350  $V_{pp}$ . The vertical profile of ion density is aligned with the axis of a grid hole. Inset in (b) : Ion density profile along the electrodes, 7 mm above the ground electrode. The color scale is logarithmic to highlight gradients at low and high intensities.

profiles between the two gases has been studied with the use of numerical simulation and is discussed in chapter 6.

The ion density profile along the electrodes in the grid reactor in argon (Fig. 5.6(b)) shows again a strong influence from the dense plasma in the insertion hole for the Langmuir probe scan along the electrodes. However, the ion density is even in the center of the reactor and shows no variation caused by the dense localised plasma in the grid holes.

## 5.2 Self-bias and conduction of RF currents through holes

In this section, the self-bias potential ( $V_{sb}$ ) in the parallel-plate and grid reactors are discussed. The self-bias potential is particularly important for the ion bombardment energy since it influences the time-averaged plasma potential as shown explicitly in equations 2.1.18 and 2.1.20. In section 2.1.1, it was shown how  $V_{sb}$  varies with the ratio of RF electrode area in contact with the plasma ( $A_{RF}$ ) and ground electrode area in contact with the plasma ( $A_{gnd}$ ) (Eq. 2.1.29). To highlight the variations of  $V_{sb}$  between the parallel-plate reactor and the grid reactor, it was decided to divide  $V_{sb}$  by the peak-to-peak voltage ( $V_{pp}$ ). Since, to a reasonable approximation,  $\bar{V}_b \propto$

$V_{pp}$  where  $\bar{V}_b$  is the time-averaged ground sheath potential (Eq. 2.1.29), therefore,  $\frac{V_{sb}}{V_{pp}} \propto \left(1 - \frac{A_{RF}}{A_{gnd}}\right)^q$  which, for a given  $A_{RF}/A_{gnd}$ , is constant to a first approximation. The results are shown in figure 5.7. There, it is seen that  $V_{sb}$  is slightly negative in the parallel-plate reactor in both gases. In this reactor,  $A_{RF}$  is the RF electrode area and  $A_{gnd}$  is the grounded electrode area plus the area of the sidewalls. Therefore,  $A_{RF} \leq A_{gnd}$  hence there is a small electrode asymmetry and the measured self bias is slightly negative. This figure shows a strong negative self-bias in the grid reactor in both gases. This negative self-bias is a consequence of the plasma present in the volume below the grid as shown by the optical emission and density measurements (Fig. 5.5 and 5.6). Therefore, in the grid reactor,  $A_{gnd}$  includes the grounded electrode area, the sidewalls area plus the area of the grounded grid in contact with the plasma (potentially both sides of the grid and the holes). Hence  $A_{RF}$  is only slightly increased by the structure in the RF electrode whereas  $A_{gnd}$  is strongly increased. In this reactor, the ion density is asymmetric, therefore, the influence of the surfaces area must be weighted by the density at their sheaths edges as discussed in equation 2.1.30. Therefore, to a first approximation in hydrogen, the grid area in contact with the plasma counts 13 times ( $\alpha^{\frac{q}{2}}$ ,  $q = 2.5$ ) more than the grounded electrode and sidewalls since the density is roughly 8 times higher next to the grid.

Figure 5.7(a) also shows that, in hydrogen,  $V_{sb}/V_{pp}$  is nearly constant in both reactors. However, in argon (Fig. 5.7(b)) this ratio varies significantly with  $V_{pp}$ . This variation is not fully understood and it could be due to changes in the density profile with  $V_{pp}$ . Figure 5.7 also shows that the self-bias in the grid reactor is lower in argon compared to hydrogen. The electrode area asymmetry is, to a first approximation, the same in both reactors hence it could be expected to measure similar self-bias with both gases. This difference in  $V_{sb}$  is probably a consequence of the different ion density profiles in the two gases (see Eq. 2.1.30, Fig. 5.5 and Fig. 5.6). It is also possible that the argon plasma, since it is known to expand more easily than hydrogen plasma, has a better coverage of the RF electrode area, thereby affecting the area asymmetry. Hence, the grid reactor design makes available the front and back of the grid for electrode area asymmetry and the gas determines the area in contact with the plasma and sheaths capacitances via the density profiles at these surfaces.

The strong negative self-bias caused by the grounded grid shows that a relatively important portion of the RF current flows toward the grounded sheath below the grid. Without this, the electrode asymmetry in the grid reactor would be small. As

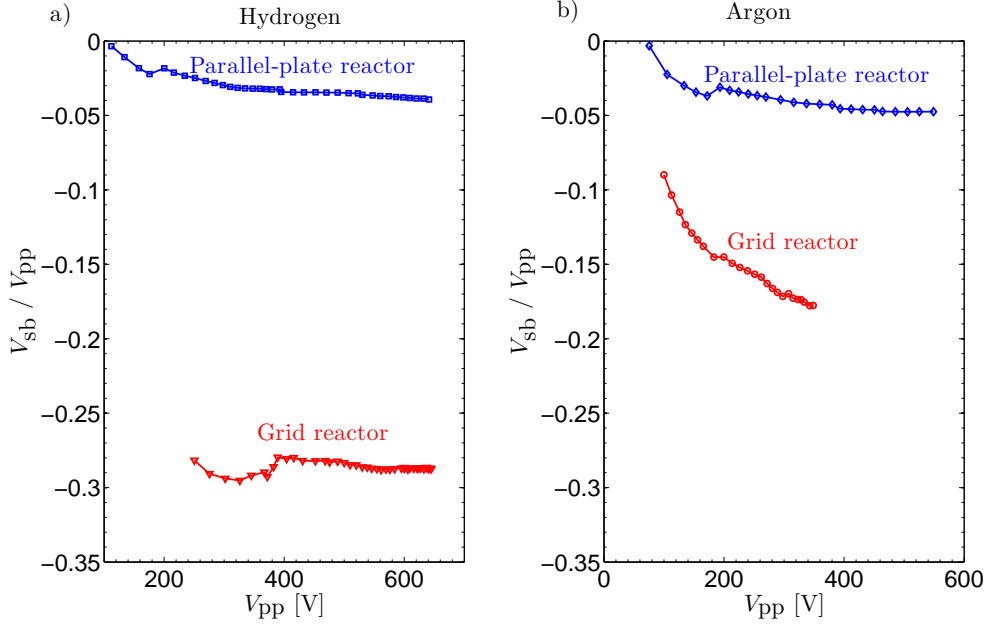


**Figure 5.7:** Measured ratio of self-bias voltage ( $V_{sb}$ ) to the peak-to-peak voltage ( $V_{pp}$ ) as a function of  $V_{pp}$  in a parallel-plate reactor and in a grid reactor (a) in hydrogen and (b) in argon.

the RF current flows through the dense plasma in the holes of the grounded grid, the plasma potential is also conducted through the grid. Since the hydrogen and argon plasmas are good conductors, it is expected that the plasma potential is conducted from one side of the grid to the other without a significant drop.

In conclusion, the grid reactor, when the plasma expands to the volume below the grid, is a novel highly asymmetric reactor (unequal electrode areas) whilst maintaining a uniform plasma above the substrate area. The strong negative self-bias resulting from this electrode asymmetry plays a strong role in reducing the ion bombardment and it will be discussed in detail in section 5.3.

### 5.2.1 Plasmoid and RF current transmission

To study the influence of the grid holes diameter on the transmission of RF current through those holes, an experiment was undertaken in the small area reactor described in section 3.1.1. In this reactor, the grid was first replaced by a plate in which a diaphragm was installed as shown in figure 5.8. The diaphragm opening was remotely controlled so that the hole diameter could be varied without interrupting the plasma. If the diaphragm was partially open, the plasma located in the upper chamber entered the diaphragm hole and flowed to the lower chamber as shown in figure 5.9. By changing the diaphragm diameter, the opening area between the two chambers through which the RF current flowed was varied. The results in

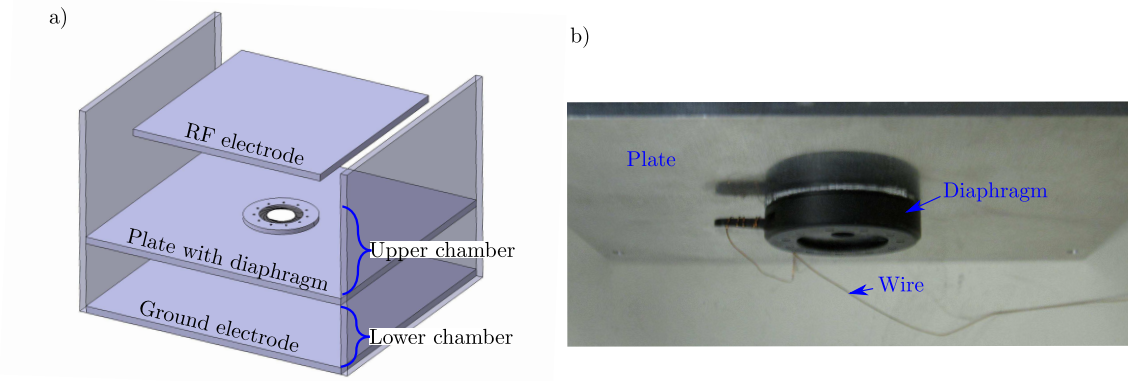


**Figure 5.8:** (a) Schematic of the test reactor described in section 3.1.1 in which the grid is replaced by a grounded plate with a diaphragm at its center and the RF electrode has structures as those used in the grid reactor. (b) Photograph of the plate, the diaphragm and the wire used to remotely control the diameter of the diaphragm.

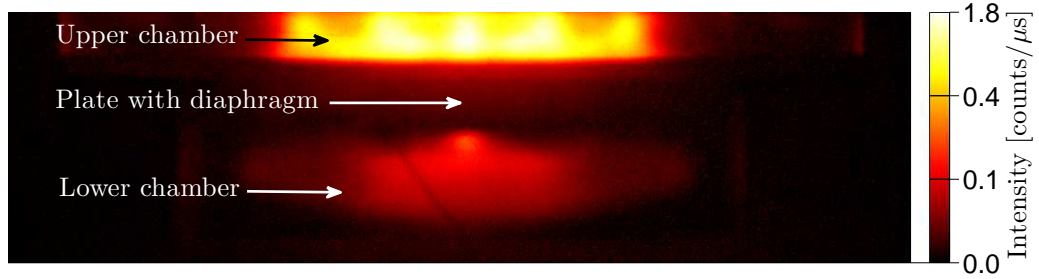


**Figure 5.9:**  $H_\alpha$  emission intensity in a reactor with an open diaphragm in a grounded plate in hydrogen at 100 Pa. The plasma is seen in both the upper and lower chambers. The color scale is logarithmic to highlight gradients at low and high intensities.

figure 5.10, show that the hole diameter had no influence on  $V_{sb}/V_{pp}$ . Hence the portion of RF current flowing to the ground sheaths in the lower chamber was independent of the diaphragm diameter. As a consequence, the RF current density flowing through the diaphragm increased strongly for small diameters, resulting in a bright and probably dense plasma around the hole. This surprising result is of importance for RF plasma reactors as it shows that even a small hole filled with a plasma can significantly affect the self-bias potential and thus modify the plasma parameters.

To more thoroughly investigate the influence of RF current conduction through the plasma in a small hole, another experiment was conducted and the results are summarised in [72]. For this study, the grounded plate and diaphragm of figure 5.8 were replaced by a thin stainless steel mesh as illustrated in figure 5.11. The mesh wires diameter was 0.2 mm with a pitch of 0.5 mm. The mesh geometry was regular

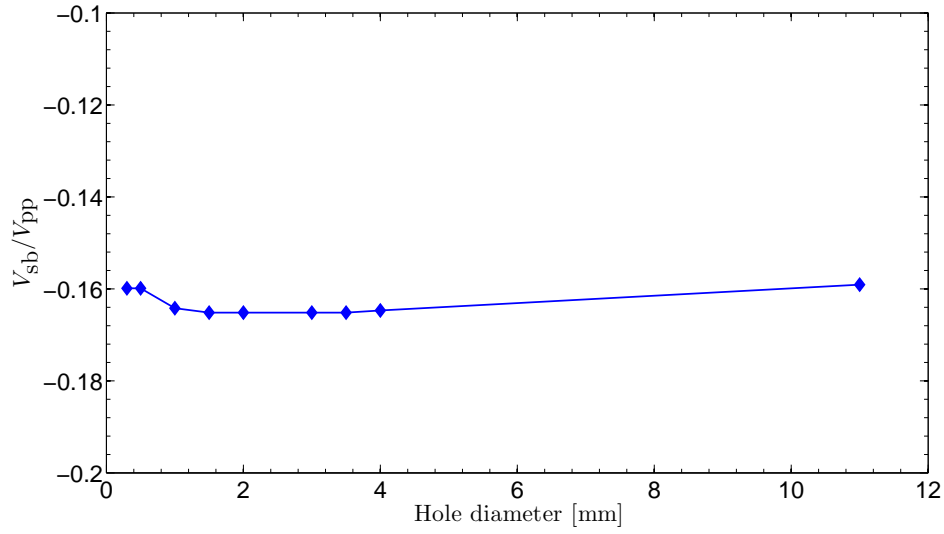


**Figure 5.10:** Measured ratio of self-bias voltage ( $V_{sb}$ ) to the RF peak-to-peak voltage ( $V_{pp}$ ) as a function of the diaphragm hole diameter, in the test reactor with a diaphragm in a grounded plate, in hydrogen at 100 Pa.

except for one slightly larger orifice (0.7 mm diameter) in its central region, used to ensure that the dense plasma ignited there reproducibly. This mesh, similar to the grounded plate and grounded grid in the previous experiments, separated the reactor into two chambers. The upper chamber included a RF electrode, with structure as those used in the grid reactor, whereas, the lower chamber was a grounded enclosure (a Faraday cage) except for the holes in the mesh. Experiments were performed in hydrogen at 100 Pa to help stabilizing the plasma in the larger hole.

In this study, the dense plasma in a tiny hole is defined as a plasmoid. This definition

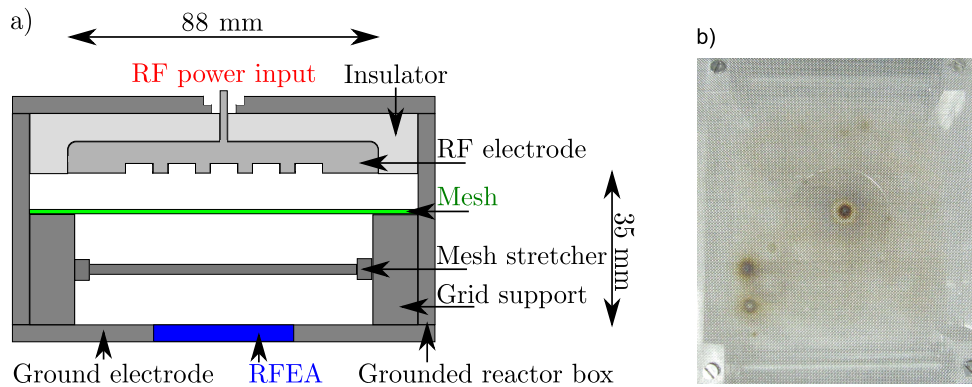


**Figure 5.11:** (a) Schematic of the test reactor described in section 3.1.1 where the grid is replaced by a mesh with a larger hole at its center. The mesh stretcher limits the bending of the mesh under its own weight. (b) Photograph of the mounted mesh viewed from above.

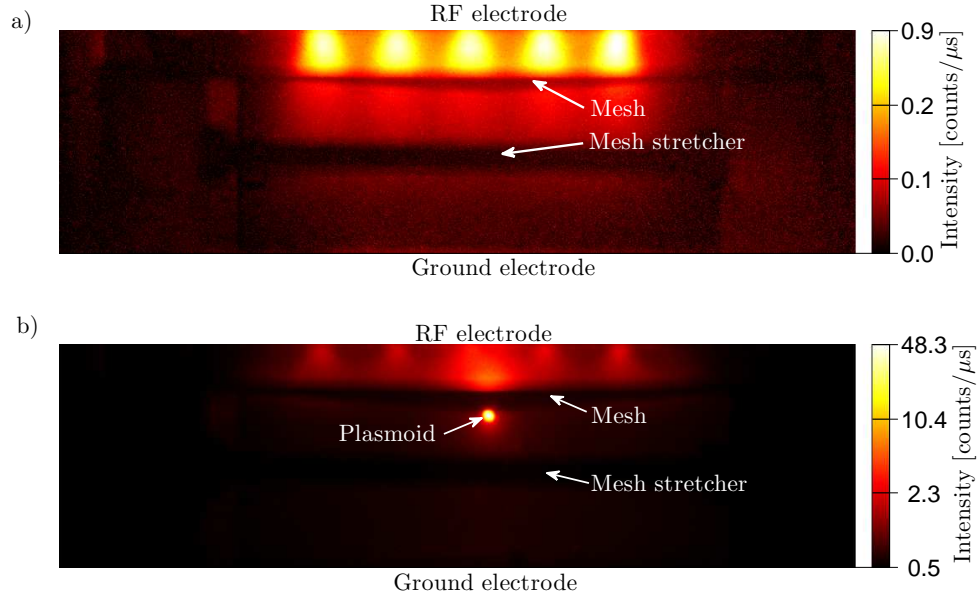


**Figure 5.12:** Time-averaged optical emission intensity of  $H\alpha$  in the test reactor with a mesh. (a) plasma only present in the chamber above the mesh in absence of a plasmoid. (b) plasma present in both chambers with a plasmoid ignited in the mesh orifice. The plasmoid intensity strongly dominates the other emission intensity. The plasma above the mesh is  $2.5\times$  stronger in (b). The color scales are logarithmic to highlight gradients at low and high intensities.

follows the general description of Chapman [73] of "... a volume of more intense glow than its surroundings." Different definitions describe plasmoids as resonance-sustained RF discharges [74, 75] or as plasma-magnetic entities [76, 77]. Plasmoids can spontaneously ignite in one hole of a grounded grid, mesh or plate used to confine a plasma. Plasmoids resemble a hollow cathode forming in a grounded cavity (cathode) maintained by the positive RF plasma potential (anode), except that in this case, the plasmoid also sustained a RF plasma on the other side of the grid by conducting an RF electron current between the plasmas via the plasmoid as discussed previously.

#### 5.2.1.1 General observations: Emission intensity and self-bias potential

When the RF plasma was initially ignited, at a peak-to-peak voltage of 850 V, the plasma was confined entirely inside the upper chamber, as shown in figure 5.12(a). The plasma RF sheath, which was 2 or 3 mm thick, did not penetrate into the mesh holes or its 0.7 mm-diameter orifice because it was too thick to be conformal with their contours. The mesh therefore acted as a featureless, uniform equipotential plane at ground potential. The cylindrical cavities of the RF electrode structure are filled with plasma intensified by the concentration of electron density along the axis

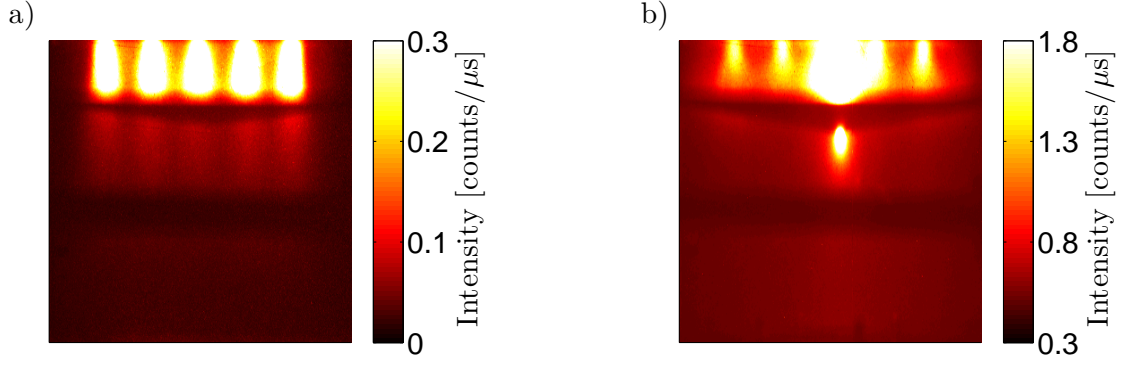


**Figure 5.13:** Time-averaged optical emission intensity of  $H_{\alpha}$  in the small area reactor with a mesh (a) without plasmoid and (b) with a plasmoid. In this figure, the color scale is linear and does not cover the full range of intensity. This different color scale compared to figure 5.12 was used to highlight the strong increase of emission intensity below the mesh when the plasmoid is present.

of these cavities (hollow cathode effect) [73, 78]. This is shown by the regular array of more intense glows above the mesh in figure 5.12(a).

In figure 5.14, the measured ratio of self-bias voltage to the peak-to-peak voltage,  $V_{sb}/V_{pp}$  is shown as a function of  $V_{pp}$ . This figure shows two different regimes : In the first regime ( $A \leftrightarrow B$ ) the plasma was only present above the mesh, there was no plasmoid and  $V_{sb}/V_{pp} > 0$  (see Fig. 5.12(a)); in the second regime ( $D \leftrightarrow E$ ) the plasmoid sustained a plasma below the mesh and  $V_{sb}/V_{pp} < 0$  (see Fig. 5.12(b)). These two situations were separated by transitions :  $B \rightarrow C$  and  $E \rightarrow F$ .

Without the plasmoid, following the curve  $A \rightarrow B$ , the sheath capacitance due to the high density plasmas next to the RF electrode was larger than the combined sheath capacitance of the grounded sidewalls and mesh and therefore the measured self-bias voltage was positive (see Sec. 2.1.1, [28]). The measured ratio  $V_{sb}/\tilde{V}_{pp} \sim +0.15$  remained approximately constant along  $A \rightarrow B$ .

When the RF voltage was increased along  $A \rightarrow B$  as far as point  $B$  in figure 5.14, an intense plasmoid spontaneously ignited in the mesh central orifice as shown in figure 5.12(b) and the self-bias voltage simultaneously dropped to a strongly negative value  $V_{sb}/V_{pp} \sim -0.3$  at  $C$  where conditions are again stable. The observed drop in  $V_{pp}$  from point  $B$  (850 V) to  $C$  (650 V) depended on the modified distribution of RF power between the RF external circuit and the plasma with plasmoid. It should be noted that the RF power density necessary to ignite the plasmoid,  $\sim 1.5 \text{ Wcm}^{-2}$ , was about an order of magnitude higher than for usual plasma processing conditions. The plasmoid emission intensity dominated the surrounding plasma intensity, even though the upper plasma became  $\sim 2.5\times$  brighter compared to immediately before



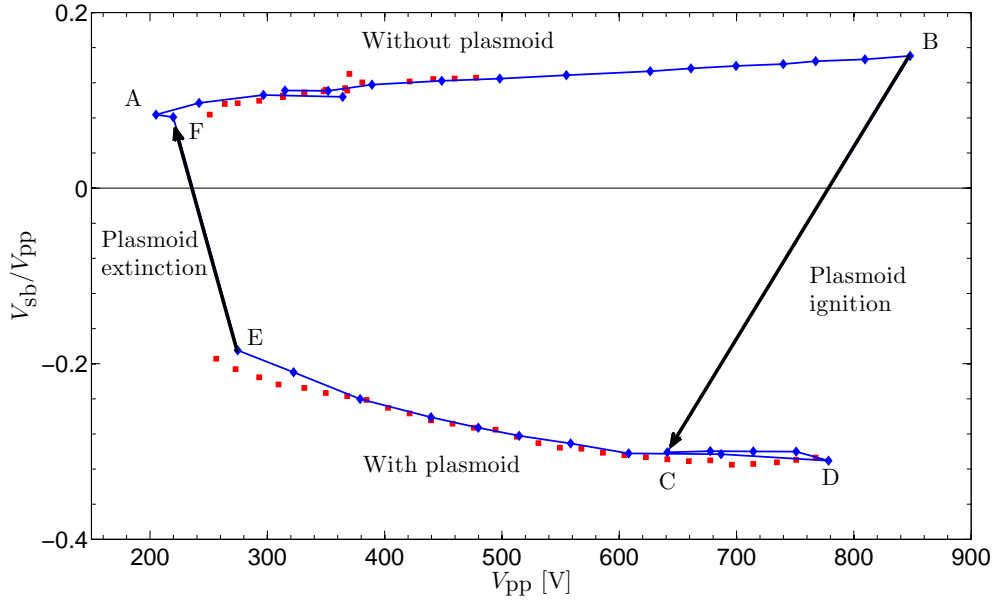


**Figure 5.14:** The measured ratio of self-bias voltage to the peak-to-peak voltage,  $V_{sb}/V_{pp}$ , as a function of  $V_{pp}$  in hydrogen at 100 Pa. Along  $A \rightarrow B$ , the plasma is only present above the mesh, there is no plasmoid. The transition from  $B$  to  $C$  is caused by the plasmoid ignition, accompanied by a faint plasma below the mesh and a strong drop in self-bias voltage. Along  $D \rightarrow E$ , the plasmoid sustains a plasma below the mesh. The plasmoid extinguishes during the transition from  $E$  to  $F$ . Each point corresponds to a measurement in steady-state conditions, whereas each arrow  $B \rightarrow C$  and  $E \rightarrow F$  represents a spontaneous transition. The blue diamonds and red squares represent two measurement series separated by hours of plasma.

the plasmoid. Because of its dominant emission, it could have been assumed that the plasmoid was a straightforward hollow cathode burning inside the orifice [73]; however, the strongly negative self-bias voltage indicated that the effective capacitance to ground had also strongly increased. On closer inspection (Fig. 5.13), it was also seen that emission intensity below the mesh increased by  $\sim 20\times$  with the plasmoid, especially below the mesh stretcher. This increased intensity was the consequence of a plasma below the mesh. The plasma in the chamber below the mesh had a comparatively weak intensity because of the lower RF sheath voltage to ground due to the strong self-bias voltage.

The appearance of this plasma in the lower chamber was also shown by the ion flux and energy measured by the RFEA at the bottom electrode, shown in figure 5.15. Without plasmoid, the only source of ions is the plasma above the mesh. Those ions are accelerated by the sheath above the mesh but they lose their energy by collisions with the gas molecules between the mesh and the RFEA. Hence, the current density measured by the RFEA is small and the ions have an energy close to

0 eV. However, with the plasmoid, the ions are accelerated in the sheath separating the plasma below the mesh from the RFEA. Their travelling distance between the plasma and the RFEA is much smaller hence they lose less energy by collisions. As a consequence, the measured current density is higher and the maximal ion energy is  $19 \pm 2$  eV.

In this lower chamber, the plasma comes into contact with additional grounded surfaces (the underside of the mesh, the chamber bottom, and its sidewalls) which almost triple the total ground surface area in situation *C* compared to the initial situation *B*, hence the fall in  $V_{sb}/V_{pp}$  in figure 5.14. Estimations of the effective ground area, the fraction of the total RF current conducted through the plasmoid, and the current density in the plasmoid are given in section 5.2.1.2.

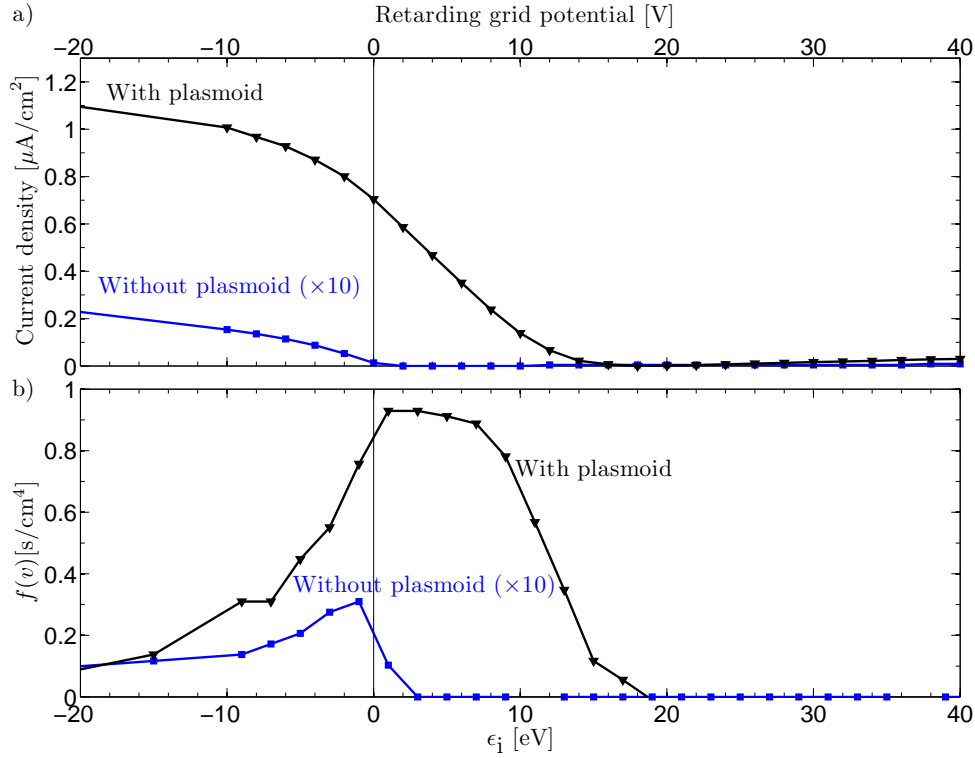


**Figure 5.15:** (a) Current density as a function of the retarding potential and (b) ion velocity distribution ( $f(v)$ ) as a function of the ion bombardment energy ( $\epsilon_i$ ) without plasmoid and with plasmoid at 550  $V_{pp}$  and 100 Pa in hydrogen.

The simultaneous appearance of the plasmoid with the lower chamber plasma and the large drop in self-bias voltage from +127 V to -193 V was the principal observation of this work. Such a strong drop in self-bias could only be explained by a major change in the electrode asymmetry caused by the plasmoid conducting RF plasma current through to the other side of the grounded mesh. By using two similar size

chambers in this work, the observed effect was very clear.

Once the plasmoid had appeared, the RF voltage could be varied along  $D \rightarrow E$  (Fig 5.14) to values much lower than at  $B$ , whilst the self-bias became less negative as the lower plasma gradually shrank away from the grounded walls towards the plasmoid as observed by eye. Eventually, at point  $E$  in figure 5.7, the plasmoid and the lower plasma suddenly extinguished simultaneously and the self-bias was again positive with plasma only above the mesh at point  $F$ . The cycle  $F \rightarrow B \rightarrow C \rightarrow E \rightarrow F$  could be repeated, with the plasmoid always striking in the same orifice, although the strike voltage at  $B$  and the extinction voltage at  $E$  depended apparently on the surface condition around the orifice, as discussed below in section 5.2.1.4. If the RF voltage was increased beyond  $C$  along  $C \rightarrow D$ , then at some point when the RF plasma potential was high enough one or several additional plasmoids would ignite.

### 5.2.1.2 Plasmoid ignition, potentials and currents

At first glance, the plasmoid could be mistaken with a hollow cathode plasma in the mesh orifice. In a hollow cathode plasma, the normal ejection of electrons by the sheath electric field around the inside of a cavity causes an enhanced concentration of electron density along the axis of the cavity [73, 78]. This axial concentration effect does not specifically refer to the "pendulum" phenomenon of oscillating electrons in other definitions of the hollow cathode [79]. In this study, the aspect ratio of orifice height to orifice diameter is rather unfavorable for a hollow cathode discharge because the thin flat mesh provides only a short axis for electron confinement compared to the long axis of a typical cylindrical cavity. Furthermore, the mesh wires do not form a concave cavity and the sheath electric fields are divergent instead of concentrating electrons towards the axis. The plasmoid geometry is contrasted with a typical hollow cathode geometry in figure 5.16. Contrarily to the hollow cathode shown in figure 5.16(b), the plasmoid funnels high density rf current between the upper and lower chamber and this results in a significant heating mechanism for the plasmoid as discussed in section 5.2.1.3.

The orifice in which the plasmoid exists is smaller than the standard RF glow discharge sheath width ( $\sim 1 - 10$  mm). This is possible due to the locally-high plasma density of the plasmoid. Starting from a low RF voltage, along  $A \rightarrow B$  (see Fig. 5.14), the plasma density approaching the high power point  $B$  begins to increase locally above the orifice as the RF plasma sheath starts to deform in towards it. This locally-enhanced plasma density will draw a higher plasma power density. The positive feedback of this effect would lead to a rapid collapse of the plasma

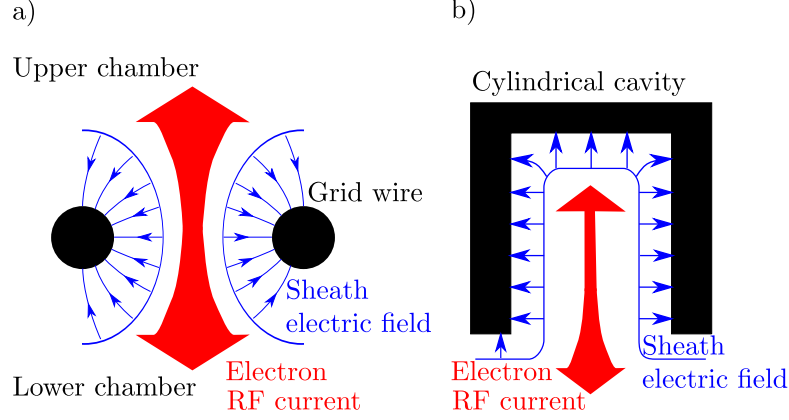


**Figure 5.16:** The geometry and sheath electric fields for (a) a plasmoid discharge in a mesh; and (b) a typical hollow cathode discharge in a closed cylindrical cavity. The divergent field in the mesh arrangement is less favorable for concentrating the electron flux on axis and sustaining a hollow cathode discharge. However, large RF currents can funnel through the open mesh in contrast to the closed cylinder.

sheath into the orifice [78] and spontaneous formation of a plasmoid. This happens first above the widest aperture in the grounded mesh, which is why the wider orifice was used in this experiment to ensure reproducible ignition there.

When the plasmoid spontaneously strikes at  $B$ , the majority of the plasma RF potential is conducted via the plasmoid into the lower chamber. The strong light emission and the drop observed in the numerical simulation for the grid reactor (Fig. 6.5) suggests that a potential drop through the mesh of the order of 5 to 10 V could be expected. Above the mesh, the time-averaged plasma potential with respect to ground can be roughly estimated [29, 31] as  $\bar{V}_{\text{cap}} \simeq \frac{1}{2} \left( \frac{V_{\text{pp}}}{2} + V_{\text{sb}} \right)$  (Eq. 2.1.18), assuming capacitive sheaths and an equipotential plasma. Using the results of figure 5.14 at points  $B$  and  $C$  respectively for the profiles  $\bar{V}_{\text{cap}}(z)$  in figures 5.17(a) and (b), it is clear that the strong drop in self bias voltage due to the plasmoid ignition also reduces the time-averaged plasma potential, from  $\sim 276$  V to  $\sim 66$  V. The sheath voltage between the plasma and the mesh falls in the same proportion, and consequently the ignition of other plasmoids will be inhibited so that higher RF power is necessary to form additional plasmoids.

This plasmoid property of reducing the plasma potential by dropping the self-bias distinguishes it from a hollow cathode discharge in a closed cavity (figure 5.16) where the plasma potential is not strongly changed. Hence multiple arrays of hollow cathode-like discharges can easily be obtained in the structure of the RF electrode and in [80–85], as shown by the structured RF electrode in figure 5.12(a) and (b), in contrast to the single plasmoid whose ignition inhibits the appearance of other

plasmoids. This is a fundamental difference between a plasmoid in a grid and a hollow cathode discharge in a closed cavity.

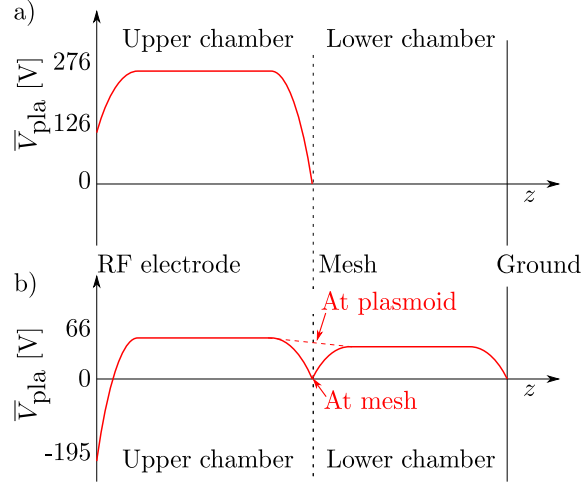


**Figure 5.17:** The estimated profile of time-averaged plasma potential amplitude ( $\bar{V}_{\text{cap}}$ ) along the reactor height ( $z$ ) for: (a) the point *B* of figure 5.7, before plasmoid ignition; (b) the point *C* of figure 5.7, after plasmoid ignition. The dotted line represents the plasma potential along the axis of the plasmoid between the upper and lower chambers. The strong drop in self bias voltage due to plasmoid ignition reduces the plasma potential.

Similarly to the discussion held in section 2.1.1, the RF voltage amplitude across the RF sheath, from figure 5.17, is  $\simeq V_{\text{pp}}/4 - V_{\text{sb}}/2$  [29, 31]. Continuity of RF current ( $\tilde{I}_{\text{RF}}$ ) across the discharge via sheath displacement current therefore requires:

$$\tilde{I}_{\text{RF}} = C_{\text{RF}} \left( \frac{V_{\text{pp}}}{4} - \frac{V_{\text{sb}}}{2} \right) = C_{\text{g}} \left( \frac{V_{\text{pp}}}{4} + \frac{V_{\text{sb}}}{2} \right), \quad (5.2.1)$$

where  $C_{\text{RF}}$  is the effective capacitance of the sheath at the RF electrode and  $C_{\text{g}}$  is the net effective capacitance of the sheaths at all the ground surfaces. Accounting for the sheath voltage dependence of the sheath width and density [28, 86], the ratio of the corresponding electrode areas is:

$$\frac{A_{\text{g}}}{A_{\text{RF}}} = \left[ \frac{1 - 2V_{\text{sb}}/V_{\text{pp}}}{1 + 2V_{\text{sb}}/V_{\text{pp}}} \right]^{1/q}, \quad (5.2.2)$$

where  $q$  depends on the sheath model used; experiments suggest a range  $1.5 < q < 2.5$  (see Sec. 2.1.1 and [28, 86, 87]). The lower limit in  $-0.5 < V_{\text{sb}}/V_{\text{pp}} < 0.5$  corresponds to the ground sheath capacitance being much greater than the RF electrode sheath capacitance, and *vice versa* for the upper limit [29, 31]. Since the RF electrode area is the same and the discharge structure in the top chamber is similar throughout these experiments, the drop in  $V_{\text{sb}}/V_{\text{pp}}$  from +0.2 at *B* to -0.3

at  $C$  (Fig. 5.14) when the plasmoid ignites can therefore be interpreted as a relative increase in the ground sheath effective area caused by the plasmoid:

$$\frac{A_g^{\text{plasmoid}}}{A_g} \sim \left[ \frac{(1 - (-0.6))}{(1 + (-0.6))} \bigg/ \frac{(1 - 0.3)}{(1 + 0.3)} \right]^{1/q} = 2.2 \rightarrow 3.8, \quad (5.2.3)$$

according to the chosen value of  $q$ , where  $A_g^{\text{plasmoid}}$  is the combined ground sheath effective area in presence of the plasmoid. This estimation suggests that the effective grounded area is at least doubled by the plasmoid, presumably by acting as a conducting bridge between the upper and lower chambers. This agrees with the observations in section 5.2.1.1, and provides a self-consistent description of the strong drop in self-bias in figure 5.14 on plasmoid ignition. Furthermore, since the ground sheath area in the upper chamber has not changed, this implies that roughly one half of the total RF current now passes via the plasmoid to the ground surfaces in the lower chamber. The RF current through the plasmoid would then be similar to the RF current to the upper ground electrode. The RF current density to each of these is therefore in inverse proportion to their surface areas. For the electrode and orifice dimensions given in figure 5.11, the current density in the plasmoid is at least  $10^4 \times$  greater than in the surrounding plasma.

In figure 5.10, it was demonstrated by experiment that the capacitance to ground of the plasmoid itself was comparatively insignificant and did not influence the above area estimations because the measured self-bias was independent of the hole diameter when the mesh was replaced by a grounded steel plate with a variable diaphragm. This experiment also showed that the mesh transparency played no role in the plasmoid properties.

A typical hollow cathode discharge, in figure 5.16(b), conducts RF current to its own small ground area, whereas a plasmoid in a mesh has the supplementary property of conducting RF current to external grounded areas which are many orders of magnitude larger than its own cross-section. The plasmoid in an orifice connecting an RF plasma to a grounded chamber therefore has the additional possibility of ohmic heating due to very high RF electron current density, as well as the characteristics of a hollow cathode discharge. Once local heating occurs, thermal emission and secondary electron emission will contribute to sustain the plasmoid even when the RF voltage is reduced to much lower amplitude than the ignition voltage at  $B$ , as shown by the curve  $E \rightarrow D$  in figure 5.14.

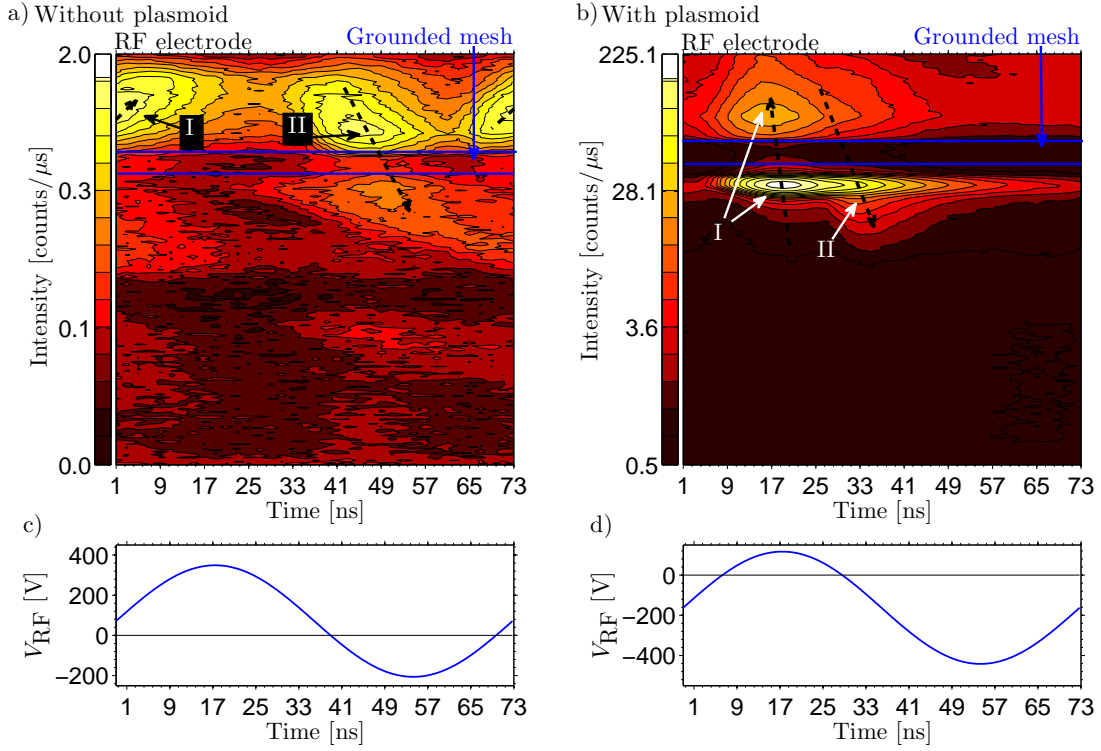


**Figure 5.18:** Vertical profile of  $H_\alpha$  emission intensity as a function of time during a RF cycle in the small area reactor with a mesh (a) without plasmoid and (b) with plasmoid. Potential on the RF electrode (c) without plasmoid and (d) with plasmoid. The dashed arrows in (a) and (b) show the expected direction of electrons flows. The color scales are logarithmic to highlight gradients at low and high intensities.

### 5.2.1.3 Phase-resolved optical emission imaging of plasmoids

The phase evolution of the plasma with and without a plasmoid was measured with phase-resolved optical emission spectroscopy (see Sec. 4.3). Figure 5.18(a) shows that without a plasmoid, the observed electron heating mechanisms are similar to those in parallel-plate reactors [61–63], i.e two strong emission patterns are visible. In the first pattern (maximum at  $\sim 5$  ns), electrons are accelerated toward the RF electrode. In the second mechanism ( $\sim 45$  ns) the electrons are ejected from the RF electrode toward the mesh. A trail of these energetic electrons can be seen below the grid as some of them pass through it. These energetic electrons coming from above the mesh are responsible for the faint light seen below the mesh in the time-averaged figure 5.12(a). Due to the small distance between the RF electrode and the grounded mesh, it is difficult to discern which mechanism between field reversal or electron expulsions from the sheath is responsible for these emission patterns. Based on the RF electrode potential which is still far from its extrema when those phenomena occur, the emission patterns are most likely caused by the electron expulsions from the ground and RF sheaths. Figure 5.18(b) shows the emission intensity with the plasmoid. There the pattern with the dominant intensity is located just below the plasmoid hole. This pattern occurs slightly after the maximum of the RF potential, just after the time when the RF sheath has drawn a strong RF current to reach its maximum potential. From the self-bias potential discussion, it was shown that a strong part of this RF current is flowing to the ground sheath on the lower chamber. This RF current must therefore flow back to the RF electrode and the only conduction channel is to funnel through the plasmoid hole. Hence it is thought that this bright emission is caused by the dense RF current flowing to the RF electrode sheath. This strong heating could be a dominant source of ionisation for the plasmoid. Figure 5.18(b) also shows a second pattern (maximum  $\sim 30$  ns) similar to the one observed without a plasmoid. This pattern is due to the electron flow away from the RF electrode, again probably due to the electron expulsion from the RF electrode.

### 5.2.1.4 Plasmoid detection and damage limitation

Here, it has been shown that by widening a hole in the grid, the position of the plasmoid breakdown could be controlled. Plasmoid ignition is thus very sensitive to precise geometrical constraints and is not a random process. Once ignited, the surface degradation caused by the plasmoid would often tends to aggravate the de-



fect of this particular aperture and so a plasmoid would be likely to re-strike at this same place in subsequent plasma processing cycles. Local heating by the plasmoid is evidenced, in increasing severity, by blue/black discoloration in concentric rings, a rough pitted surface, eroded edges [78], and even melting around its orifice with ejected metal droplets. The dark colour around the central hole of figure 5.11(b) shows the damage on the central hole after a few hours of operation. Following this change in condition, the ignition of the plasmoid became easier with time as shown by the red squares in figure 5.14. As these plasmoids can be quite harmful both in modifying the plasma conditions and eventually damaging the reactor itself, they need to be detected. Industrial RF plasma reactors generally have small orifices for gas input (showerhead) and gas output (pumping grids). These reactors typically have little or no visual access, in which case monitoring the self-bias voltage can be a convenient diagnostic for the appearance of plasmoids. Compared to the measurements made in the double chamber of this work, the change in self-bias voltage due to a plasmoid in the pumping grid of a symmetric large-area RF reactor will be smaller because the grid area is generally much less than the ground electrode area.

#### 5.2.1.5 Plasmoid conclusions

This section investigated the properties and consequences of plasmoid ignition in a grounded grid used to confine a RF glow discharge. A plasmoid in a hole conducts the plasma RF currents through to the other side of the hole, increasing the effective grounded area and hence the electrode area asymmetry of the RF plasma. The self-bias falls strongly, and from this it was deduced that a significant fraction of the total RF current was conducted via the plasmoid to ground on the other side of the mesh. This implied a plasmoid current density orders of magnitude higher than in the RF plasma. The drop in plasma potential due to ignition of the first plasmoid inhibits the formation of other plasmoids, and so higher rf powers are necessary to form additional plasmoids. A similar but weaker plasma potential drop is also observed in the grid reactor when the plasma has a breakdown in one or a few holes. The RF power must be increased until all holes are filled and it can be decreased afterwards.

The high RF current density passing through a plasmoid contributes to the power dissipation in a plasmoid compared to a hollow cathode discharge. A strong light emission of the plasmoid is measured shortly after field reversal at the RF electrode and is probably associated with the RF current funnelling from the ground sheath below the mesh to the RF electrode.

Hydrogen: 50 Pa					
Reactor	$V_{pp}$	$V_{sb}$	$\bar{V}_{cap}$	$E_i$	$\bar{\epsilon}_i$
parallel-plate reactor	350	-15	80	66	25
Grid reactor	350	-95	40	17	7

Argon: 50 Pa					
Reactor	$V_{pp}$	$V_{sb}$	$\bar{V}_{cap}$	$E_i$	$\bar{\epsilon}_i$
parallel-plate reactor	350	-15	81	76	28
Grid reactor	350	-57	55	41	15

**Table 5.1:** Time-averaged plasma potential assumin capacitive sheaths ( $\bar{V}_{cap}$ ), maximum ion bombardment energy ( $E_i$ ) and mean ion bombarding energy ( $\bar{\epsilon}_i$ ) in the parallel-plate and grid reactor in both gases at 50 Pa and 350  $V_{pp}$

From their influence on the self-bias and also their potential damage of the hole in which they ignite, plasmoids in grounded grids of RF plasma reactors can therefore be particularly destructive.

In the grid reactor, the RF current flow is distributed through the holes of the grounded grid in contrast to the single plasmoid. This grid has many wider holes, therefore the current density in individual holes is weaker and the reactor can operate over many hours without observed damage to the grid holes.

### 5.3 Influence of the self-bias potential on the ion bombardment energy

The previous section has shown that, in a RF CCP reactor, a significant part of the RF current can flow through the hole(s) in a plate if there is plasma in that hole. It results in a strong negative  $V_{sb}$  which reduces the plasma potential hence reducing ion bombardment energy on grounded surfaces. In this study, the ion bombardment energy has been measured with a RFEA described in section 4.4 and typical results are shown in figures 5.19(a) and 5.19(b). These ion velocity distributions were measured at  $V_{pp} = 350$  V and 50 Pa in both gases and in the parallel-plate reactor and the grid reactor. The maximum ion bombardment energies ( $E_i$ ) and mean bombarding energies ( $\bar{\epsilon}_i$ ), calculated with:  $\bar{\epsilon}_i = \sum_j f(v_j) \frac{1}{2} m(v_j)^2 / \sum_j f(v_j)$ , are listed in table 5.1.

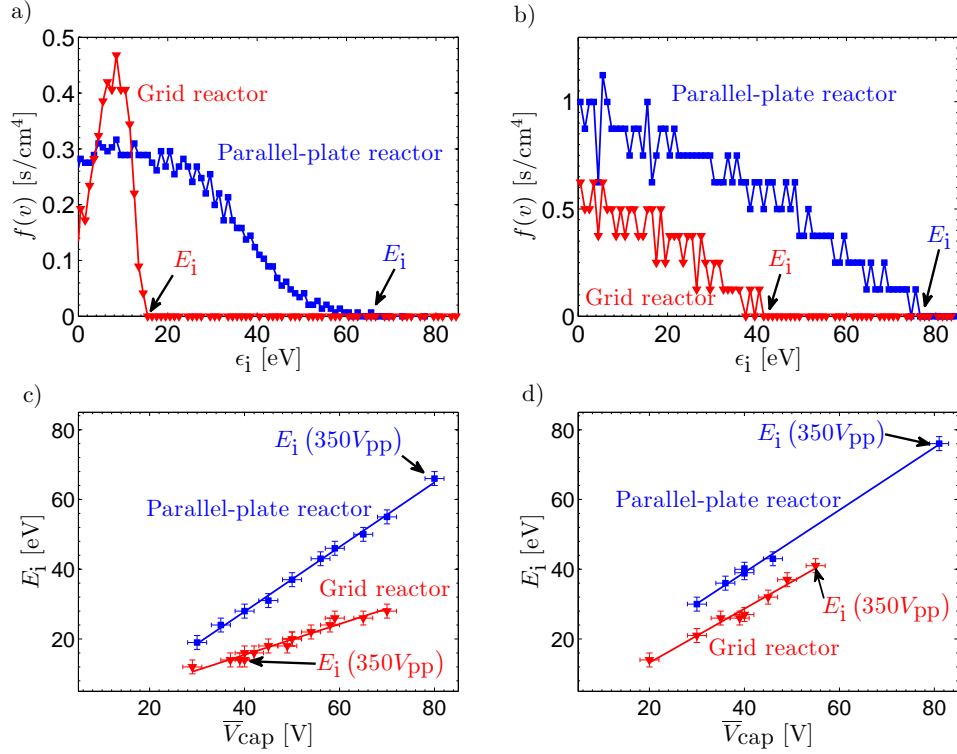


**Figure 5.19:** Ion velocity distribution ( $f(v)$ ) in the parallel-plate reactor and grid reactor at  $V_{pp} = 350$  V (a) in hydrogen at 50 Pa and (b) in argon at 50 Pa. The intensity of the ion velocity distributions are not corrected for the geometrical and collisional transparencies (see Sec. 4.4 and [37]).  $E_i$  as a function of the estimated time-averaged plasma potential assuming capacitive sheaths ( $\bar{V}_{cap}$ ), (c) in hydrogen at 50 Pa and (d) in argon at 50 Pa. The lines in (c) and (d) are guides for the eye.

Here it is important to remember that, although the measured ion velocity distributions are shown, there could be some distortion in the measured shape of these distributions due to the collisions inside the RFEA. In argon the dominant collisions are charge-exchange which does not affect the resolution, however in hydrogen, due to the complex ion chemistry, there could be some distortion as discussed in section 4.4.1. However, here the main interest is to measure how the reactor geometry affects the bombardment, especially the high energy ions which are more likely to cause defects. Hereby, small distortions of the distributions can be tolerated as the same RFEA is used to measure the ion bombardment in both reactors. To simplify the discussion on the variation of ion bombardment energy, it was chosen to monitor the maximum ion bombardment energy ( $E_i$ ) as the latter correlates well with variations of plasma potential as shown later.

Figure 5.19(a) and (b) show that the ion bombardment energy is clearly lower in the grid reactor. This reduction is stronger in hydrogen than in argon for reasons which will be discussed in section 5.4. The mean ion bombardment energies listed in table 5.1 also show a clear energy reduction in the grid reactor. The noise seen in the argon measurements ( Fig. 5.19(b)) is the measurement bit noise due to the weak measured currents in argon.

To quantify the reduction of  $E_i$  due to  $V_{sb}$ , the time-averaged plasma potential ( $\bar{V}_{pla}$ ) is estimated in both reactors. In the parallel-plate reactors at 13.56 MHz, the sheath impedance is expected to be dominantly capacitive. In the case of purely capacitive sheaths, the plasma potential is sinusoidal. Therefore, provided that the floating potential ( $V_f$ ) is negligible in comparison to  $\bar{V}_{pla}$ , the time-averaged plasma potential calculated assuming capacitive sheath ( $\bar{V}_{cap}$ ) is [31, 73] (see Sec. 2.1):

$$\bar{V}_{cap} = \frac{V_{pp}}{4} + \frac{V_{sb}}{2}.$$

To estimate the potential in the grid reactor, the sheaths are also assumed to be capacitive to a first approximation and the time-averaged plasma potential is estimated using  $\bar{V}_{cap}$ .

The measured maximum ion bombardment energy as a function of  $\bar{V}_{cap}$  in both reactors and both gases are shown in figure 5.19(c) and (d). There, it is seen that  $E_i \propto \bar{V}_{cap}$  in all conditions. In argon, in the parallel-plate reactor,  $E_i \simeq \bar{V}_{cap}$  as expected at this pressure in argon where a few ions, most probably  $ArH^+$ , have no significant energy loss as they cross the sheath. Whereas, in the grid reactor in argon,  $E_i < \bar{V}_{cap}$ . This result is surprising because, for equivalent time-averaged plasma potential and the same gas pressure in both reactors, it would be expected

that  $E_i$  should be similar at a given  $\bar{V}_{\text{cap}}$ . Indeed, since the ions enter the sheath at the same potential and, as the sheaths have similar thickness and neutral density, the collisional losses should be similar. However, figure 5.19 (d) shows a systematic lower energy in the grid reactor.

In hydrogen  $E_i < \bar{V}_{\text{cap}}$  in all conditions as shown in figure 5.19(c). Due to the complex sheath in hydrogen, the argument of similar collisions in the both reactors with the complex hydrogen sheaths will be briefly discussed in section 5.4. Nonetheless, in hydrogen too, the ion bombardment energy at similar  $\bar{V}_{\text{cap}}$  is also systematically lower in the grid reactor.

This difference in  $E_i$  at a given  $\bar{V}_{\text{cap}}$  and the good agreement between  $\bar{V}_{\text{cap}}$  and  $E_i$  in the parallel-plate reactor in argon indicates that  $\bar{V}_{\text{pla}} < \bar{V}_{\text{cap}}$  in the grid reactor. Therefore, although the strong negative  $V_{\text{sb}}$  reduces the ion bombardment energy in the grid reactor, it is not the sole phenomenon reducing the ion bombardment energy. The other phenomena are studied in the following section.

## 5.4 Influence of plasma evolution on the ion bombardment

To further investigate the phenomena responsible for the low maximum ion energy in the grid reactor, the phase-evolution of the plasma light-emission was measured with PROES as described in section 4.3. In the parallel-plate reactor, the emission patterns and their underlying physical phenomena have been extensively studied in hydrogen [61–63] and argon [88]. The light emission patterns in the parallel-plate reactor in hydrogen is shown in figure 5.20(a). The patterns  $I_{\text{RF}}$  and  $I_{\text{Gnd}}$  are caused by the electric field reversal in the RF and ground sheaths and patterns  $II_{\text{RF}}$  and  $II_{\text{Gnd}}$  by the electron expulsion from the RF and ground sheaths (see Sec. 4.3). The fields inside the sheaths for the  $V_{\text{pp}}$  used in this study are probably too weak to observe the additional weaker patterns found in the literature [61, 62].

Measurement in the grid reactor is shown in figure 5.20(b). The patterns at the RF sheath edge are much brighter whereas they are difficult to observe at the ground sheath edge. There, only a strongly attenuated pattern  $II_{\text{Gnd}}$  is visible. This change in pattern intensities is the consequence of the strong negative  $V_{\text{sb}}$ . The pattern  $II_{\text{RF}}$  shows that the energetic electrons expelled from the RF sheath flow through the grid hole and go relatively deeply into the bulk of the plasma below the grid. The phases at which the patterns appear at the RF electrode in the grid reactor are similar to those observed in the parallel-plate reactor. However, the phases of the

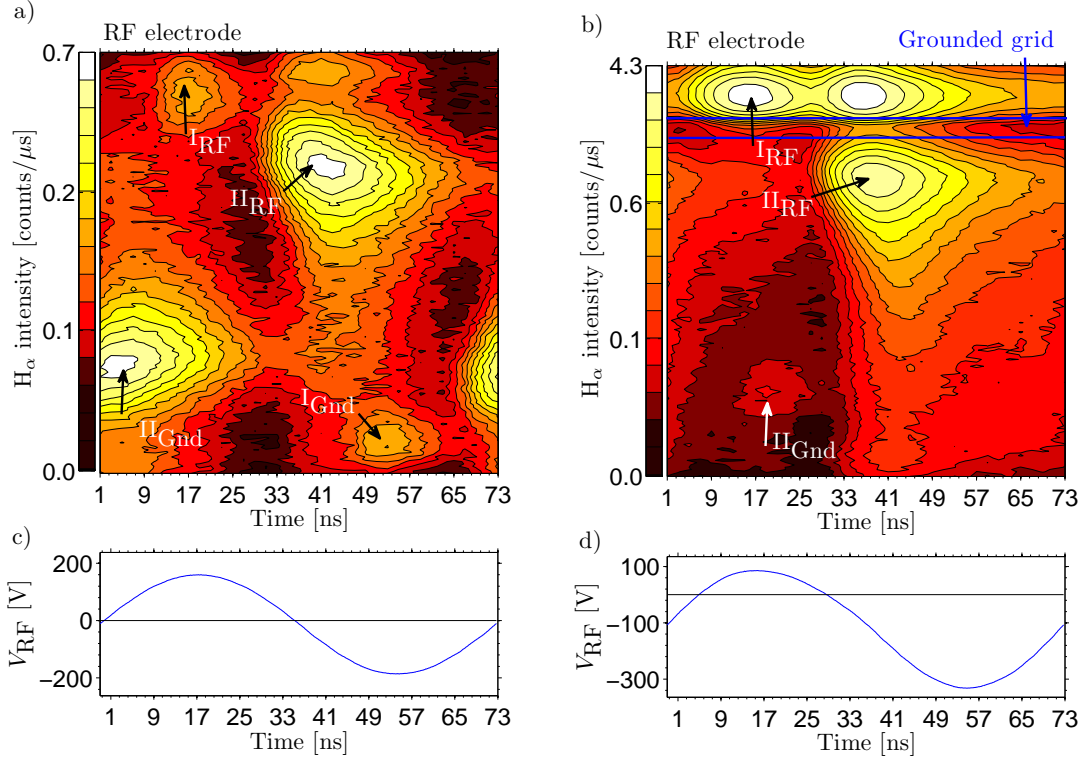


**Figure 5.20:** Vertical profile of  $H_\alpha$  emission intensity as a function of time during a RF cycle in (a) the parallel-plate reactor and (b) the grid reactor. The vertical profiles are aligned with respectively the reactor center and the axis of a grid hole. The patterns of emission intensity are labelled I-II (see text). The colorscale follows a logarithmic progression to display a wider range of intensity variations. The potential on the RF electrode is shown in (c) and (d).

patterns at the ground sheath differ. In the grid reactor, the maximum of pattern  $II_{Gnd}$  appears at  $19 \pm 2$  ns whereas it appears at  $3 \pm 2$  ns in the parallel-plate reactor (Tab. 5.2). This time shift of  $16 \pm 4$  ns is an indication that the ground sheaths in both reactors have different time evolutions.

The PROES results in argon are shown in figure 5.21. With this gas the ratio of electron to ion mobility is higher therefore the field reversal in the sheath is less likely to occur [61] and patterns  $I_{RF}$  and  $I_{Gnd}$  are not observed. Therefore, in the parallel-plate reactor, only the patterns  $II_{RF}$  and  $II_{Gnd}$  are visible in figure 5.21(a). This figure shows that the patterns intensity in argon take longer to decrease due to the longer lifetime of the observed excited states (see Sec. 4.3).

The argon emission in the grid reactor is shown in figure 5.21(b). There, the pattern  $II_{RF}$  is much brighter at the RF electrode due to the self-bias as was the case in hydrogen. However, in argon, the time shift of the pattern  $II_{Gnd}$  between the two reactors is  $4 \pm 4$  ns which is of the order of the time resolution. Therefore it can be expected that the ground sheaths have a similar time evolution in both reactors in

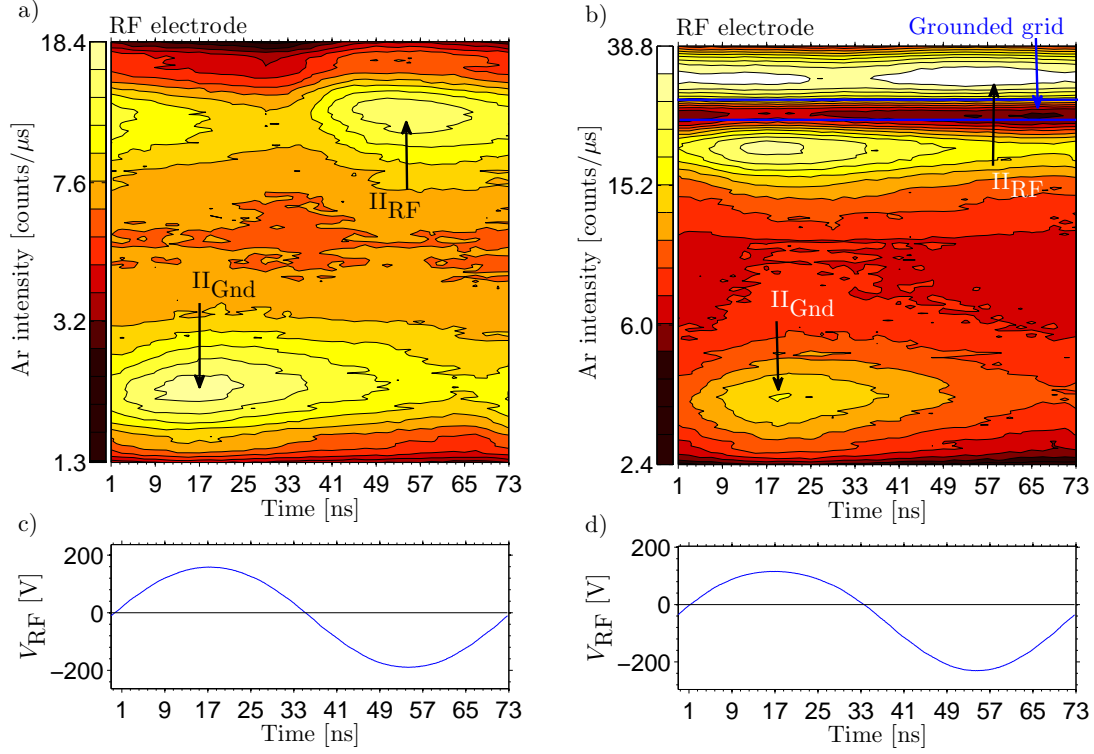


**Figure 5.21:** Vertical profile of argon (750 nm) emission intensity as a function of time during a RF cycle in (a) the parallel-plate reactor and (b) the grid reactor. The vertical profiles are aligned with respectively the reactor center and the axis of a grid hole. The patterns of emission intensity are labelled I-II (see text). The colorscale follows a logarithmic progression to display a wider range of intensity variations. The potential on the RF electrode is shown in (c) and (d).

this gas. Figure 5.21(b) also shows another pattern just below the grid at  $19 \pm 2$  ns. This pattern is not visible in hydrogen and its origin is unclear. It could be due to the ground sheath in the vicinity of the grid hole or may be due to a phenomenon similar to the one observed during the electron funnelling in the plasmoid study (see Sec. 5.2.1). However, this pattern has not been studied further as it was outside the main interest of this thesis.

Figures 5.20 and 5.21 all show the pattern  $\Pi_{\text{Gnd}}$ . The position of the maximum intensity from this pattern was used to estimate the maximal ground sheath width [89]. The ground sheath width in both gases and reactors are listed in table 5.2. These measurements show that the ground sheath widths are nearly identical in both reactors and both gases. This measurement reinforces the idea that the ion bombardment at a given  $\bar{V}_{\text{pla}}$  should be similar in both reactors.

The PROES images of the grid reactor shown here were made with vertical profiles centred on the hole axis. PROES images with profiles centred between the holes axis

	H <sub>2</sub>		Ar	
	Time [ns]	Sheath width [mm]	Time [ns]	Sheath width [mm]
parallel-plate	3±2	9±1	15±2	6±1
Grid	19±2	7±1	19±2	6±1

**Table 5.2:** Time and position of the maximum from pattern  $\Pi_{\text{Gnd}}$  in both reactors and both gases. This position is a measure of the maximal ground sheath width.

or at different positions were also taken but they showed no additional information relevant to the discussion and are therefore not shown here.

To further study the time evolution of the plasma in both reactors, the plasma potential waveforms were measured with a capacitive probe described in section 4.5. The waveforms during two RF cycles in hydrogen and argon are shown in figures 5.22(a) and (b). In hydrogen, the plasma potential is sinusoidal in the parallel-plate reactor but it is strongly non-sinusoidal in the grid reactor. In argon a similar but less pronounced variation is observed. To study this effect in more detail, the frequency spectra of these waveforms are shown in figures 5.23 and 5.24. The amplitude ratios of the higher harmonics relative to the first harmonic are listed in table 5.3.

In the parallel-plate reactor in hydrogen (a), the plasma potential ( $V_{\text{pla}}$ ) contains only  $< 10\%$  of the second harmonic as expected from such a reactor at 13.56 MHz [28, 31]. Hence the measured waveform shown in 5.22(a) is closely similar to a sinusoidal waveform. Therefore, the time-averaged plasma potential in the parallel-plate reactor in hydrogen can be reasonably approximated by the purely capacitive sheath approximation ( $\bar{V}_{\text{cap}}$ ) as done previously. In argon, the second harmonic content is higher ( $\sim 15\%$ ) and a deviation from a pure sinusoidal waveform can be seen in figure 5.22(c). A slight deviation between the real time-averaged plasma potential and  $\bar{V}_{\text{cap}}$  could be expected although it will be seen that this effect is lost in the error due to estimation of the floating potential in argon. A similar waveform in argon was measured by [68].

In the grid reactor, the waveform of the plasma potential measured in hydrogen shown in figure 5.22(b) is clearly non-sinusoidal and follows more closely the positive potential on the RF electrode. This waveform is composed of a sinusoidal signal at 13.56 MHz, but the amplitude of the second and third harmonics with respect to the first harmonic are respectively  $\sim 50\%$  and  $\sim 19\%$  in hydrogen and  $\sim 20\%$  and  $\sim 1\%$  in argon. These plasma potential waveforms are similar to those in plasmas with resistive sheaths [29, 31] usually observed when the Bohm current becomes significant compared to the capacitive current in the sheath, at low frequency ( $< 100$  kHz) or



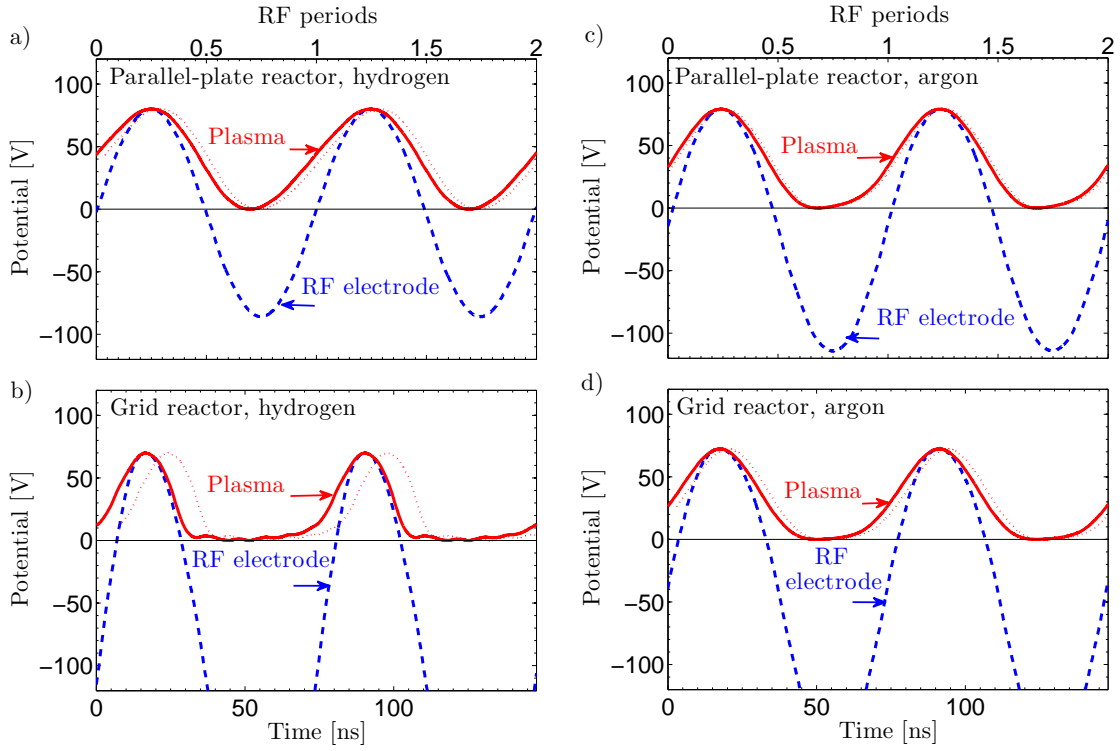


**Figure 5.22:** RF electrode potential measured by the voltage probe and oscillations of the plasma potential measured by the capacitive probe in (a) hydrogen in the parallel-plate reactor, (b) hydrogen in the grid reactor, (c) argon in the parallel-plate reactor and (d) argon in the grid reactor. The (red dashed) line shows the measured plasma potential with the phase lag from the plasma impedance (see Eq. 4.5.1).

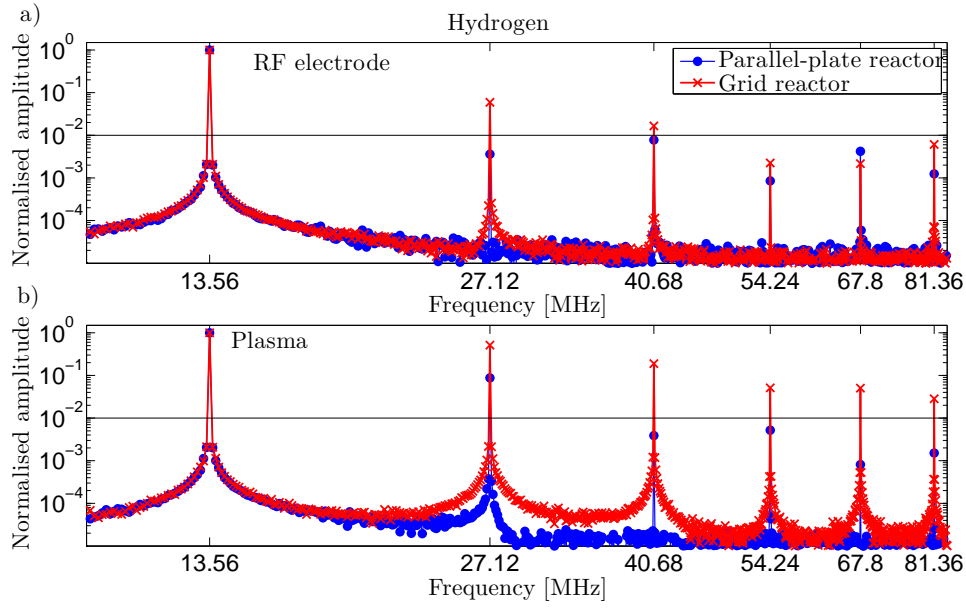


**Figure 5.23:** Spectral decomposition of (a) the potential on the RF electrode ( $V_{\text{RF}}$ ) and (b) the oscillation of the plasma potential in hydrogen. The decomposition is calculated with a Fast Fourier Transform algorithm and the amplitudes are normalised to the amplitude of the first harmonic.

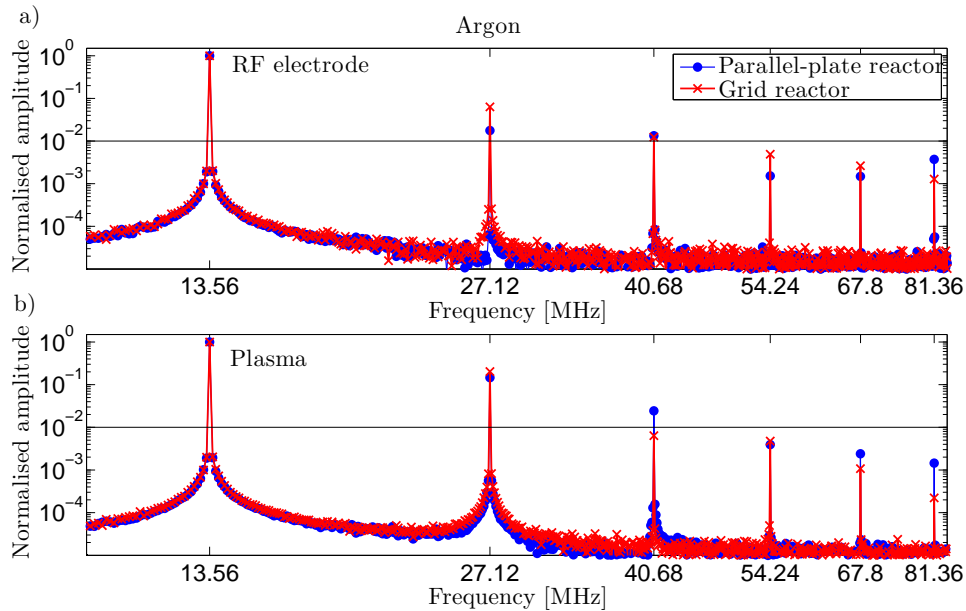


**Figure 5.24:** Spectral decomposition of (a) the potential on the RF electrode ( $V_{\text{RF}}$ ) and (b) the oscillation of the plasma potential in argon. The decomposition is calculated with a Fast Fourier Transform algorithm and the amplitudes are normalised to the amplitude of the first harmonic.

high plasma density (see Eq. 2.1.5). The measured resistive potential in the grid reactor in hydrogen could be a consequence of the peaked higher plasma density in the grid hole (measurement in Fig. 5.5 and simulation in Fig. 6.3). This high density close to the grid implies a strong Bohm current in the neighbouring sheaths which could have this effect on the plasma potential waveform (see Sec. 2.1). The weaker effect observed in argon could then be explained by the plasma density which is less peaked close to the grid hole (measurement in Fig. 5.6 and simulation in Fig. 6.2) and by the slower Bohm velocity due to the heavier mass of argon. The waveforms measured in the parallel-plate reactor in hydrogen (Fig. 5.22(a)) show that the plasma potential increases right after reaching its minimum value. However, the measured waveform in the grid reactor in hydrogen (Fig. 5.22(b)) shows that the plasma potential remains close to its minimum value for a longer period before it increases again. Therefore, the electron expulsions from the ground sheath, caused by the potential increase in the ground sheath, occurs later in the grid reactor compared to the parallel-plate reactor. This shift in the phase of the ground sheath expansion agrees with the observed phases of the pattern  $\Pi_{\text{Gnd}}$  in figure 5.20(a) and (b). The potential waveform measured in both reactors in hydrogen shows that, in the parallel-plate reactor, the plasma potential increases right after reaching its minimum, whereas, in the grid reactor, it remains low for a longer period. It results in a shift in time of the electrons expulsion from the ground sheath as observed by PROES in figure 5.20. The weaker difference between the two reactors in argon was also observed in the PROES measurements shown in figure 5.21.

Figure 5.22 shows that, in all conditions, the potential on the RF electrode ( $V_{\text{RF}}$ ) is highly sinusoidal and it contains only a small portion of the second harmonic. This second harmonic probably comes from a coupling to the higher harmonics of the plasma potential. This shows that the harmonics observed in the plasma potential are self-generated and are not imposed by tailored harmonics on the RF electrode as in [11].

Since the plasmas in the parallel-plate reactor and the grid reactor have different waveforms, their time-averaged potentials ( $\overline{V}_{\text{pla}}$ ) must be calculated accordingly. If the floating potential ( $V_f$ ) can be neglected ( $V_f \ll \overline{V}_{\text{pla}}$ ), the time-averaged plasma potential for a plasma with purely capacitive sheaths ( $\overline{V}_{\text{cap}}$ ) can be calculated using equation 2.1.18 whereas for a plasma with purely resistive sheaths ( $\overline{V}_{\text{res}}$ ) equation 2.1.20 should be used (see Sec. 2.1). If, however, the sheaths are neither purely capacitive nor resistive and furthermore  $\overline{V}_{\text{pla}}$  is close to  $V_f$ , the time-averaged plasma potential can be estimated using the measured plasma potential

H <sub>2</sub>		Harmonic frequency $f$ [MHz]				
		27.12	40.68	54.24	67.80	81.36
$V_{\text{RF}}(f)/V_{\text{RF}}(13.56 \text{ MHz})$	Parallel-plate	0.4 %	0.8 %	0.1 %	0.4 %	0.1 %
	Grid	5.9 %	1.7 %	0.2 %	0.2 %	0.6 %
$V_{\text{pla}}(f)/V_{\text{pla}}(13.56 \text{ MHz})$	Parallel-plate	8.7 %	0.4 %	0.5 %	0.1 %	0.2 %
	Grid	51.3 %	18.9 %	5.1 %	5.0 %	2.8 %

Ar		Harmonic frequency $f$ [MHz]				
		27.12	40.68	54.24	67.80	81.36
$V_{\text{RF}}(f)/V_{\text{RF}}(13.56 \text{ MHz})$	Parallel-plate	1.8 %	1.3 %	0.2 %	0.1 %	0.4 %
	Grid	6.3 %	1.2 %	0.5 %	0.3 %	0.1 %
$V_{\text{pla}}(f)/V_{\text{pla}}(13.56 \text{ MHz})$	Parallel-plate	14.6 %	2.4 %	0.4 %	0.2 %	0.1 %
	Grid	20.3 %	0.7 %	0.5 %	0.1 %	0.0 %

**Table 5.3:** List of relative harmonic amplitudes of the RF electro potential and the oscillations of the plasma potential in both reactors and both gases.

waveform ( $\tilde{V}_{\text{pla}}$ ) and equation  $\bar{V}_{\text{pla}} = \underbrace{\frac{T_e}{e} \ln \left( \frac{J_{\text{esat}}}{J_{\text{isat}}} \right)}_{=V_f} + \frac{T_e}{e} \ln \left[ \frac{1}{\tau} \int_0^\tau e^{-e\tilde{V}_{\text{pla}}(t)/T_e} dt \right]$  (see

Eq. 2.1.12). However, the floating potential is not measured and must be estimated. To do so, an electron temperature of  $T_e = 3 \text{ eV}$  was assumed in both gases and therefore  $V_f = \frac{T_e}{e} \ln (M_i/2\pi m_e)^{\frac{1}{2}} \simeq 11 \text{ V}$  in hydrogen and  $\sim 16 \text{ V}$  in argon. The error caused by this estimation is therefore larger in argon compared to hydrogen due to the difference in ion mass.

Figure 5.25(a) shows the time-averaged plasma potential in hydrogen calculated with the equations 2.1.18, 2.1.20 and 2.1.12. In the parallel-plate reactor, the estimated time-averaged plasma potential ( $\bar{V}_{\text{pla}}$ ) is in good agreement with the calculation assuming purely capacitive sheaths ( $\bar{V}_{\text{cap}}$ ). The influence of  $V_f$  is still small at these plasma potentials. In the grid reactor, however,  $\bar{V}_{\text{pla}}$  is lower than  $\bar{V}_{\text{cap}}$ . This shows that the non-sinusoidal plasma potential waveform is responsible for further reducing the time-averaged plasma potential in the grid reactor. Figure 5.25(a) also shows that the estimated  $\bar{V}_{\text{pla}}$  is higher than  $\bar{V}_{\text{res}}$  since  $V_{\text{pla}}(t)$  does not perfectly follow the positive RF electrode potential and also because  $V_f$  becomes significant when  $\bar{V}_{\text{pla}} \simeq V_f$ . Using figure 5.25(a), the respective influence of both the self-bias potential and the plasma potential waveform are illustrated in figure 5.26. There the arrows labelled  $V_{\text{sb}}$  shows that the main reduction of  $\bar{V}_{\text{pla}}$  is caused by the strong negative

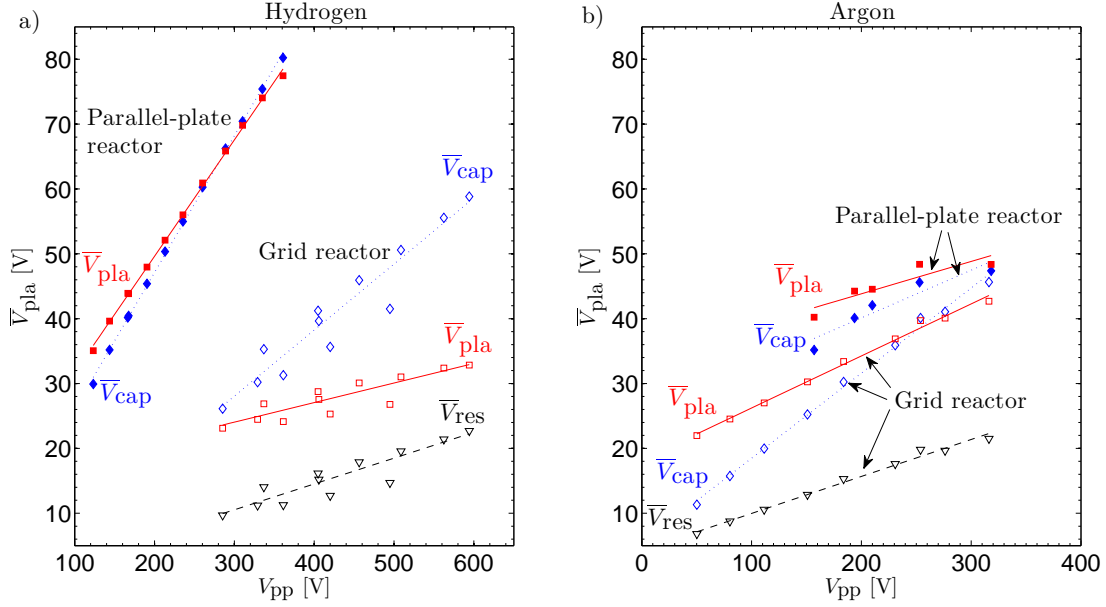


**Figure 5.25:** Time-averaged plasma potential assuming capacitive sheaths ( $\bar{V}_{\text{cap}}$ ) (Eq. 2.1.18), time-averaged plasma potential assuming resistive sheaths ( $\bar{V}_{\text{res}}$ ) (Eq. 2.1.20) and calculated time-averaged plasma potential ( $\bar{V}_{\text{pla}}$ ) (Eq. 2.1.12) as a function of the peak-to-peak voltage ( $V_{\text{pp}}$ ) in the parallel-plate reactor and grid reactor (a) in hydrogen and (b) in argon. The lines are guides for the eye.

$V_{\text{sb}}$  in the grid reactor. The second arrow, labelled “waveform”, shows that the plasma potential waveform reduces the potential from  $\bar{V}_{\text{cap}}$  to  $\bar{V}_{\text{pla}}$ .

In argon, the difference in plasma potential waveforms and of self-bias are weaker, thus the results shown in figure 5.25(b) are less clear. The time-averaged plasma potential is also lower in the grid reactor but the difference is smaller. This smaller difference between the  $\bar{V}_{\text{pla}}$  in both reactors explains why the reduction in ion bombardment energy observed in argon (Fig. 5.19(b)) is smaller than the one observed in hydrogen (Fig. 5.19(a)).

Due to the non-strictly sinusoidal waveform measured in the parallel-plate reactor in argon (Fig. 5.22(b)), it could be expected that  $\bar{V}_{\text{pla}} < \bar{V}_{\text{cap}}$  in this reactor, however the waveform influence is probably smaller than the error caused by the estimation of the floating potential. Figure 5.25(b) also shows that  $\bar{V}_{\text{pla}} > \bar{V}_{\text{cap}}$  at low  $V_{\text{pp}}$  but this could also be caused by the error in estimating  $V_{\text{f}}$ . Finally,  $\bar{V}_{\text{res}} \ll \bar{V}_{\text{pla}}$  in argon as could be expected from the measured waveform in which the second harmonic amplitude is only 20%.

Using the estimated  $\bar{V}_{\text{pla}}$ , the measured  $E_i$  is represented against  $\bar{V}_{\text{pla}}$  in figures 5.27(a) and (b). These figures show that  $E_i$  for a  $\bar{V}_{\text{pla}}$  are now nearly equal in both reactors. This agreement gives confidence in the diagnostic method used

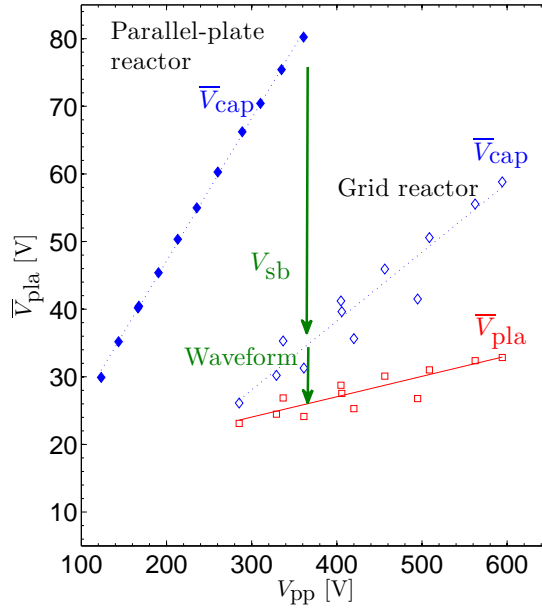


**Figure 5.26:** Illustration of the influence of  $V_{sb}$  and the plasma potential waveform in reducing the time-averaged plasma potential. The data are taken from figure 5.25

to measure  $\bar{V}_{pla}$  and  $E_i$ . As discussed in the analysis of figures 5.19(c) and (d), it was expected that  $E_i$  for a given  $\bar{V}_{pla}$  would be similar in both reactors. This correspondence between  $\bar{V}_{pla}$  and  $E_i$  in the two reactors indicates that the mechanisms included in the calculation of  $\bar{V}_{pla}$  are the dominant phenomena responsible for reducing  $\bar{V}_{pla}$  in the grid reactor. These phenomena are  $V_{sb}$  and the plasma potential waveform. Any other phenomena significantly reducing the ion bombardment energy would shift  $E_i$  toward lower energies in the grid reactor. Figure 5.27(a) indeed shows a small but systematic deviation of the order of the measurement resolution. This shift could be due to the choice of electron temperature or be caused by other phenomena having a smaller influence on the ion bombardment energy. In hydrogen, there are two valuable candidates:

- 1) As the observed ionisations profiles in both reactors are quite different (Fig. 5.5 and Fig. 5.6), the ion composition inside the ground sheaths could be different. In the parallel-plate reactor, a significant portion of ions are created at the grounded sheath edge or even within this sheath during field reversal. This reactor has therefore a source of  $H_2^+$  ions close to the sheath whereas, in the grid reactor, the vast majority of ions are produced above the grid and they probably arrive at the ground sheath in the form of  $H_3^+$  ions. A change of ion composition influences the collision chemistry inside the sheath and therefore

the energy of the ions reaching the substrate. This hypothesis can be tested by comparing the ion velocity distribution in both reactors for a given  $E_i$  as shown in figure 5.28. This figure shows that, in hydrogen, the distribution decreases from a maximum around 0 eV in the parallel-plate reactor whereas it increases toward a maximum at 13 eV in the grid reactor. In argon however, the distributions in the parallel-plate reactor and the grid reactor are nearly identical. The difference of ion velocity distributions observed in hydrogen is thought to be linked to the complex hydrogen chemistry in the sheath and the production of ions therein. However this could not be verified further with the diagnostics and simulation used in this study. This different ion composition could therefore be responsible for the remaining difference between  $\bar{V}_{\text{pla}}$  and  $E_i$  in both reactors in figure 5.28(a).

- 2) The second candidate to explain the remaining discrepancy is discussed in the numerical section 6.3. The results there show a small but non-negligible drop of the plasma potential between the plasma above grid and the one below. The physics behind this drop is not certain although it seems to be connected to the field reversal in hydrogen. This drop is also seen in argon but its amplitude is smaller than the energy resolution of the different diagnostics.

In argon, the remaining difference between  $\bar{V}_{\text{pla}}$  and  $E_i$  in both reactors could be due to the estimation of the floating potential, as discussed previously. Figure 5.27(b) also shows that, for  $\bar{V}_{\text{pla}}$  above 40 V,  $E_i \sim \bar{V}_{\text{pla}}$ . This is expected in this gas at 50 Pa where  $\text{ArH}^+$  ions cross the sheath without charge exchange collision and their loss by elastic collision is negligible. In hydrogen,  $E_i < \bar{V}_{\text{pla}}$  due to the ions collisions within the sheath. Although this was already discussed in section 5.3, it is important to remind that, in hydrogen at 50 Pa, the collisions with the gas are reducing the ion bombardment energy. However, this energy reduction by collisions is, to a major extent, not modified by the reactor geometry. A slight influence due to geometry was discussed above as possible reason for the remaining small deviation between the two reactors in figure 5.27(a).

Figures 5.27(c) and (d) illustrate how the  $E_i$  increase with  $V_{\text{pp}}^2$ , which is, to a first approximation, proportional to the power injected into the reactor (see Fig. 3.11). In hydrogen, the maximum ion bombardment energy in the grid reactor is comprised between 10 to 30 eV even at high injected power whereas, in the parallel-plate reactor,  $E_i$  quickly rises up to 65 eV. This fundamental result shows that the ion energy at a grounded surface in the grid reactor is much smaller than for the parallel-

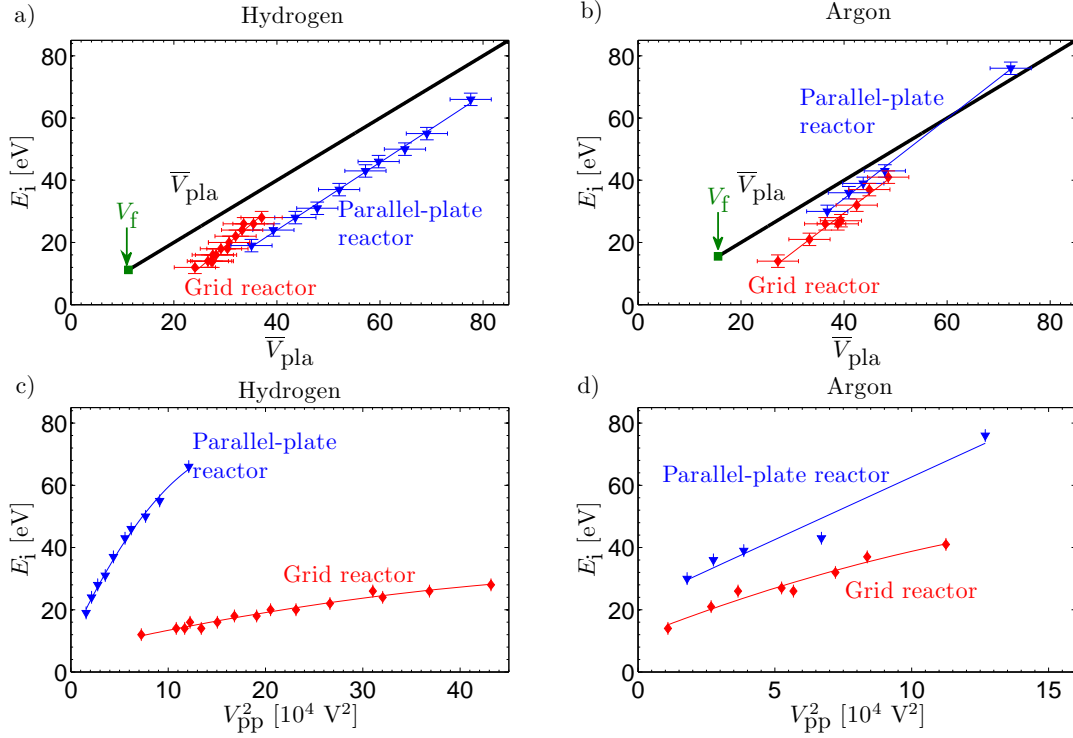


**Figure 5.27:** Maximum ion bombardment energy ( $E_i$ ) in the parallel-plate reactor and the grid reactor as a function of the estimated time-averaged plasma potential ( $\bar{V}_{\text{pla}}$ ) (a) in hydrogen and (b) in argon. The straight thick black line indicates  $\bar{V}_{\text{pla}}$  which is the upper limit of the ion bombardment energy in a high frequency plasma [29].  $E_i$  in the parallel-plate reactor and the grid reactor as a function of the square of the peak-to-peak voltage ( $V_{\text{pp}}^2$ ) (c) in hydrogen and (d) in argon.  $V_{\text{pp}}^2$  is an indicator for the RF power injected into the reactor (see Fig 3.11). The lines through the datapoints are guides for the eye.

plate reactor at similar RF voltages. In argon the difference is weaker but  $E_i$  in the grid reactor is also lower in all measurements. The different behaviour of  $E_i$  in both reactors is a direct consequence of the lower time-averaged plasma potential for the reasons discussed previously.

## 5.5 Parameter study of the grid reactor geometry

### 5.5.1 Sensitivity to grid geometry

The reduction of ion bombardment energy caused by the insertion of a grounded grid has been shown in the previous sections. This was shown using one grid reactor geometry shown in figure 3.1. However, during this thesis, many different grid reactor geometries have been tested. The results of these tests are summarised in figure 5.29(a) where it is shown that all tested grid reactors have an ion bom-



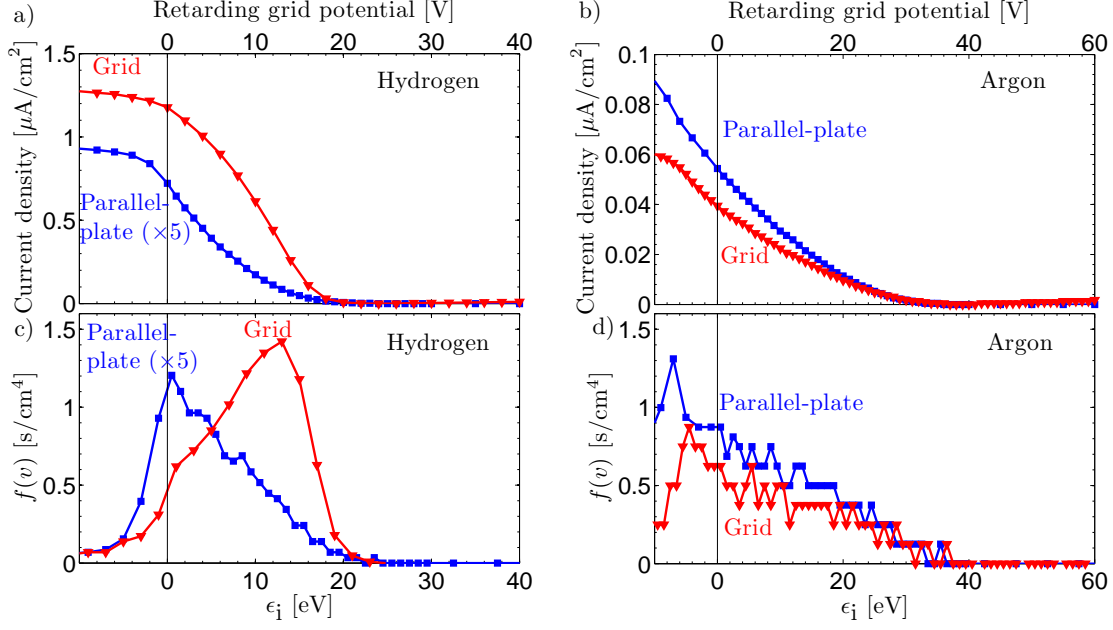
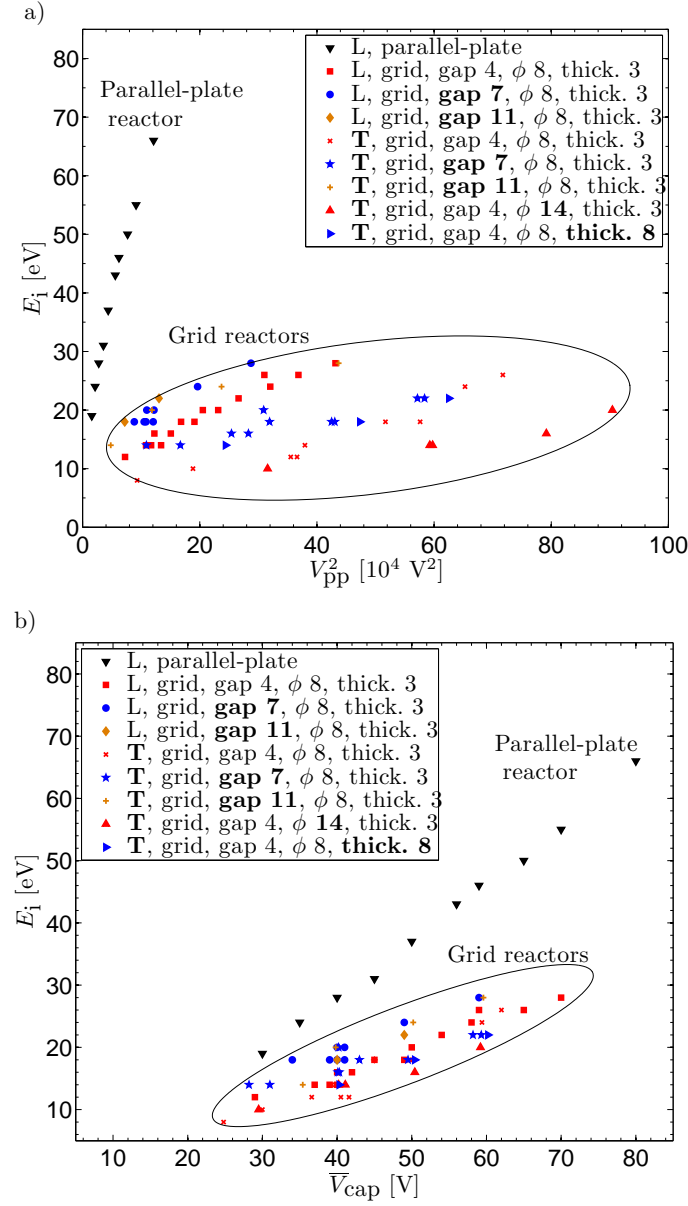


**Figure 5.28:** Current density as a function of the retarding grid potential (a) in hydrogen and (b) in argon. Ion velocity distribution ( $f(v)$ ) as a function of the ion bombardment energy ( $\epsilon_i$ ) (c) in hydrogen and (d) in argon. These data have been chosen so that  $E_i$  are similar in both reactors.

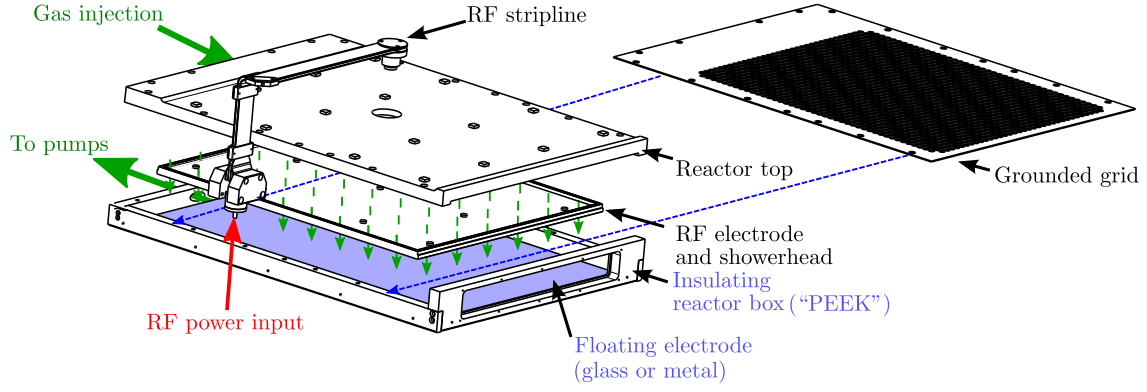
bombardment energy lower than in the parallel-plate reactor. The principal difference between the  $E_i$  in all these grid configurations is the amplitude of the self-bias in each reactor. The tests performed in the “test reactor”, presented in section 3.1.1 (labelled “T” in Fig. 5.29), have a stronger  $V_{sb}$  due to the larger influence of the sidewalls in this small reactor. Aside from the reactor size, figure 5.29 shows that  $V_{sb}$  is also influenced by the grid reactor geometry. However, these variations of  $V_{sb}$  are small compared to the strong difference in  $V_{sb}$  between the parallel-plate reactor and all the grid reactors.

Figure 5.29(b) shows the  $E_i$  as a function of  $\bar{V}_{cap}$  in the tested grid reactors. This figure shows that all the grid reactor configurations have a non-sinusoidal plasma potential waveform.

Figure 5.29 shows that the important parameters to obtain low ion bombardment energy are the presence of the grid and that the plasma flows to the other side of the grid. The actual grid holes diameter, grid thickness or distance between the grid and RF electrode have only limited impact on the ion bombardment energy. This weak variation of  $E_i$  within the grid reactor geometry could permit to optimize the geometry, e.g. the radical flux to the ground electrode could be increased by using a grid with a higher transparency.



**Figure 5.29:** (a)  $E_i$  in hydrogen as a function of the square of the peak-to-peak voltage ( $V_{pp}$ ) in different reactor geometries. (b) Maximum ion bombardment energy ( $E_i$ ) in hydrogen as a function of the estimated time-averaged plasma potential assuming capacitive sheath ( $\bar{V}_{cap}$ ) in different reactor geometries. The labels for the different reactor geometries are : L the large area reactor described in figure 3.1 and used in the vast majority of this work; T the test reactor described in 3.1.1; The “gap” is the distance between the grid and the RF electrode (standard is 4 mm).  $\phi$  is the diameter of the grid holes (standard is 8 mm); “thick” is the grid thickness (standard is 3 mm). The bold type indicates the parameters which differ from the standard case (L, grid, gap 4 mm,  $\phi$  8 mm, thick. 3 mm)



**Figure 5.30:** Modification of the standard grid reactor setup shown in figure 3.1 so that the reactor baseplate is electrically insulated from the rest of the reactor or the vacuum chamber. The sidewalls are changed to insulator (PEEK) and the baseplate was either made of glass or metal.

### 5.5.2 Partially floating substrate and DC biasing

In this section, a possibility to tune the ion bombardment by changing the potential of the reactor baseplate was explored. The baseplate potential was insulated from the rest of the reactor and from the vacuum chamber as shown in figure 5.30. This reactor setup allowed to select the coupling to ground from the baseplate, i.e. grounding the baseplate as done previously or biasing it to a “partially floating” potential (see Eq. 2.1.24) or to impose a DC bias. The latter was obtained by wiring the baseplate to external batteries. With this reactor setup, the plasma was less stable thus the pressure was raised to 70 Pa.

When the baseplate and sidewalls are set to a floating potential, they do not conduct the RF currents. Therefore, the grounded area in contact with the plasma was reduced and the self-bias potential was expected to be weaker.

The self-bias measurement in figure 5.31, shows instead that the self-bias was nearly identical in these different conditions. This shows that the surfaces of grounded electrode and sidewalls have nearly no influence on  $V_{sb}$ . This result is probably a direct consequence of the weighing of the ratio of surface areas by the respective densities at their sheath edges (Sec. 2.1.1, Eq. 2.1.30 and Sec. 5.2). In hydrogen, the density close to the grid was approximatively 8 times higher than at the ground electrode and sidewalls and therefore the electrode area close to the grid had a stronger influence on  $V_{sb}$ . This argument is also supported by the weak trend observed between the different configuration of figure 5.31. The standard grid reactor had a lower self-bias voltage as it had the larger grounded surface (the sidewalls and grounded electrode). Without the baseplate, the plasma leaked out of the reactor and part of

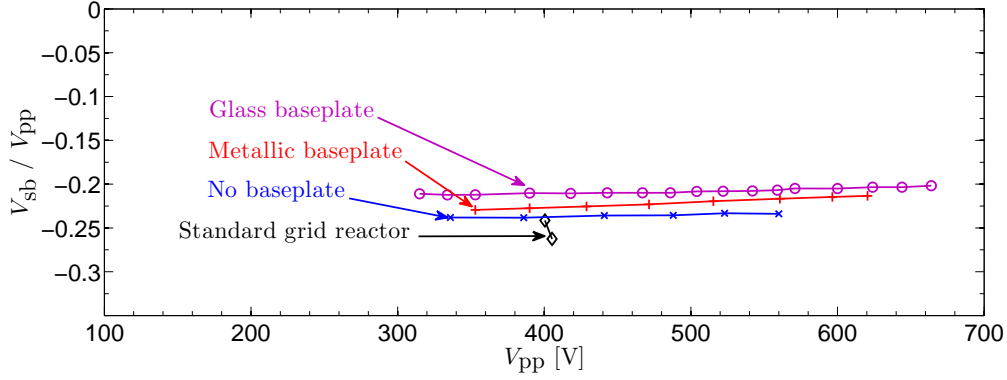


**Figure 5.31:** Measured ratio of self-bias voltage ( $V_{sb}$ ) to the RF peak-to-peak voltage ( $V_{pp}$ ) as a function of  $V_{pp}$  in different configurations of grid reactor in hydrogen at 70 Pa.

it diffused far enough to conduct some RF current to the grounded vacuum chamber surrounding the reactor. Hence, in this configuration,  $V_{sb}$  was slightly weaker than for the grid reactor. With a metal or glass floating baseplate, the plasma was again confined in the reactor but since the baseplate was floating (or “partially floating”), it only conducted a small portion of RF current to ground and  $V_{sb}$  was weaker. The difference between the metal and glass baseplates was probably due to the lower coupling to ground of the glass baseplate which also had the highest  $V_{sb}$ .

The principal objective with these different baseplates was to measure the influence of a floating baseplate on the ion bombardment energy. The results are shown in figure 5.32 and it is seen that  $E_i$  can be further reduced using the floating baseplate. Furthermore,  $E_i$  with the floating baseplate was nearly independent of  $V_{pp}$ . This figure also shows that for a fixed  $V_{pp}$ , the ion flux was higher in the grounded condition. This shows that the influence of setting the substrate to a floating potential is more complex than just reducing the ion bombardment energy to that surface. The decrease in ion flux could be due to a variation of the ionisation profile. This change in ionisation profile could in turn be related to a shift toward the RF electrode of the position of the maximum ionisation. Or, this change could be explained by the weaker sheath above the substrate in the partially floating condition. The resulting lower electron temperature at this weaker sheath edge would produce less ionisation, hence the ion flux would be reduced.

The measured ion bombardment energies with the floating metal baseplate shown in figure 5.33 where they are compared to the measurements done in the standard grid reactor discussed in the previous section 5.4. This figure shows that  $E_i$  in the grid reactor at 50 and 70 Pa are similar. This is important as the floating measurements are done at 70 Pa. This figure also shows that the  $E_i$  in the case of the floating metal

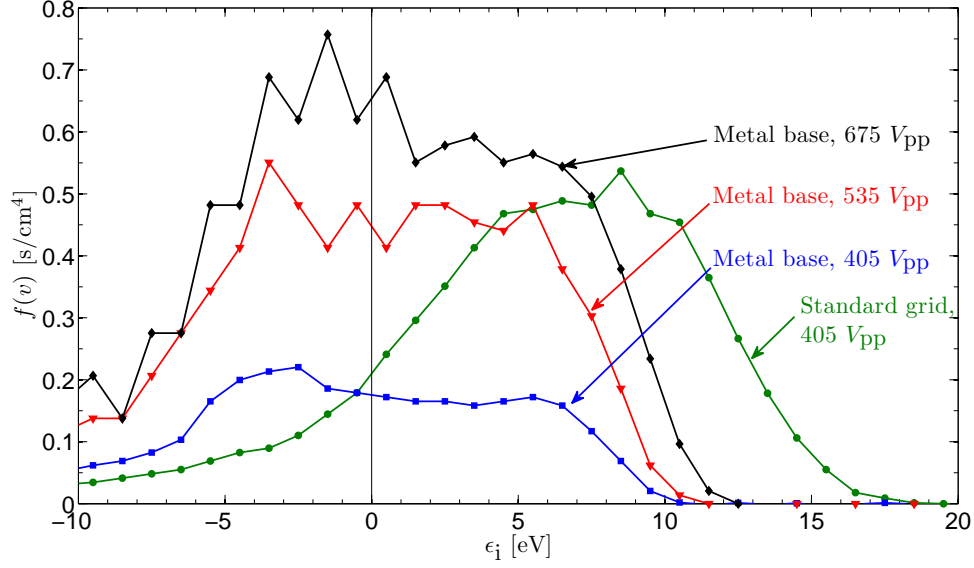


**Figure 5.32:** Ion velocity distribution ( $f(v)$ ) at different  $V_{pp}$  in different configurations of grid reactors in hydrogen at 70 Pa. The reactor configurations are: the grid reactor with grounded sidewalls shown in figure 3.1 (labelled “Standard grid”) and the grid reactor with floating sidewall and a floating metal baseplate (labelled “metal base”)

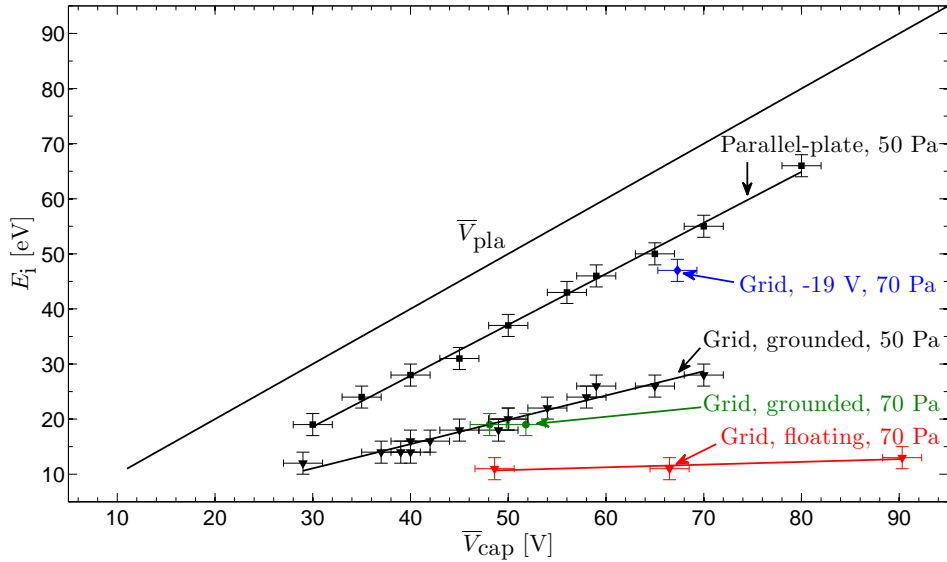


**Figure 5.33:**  $E_i$  as a function of the estimated time-averaged plasma potential assuming capacitive sheaths ( $\bar{V}_{cap}$ ) in different reactor configurations in hydrogen. The measurement (color) in the grid reactor at different bias (grounded, floating and biased) are made at 70 Pa. The measurements (black) in the grounded grid reactor and the parallel-plate reactor at 50 Pa are shown for reference with the measurement discussed in the previous sections (see Fig. 5.19).

baseplate are significantly lower than for the grid reactor and that they remain low even at high  $\bar{V}_{\text{cap}}$ . These energies are close to the floating potential and they are therefore probably close to the minimum ion bombardment energy for a surface in contact with a plasma at this pressure.

In the experience with the floating substrate, the impedance to ground of the substrate baseplate should be sufficiently large to reduce the potential drop through the sheath (see Eq. 2.1.24). However, the capacitance per unit area of the sheath above the baseplate and RFEA was relatively small ( $\sim 1.1 \text{ nFm}^{-2}$ ,  $\sim 280 \text{ pF}$  for the baseplate area) and therefore it was not simple to reduce the parasitic capacitances of the both baseplate and RFEA such that their impedances were significantly larger than the sheath impedance. This difficulty was apparent when the baseplate material was changed from metal to glass. With the metal baseplate, the area of the sheath coupling the RFEA to the plasma is similar to the baseplate area. However, with the glass baseplate, the RFEA was coupled to the plasma only through the small area above the RFEA. On the other hand, the impedance to ground of the RFEA was even higher with the glass baseplate because, with this baseplate, the RFEA filter was installed closer to a ground wall. Therefore, a higher voltage drop through the sheath with the glass baseplate was expected. Indeed The measurements with this baseplate showed a higher maximum ion bombardment energies and the sheath edge was then bright enough to be observed by eye. This stronger emission is another sign of stronger fields in the sheath with the glass baseplate.

It has been suggested that this mechanism of reducing the ion bombardment energy using a floating baseplate would be used inside a parallel-plate reactor to avoid the added complexity of the grid reactor. However, if the baseplate was truly floating, the only ground reference in the parallel-plate reactor would be the reactor sidewalls. As the RF current could only go there, strong plasma non uniformity would arise towards the sidewalls. If the baseplate was partially coupled to ground, it would act as a capacitive divider and would have similar effect as if the RF power was simply decreased. The only possibility would be to immerse the baseplate into the plasma although there, the back of the baseplate would be coated when reactive gases are used, strongly decreasing the gas utilisation efficiency.

Instead of trying to further reduce the ion bombardment energy in the grid reactor, the metal baseplate offers the possibility to be biased with a DC potential, thereby increasing the bombardment energy by a desired quantity. This was tested by connecting a set of batteries to the baseplate. A low pass filter was placed before the batteries to protect them from the RF. The bias was  $-19 \text{ V}$  and the result is shown

in figure 5.33. The bias has a strong effect on the ion bombardment energy and, with it,  $E_i$  is nearly as high as in the parallel-plate reactor. As the plate is biased negatively, it draws a current similar to what a Langmuir probe does. The measured current here varies between 50 to 210 mA as  $V_{pp}$  is swept from 430 to 620 V. These currents are in the range expected from an ion saturation current and they probably do not cause a strong perturbation into the plasma nor would they be difficult to supply. This shows that adding a DC bias offers a simple possibility to tune the ion bombardment starting from the low  $E_i$  of a grid reactor to higher energies. However, a major difficulty with this DC bias is that any insulating substrate or coating would simply charge and screen this bias. However it may be possible to circumvent this by using a RF bias instead, benefiting from the self-bias which would build on this baseplate.

## 5.6 Conclusion on ion bombardment energy

In the parallel-plate reactor, the electrode areas are nearly symmetric hence the self-bias potential is nearly zero. However, in the grid reactor geometry developed in this study, the plasma is present above and below the grounded grid. Therefore the grid reactor makes the front and back of the grid available for electrode area asymmetry and the gas determines the self-bias via the density profiles at these surfaces (sheath capacitance). It was shown that the presence of the grid does not impact the ion density uniformity along the electrodes necessary for large area deposition. This is because the plasma goes through the holes uniformly over all the grid surface. Hence, the grid reactor is a uniform reactor with highly asymmetric electrode areas and consequently a strong negative self-bias potential.

It was shown that this self-bias voltage strongly reduces the time-averaged plasma potential and that it is the principal mechanism reducing ion bombardment energy ( $\epsilon_i$ ) in the grid reactor. The second mechanism reducing  $\epsilon_i$  was revealed by the differences in temporal evolution of the plasma optical emission and it was studied by measuring the plasma potential waveform in the two reactors. These measurements in hydrogen have shown that, contrary to the parallel-plate reactor, the plasma potential waveform in the grid reactor is non-sinusoidal. This waveform is similar to that of a plasma with resistive sheaths. Using the measured waveforms, the time-average plasma potential ( $\bar{V}_{pla}$ ) was calculated in each reactor. This showed that the non-sinusoidal waveform in the grid reactor contributes to reducing  $\bar{V}_{pla}$ . Measurements in argon showed a similar trend although the phenomena were less

clear.

It was shown that, for at given  $\bar{V}_{\text{pla}}$ , the measured maximum ion bombardment energies ( $E_i$ ) are nearly equivalent in both reactors and gases. This equivalence showed that the two main phenomena responsible for reducing the plasma potential in the grid reactor were the self-bias and plasma potential waveform. The existence of other phenomena was briefly discussed.

As a result of the low time-averaged plasma potential in the grid reactor, the measured  $E_i$  remains low in a broad range of RF peak-to-peak voltages. The low ion bombardment in this reactor is therefore a consequence of the grid reactor design. Therefore, with this reactor, pressure, frequency and RF power can be chosen for their influence on the deposition rate and film properties instead of for reducing the ion bombardment energy. Furthermore, it was shown that the grid geometry could be varied without significantly changing the ion bombardment energy, giving the possibility to further optimize the grid geometry to reduce the breakdown voltage or increase the flux of radicals toward the substrate.

Finally, setting the substrate holder to a floating potential showed that  $E_i$  can be even further reduced. If in contrary, imposing a negative DC bias to the substrate holder increases  $E_i$  by a desired quantity.



# Chapter 6

## Numerical fluid simulation results

### 6.1 Simulated geometry

The model for the two fluid simulation used in this chapter is described in section 2.3. This model has been developed with the aim of making it as simple as possible, but not simpler. The simulation was done in a two-dimensional cylindrical geometry, each gas had only one ion specie ( $\text{Ar}^+$  and  $\text{H}_2^+$ ) and the reactions were reduced to their minimum necessary: ionisation and one high energy excitation for argon; ionisation, one high energy excitation and one low energy (i.e. rovibrational) excitation for hydrogen (see Sec. 2.3 and Tab. 2.1). Therefore it cannot be expected that the simulation will reproduce the full complexity of a real plasma. However, this section will show that all the effects discussed in chapter 5 are nonetheless reproduced by this simple model. The simulation conditions were a peak-to-peak potential of 350 V, gas pressure of 50 Pa and gas temperature of 300 K, similar to the experimental conditions.

The simulation geometries in the parallel-plate and the grid reactors are shown in figure 6.1. Both geometries were axisymmetric as this symmetry was more relevant in the grid reactor. Only a small portion of each reactor was simulated to limit the calculation time. In the parallel-plate reactor, this geometry was similar to the real reactor except that it did not account for the influence of sidewalls. In the grid reactor however, only one cylindrical hole was simulated. This axisymmetry and the continuity condition at the right hand side boundary does not account for the influence of the neighbouring holes nor for the reactor sidewalls. These influences would only be included in a three-dimensional models which are highly time-consuming. This difference between simulated and real geometry could have some influence on the results presented in this section, for example, on the calculated

Boundary name	Electrical boundary	Particle flow boundary
RF electrode (wall)	$V_{\text{RF}}$	$\Gamma_{\alpha,\text{wall}}$ (Eq. 2.3.10, 2.3.11, 2.3.12)
Grounded surface (wall)	0 V	$\Gamma_{\alpha,\text{wall}}$ (Eq. 2.3.10, 2.3.11, 2.3.12)
Symmetry boundary	$\hat{n} \cdot \epsilon_0 E = 0$	$\Gamma_{\alpha} \cdot \hat{n} = 0$

**Table 6.1:** List of boundaries conditions for the numerical simulation.  $\hat{n}$  is the normal to the boundary.

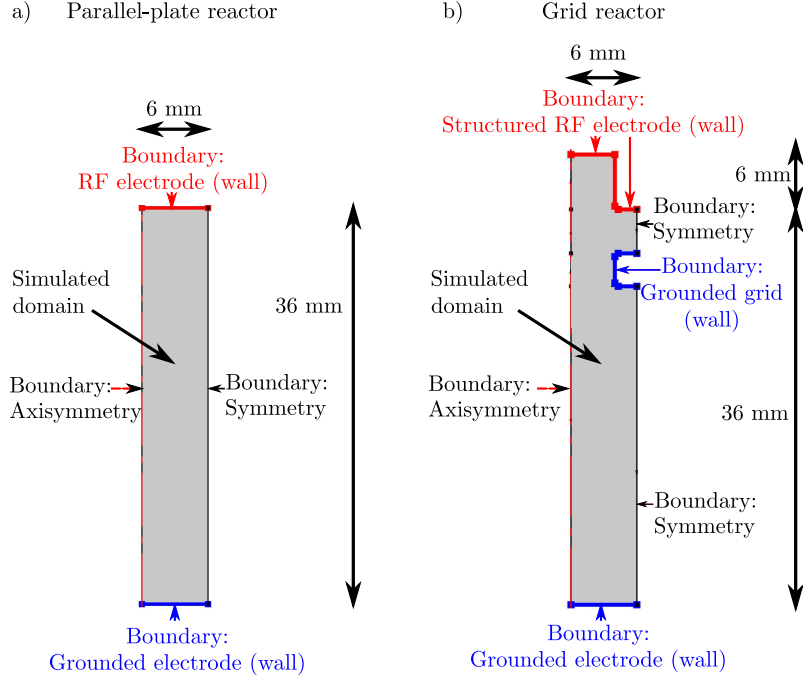


**Figure 6.1:** Geometry and boundaries for the simulation (a) in the parallel-plate reactor and (b) in the grid reactor. The boundaries are split into three groups listed in table 6.1. The 6 mm deep cylindrical structure in the RF electrode of the grid reactor is shown. This figure is a reminder and was shown in section 2.3.

self-bias potential listed in table 6.2.

The simulations were run for a time equivalent to 2000 cycles to ensure convergence. No adjustments were made in order to force a better agreement between the simulation results and the measurements presented in the previous section, that is, there were no fitted parameters in this model.

## 6.2 Time-averaged plasma densities

The work done on the simulation was partially triggered by the difference between the measured density profiles in hydrogen and in argon in the grid reactor (see Sec. 5.1 Fig. 5.5 and Fig. 5.6). However, before analysing the simulation results

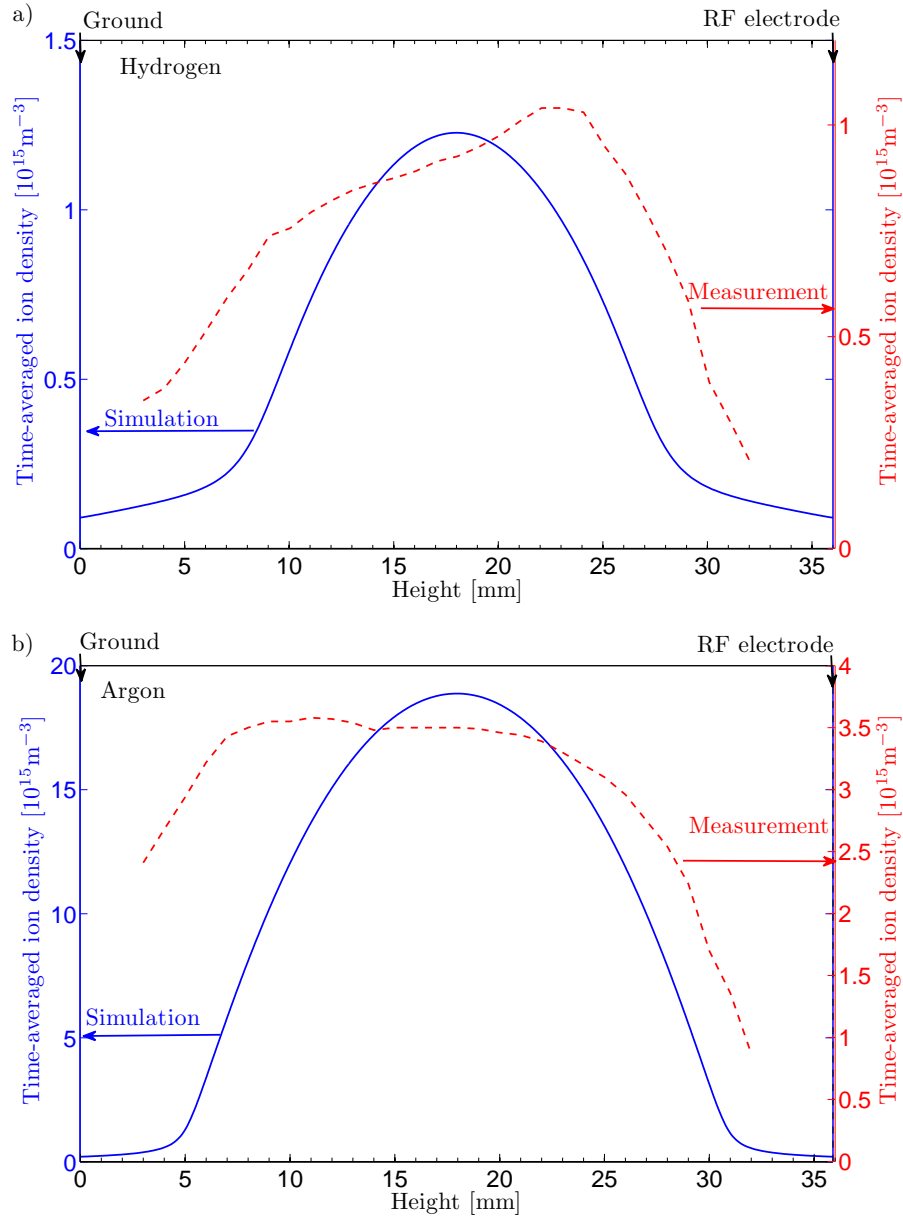


**Figure 6.2:** Vertical time-averaged ion density profiles calculated by the numerical simulation and measured with the Langmuir probes in a parallel-plate reactor (a) in hydrogen, (b) in argon. The measured densities were shown and discussed in section 5.1.

in the grid reactor, the simulation was benchmarked with the results obtained in the parallel-plate reactor as in figure 6.2. In the parallel-plate reactor, the profile of the simulated density is similar to the measured density. The simulated results are closer to the theoretical diffusive distribution profile (see Sec. 5.1 and [86]) than the measured density but this could be expected since the simulation does not include perturbations from the sidewalls nor perturbation from the probes themselves. In hydrogen, the magnitude of the measured and simulated densities are in good agreement. In argon however, the simulated density is five times higher than the measured density. This difference could be due to one of the parameters used in the argon simulation such as a too low ion mobility or too high ionisation rate constant and/or be caused by the absence of argon metastable states in the simulation. The parameters were not adjusted to better fit the results.

Since the general profiles of the density were reproduced in a parallel-plate reactor, the simulation was run in the grid reactor and the results are shown in figure 6.3. This shows that the simulation reproduces the differences observed in both gases namely, the hydrogen density decreases more strongly below the grid than in argon and the argon density profile has a density maximum below the grid. Reproducing these features was the part of motivation for the modelling. In hydrogen (Fig. 6.3(a)), both profiles show a density peaked inside the grid hole and the absolute densities are nearly equal. The simulation shows the beginning of a second peak at 17 mm which is not reproduced in the measurements but the agreement is surprisingly good otherwise. In argon (Fig. 6.3(b)), the general shape of the profile, with a strong maximum below the grid and one above it, is reproduced. The two profiles differ in the position of the maximum below the grid and in the magnitude of the density. Here again, the simulated density in argon is much higher than the measured density.

Since the difference in density profiles between the two gases is reproduced by the simulation and since the simulation has only a handful of parameters, this gives the opportunity to enquire as to which gas property could be responsible for this change in density profile. To do so, the simulation was run with two hypothetical gases: one having hydrogen diffusions and mobilities coefficients and argon rate constants, and the second with hydrogen rate constants and argon diffusions and mobilities coefficients. The results are shown in 6.4(a). Here the densities have been normalised to simplify the comparison. The two gases having the argon rate constants both show a maximum of density above the grid and another maximum below the grid. This double peaked profile is similar to the profile measured in argon. The gases with the

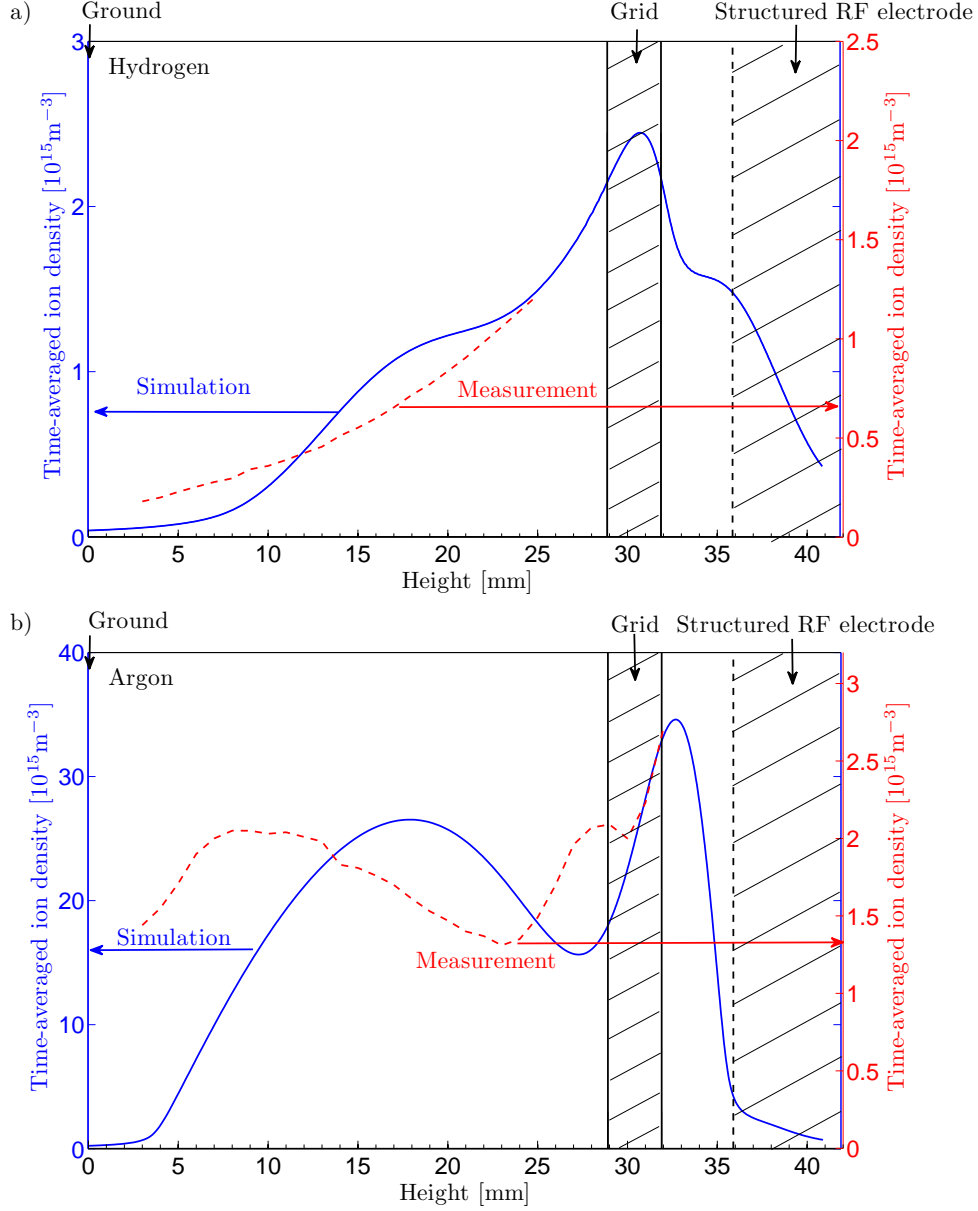


**Figure 6.3:** Vertical time-averaged ion density profiles on the hole axis calculated by the numerical simulation and measured with Langmuir probes in the grid reactor (a) in hydrogen and (b) in argon. In the grid reactor, the RF electrode is structured therefore the simulated densities extend into the 6 mm deep structure in the RF electrode. The measured densities were shown and discussed in section 5.1

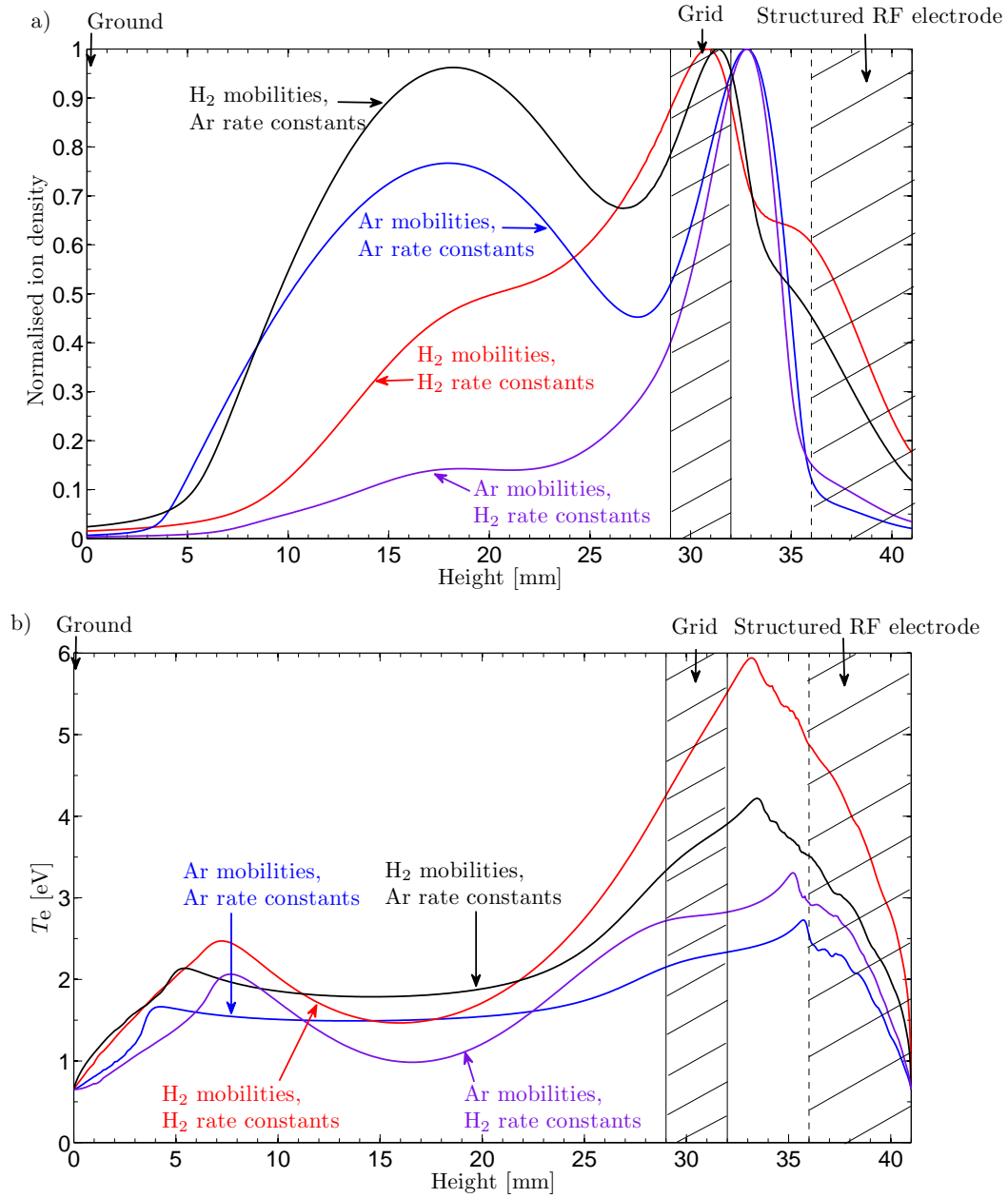


**Figure 6.4:** Comparison of (a) the normalised vertical time-averaged ion density profiles and (b) the normalised vertical time-averaged electron temperature profiles calculated by the numerical simulation in the grid reactor in four different gases: hydrogen, argon, a gas with hydrogen diffusions and mobilities coefficients and argon rate constants and a gas with hydrogen rate constants and argon diffusions and mobilities coefficients.

	H <sub>2</sub>		Ar	
	$V_{sb}$ [V]	$V_{sb}/V_{pp}$	$V_{sb}$ [V]	$V_{sb}/V_{pp}$
parallel-plate reactor	0.0	0	0.2	0
Grid reactor	-47.5	-0.14	-59	-0.17

**Table 6.2:** List of self-bias potentials calculated by the simulation.

hydrogen rate constants however both show a single maximum in the grid, similarly to the measured profile in hydrogen. The principal difference in the rate constants between the two gases is the addition of the rovibrational excitation which is not present in atomic gases like argon. Without this rovibrational cross-section, only the few electrons in the high energy part of the electron distribution have enough energy to excite or ionise the gas. However, when this low energy excitation is added, it acts as a sink for the energy of the cold electrons which can still lose energy into this rovibrational mode of the molecule. To test this hypothesis, the electron temperature of these gases are compared in figure 6.4(b). The two gases having hydrogen rate constants indeed show a temperature drop in the bulk below the grid which is consistent with the idea that electrons lose more energy into the low energy excitations. These simulation results indicate that the strong difference in measured density profiles between the atomic argon and molecular hydrogen gases could be due to the presence of the low energy rovibrational excitations in the molecular gas.

### 6.3 Self-bias, plasma potential and time evolution

The self-bias potentials calculated by the numerical simulation (Eq. 2.3.15) are listed in table 6.2. Compared to the measured self-bias shown in figure 5.7, the simulation also shows a clear increase of self-bias with the insertion of the grid. The simulated  $V_{sb}$  in the parallel-plate reactor are close to zero as expected in the perfectly symmetric simulated reactor. In the grid reactor, in argon, the magnitude of the simulated self-bias is close to the measured one. However, in hydrogen, the simulated self-bias is  $\sim 50$  % smaller than the measured one. The self-bias potential is a parameter which relies strongly on the electrode areas in contact with the plasma, and since, here, only a 2D simulation is used to approximate a 3D grid, this divergence is not surprising. The general agreement of a stronger negative self-bias potential with the addition of the grid, is therefore surprisingly good.

In chapter 5, it was proposed that the plasma potential is conducted through the grid by the plasma. Therefore it was assumed that the plasma potential was uniform

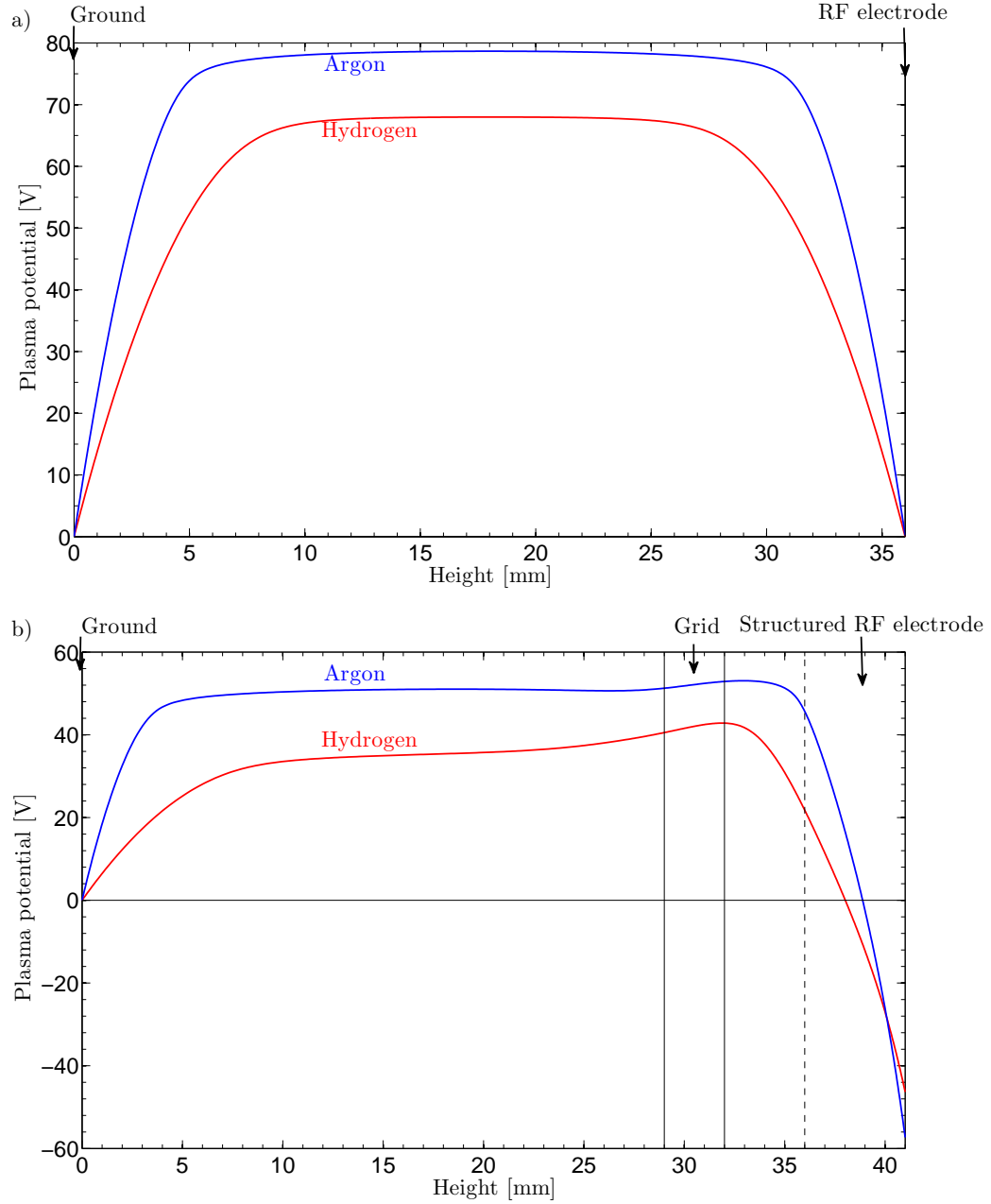


**Figure 6.5:** Vertical profile of the time-averaged plasma potential calculated by the numerical simulation (a) in the parallel-plate reactor and (b) in the grid reactor. The profiles are aligned on the hole axis in the grid reactor.



(quasi-equipotential) throughout the plasma. This hypothesis was tested with the numerical simulation by calculating the time-averaged plasma potential in both gases and reactors. The results are shown in figure 6.5. In the parallel-plate reactor, the time-averaged plasma potentials are indeed almost even. Before discussing  $\bar{V}_{\text{pla}}$  in the grid reactor, the magnitude of the time-averaged plasma potentials in the parallel-plate reactor (Fig. 6.5) are discussed.  $\bar{V}_{\text{pla}}$  is lower in hydrogen compared to argon. This surprising result is explained by the time evolution of the plasma potentials shown in figure 6.6. In hydrogen, the plasma potential drop through the sheath is usually positive, except during field reversal. When the field is reversed in the sheath, the plasma potential is then lower than that of the wall toward which the field reversal drives the electrons. This can be seen at 22 ns when the bulk plasma potential is lower than the potential at the RF electrode and at 52 ns where the bulk plasma potential is lower than 0 V.

In argon, (Fig. 6.6(b)), there is no strong field reversal and therefore the bulk potential remains close to, or higher than, the potential on the walls. This strong field reversal effect in hydrogen is the reason for the lower simulated time-averaged potential. The red and blue lines in figure 6.6(a) show the difference in the plasma potential profile depending on whether the potential on the RF electrode is increasing or decreasing. This shows how the plasma potential is lagging behind the electrode potential in hydrogen for the similar reason as in the field reversal effect. The real magnitude of this effect is unknown since the simulation model a simplified situation and therefore only gives qualitative results.

The simulated time-averaged plasma potential in the grid reactor are shown in figure 6.5(b). Here also, the vast majority of the plasma potential is conducted through the grid in both gases. In argon, there is a slightly higher potential just above the grid but the potential difference is in the range of the measurement resolution. In hydrogen however, the difference between the potentials above and below the grid is stronger. The discussion on the time-averaged plasma potential in the parallel-plates reactor suggests that field reversal could be the underlying reason. This will indeed be supported by the discussion of the plasma time evolution in the grid reactor (Fig. 6.8). This potential drop was not accounted for during the discussion on the phenomena responsible for the lower ion bombardment energy in the grid reactor (Ch. 5). This could therefore explain the remaining difference between the estimated time-average plasma potential and the measured maximum ion bombardment energy in figure 5.27(a) as discussed in section 5.4.

The time evolution of the vertical profiles of different plasma parameters in the

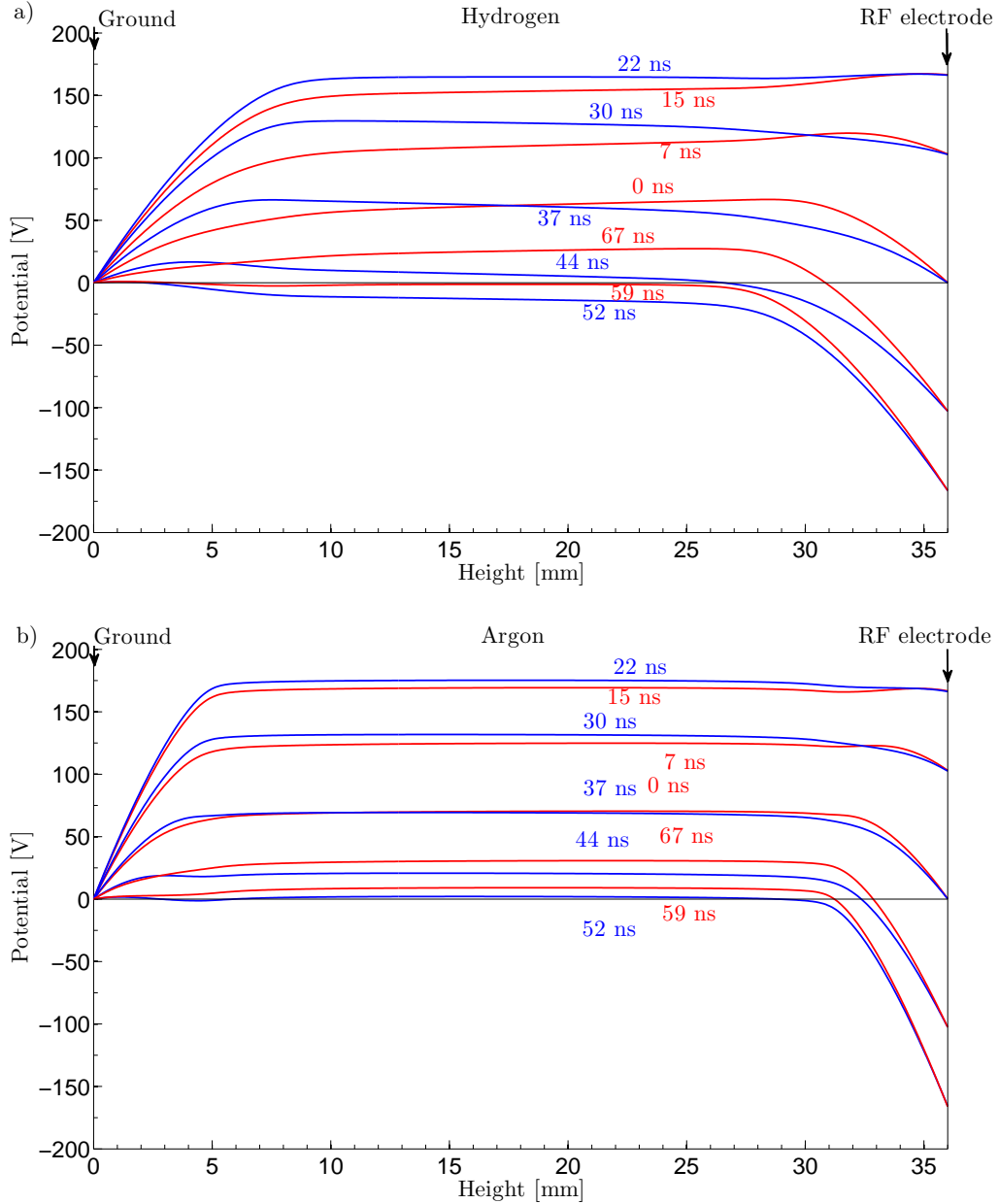


**Figure 6.6:** Vertical profile of the plasma potential calculated by the numerical simulation in the parallel-plate reactor (a) in hydrogen and (b) in argon. The red lines are used when the potential on the RF electrode is increasing and blue when it decreases.

grid reactor in argon is shown in figure 6.7. The plasma potential is nearly flat at all times and only a small deviation can be seen close to the RF electrode as the potential increases toward its maximum. This small deviation during part of the phase has only a small influence on the time-averaged plasma potential as shown in figure 6.5. The densities are mostly constant in time except within the sheaths but the variations there are hardly visible with the linear scale used in this figure. The electron temperature shows strong oscillations above the grid with temperatures up to 5 eV. These oscillations are reflected in the production rate of excited states discussed below. In hydrogen (Fig. 6.8), a strong increase of the plasma potential close to the RF electrode is seen when the potential is close to its maximum. This plasma potential gradient at this phase is the reason for the drop in the time-averaged plasma potential shown in figure 6.5. The phase at which this potential gradient appears seems to coincide with the field reversal in hydrogen as will be discussed below. Figure 6.8 shows that the evolution of ion and electron densities are changing with time and that the electron density is smaller during the local increase of plasma potential, as expected. Finally, it can also be seen that the electron temperature oscillate strongly above the grid and with temperatures up to 11 eV.

To better visualise the phase at which this phenomenon occurs, the vertical profiles of the plasma potential and the production rate of excited states ( $k_{\text{ex}}(T_e)n_e n_n$ ), in hydrogen, are shown in figure 6.9(a-c). In these figures, the production rate of excited states is used to compare the simulated patterns to those measured with the phase-resolved optical emission spectroscopy shown in figure 5.20. The simulation reproduces well the phases at which the strong patterns  $I_{\text{RF}}$  and  $II_{\text{RF}}$  were measured as well as the time shift and location of  $II_{\text{Gnd}}$ . The biggest difference between the measured and simulated patterns is that the measured pattern  $II_{\text{RF}}$  has a trail going further into the bulk. This trail is made by the energetic electrons expelled from the sheath and which continue to travel through the bulk due to their inertia. This ballistic effect cannot be reproduced by the simulation fluid model in which the electrons are treated as a single fluid. Concerning the vertical gradients of plasma potential, this figure shows that the maximum of the field reversal pattern ( $I_{\text{RF}}$ ) takes place when the vertical gradient of the plasma potential is the strongest (Fig. 6.9(b)). This supports the idea that this plasma potential gradient is caused by the strong field reversal in hydrogen. This would also explain why this phenomenon is less pronounced in argon.

The vertical profiles of plasma potential and production rate of excited states in

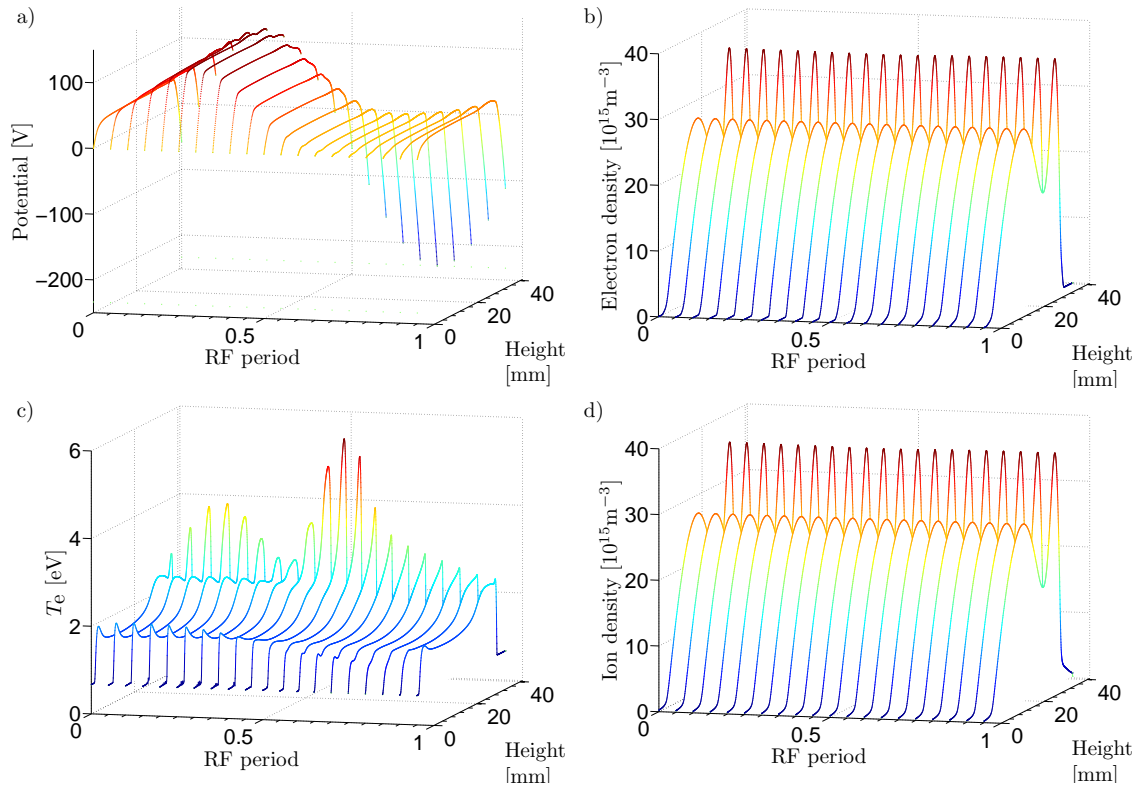


**Figure 6.7:** Time evolution of (a) the plasma potential, (b) the electron density, (c) the electron temperature and (d) the ion density in the grid reactor at the hole axis in argon calculated by the numerical simulation.

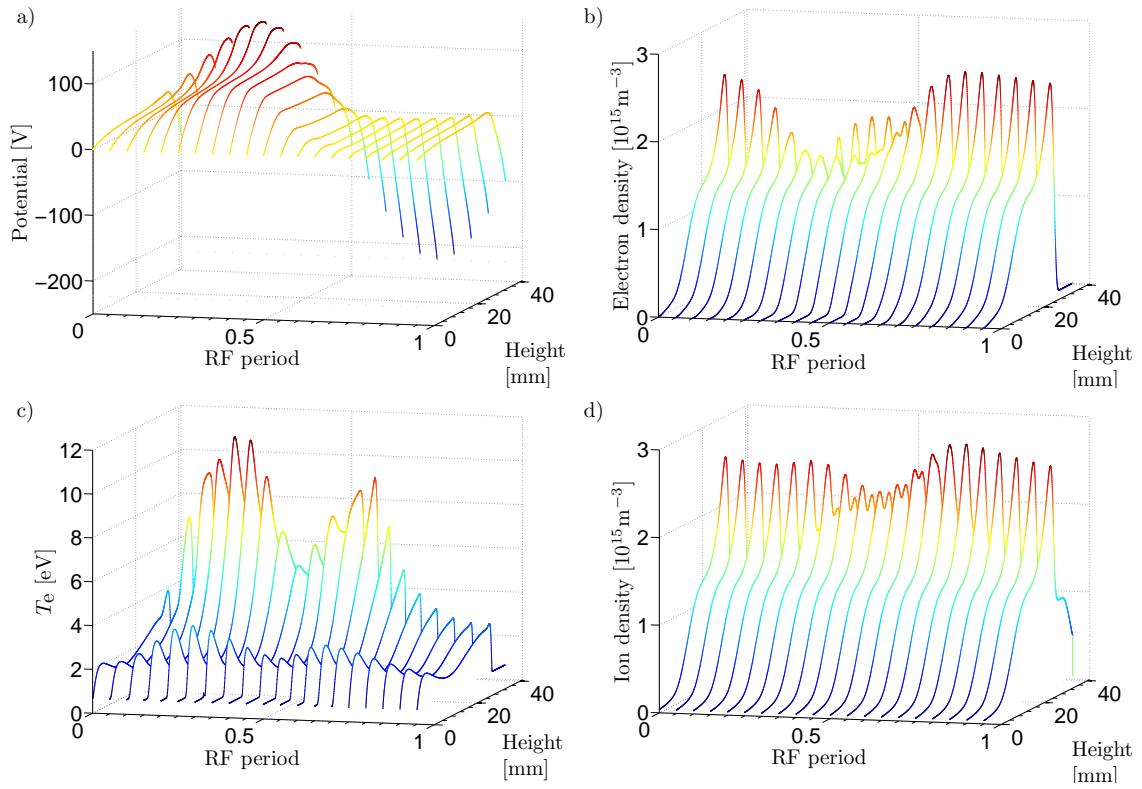


**Figure 6.8:** Time evolution of (a) the plasma potential, (b) the electron density, (c) the electron temperature and (d) the ion density in the grid reactor at the hole axis in hydrogen calculated by the numerical simulation.

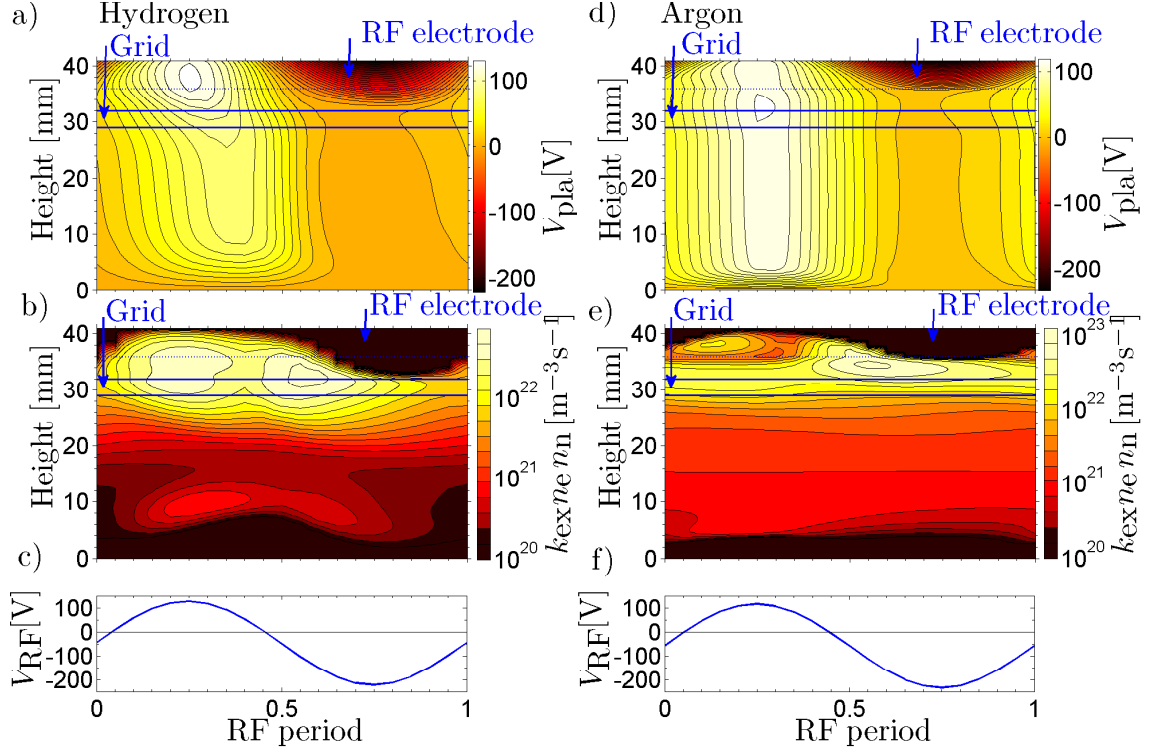


**Figure 6.9:** Vertical profiles at the hole axis of (a) the plasma potential, (b) the production rate of excited states ( $k_{\text{ex}}(T_e) n_e n_n$ ) and (c) the potential on the RF electrode as a function of the RF period in the grid reactor in hydrogen. Vertical profiles at the hole axis of (d) the plasma potential, (e) the production rate of excited states ( $k_{\text{ex}}(T_e) n_e n_n$ ) and (f) the potential on the RF electrode as a function of the RF period in the grid reactor in argon. In (b) and (e), the colorscale follows a logarithmic progression as in the figures 5.20 and 5.21.

argon are shown in figure 6.9(d-f). There too, a good agreement is found with the PROES measurement shown in figure 5.21. This figure also shows that the plasma potential is nearly constant through the plasma at all times.

Similar figures in the parallel-plate reactor are shown in figure 6.10 for reference. There again, good agreement with the measurements is found, including the symmetric aspect of the patterns at both sheaths. Only patterns  $II_{\text{RF}}$  and  $II_{\text{gnd}}$  are observed in argon due to the lack of field reversal. These patterns agree well with previous studies [90, 91].

In the experimental section 5.4 (Fig. 5.22), it was shown that the plasma potential waveforms in the grid and parallel-plate reactors are strongly different and that this has an impact on the time-averaged plasma potential. Here, the time evolutions of the plasma potential calculated by the simulation are shown in figure 6.11. In the parallel-plate reactor (Fig. 6.11(a) and (b)), the waveforms are sinusoidal in both gases as would be expected in this reactor. A similar sinusoidal waveform

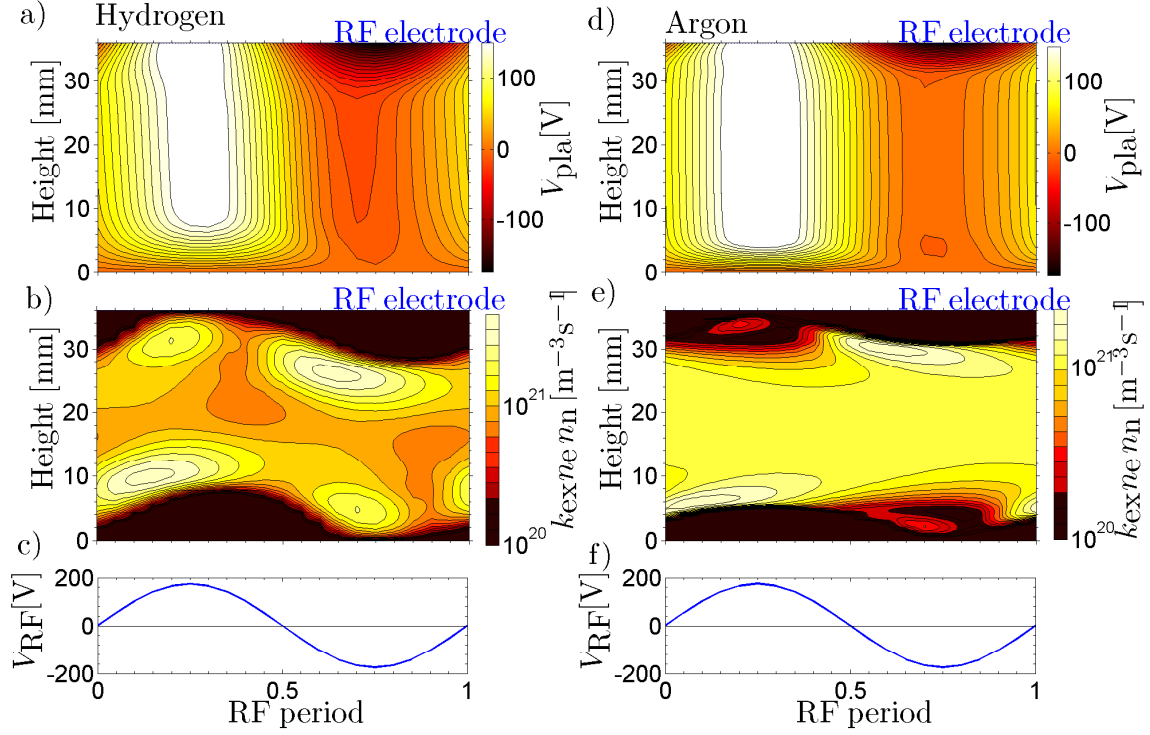


**Figure 6.10:** Vertical profiles on the hole axis of (a) the plasma potential, (b) the production rate of excited states ( $k_{\text{ex}}(T_e)n_en_n$ ) and (c) the potential on the RF electrode as a function of the RF period in the parallel-plate reactor in hydrogen. Vertical profiles on the hole axis of (d) the plasma potential, (e) the production rate of excited states ( $k_{\text{ex}}(T_e)n_en_n$ ) and (f) the potential on the RF electrode as a function of the RF period in the parallel-plate in argon. In (b) and (e), the colorscale follows a logarithmic progression as in the figures 5.20 and 5.21.

was also measured in hydrogen (Fig. 5.22(a)). However, the measured waveform in argon (Fig. 5.22(c)) was less sinusoidal compared to the simulated waveform. In the grid reactor, the simulated plasma potential profiles (Fig. 6.11 (c) and (d)) show non-sinusoidal waveforms remarkably similar to the measured waveforms in figure 5.22. Therefore, the simulation reproduces the change in plasma potential waveform caused by the grid design.

Figure 6.11(c) and (d) also show a small phase shift between the position of the maximum of  $V_{RF}$  and the maximum of plasma potential close to the ground electrode. This phase shift is small in the parallel-plate reactor, slightly stronger in the grid reactor in argon and significant in the grid reactor in hydrogen. This phase shift is similar to the one measured experimentally ( see Fig. 5.22) and it was briefly discussed in section 4.5.

## 6.4 Conclusion

The simulation used in this section is extremely simple compared to the complex and more complete simulations present in the literature [32,33]. However, this section showed that this model is capable of reproducing the experimental observations with surprisingly good accuracy. Therefore the few chosen parameters are essential to the reproduction of the various phenomena observed.

Experimental Langmuir probes measurements had shown that the ion density profiles in the grid reactor were different in the two gases. This difference was also reproduced by the simulation. Furthermore, it was suggested that this difference was probably caused by the low energy (rovibrational) excitations present in molecular gases (hydrogen) but absent in monoatomic gases (argon).

The simulated self-bias potentials showed the same trend as the measured ones. Furthermore, the simulation showed that the conduction of plasma potential through the grid holes occurs without significant voltage drop in argon but that there is a non negligible drop in hydrogen. This drop was not accounted for in the ion bombardment energy analysis in chapter 5 and, as discussed, it could account for the remaining discrepancy between the measured ion bombardment energy at a given time-averaged plasma potential in both reactors (Fig. 5.27). It is suggested that the field reversal is responsible for this potential drop through the grid hole. This argument is supported by comparing the simulated phase and location of the potential gradient with the simulated production rate of excited states as well as with the PROES measurements.



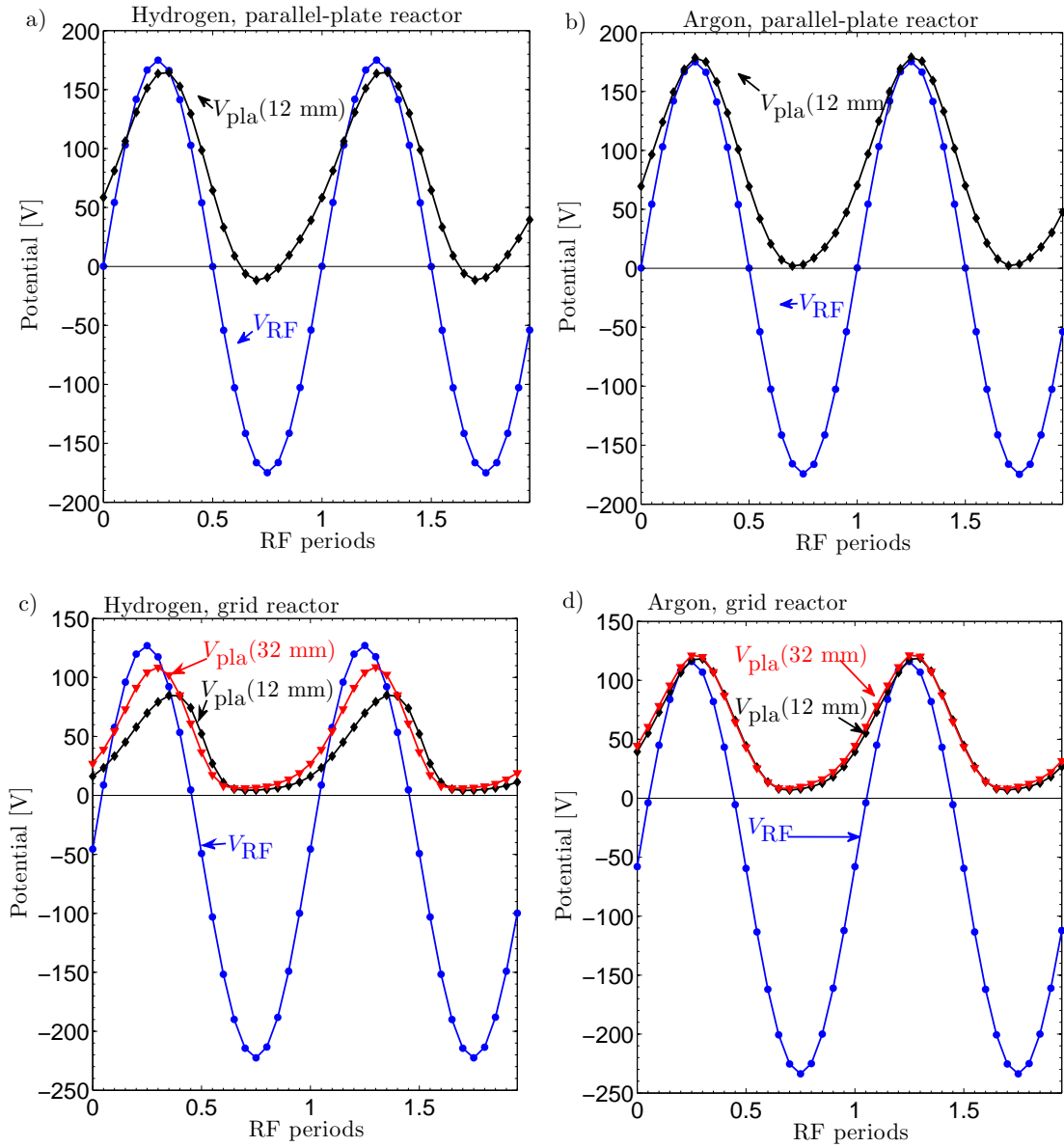


**Figure 6.11:** Numerical simulations of the RF electrode potential and plasma potential in the parallel-plate reactor (a) in hydrogen and (b) in argon, and in the grid reactor (c) in hydrogen and (d) in argon. These simulations are very similar to the capacitive probe measurements shown in figure 5.22.

The capacitive probe measurement had shown that the plasma potential waveforms were different in both reactors and that this was contributing to the reduction of ion bombardment energy in the grid reactor. These measured plasma potential waveforms were also accurately reproduced by the simulation.

Finally, the good reproduction of the phenomena observed experimentally by the numerical simulation strengthens the confidence in both methods. This combined approach had been used for a deeper investigation in the underlying physical reasons for several of the observed phenomena.

# Chapter 7

## Layer deposition and solar cell quality

In this section, the deposition of hydrogenated microcrystalline silicon ( $\mu\text{c-Si:H}$ ) material obtained from both the parallel-plate reactor and the grid reactor (see Ch. 3.1) are compared. The deposition, material and solar cell characterizations are the work of D. Dominé, X. Wang, T. Gaillard, M. Marmelo, G. Monteduro and U. Kroll [92, 93]. This work was done at Oerlikon Solar-Lab, the research lab of Oerlikon Solar. As the prime objective of this thesis was the development of the plasma source and the analysis of the plasma properties therein, only a portion of the work done by Dominé et al., on material deposition and analysis, is presented here.

The grid reactor used in this section is a semi-industrial grid reactor, built following the grid reactor design developed in this study (see Sec. 3.1). The RF electrode area is  $0.16 \text{ m}^2$ . The distance from the RF electrode to the grounded grid is 7 mm instead of the 4 mm used previously. The choice to use a larger distance was motivated by the reduction of the breakdown voltage at low pressures (see Sec. 3.2.1). The RF frequency used in this grid reactor is 40.68 MHz instead of the 13.56 MHz used previously. This higher frequency was justified by a higher deposition rate, as shown in section 7.1, since higher deposition rate is important for the deposition of thin film solar cells.

Before discussing the results of deposition and material quality, measurements of the maximum ion bombardment energies ( $E_i$ ) in the grid reactor used by Oerlikon Solar-Lab for different pressures and RF powers are presented in table 7.1. The measured  $E_i$  are in a similar range as the ones measured in the grid reactor presented in the chapter 5. It is difficult to do a more direct comparison between these  $E_i$  and

Pressure [Pa]	RF power [W]	RF power density [W/cm <sup>2</sup> ]	$E_i$ [eV]
0.5	700	0.42	26
0.6	700	0.42	26
0.6	500	0.30	22
1	700	0.42	22
1	500	0.30	18
1	200	0.12	8

**Table 7.1:** Maximum ion bombardment energy ( $E_i$ ) measured in Oerlikon Solar-Lab grid reactor. These pressures and powers are standard conditions used in the following depositions.

the ones discussed in chapter 5 because the grid reactor at Oerlikon Solar-Lab had no RF voltage probe mounted on its RF electrode. Therefore neither the peak-to-peak potential nor time-averaged plasma potential, used in chapter 5 as a reference to compare ion bombardment in different reactors, could be used here. The RF powers shown in 7.1 were measured at the RF generator. These powers include the RF power injected into the plasma and the power dissipated into the matching and reactor (ohmic losses) which are specific to each reactor setup (see Sec. 3.2.2, Fig. 3.11). Therefore they cannot be used for direct comparison with previous measurements, but they are nonetheless useful to give an indication of the used RF power. Nevertheless, since the ion bombardment energies in this grid reactor and the one discussed in chapter 5 are of similar magnitudes, it is reasonable to assume that the mechanisms described in chapter 5 also apply to the grid reactor used by Oerlikon Solar-Lab. This is supported by the self-bias measurements in this grid reactor. These measurements showed a strong negative self-bias ( $\sim -100$  V) similar to those measured in section 5.2. This negative self-bias potential is a sign of the plasma conducting the RF potential through the grid to the volume below the grid. This effect was shown to be linked to the phenomena responsible for the low ion bombardment in the grid reactor (see Sec. 5.2).

## 7.1 Deposition rates

The primary aim of this grid reactor design is to improve the quality of deposited  $\mu\text{c-Si:H}$  thin films with the hope to improve solar cell efficiencies by reducing the ion bombardment energy. This reactor design was developed to reduce the ion bombardment at low pressure (around 50 Pa) and was not developed to have high deposition rates. However, deposition rate is an important aspect for the industrial

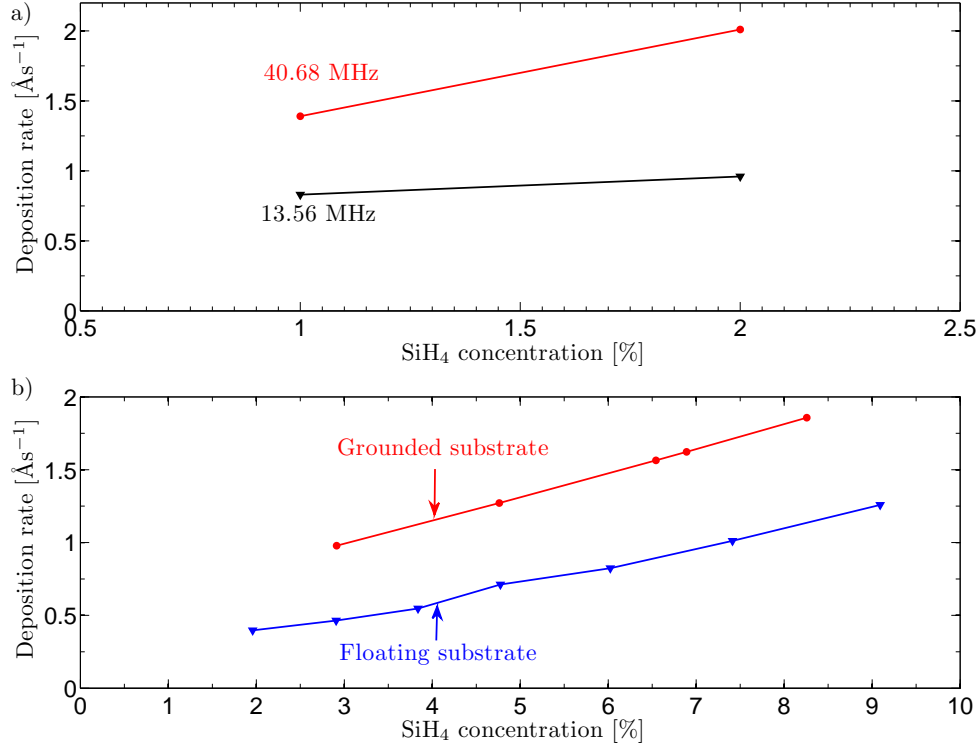


**Figure 7.1:** (a) Deposition rate as a function of the  $\text{SiH}_4$  concentration in the grid reactor at 13.56 and 40.68 MHz at 60 Pa and 700 W. (b) Deposition rate as a function of the  $\text{SiH}_4$  concentration, at 100 Pa and 700 W, with a grounded and partially-floating substrate as an example of a parameter study on the deposition rate.

production of thin films and therefore the typical deposition rates of the grid reactor and the parallel-plate reactors are compared here.

In the parallel-plate reactor, the deposition rate for state-of-the-art  $\mu\text{c-Si:H}$  is typically between 3 to 5  $\text{\AA s}^{-1}$ . In the grid reactor, without reactor optimisation, the deposition rate is only 1 to 2  $\text{\AA s}^{-1}$  as shown in figure. 7.1(a). This lower deposition rate is not surprising. Indeed, in section 5.1, it was shown that the parallel-plate reactor and the grid reactor have different ionisation profiles (Fig. 5.2 and 5.5). In the grid reactor, the ionisation rate is maximum above the grid hole and the plasma below the grid is relatively cold. Therefore, the majority of radicals are created above the grid hole. However, above the grid, these radicals have a strong probability to quickly diffuse to the grid or the RF electrode and react or stick on these surfaces. Therefore, out of these produced radicals, only a small fraction travel through the grid hole to the substrate. This contrasts strongly with the parallel-plate symmetric reactor in which the plasma emission at the ground sheath edge is similar to the one at the RF sheath edge and therefore a larger portion of the radicals are produced close to the substrate.

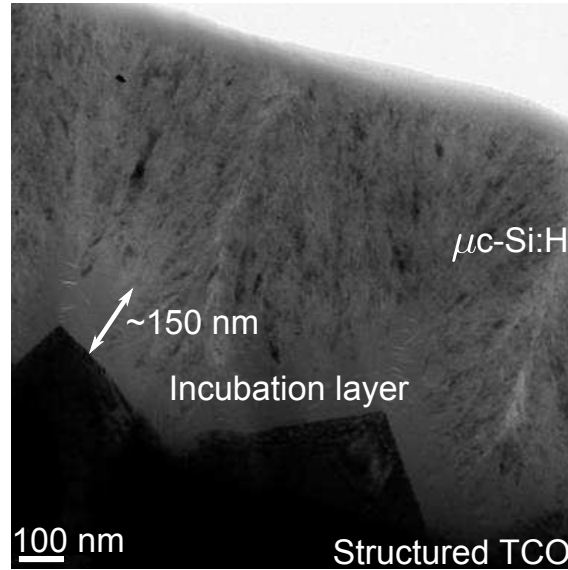
This lower deposition rate, associated with the loss of radicals on the grid, was discussed for triode reactor geometries [27]. There the problem is greater since all radicals are produced above the grid because the grid is used to confine the plasma above it. In the grid reactor developed in this study, the radicals produced inside or below the grid hole have a higher probability of reaching the substrate than those produced above the grid. The deposition rate is therefore related to the position of the maximum of ion density with respect to the centre of the grid hole. The position of this maximum is suspected to vary with process parameters such as the pressure. It might be possible to increase the deposition rate in the grid reactor if the shape of the grid holes was modified in a way that the position of this maximum ionisation was influenced or if the grid transparency was increased.

Figure. 7.1(a) also shows the gain in deposition rate as the RF frequency was increased from 13.56 to 40.68 MHz. With a silane concentration of 2%, the deposition rate increases from 1 to 2 Å s<sup>-1</sup>. This gain in deposition rate was important to deposit thick layers and cells in a reasonable time and motivated the use of 40.68 MHz for the following deposition results.

Figure. 7.1(b) shows an example of a parameter scan used to find higher deposition rates. This figure also shows that the deposition rate is reduced when the substrate is set to a partially floating electrical bias (see Sec. 5.5.2). This partially floating bias was used to further reduce the ion bombardment energy. This lower deposition rate in the partially floating condition shows that the influence of this substrate bias is more complex than simply reducing the ion bombardment energy. A similar decrease of ion flux was observed in the RFEA measurement in a partially floating condition. This decrease could be due to a shift toward the RF electrode of the maximum ionisation rate. Or, since the sheath above the substrate is weaker in the partially floating condition, this reduced flux could be the consequence of a lower electron temperature at this weaker sheath edge.

## 7.2 Raman crystallinity

The crystalline volume fraction or “crystallinity” of a deposited  $\mu\text{c-Si:H}$  layer often changes along its growth. For  $\mu\text{c-Si:H}$  deposited on glass or TCO, the first tens of nanometers of the layer are usually amorphous (incubation layer) until nucleation occurs. From these nucleation points, the crystals grow wider as the layer grows, becoming columnar structures embedded in an amorphous matrix. This amorphous material passivates the defects at the boundaries of the columnar nanocrystals.



**Figure 7.2:** Transmission Electron Microscope (TEM) image of a  $\mu\text{c-Si:H}$  layer on a structured TCO taken by E. Vallat-Sauvain [92].

Therefore, the amorphous matrix and/or passivation of bounds by hydrogen are necessary to minimize the defect density in  $\mu\text{c-Si:H}$  hence minimizing the recombination rate of photogenerated charge carriers and the crystallinity should remain around 50 % over the total thickness [94–97].  $\mu\text{c-Si:H}$  layers with a too high crystallinity also suffer from post oxidation.

Here, the crystallinity of the  $\mu\text{c-Si:H}$  is determined with a technique called Raman spectroscopy. The Raman shift (shift in wavelength) of light reflected by the substrate bears information of its interaction with the phonons in the probed material and hence of the material crystallinity [98]. The crystallinity variation along the direction of growth is estimated using a focused green laser beam with a wavelength of 532 nm and therefore a short penetration depth into the  $\mu\text{c-Si:H}$ . The beam can be focussed on the  $\mu\text{c-Si:H}$  layer from the glass side, in which case the measurement is sensitive to the beginning of the growth, or be focussed from the layer side, providing a measurement sensitive to the end of the growth.

In the parallel-plate reactor, the crystallinity typically varies from 45-50% at the beginning of the growth and ends at 60-65%. In the grid reactor, the amorphous incubation layer tended to be thicker as shown in figure 7.2 reducing the crystalline fraction at the glass side. This is probably due to the lack of ion bombardment to help the nucleation [92]. To favour this nucleation process, the  $\text{SiH}_4$  concentration could be decreased but then the crystallinity increase along the growth is too high. To compensate this effect, the silane dilution was varied during the beginning of the

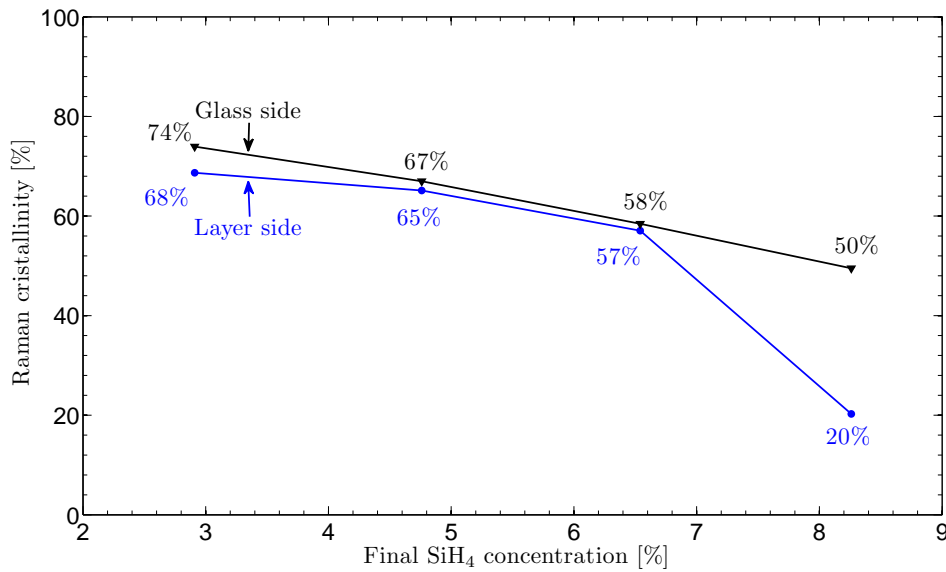


**Figure 7.3:** Raman crystallinity measured on the glass and layer sides as a function of the stabilized SiH<sub>4</sub> concentration. The SiH<sub>4</sub> concentration was varied at the beginning of the growth to reduce the crystallinity gradient through the growth. The initial SiH<sub>4</sub> concentration was 2.9%. The pressure used here was 100 Pa and the power was 700 W

deposition (10% of the total thickness). The gas flows were then held constant as it is usually the case. The resulting crystallinity measured on both sides as a function of the final silane concentration is shown in figure 7.3. Using this gradient technique, stable crystallinity of 50-60 % was obtained through the layer. This figure also shows that for a final SiH<sub>4</sub> concentration below 4.5%, the crystallinity is too high whereas at a concentration of 8.3% the layer becomes amorphous as it grows.

### 7.3 Fourier transform infrared absorption spectroscopy

In this section, the Fourier Transform Infrared (FTIR) absorption spectra of the layers were measured. This technique is often used to probe the different chemical bonds present inside the layer. The principle is to illuminate the deposited layer with infrared light and measure the absorption spectra. Typical absorption spectra are shown in figure 7.4. This figure shows three different sets of curves. The sets labelled “floating” show a broad Si-O<sub>x</sub> peak located between 950-1200 cm<sup>-1</sup> which appeared a few months after deposition. This Si-O<sub>x</sub> peak and its increasing intensity with time is a clear sign of post oxidation [99] of the layer. The intensity of this



peak increases with time as oxygen and/or water vapor diffuses into the layer and binds onto unpassivated silicon bonds. This post oxidation is an indication of higher layer porosity and a sign of poor cell properties. In contrast, on the other set of curves in grounded condition, this Si-O<sub>x</sub> peak does not increase significantly with time. Therefore, better cell properties can be expected from this layer.

Many FTIR measurements were done on the layers produced in the grid reactor. These measurements indicated that the layers were more prone to higher porosity than layers produced with a parallel-plate reactor. However, when the substrate was grounded in the grid reactor, a careful SiH<sub>4</sub> concentration gradient during growth permitted to deposit compact material, avoiding the increase of this Si-O<sub>x</sub> peak as shown in figure 7.4. On the other hand, with the partially floating substrate, the post oxidation could not be avoided and the spectra were similar to those shown in figure 7.4. This post oxidation problem would be expected to disappear as the crystallinity of the layer is reduced, however, with the partially floating substrate, even amorphous layers were not exempt from post oxidation as shown by the two sets of curves with partially floating substrates. Here the crystalline fraction of these two layers is indicated by the  $V_{oc}$  of the cells these layers are embedded in. The  $V_{oc}$  is influenced by the bandgaps (1.1 eV for  $\mu cSi:H$  and 1.8 eV for  $aSi:H$ ) and the typical  $V_{oc}$  in a good microcrystalline cell is 520 mV whereas  $V_{oc}$  are typically 900 mV in good quality amorphous solar cells. Here, the set of curves with a  $V_{oc}$  of 503 mV is microcrystalline whereas the cell with a  $V_{oc}$  of 560 mV is an amorphous cell of poor quality, as expected from the post oxidation signature of this layer.

It has been suggested [100, 101] that porosity could be the consequence of a lack of ion bombardment which could otherwise promote the surface mobility of radicals reaching the growing surface. This could explain the high porosity observed in the layer deposited in the grid reactor. This suggests that there could be an optimum ion bombardment energy in which case the best solution would be to tune the ion energy instead of simply reducing it.

## 7.4 Defect density

In this study, the defect density is characterized by the sub-bandgap absorption  $\alpha_{0.8 \text{ eV}}$  using Fourier Transform Photocurrent Spectroscopy (FTPS) [102]. The sub-bandgap absorption reflects the defect density. A higher defect density will result in a higher probability that a electron-hole pair, photo generated in the material, will recombine inside the material instead of contributing to the current. This effect

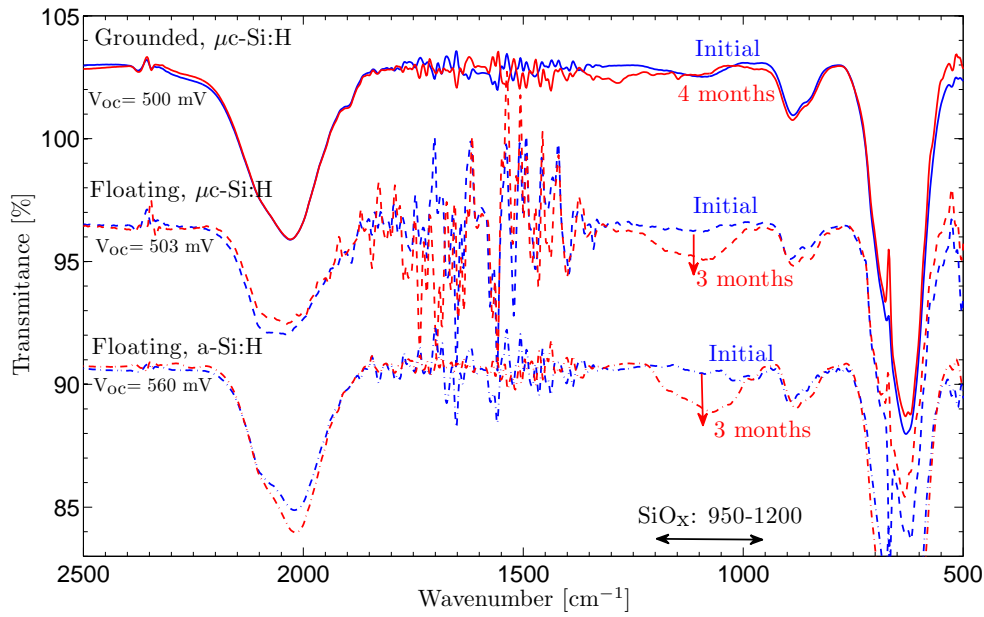


**Figure 7.4:** Fourier Transform Infrared (FTIR) transmission spectra from layers deposited in the grid reactor with a grounded and a partially floating substrate. The measurements are taken shortly after deposition and a few months after deposition to show the post oxidation. The curves are shifted vertically to improve the visibility.

reduces the cell efficiency.

In the literature, there is a general consensus that high ion bombardment energy is detrimental for the deposition of silicon solar cells [10, 13–15, 17, 20–24, 26, 100, 103–107]. Although the actual reason behind this detrimental influence is still unclear (damage to surfaces or lattice [17, 24, 103, 105], microvoids and higher hydrogen content [21], more defect density [23], internal stress [15, 104], sputtering [106, 107], ...), it is clear that “ion bombardment may introduce severe substrate modifications, but which are subtle and difficult to detect” [107]. It is also argued that a certain amount of “low” ion bombardment energy could in fact be beneficial to enhance carrier/surface mobility [17, 26, 100, 101], improve the material compactness and that ions should have an optimum energy around 20 eV [26, 100]. Based on this consensus, the defect density of the layers deposited with the grid reactor (i.e. under low ion bombardment) are compared with other layers deposited under low ion bombardment in the parallel-plate reactor. The low ion bombardment in the parallel-plate reactor was obtained by operating the reactor at 100 Pa and 81.36 MHz. The higher pressure reduces the ion bombardment by an increased collision rate (see Sec. 2.2) and the higher frequency reduces the voltage through the sheath as discussed in [4]. Figure 7.5 shows that the defect density in the grid reactor is slightly higher than

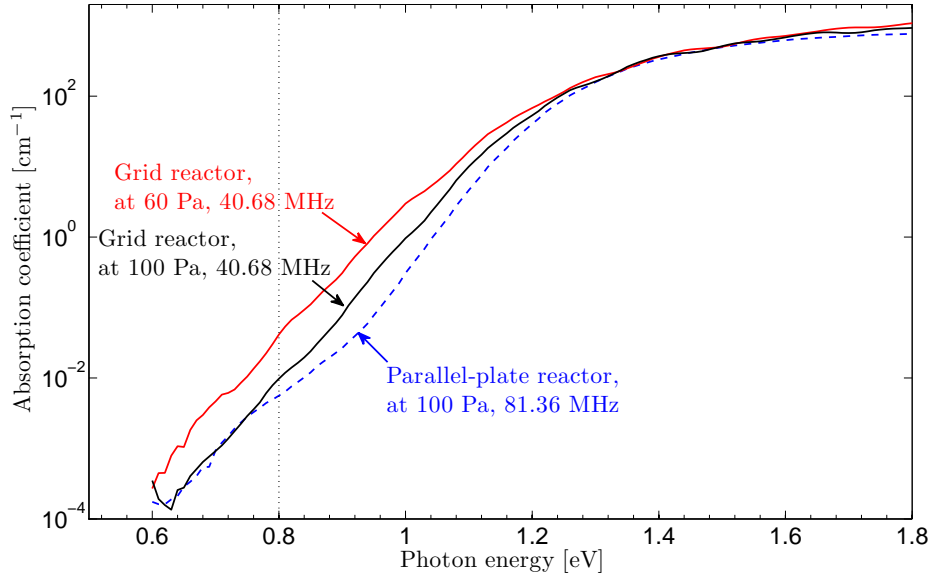


**Figure 7.5:** Absorption coefficient ( $\alpha$ ), as a function of the photon energy, of intrinsic layers deposited in the grid reactor and of the state of the art intrinsic layer deposited in a parallel-plate reactor at 81.36 MHz. The defect density is reflected by the sub-bandgap absorption coefficient at 0.8 eV ( $\alpha_{0.8 \text{ eV}}$ ), indicated by the dotted line.

the one in the low ion bombardment energy parallel-plate reactor. This figure also shows that the defect density in the grid reactor decreases with the pressure. This decrease could be an indication that the ion bombardment at 60 Pa was still causing defects [10], although the defect density can come from many different sources so no clear conclusion could be drawn here. For example, the difference between the grid reactor and low ion bombardment parallel-plate reactor could also be due to an increased layer porosity as discussed in section 7.3.

## 7.5 Cell efficiency

The solar cell efficiency is, together with the deposition rate, one of the key parameters determining the economic viability of a solar cell production technology. The hope with this grid reactor was that, by reducing the ion bombardment, a smaller defect density would lead to a higher cell efficiency. The previous section showed that the defect densities of the intrinsic layers deposited in the grid reactor were not better than the state of the art material produced with a low ion bombardment parallel-plate reactor. In this section, the efficiencies of cells deposited in both reactor types are compared.

During this study, the focus was put on developing intrinsic (I) layers in the grid

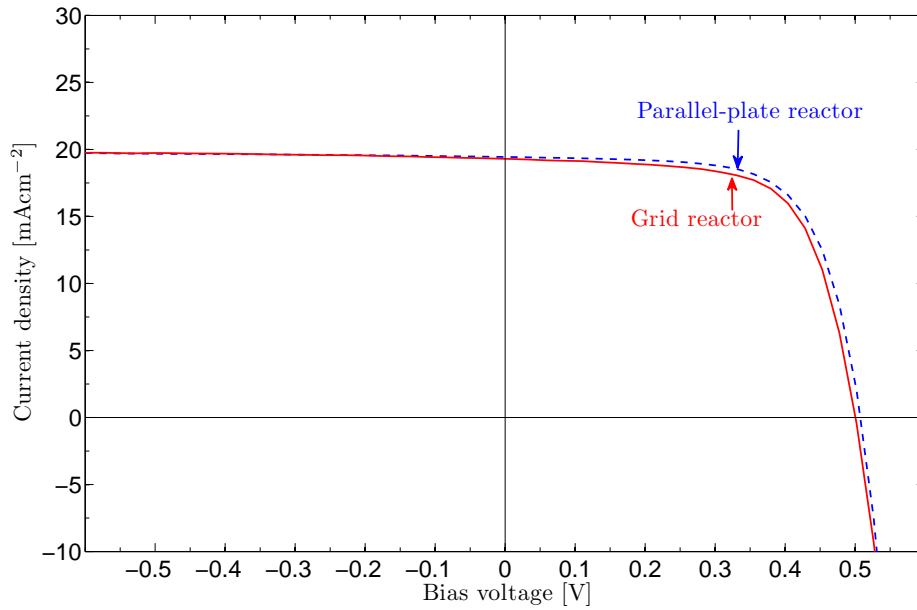


**Figure 7.6:** Current-Voltage (I-V curve) response of hopping cells ( area of  $0.25 \text{ cm}^2$ ) done in the grid reactor and the parallel-plate reactor working in a low ion bombardment regime.

reactor, therefore the other layers (P and N type) must be deposited in another reactor. Consequently, the cells were transported from one reactor to another after the P type and I layers and they were brought in contact with atmosphere during these transports (so called “hopping cells”). In order to compare the results of hopping cells with an intrinsic layer from the grid reactor, the hopping technique was also applied to cells deposited in the parallel-plate reactor. This means that, for the cells deposited in the parallel-plate reactor, all layers were done in the same reactor but the cells are nonetheless brought to atmosphere between each layer.

The efficiencies of the cells were measured by illuminating them under a standard 1.5 atmospheres solar spectrum and by measuring the current-voltage response of the solar cell (I-V curve). The parameters extracted from this curve are: The open circuit voltage ( $V_{oc}$ ) which is the electrical potential through the cell in the open circuit condition; the short circuit current ( $J_{sc}$ ) which is the photocurrent density extracted out of the cell at zero voltage bias; the Fill Factor (FF) which indicates the ratio of the maximum obtainable power to the maximum theoretical power given by the product ( $V_{oc} \cdot J_{sc}$ ); and the cell efficiency ( $\eta$ ). The I-V curve of the best hopping solar cells in the grid reactor and parallel-plate reactor are shown in figure 7.6 and the parameters are listed in table 7.2. This figure shows that the efficiencies are nearly equal in both reactors and so are the open circuit voltages  $V_{oc}$  and short circuit currents  $J_{sc}$ .

	Parallel-plate reactor	Grid reactor
Voc [mV]	507	500
FF [%]	68.0	67.1
J <sub>sc</sub> [mAcm <sup>-2</sup> ]	19.44	19.31
$\eta$ [%]	6.7	6.5

**Table 7.2:** Parameter for the solar cells shown in figure 7.6. The cell in the parallel-plate reactor is deposited in a low ion bombardment condition. The cell thickness are respectively 1.2 and 1.7  $\mu\text{m}$  for the grid reactor and the parallel-plate reactor respectively.

To deepen the analysis between the two cells, their External Quantum Efficiencies (EQE) were measured. The EQE gives the ratio of electron-holes pairs collected at the terminal of the solar cells to the number of incident photons. It is a combined measure of the conversion efficiency of an incident photon to an electron-hole pair (quantum efficiency) and the recombination events of those photocarriers during their transport within the solar cell (collection efficiency). This EQE curve in the range of interest for  $\mu\text{c-Si:H}$  cells (from 350 to 1100 nm) is shown in figure 7.7(a). This figure shows that even though the two cells have the same efficiency, their EQE spectra are different. The EQE of the hopping cell from the grid reactor is higher than the one from the parallel-plate reactor for wavelengths shorter than 600 nm and the ratio is reversed at higher wavelengths.

In the parallel-plate reactor, the lower EQE below 600 nm is a typical signature of a too thick P layer. The light enters the cell through this P layer and therefore the thickness of the P layer influences the light absorption. The influence of this thickness is stronger at lower wavelengths due to the higher absorption probability of  $\mu\text{c-Si:H}$  at lower wavelengths compared to higher wavelengths. Light absorption in the doped layer is detrimental for the EQE because, due to the doping of these layers, their defect density is higher. Therefore, the thinner P layer in the grid reactor implies a reduced absorption of lower wavelengths inside the P layer and a higher EQE at these wavelengths [92].

At wavelengths above 600 nm, the EQE is lower for the grid reactor solar cell. This reduced EQE could be explained by the thinness of the intrinsic layer (1.2  $\mu\text{m}$  instead of 1.7  $\mu\text{m}$  for the parallel-plate reactor solar cell). If the I layer is too thin, then part of the incident light is not absorbed inside the intrinsic layer, reducing the EQE [92].

These differences in layer thickness are probably responsible for most of the difference in the EQE from both reactors. These differences in layer thickness could be

solved by optimizing the cells. The EQE measurements also show that both cells have problems in the transport properties of their intrinsic layers. The transport properties are highlighted by the ratio of the EQE curves at the two biases (0 V and -1 V) shown in figure 7.7(b). The -1 V forward bias strongly improves transport properties and therefore the difference between the EQE with and without this bias show loss of EQE due to the transport properties of the I layer.

In the parallel-plate reactor, the low EQE ratio below 500 nm followed by a high ratio is symptomatic of an intrinsic layer slightly contaminated by boron from the P-layer close to the P-I interface [92]. This contamination increases the defect density and therefore the recombination rate within the first nanometres of the intrinsic layer. In the grid reactor, the EQE ratio is high below 500 nm and decreases for higher wavelengths. This is most probably due to a deformation of the electric field profile within the thickness of the intrinsic  $\mu\text{c-Si:H}$  material. In this view, the drift of the photo-carriers is enhanced by an increased electric field close to the P-I interface which is counterbalanced by a weaker field in the bulk, leading to more recombination for photocarriers photo-generated in the bulk by the red and infrared part of the incident spectrum. The deformation of the electric-field profile is suspected to be caused by  $\text{O}_2$  contamination of the bulk and/or  $\text{H}_2\text{O}$  adsorption at the surface of the possible porosity in the layer as discussed previously [92].

In section 7.4, it was shown that the defect density in the grid reactor was not lower than for other low ion bombardment reactors. Figure 7.5 showed an improvement in defect density when the pressure was increased in the grid reactor. This indicates that further reducing the ion bombardment in this reactor could be beneficial. To do so, the substrate of the grid reactor was set to a partially floating potential similar to the configuration described in section 5.5.2. Here the reactor construction did not permit a large gap between the substrate holder and the grounded wall. Therefore the capacitive coupling to ground was still significant and the substrate was only partially floating (see Sec. 2.1). Nonetheless, the ion bombardment should have been reduced with this partially floating substrate. However, on the contrary, the results from the cells deposited with a partially floating condition were worse than those obtained with a grounded substrate. The collection efficiency of the partially floating cells was poor for high wavelengths and they showed sign of post oxidation (see Sec. 7.3). However, it is hard to conclude whether the reduction of ion bombardment was responsible for the lower cell quality, or if it was due to the layer porosity or to another influence of the partially floating substrate on the plasma parameters (see Sec. 7.1). Nonetheless, this result reinforces the idea that the optimal ion

bombardment energy might not be the lowest possible energy and that low ion bombardment energy could have beneficial effect in PECVD reactors [26, 100].

## 7.6 Conclusion

The grid reactor was developed with the aim of depositing  $\mu\text{c-Si:H}$  layers with a lower defect density by reducing the ion bombardment energy. This bombardment energy is reduced with the use of a developed reactor design. This method for reducing the ion bombardment was proposed as an alternative to the use of high gas pressure or VHF frequencies which have disadvantages for large area deposition. This chapter has shown the deposition results obtained at Oerlikon Solar-Lab by D. Dominé et al. The deposition rate in the grid reactor is lower than in the parallel-plate reactor due to the difference in ionisation profiles between these two reactor types. The crystallinity of layers deposited in the grid reactor was discussed. To maintain an optimal crystallinity throughout the deposited layer in the grid reactor, the  $\text{SiH}_4$  flux had to be adapted during growth. The necessity to vary the  $\text{SiH}_4$  flow (called “silane profiling”) was also revealed by FTIR spectra. This flux variation was necessary to prevent the porosity of layers deposited in the grid reactor. It was suggested that this porosity could be the consequence of the lack of ion bombardment in this reactor.

In the literature, there is a general consensus that high ion bombardment energy is detrimental for the deposition of silicon solar cells [10, 13–15, 17, 20–24, 26, 100, 103–107]. Therefore, in this study, the defect density of the layers deposited in the grid reactor were compared with layers deposited in a parallel-plate reactor also having low ion bombardment energy (reactor operated at higher pressure and RF frequency). It was shown that the material deposited in the grid reactor is similar to the state-of-the-art layers from this low ion bombardment energy parallel-plate reactor, but they are not better. This could be caused by a remaining porosity of the material deposited with the grid reactor, despite the silane profiling technique applied during deposition.

In line with the results of the defect density, hopping cells with intrinsic layers deposited in the new grid reactor and in a parallel-plate reactor with low ion bombardment energy were compared. These results showed that the best cells obtained in the grid reactor approach the performance of the reference cells in the parallel-plate reactor in which the ion bombardment energy is reduced with pressure and/or higher RF frequency. This suggests that, between reactors having low ion bombardment

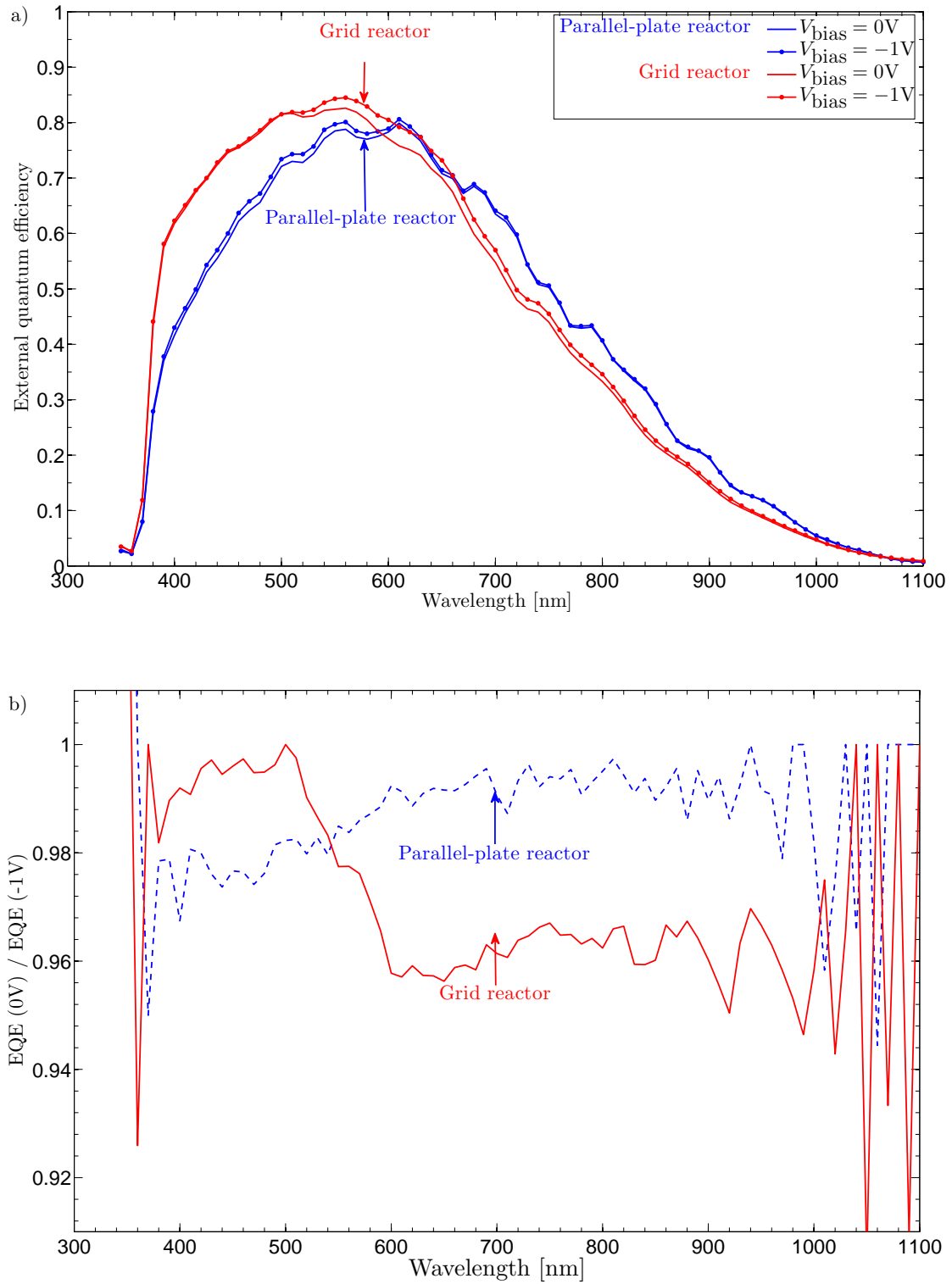


**Figure 7.7:** (a) External Quantum Efficiency (EQE) of hopping cells in the parallel-plate and the grid reactors. The EQE are shown for a forward bias of 0 V or -1 V. (b) Ratios of EQE at biases of 0 and -1 V for each cell.



energy, the ion bombardment is not a dominant problem. Other parameters, such as  $\text{SiH}_3\text{:SiH}_2$  radical density ratio and fluxes, layer contaminations, porosity, could be more important for the growth process and the dominant ones remain yet to be identified. Therefore, the improvements which can be made using the grid reactor would probably have too little impact for a real advantage in solar cell production. Furthermore, the lower deposition rate and engineering difficulties discussed in section 3.2.2 render this grid reactor less practical for large area production than the current state-of-the-art parallel-plate reactors.



# Chapter 8

## Final conclusions and outlook

This work has presented the development and investigations of a grid reactor geometry for the deposition of large area thin films under low ion bombardment energy. This grid reactor was developed based on the parallel-plate reactor currently used in the display and the photovoltaic industries. The aim of this reactor design was to study the influence of the reactor geometry on the plasma in order to reduce the ion bombardment energy. This approach differs from the classical approach in capacitively-coupled large area reactors where high gas pressure and very high frequencies are used to reduce the ion bombardment energy.

During the design of the grid reactor, it was shown that the addition of the grid increases the RF power necessary for plasma breakdown at low pressure. The grid lowers the RF electrode impedance causing strong ohmic losses. Furthermore, the breakdown voltage itself is higher at low pressure due to the proximity between the grid and RF electrode. It was shown that this distance is a central parameter of this reactor design and that it needs to be a compromise between minimising the breakdown voltage while preventing the plasma from shrinking into the volume between the grid and the RF electrode. It was also shown that structuring the RF electrode helped to reduce the breakdown voltage at the desired gas pressure.

At the beginning of the project, it was thought that a dense plasma would form in the grid hole and be confined there as illustrated in [56]. Instead, measurements quickly showed that a dense plasma indeed forms in the grid holes, but the plasma also spreads out into the volume between the grounded electrode and the grid. The plasma conducts the RF current through the grid holes to the large grounded surface below the grid. This phenomena makes the front and back of the grid available for electrode area asymmetry. The gas type then determines the areas in contact with the plasma and the sheath capacitances via the density profiles at these surfaces.

It results a strong negative self-bias potential which plays an important role in reducing the ion bombardment energy to the substrate. Measuring the ion density profiles showed that the lateral uniformity of the density above the substrate was unperturbed by the grid. Hence the grid reactor has strong electrode asymmetry while retaining good uniformity over a large area.

By studying the conduction of the RF current through the grid holes, it was found that RF current flowing through the plasma in a hole is independent of that hole diameter. This showed that a tiny hole in a surface can conduct large RF currents to the other side of that surface, which can lead to a variation of the self-bias potential or even to permanent damages. This effect is important for reactor design as plasmas are often confined by plates containing small holes such as pumping grids. Furthermore, it was shown that the funnelling of the RF currents as it flows toward the RF electrode during field reversal is a strong heating mechanism for these dense plasmas in tiny holes.

The analysis of the ion bombardment energy showed that the negative self-bias potential strongly reduces the ion bombardment energy in the grid reactor. However, it was also shown that this mechanism alone was not sufficient to explain the measured reduction of ion bombardment energy. The latter also depends on the time-averaged plasma potential hence it is influenced by the time evolution of the plasma. The time evolution in parallel-plate reactors at 13.56 MHz is sinusoidal and it was expected that this would also be the case in the grid reactor. However, PROES measurements showed that the time evolution of the ground sheath in the grid reactor was different from that in the parallel-plate reactor. This observation was supported with capacitive probe measurements which showed that the plasma potential waveform in the grid reactor is strongly non-sinusoidal. It was suggested that this waveform is a consequence of the dense plasma formed inside the grid hole. This particular potential waveform in the grid reactor leads to a further reduction of the time-averaged plasma potential in the grid reactor.

It was shown that the self-bias and the plasma potential waveform are the two dominant factors responsible for lowering the ion bombardment energy in the grid reactor. These two factors are tied to the dense plasma in the grid hole expanding into the volume below the grid and are thus consequences of the reactor geometry. The possibility of other phenomena reducing the ion bombardment energy was discussed. It was also shown that changing the grid design had little influence on those two factors and that the ion bombardment energy remained below 30 eV in a large range of peak-to-peak potentials.

The grid reactor design also offers the possibility to influence the ion bombardment energy by adding a bias to the substrate while keeping a uniform ground reference for the plasma. It was therefore shown that, by insulating the substrate from DC and RF currents, the ion bombardment energy was further reduced to energies of 11 eV. Instead of setting the substrate to a floating potential, adding a negative DC bias permitted the raising of the ion bombardment energy by a desired quantity.

In parallel to these experiments, a numerical fluid simulation using a simple model was developed. The obtained results showed very good agreement with the experiments. All observed phenomena were also reproduced by the simulation, strengthening confidence in both approaches. The simulation results suggest that the measured difference in ion density profiles between the two gases is a consequence of the rovibrational excitation cross-section present in molecular gas (hydrogen) and absent in monoatomic gases (argon). This molecular excitation increased the loss rate of cold electrons, changing the gradient of electron temperature and thereby the density profiles.

Finally, a semi-industrial grid reactor prototype was built to study the deposition of microcrystalline thin film intrinsic layers and solar cells. The results showed that the deposition rate in the grid reactor is lower by a factor of two compared to the parallel-plate reactors. This low deposition rate is a consequence of the high ionisation rate above the grid holes as radicals produced there are likely lost to the grid and RF electrode and not contributing to the deposition. This grid reactor was not developed for high deposition rates.

It was discussed that, to obtain a stable crystallinity throughout the deposited layer in the grid reactor, the  $\text{SiH}_4$  flow had to be adapted during growth. The necessity to vary the  $\text{SiH}_4$  flow was also revealed by FTIR spectra as this flux variation was necessary to prevent the porosity of layers deposited in the grid reactor. It was suggested that this porosity could be the consequence of the lack of ion bombardment in this reactor.

In the literature, there is a general consensus that high ion bombardment energy is detrimental for the deposition of silicon solar cells [10, 13–15, 17, 20–24, 26, 100, 103–107]. Therefore, in this study, the defect density of layers deposited in the grid reactor were compared with layers deposited in a parallel-plate reactor having also low ion bombardment energy (reactor operated at higher pressure and RF frequency). It was shown that the material deposited in the grid reactor is almost comparable to state-of-the-art layers from this parallel-plate reactor, but they are not better. This difference could be caused by a remaining porosity of the material

deposited in the grid reactor, despite the silane profiling technique applied during deposition.

In line with the results of defect density, hopping cells with intrinsic layers deposited in the new grid reactor or in a parallel-plate reactor with low ion bombardment energy were compared. These results show that the best cells obtained in the grid reactor approach the reference cells in the parallel-plate reactor in which the ion bombardment energy is reduced by means of higher gas pressure and/or higher RF frequency. This suggests that, between reactors having low ion bombardment energy, the ion bombardment is not a dominant problem. Other important parameters for the growth process remain to be identified ( $\text{SiH}_3\text{:SiH}_2$  radical density ratio and fluxes, layer contaminations, porosity). Therefore, the improvements which can be made using the grid reactor would probably have too little impact for a real advantage in solar cell production. Furthermore, the lower deposition rate and additional engineering difficulties of this grid reactor design render this grid reactor less practical than the parallel-plate reactor for large area production.

Therefore, although this reactor has interesting plasma properties, the material properties and engineering difficulties do not justify a change in reactor technology. This reactor design will however remain a useful tool for the study of layers deposited under low ion bombardment energy.

# Appendix A

## Appendix: Derivation of the momentum conservations

This appendix show steps in the derivation of the continuity equations for the fluid simulation model used in this study. These steps are useful for the discussion on the construction of the fluid model in section 2.3.

A description of a system of  $N$  particles is given by the “one particle distribution”  $f_\alpha$  [43] where  $\alpha$  is a type of particle (i.e ion, electron). The one particle distribution is given by  $\bar{n}_\alpha f_\alpha = N_\alpha \int F(x_1, x_2, \dots, x_n, v_1, v_2, \dots, v_n, t) dx_2 \dots dx_n dv_2 \dots dv_n$ , where  $\bar{n}_\alpha = \frac{N_\alpha}{V}$  is the particle density and  $F(x_1, x_2, \dots, x_n, v_1, v_2, \dots, v_n, t)$  is the “distribution function” [43].

The evolution of the one particle distribution is given by the Boltzmann equation [43]:

$$\frac{\partial}{\partial t} f_\alpha + v_1 \frac{\partial}{\partial x_1} f_\alpha + a^E \frac{\partial}{\partial v_1} f_\alpha = \frac{\partial}{\partial t} f_\alpha|_c \quad (\text{A.0.1})$$

where  $a^E$  is the acceleration due to external forces (such as electric fields) and  $\frac{\partial}{\partial t} f_\alpha|_c$  is due to inter-particle collisions. Integrating the one particle density with different moments of the velocity gives the macroscopic quantities [43]:

$$\int \bar{n}_\alpha f_\alpha dv_1 = n_\alpha(x_1, t) \quad (\text{A.0.2})$$

$$\int \bar{n}_\alpha v f_\alpha dv_1 = n_\alpha v_\alpha = \Gamma_\alpha(x_1, t) \quad (\text{A.0.3})$$

$$\int \bar{n}_\alpha m_\alpha (v - v_\alpha)^2 f_\alpha dv_1 = P_\alpha(x_1, t) \quad (\text{A.0.4})$$

...

where  $v_\alpha$  and  $P_\alpha$  are the mean velocity and the pressure tensor for the particles  $\alpha$  at  $x_1, t$ . Since  $P$  is calculated from the one particle distribution,  $P$  is, by construction,

the partial pressure of particle species  $\alpha$  and not the total pressure. Therefore, in isotropic systems, the state equation for  $P$  is:  $P_\alpha = n_\alpha k_B T_\alpha$ , where  $T_\alpha$  is the temperature in kelvins.

Integrating Boltzmann equation with different moments gives the continuity equations. The lower moment (Eq. A.0.2) gives the particle conservation [43]:

$$\frac{\partial}{\partial t} n_\alpha + \nabla \cdot n_\alpha v_\alpha = S - L, \quad (\text{A.0.5})$$

where  $S$  and  $L$  are the source and loss rate of particles. Here the evolution of the zero moment equation ( $n_\alpha$ ) depends on  $v_\alpha$ , which is given by the first moment equation (Eq. A.0.3). This momentum equation, as all the other momentum equations, depends on a higher order moment. This infinite progression is closed by using a state equation to link a higher order moment to a smaller order moment. Typical closures are:  $P = n_\alpha k_B T_\alpha$  (chosen here) or  $P_\alpha = An_\alpha^{\frac{5}{3}}$  (for adiabatic processes). Choosing even these simple closures still leads to considerable complexity. It is important to note that this closure is a choice affecting the physics of the model. To illustrate the importance of the choices made to construct these models, N. A. Krall and A. W. Trivelpiece [43] explain that “the fluid theory, though of great practical use, relies heavily on the cunning of its user”.

With the closure  $P = n_\alpha k_B T_\alpha$ , the momentum conservation (first order moment) gives [28, 43]:

$$m_\alpha n_\alpha \left[ \frac{\partial}{\partial t} v_\alpha + v_\alpha \cdot \nabla v_\alpha \right] = q_\alpha n_\alpha E - \nabla P_\alpha - m_\alpha n_\alpha \nu_{m,\alpha} v_\alpha \quad (\text{A.0.6})$$

where  $q_\alpha$  is the electric charge, the external forces are caused by an electric field  $E$ , the collision term  $\int m_\alpha v_\alpha \frac{\partial}{\partial t} f_\alpha|_c dv = m_\alpha n_\alpha \nu_{m,\alpha} v_\alpha$  where  $\nu_{m,\alpha}$  is the momentum transfer frequency. In this study  $\nabla P_\alpha = k_B (n_\alpha \nabla T_\alpha + T_\alpha \nabla n_\alpha)$  since the electron temperature gradient ( $\nabla T_e/T_e$ ) can be non negligible compared to the density gradient ( $\nabla n_e/n_e$ ). This term is also kept by other studies [45, 46], though studies often suppose an isothermal plasma [44]. This temperature gradient term is dropped for ions since their temperature is in equilibrium with the gas and is therefore isothermal to a good approximation.



# Appendix B

## Appendix: Conformal transformation

This sections describes developments for the analytical calculation of the electric potential within a RFEA using the method of conformal transformations [66]. The scheme of this transformation is shown in figure B.1 and discussions of the results are done in section 4.4.3.

The potential is calculated at first in a simple coordinate system ( $\mathcal{Z}$ ), a circle with a set of wires. There, the potential is given by:

$$\begin{aligned} V(\rho, \theta) &= -\frac{q_{\text{col}}}{2\pi\epsilon_0} \ln(l_{\text{col}}) - \frac{q_{\text{sec}}}{2\pi\epsilon_0} \ln(l_{\text{sec}}) - \frac{q_{\text{sel}}}{2\pi\epsilon_0} \ln(l_{\text{sel}}) \\ &\quad - \frac{q_{\text{p}}}{2\pi\epsilon_0} \ln(l_{\text{p}}) \\ l_{\text{col}} &= \rho \\ l_{\text{sec}} &= (\rho^2 + \rho_{\text{sec}}^2 - 2\rho\rho_{\text{sec}} \cos \theta)^{\frac{1}{2}} \\ l_{\text{sel}} &= (\rho^2 + \rho_{\text{sel}}^2 - 2\rho\rho_{\text{sel}} \cos \theta)^{\frac{1}{2}} \\ l_{\text{p}} &= (\rho^2 + \rho_{\text{p}}^2 - 2\rho\rho_{\text{p}} \cos \theta)^{\frac{1}{2}} \end{aligned} \tag{B.0.1}$$

where  $q_j$  is the charge on each wire and  $l_j$  the distance to each wire. After the conformal transformation to potential in a more complicated coordinate system  $\mathcal{W}$  (here the RFEA geometry) is given by the conformal transformation :

$$\mathcal{W}(x, y) = \frac{2\pi}{a} \ln \mathcal{Z}(\rho, \theta), \tag{B.0.2}$$

where the two coordinate systems are shown in figure B.1 and  $a$  is the distance between the wires within a mesh. Using this coordinate transformation,  $\rho = e^{\frac{2\pi x}{a}}$ ,

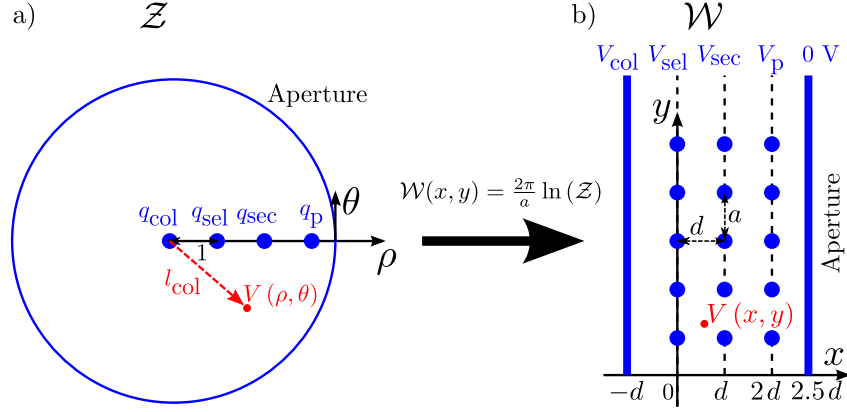


**Figure B.1:** Potential in (a) the simple  $\mathcal{Z}$  system and (b) the  $\mathcal{W}$  system (the RFEA).  $q_j$  and  $V_j$  are the charge and potential on each grid,  $a$  is the distance between the wires in the grid,  $d$  the distance between each grid. In the RFEA,  $a \ll d$ . This figure was shown in section 4.4.3

$\theta = \frac{2\pi y}{a}$  and the general form of the voltage in  $\mathcal{W}$  is:

$$\begin{aligned}
 V(x, y) = & -\frac{q_{\text{col}}}{4\pi\epsilon_0} \ln \left[ e^{\frac{4\pi x}{a}} \right] - \frac{q_{\text{sec}}}{4\pi\epsilon_0} \ln \left[ e^{\frac{4\pi x}{a}} + 1 - 2e^{\frac{2\pi x}{a}} \cos \left( \frac{2\pi y}{a} \right) \right] \\
 & - \frac{q_{\text{sel}}}{4\pi\epsilon_0} \ln \left[ e^{\frac{4\pi x}{a}} + e^{\frac{4\pi d}{a}} - 2e^{\frac{2\pi(x+d)}{a}} \cos \left( \frac{2\pi y}{a} \right) \right] \\
 & - \frac{q_{\text{p}}}{4\pi\epsilon_0} \ln \left[ e^{\frac{4\pi x}{a}} + e^{\frac{8\pi d}{a}} - 2e^{\frac{2\pi(x+2d)}{a}} \cos \left( \frac{2\pi y}{a} \right) \right] + C \quad (\text{B.0.3})
 \end{aligned}$$

To determine the constant  $C$  and link the charges  $q_j$  to the potentials ( $V_j$ ) on each grid, the potential is calculated at the border of each grid. Since  $d \gg a$ , only the terms in  $e^{\frac{d}{a}}$  with the higher orders are kept in each logarithm as shown below:

$$\ln \left[ e^{\frac{10\pi d}{a}} + e^{\frac{4\pi d}{a}} - 2e^{\frac{7\pi d}{a}} \cos \left( \frac{2\pi y}{a} \right) \right] \simeq \ln \left[ e^{\frac{10\pi d}{a}} \right] \quad (\text{B.0.4})$$

Therefore, using equation B.0.3 with equation B.0.4 and the relation  $1 - \cos(2\theta) =$

$2 \sin^2(\theta)$ , the boundaries conditions at each grid are:

$$\begin{aligned} V\left(\frac{5}{2}d, y\right) = 0 &= -\frac{5d}{2a\epsilon_0}(q_{\text{col}} + q_{\text{sec}} + q_{\text{sel}} + q_{\text{p}}) + C \\ \Rightarrow C &= \frac{5d}{2a\epsilon_0}(q_{\text{col}} + q_{\text{sec}} + q_{\text{sel}} + q_{\text{p}}) \end{aligned} \quad (\text{B.0.5})$$

$$V(-d, y) = V_{\text{col}} = -\frac{d}{a\epsilon_0}\left(\frac{7}{2}q_{\text{col}} + \frac{5}{2}q_{\text{sec}} + \frac{3}{2}q_{\text{sel}} + \frac{1}{2}q_{\text{p}}\right) \quad (\text{B.0.6})$$

$$\begin{aligned} V(0, r_{\text{m}}) = V_{\text{sec}} &= \frac{d}{a\epsilon_0}\left(\frac{5}{2}q_{\text{col}} + \left[\frac{5}{2} - \frac{a}{2\pi d} \ln\left[2 \sin\left(\frac{\pi r_{\text{m}}}{a}\right)\right]\right]q_{\text{sec}} + \right. \\ &\quad \left. + \frac{3}{2}q_{\text{sel}} + \frac{1}{2}q_{\text{p}}\right) \end{aligned} \quad (\text{B.0.7})$$

$$\begin{aligned} V(d, r_{\text{m}}) = V_{\text{sel}} &= \frac{d}{a\epsilon_0}\left(\frac{3}{2}q_{\text{col}} + \frac{3}{2}q_{\text{sec}} + \right. \\ &\quad \left. + \left[\frac{5}{2} - \frac{a}{2\pi d} \ln\left[e^{\frac{2\pi d}{a}} 2 \sin\left(\frac{\pi r_{\text{m}}}{a}\right)\right]\right]q_{\text{sel}} + \frac{1}{2}q_{\text{p}}\right) \end{aligned} \quad (\text{B.0.8})$$

$$\begin{aligned} V(2d, r_{\text{m}}) = V_{\text{p}} &= \frac{d}{a\epsilon_0}\left(\frac{1}{2}q_{\text{col}} + \frac{1}{2}q_{\text{sec}} + \frac{1}{2}q_{\text{sel}} + \right. \\ &\quad \left. + \left[\frac{5}{2} - \frac{a}{2\pi d} \ln\left[e^{\frac{4\pi d}{a}} 2 \sin\left(\frac{\pi r_{\text{m}}}{a}\right)\right]\right]q_{\text{p}}\right) \end{aligned} \quad (\text{B.0.9})$$

Were  $r_{\text{m}}$  is the grid radius, which is taken as the larger half width of the rectangular grid. The potential is therefore imposed at the position  $(x, y = r_{\text{m}})$ , on the large side of the grid. The next step is to express each  $q_j$  as functions of the  $V_j$  and to replace them in the general expression. The advantage of this transformation is that the voltages appear as linear equations in the  $q_j$ . Solving the equations requires only linear algebra but the general solution is still rather cumbersome. Here, the solution is given for the particular  $a$ ,  $r_{\text{m}}$ ,  $d$  and  $V_j$  used in this study:

$$\begin{aligned} V(x, y) \simeq &-267 - 2.7 \cdot 10^{-2}x + 1.4 \log\left[1 + e^{\frac{4\pi x}{51}} - 2e^{\frac{2\pi x}{51}} \cos\left(\frac{2\pi y}{51}\right)\right] - \\ &- 2.2 \log\left[e^{\frac{1616\pi}{51}} + e^{\frac{4\pi x}{51}} - 2e^{\frac{2\pi(404+x)}{51}} \cos\left(\frac{2\pi y}{51}\right)\right] + \\ &+ 2.0 \log\left[e^{\frac{3232\pi}{51}} + e^{\frac{4\pi x}{51}} - 2e^{\frac{2\pi(808+x)}{51}} \cos\left(\frac{2\pi y}{51}\right)\right] \end{aligned} \quad (\text{B.0.10})$$

where  $x$  and  $y$  are in  $\mu\text{m}$ . In this method, the grids are supposed to be infinitely large but this is reasonable as the width of the RFEA is 12 mm which is large with respect to the distance between grids (0.4 mm). The mesh wires are assumed to be round wires. This latter assumption has only a minor influence close to the grid wires and are discussed in section 4.4.3.



# Bibliography

- [1] W. Crookes, *On radiant matter : A lecture delivered to the British Association for the Advancement of Science, at Sheffield, Friday, August 22, 1879*. University of California Libraries, 1879. (Cited on page [1](#).)
- [2] I. Langmuir, *Oscillations in Ionized Gases*, *Proc. Nat. Acad. Sci. U. S.*, vol. 14, p. 628, 1928. (Cited on page [1](#).)
- [3] M. J. Colgan, M. Meyyappan, and D. E. Murnick, *Very high-frequency capacitively coupled argon discharges*, *Plasma Sources Sci. Technol.*, vol. 3, p. 181, 1994. (Cited on page [2](#).)
- [4] W. Schwarzenbach, A. A. Howling, M. Fivaz *et al.*, *Sheath impedance effects in very high frequency plasma experiments*, *J. Vac. Sci. Technol. A*, vol. 14, p. 132, 1996. (Cited on pages [2](#), [9](#) and [132](#).)
- [5] M. A. Lieberman, J. P. Booth, P. Chabert *et al.*, *Standing wave and skin effects in large-area, high-frequency capacitive discharges*, *Plasma Sources Sci. Technol.*, vol. 11, p. 283, 2002. (Cited on page [2](#).)
- [6] L. Sansonnens, A. A. Howling, and C. Hollenstein, *Electromagnetic field nonuniformities in large area, high-frequency capacitive plasma reactors, including electrode asymmetry effects*, *Plasma Sources Sci. Technol.*, vol. 15, p. 302, 2006. (Cited on page [2](#).)
- [7] Z. Chen, S. Rauf, and K. Collins, *Self-consistent electrodynamics of large-area high-frequency capacitive plasma discharge*, *J. Appl. Phys.*, vol. 108, p. 073301, 2010. (Cited on page [2](#).)
- [8] H. Schmidt, L. Sansonnens, A. A. Howling *et al.*, *Improving plasma uniformity using lens-shaped electrodes in a large area very high frequency reactor*, *J. Appl. Phys.*, vol. 95, p. 4559, 2004. (Cited on page [2](#).)

- [9] L. Guo, M. Kondo, M. Fukawa *et al.*, ***High Rate Deposition of Microcrystalline Silicon Using Conventional Plasma-Enhanced Chemical Vapor Deposition***, *Jpn. J. Appl. Phys.*, vol. 37, p. L1116, 1998. (Cited on page 2.)
- [10] G. Bugnon, A. Feltrin, F. Schulati-Meillaud *et al.*, ***Influence of ion bombardment on microcrystalline silicon material quality and solar cell performances***, *Proceedings of the 33rd IEEE PVSC*, p. 262, 2008. (Cited on pages 2, 132, 133, 137 and 143.)
- [11] U. Czarnetzki, J. Schulze, E. Schüngel *et al.*, ***The electrical asymmetry effect in capacitively coupled radio-frequency discharges***, *Plasma Sources Sci. Technol.*, vol. 20, p. 024010, 2011. (Cited on pages 2 and 93.)
- [12] D. Hrunski, F. Mootz, A. Zeuner *et al.*, ***Deposition of microcrystalline intrinsic silicon by the Electrical Asymmetry Effect technique***, *Vacuum*, vol. 87, p. 114, 2013. (Cited on page 2.)
- [13] D. E. Carlson, ***Polycrystalline and Amorphous Thin Film Devices***. Ed. L. L. Kazmerski, Academic Press, 1980. (Cited on pages 3, 28, 132, 137 and 143.)
- [14] Y. Uchida, T. Ichimura, O. Nabeta *et al.*, ***Effect of the Deposition Condition on Properties of  $\alpha$ -Si: F: H Films***, *Jpn. J. Appl. Phys.*, vol. 21, p. 193, 1982, supplement 21-2. (Cited on pages 3, 28, 132, 137 and 143.)
- [15] A. Matsuda, K. Kumagai, and K. Tanaka, ***Wide-Range Control of Crystallite Size and Its Orientation in Glow-Discharge Deposited  $\mu$ c-Si: H***, *Jpn. J. Appl. Phys.*, vol. 22, p. L34, 1983. (Cited on pages 3, 28, 132, 137 and 143.)
- [16] A. Matsuda and K. Tanaka, ***Investigation of the growth kinetics of glow-discharge hydrogenated amorphous silicon using a radical separation technique***, *J. Appl. Phys.*, vol. 60, p. 2351, 1986. (Cited on pages 3 and 28.)
- [17] M.-D. Shieh and C. Lee, ***Low temperature (313°C) silicon epitaxial growth by plasma-enhanced chemical vapor deposition with stainless steel mesh***, *Appl. Phys. Lett.*, vol. 63, p. 1252, 1993. (Cited on pages 3, 28, 132, 137 and 143.)

- [18] Y. Show, Y. Yabe, T. Izumi *et al.*, ***Development of triode type RF plasma enhanced CVD equipment for low temperature growth of carbon nanotube***, *Diam. Relat. Mater.*, vol. 14, p. 1848, 2005. (Cited on pages 3 and 28.)
- [19] H. S. Kang, H. J. Yoon, C. O. Kim *et al.*, ***Low temperature growth of multi-wall carbon nanotubes assisted by mesh potential using a modified plasma enhanced chemical vapor deposition system***, *Chem. Phys. Lett.*, vol. 349, p. 196, 2001. (Cited on pages 3 and 28.)
- [20] H. Sonobe, A. Sato, S. Shimizu *et al.*, ***Highly stabilized hydrogenated amorphous silicon solar cells fabricated by triode-plasma CVD***, *Thin Solid Films*, vol. 502, p. 306, 2006. (Cited on pages 3, 28, 132, 137 and 143.)
- [21] S. Shimizu, A. Matsuda, and M. Kondo, ***The determinants of hydrogen concentrations in hydrogenated amorphous silicon films prepared using a triode deposition system***, *J. Appl. Phys.*, vol. 101, p. 064911, 2007. (Cited on pages 3, 28, 132, 137 and 143.)
- [22] M. Tanaka, K. Ninomiya, N. Nakamura *et al.*, ***High-Rate Deposition of a-Si:H Film with a Separated Plasma Triode Method***, *Jpn. J. Appl. Phys.*, vol. 27, p. 14, 1988. (Cited on pages 3, 28, 132, 137 and 143.)
- [23] W. S. Yan, S. Xu, C. C. Sern *et al.*, ***Effect of mesh bias on the properties of the lateral conductivity of intrinsic microcrystalline silicon films deposited by low-frequency inductively coupled plasma***, *Appl. Phys. Lett.*, vol. 99, p. 201501, 2011. (Cited on pages 3, 28, 132, 137 and 143.)
- [24] P. Mahtani, K. R. Leong, B. Jovet *et al.*, ***High quality amorphous-crystalline silicon heterostructure prepared by grid-biased remote radio-frequency plasma enhanced chemical vapor deposition***, *J. Non-Cryst. Solids*, vol. 358, p. 3396, 2012. (Cited on pages 3, 28, 132, 137 and 143.)
- [25] I. S. Osborne, N. Hata, G. Ganguly *et al.*, ***The Effect of Mesh Bias and Substrate Bias on the Properties of a-Si:H Deposited by Triode Plasma Chemical Vapour Deposition***, *Jpn. J. Appl. Phys.*, vol. 33, p. 5663, 1994. (Cited on pages 3 and 28.)
- [26] K. Kato, S. Iizuka, G. Ganguly *et al.*, ***Electron and Ion Energy Controls in a Radio Frequency Discharge Plasma with Silane***, *Jpn. J. Appl. Phys.*, vol. 36, p. 4547, 1997. (Cited on pages 3, 28, 132, 137 and 143.)

- [27] A. Gallagher, *Amorphous silicon deposition rates in diode and triode discharges*, *J. Appl. Phys.*, vol. 60, p. 1369, 1986. (Cited on pages 3 and 128.)
- [28] M. A. Lieberman and A. J. Lichtenberg, *Principles of Plasma Discharges and Materials Processing*, 2nd ed. John Wiley & Sons, 2005. (Cited on pages 6, 7, 12, 13, 14, 17, 23, 33, 36, 59, 60, 64, 74, 79, 90 and 146.)
- [29] K. Köhler, D. E. Horne, and J. W. Coburn, *Frequency dependence of ion bombardment of grounded surfaces in rf argon glow discharges in a planar system*, *J. Appl. Phys.*, vol. 58, p. 3350, 1985. (Cited on pages 7, 9, 10, 78, 79, 90 and 98.)
- [30] K. U. Riemann, *Theoretical analysis of the electrode sheath in rf discharges*, *J. Appl. Phys.*, vol. 65, p. 999, 1989. (Cited on page 9.)
- [31] K. Köhler, J. W. Coburn, D. E. Horne *et al.*, *Plasma potentials of 13.56-MHz rf argon glow discharges in a planar system*, *J. Appl. Phys.*, vol. 57, p. 59, 1985. (Cited on pages 10, 12, 78, 79, 86 and 90.)
- [32] P. Diomede, M. Capitelli, and S. Longo, *Effect of discharge voltage on capacitively coupled, parallel plate rf hydrogen plasmas*, *Plasma Sources Sci. Technol.*, vol. 14, p. 459, 2005. (Cited on pages 14, 21 and 122.)
- [33] A. Salabas, L. Marques, J. Jolly *et al.*, *Systematic characterization of low-pressure capacitively coupled hydrogen discharges*, *J. Appl. Phys.*, vol. 95, p. 4605, 2004. (Cited on pages 14, 21 and 122.)
- [34] U. Czarnetzki, D. Luggenhölscher, and H. F. Döbele, *Investigations on ionic processes and dynamics in the sheath region of helium and hydrogen discharges by laser spectroscopic electric field measurements*, *Appl. Phys. A*, vol. 72, p. 509, 2001. (Cited on pages 14 and 15.)
- [35] J. V. Jovanović, S. B. Vrhovac, and Z. L. Petrović, *Momentum transfer theory of ion transport under the influence of resonant charge transfer collisions: the case of argon and neon ions in parent gases*, *Eur. Phys. J. D*, vol. 21, p. 335, 2002. (Cited on page 14.)
- [36] W. D. Davis and T. A. Vanderslice, *Ion Energies at the Cathode of a Glow Discharge*, *Phys. Rev.*, vol. 131, p. 219, 1963. (Cited on pages 14, 15 and 48.)



- [37] T. Baloniak, R. Reuter, C. Flötgen *et al.*, ***Calibration of a miniaturized retarding field analyzer for low-temperature plasmas: geometrical transparency and collisional effects***, *J. Phys. D: Appl. Phys.*, vol. 43, p. 055203, 2010. (Cited on pages 14, 42, 44, 48, 56 and 85.)
- [38] A. V. Phelps, ***The application of scattering cross sections to ion flux models in discharge sheaths***, *J. Appl. Phys.*, vol. 76, p. 747, 1994. (Cited on pages 14 and 46.)
- [39] M. Fivaz, S. Brunner, W. Schwarzenbach *et al.*, ***Reconstruction of the time-averaged sheath potential profile in an argon radiofrequency plasma using the ion energy distribution***, *Plasma Sources Sci. Technol.*, vol. 4, p. 373, 1995. (Cited on page 14.)
- [40] H. Müller, A. A. Howling, and C. Hollenstein, ***Power Laws for the Spatial Dependence of Electrical Parameters in the High-Voltage Capacitive RF Sheath***, *IEEE T. Plasma. Sci.*, vol. 28, p. 1713, 2000. (Cited on page 14.)
- [41] T. Šimko, V. Martišovitš, J. Bretagne *et al.*, ***Computer simulations of  $H^+$  and  $H_3^+$  transport parameters in hydrogen drift tubes***, *Phys. Rev. E*, vol. 56, p. 5908, 1997. (Cited on page 16.)
- [42] COMSOL. URL: <http://www.comsol.com> (Cited on pages 17 and 32.)
- [43] N. A. Krall and A. W. Trivelpiece, ***Principles of Plasma Physics***. McGraw-Hill, 1973. (Cited on pages 17, 145 and 146.)
- [44] D. Passchier, ***Numerical fluid models for RF discharges***, Ph.D. thesis, Utrecht university, 1994. (Cited on pages 17, 19 and 146.)
- [45] Y. Zhang, X. Xu, S.-X. Zhao *et al.*, ***Comparison of electrostatic and electromagnetic simulations for very high frequency plasmas***, *Phys. Plasmas*, vol. 17, p. 113512, 2010. (Cited on pages 17 and 146.)
- [46] D. B. Graves and K. F. Jensen, ***A Continuum Model of DC and RF Discharges***, *IEEE Transactions on plasma science*, vol. Ps-14, p. 78, 1986. (Cited on pages 17 and 146.)
- [47] COMSOL, ***The Capacitively Coupled Plasma Interface***, Tech. Rep., 2012. URL: <http://www.comsol.com> (Cited on page 18.)

- [48] J. P. Boeuf and L. C. Pitchford, *Two-dimensional model of a capacitively coupled rf discharge and comparisons with experiments in the Gaseous Electronics Conference reference reactor*, *Phys. Rev. E*, vol. 51, p. 1376, 1995. (Cited on pages 19 and 23.)
- [49] A. Salabas, G. Gousset, and L. L. Alves, *Two-dimensional fluid modelling of charged particle transport in radio-frequency capacitively coupled discharges*, *Plasma Sources Sci. Technol.*, vol. 11, p. 448, 2002. (Cited on page 21.)
- [50] G. J. M. Hagelaar and L. C. Pitchford, *Solving the Boltzmann equation to obtain electron transport coefficients and rate coefficients for fluid models*, *Plasma Sources Sci. Technol.*, vol. 14, p. 722, 2005. (Cited on pages 21 and 23.)
- [51] E. W. McDaniel and E. A. Mason, *The mobility and diffusion of ions in gases*. Wiley, 1973. (Cited on page 23.)
- [52] G. J. Nienhuis, W. J. Goedheer, E. A. G. Hamers *et al.*, *A self-consistent fluid model for radio-frequency discharges in SiH<sub>4</sub>-H<sub>2</sub> compared to experiments*, *J. Appl. Phys.*, vol. 82, p. 2060, 1997. (Cited on page 23.)
- [53] B. Legradic, *Arcing in Very Large Area Plasma-Enhanced Chemical Vapour Deposition Reactors*, Ph.D. thesis, École Polytechnique Fédérale de Lausanne, 2011. (Cited on page 23.)
- [54] V. Lisovski, J.-P. Booth, K. Landry *et al.*, *Similarity law for rf breakdown*, *EPL (Europhysics Letters)*, vol. 82, p. 15001, 2008. (Cited on page 23.)
- [55] B. Legradic, A. A. Howling, and C. Hollenstein, *Radio frequency breakdown between structured parallel plate electrodes with a millimetric gap in low pressure gases*, *Phys. Plasmas*, vol. 17, p. 102111, 2010. (Cited on pages 24 and 31.)
- [56] U. Kroll and B. Legradic, *Plasma processing apparatus and method for the plasma processing*, Patent, US 2011/0272099 A1. URL: <http://www.google.com/patents/US20110272099> (Cited on pages 25, 28 and 141.)
- [57] A. A. Howling, B. Legradic, M. Chesaux *et al.*, *Plasma deposition in an ideal showerhead reactor: a two-dimensional analytical solution*, *Plasma Sources Sci. Technol.*, vol. 21, p. 015005, 2012. (Cited on page 26.)

- [58] L. Sansonnens, *Déposition assistée par plasma radiofréquence dans un réacteur de grade surface: effets de la contamination particulaire et de la fréquence d'excitation*, Ph.D. thesis, École Polytechnique Fédérale de Lausanne, 1998. (Cited on page 35.)
- [59] J. Reader, C. H. Corliss, W. L. Wiese *et al.*, *Wavelengths and transition probabilities for atoms and atomic ions*. U.S. Dept. of Commerce, National Bureau of Standards, 1980. (Cited on page 38.)
- [60] V. Schulz-von der Gathen and H. F. Döbele, *Critical Comparison of Emission Spectroscopic Determination of Dissociation in Hydrogen RF Discharges*, *Plasma Chem. Plasma Process.*, vol. 16, p. 461, 1996. (Cited on page 39.)
- [61] U. Czarnetzki, D. Luggenhölscher, and H. F. Döbele, *Space and time resolved electric field measurements in helium and hydrogen RF-discharges*, *Plasma Sources Sci. Technol.*, vol. 8, p. 230, 1999. (Cited on pages 39, 82, 87 and 88.)
- [62] T. Gans, V. Schulz-von der Gathen, U. Czarnetzki *et al.*, *Observation of Fast Hydrogen Atoms Formed by Ion Bombarding of Surfaces*, *Contrib. Plasma Phys.*, vol. 42, p. 596, 2002. (Cited on pages 39, 82 and 87.)
- [63] M. M. Turner and M. B. Hopkins, *Anomalous Sheath Heating in a Low Pressure rf Discharge in Nitrogen*, *Phys. Rev. Lett.*, vol. 69, p. 3511, 1992. (Cited on pages 39, 82 and 87.)
- [64] C. Böhm and J. Perrin, *Retarding-field analyzer for measurements of ion energy distributions and secondary electron emission coefficients in low-pressure radio frequency discharges*, *Rev. Sci. Instrum.*, vol. 64, p. 31, 1993. (Cited on pages 43, 45, 51 and 54.)
- [65] B. L. Peko and R. L. Champion, *Total cross sections for low energy collisions of  $H_3^+$  with molecular hydrogen and rare gases*, *J. Chem. Phys.*, vol. 107, p. 1156, 1997. (Cited on page 48.)
- [66] K. R. Spangenberg, *Vacuum tubes*. McGraw-Hill, 1948. (Cited on pages 53 and 147.)
- [67] T. S. Green, *Space charge effects in plasma particle analyzers*, *Plasma Phys.*, vol. 12, p. 877, 1970. (Cited on page 56.)

- [68] V. A. Godyak and R. B. Piejak, *Probe measurements of the space potential in a radio frequency discharge*, *J. Appl. Phys.*, vol. 68, p. 3157, 1990. (Cited on pages [59](#), [60](#) and [90](#).)
- [69] N. Benjamin, *High-impedance capacitive divider probe for potential measurements in plasmas*, *Rev. Sci. Instrum.*, vol. 53, p. 1541, 1982. (Cited on page [59](#).)
- [70] S. E. Savas and K. G. Donohoe, *Capacitive probes for rf process plasmas*, *Rev. Sci. Instrum.*, vol. 60, p. 3391, 1989. (Cited on page [59](#).)
- [71] M. Chesaux, A. A. Howling, C. Hollenstein *et al.*, *Low ion energy RF reactor using an array of plasmas through a grounded grid*, *J. Vac. Sci. Technol. A*, vol. 31, p. 021302, 2013. (Cited on page [63](#).)
- [72] M. Chesaux, A. A. Howling, and C. Hollenstein, *Spurious plasmoid ignition in grid holes of RF plasma reactors detected by changes in self-bias*, *To be submitted*. (Cited on page [71](#).)
- [73] B. Chapman, *Glow Discharge Processes: Sputtering and Plasma Etching*. John Wiley & Sons, 1980. (Cited on pages [73](#), [74](#), [75](#), [77](#) and [86](#).)
- [74] R. W. Wood, *Plasmoidal High-Frequency Oscillatory Discharges in “Non-Conducting” Vacua*, *Phys. Rev.*, vol. 35, p. 673, 1930. (Cited on page [73](#).)
- [75] J. Taillet, *Resonance-Sustained Radio Frequency Discharges*, *Am. J. Phys.*, vol. 37, p. 423, 1969. (Cited on page [73](#).)
- [76] W. H. Bostick, *Experimental Study of Ionized Matter Projected across a Magnetic Field*, *Phys. Rev.*, vol. 104, p. 292, 1956. (Cited on page [73](#).)
- [77] H. Baty, *On the onset of the plasmoid instability*, *Phys. Plasmas*, vol. 19, p. 092110, 2012. (Cited on page [73](#).)
- [78] D. L. Smith, *Thin-film Deposition: Principles and Practice*. McGraw-Hill, 1995. (Cited on pages [74](#), [77](#), [78](#) and [83](#).)
- [79] L. Bárdoš, *Radio frequency hollow cathodes for the plasma processing technology*, *Surf. Coat. Technol.*, vol. 86-87, p. 648, 1996. (Cited on page [77](#).)

- [80] C. Lejeune, J. P. Grandchamp, O. Kessi *et al.*, ***Rf multipolar plasma for broad and reactive ion beams***, *Vacuum*, vol. 36, p. 837, 1986. (Cited on page 78.)
- [81] D. Korzec, M. Schott, and J. Engemann, ***Radio frequency hollow cathode discharge for large-area double-sided foil processing***, *J. Vac. Sci. Technol. A*, vol. 13, p. 843, 1995. (Cited on page 78.)
- [82] M. Sugawara and T. Asami, ***Generation of a highly uniform and dense plasma by distributing hollow cathodes on the electrode surface***, *Surf. Coat. Technol.*, vol. 74-75, p. 355, 1995. (Cited on page 78.)
- [83] Y.-B. Guo and F. C.-N. Hong, ***Radio-frequency microdischarge arrays for large-area cold atmospheric plasma generation***, *Appl. Phys. Lett.*, vol. 82, p. 337, 2003. (Cited on page 78.)
- [84] M. Tanda, M. Kondo, and A. Matsuda, ***A novel approach for the growth of  $\mu\text{-Si}$  at a high rate over 3 nm/s***, *Thin Solid Films*, vol. 427, p. 33, 2003. (Cited on page 78.)
- [85] C. Niikura, N. Itagaki, M. Kondo *et al.*, ***High-rate growth of microcrystalline silicon films using a high-density  $\text{SiH}_4/\text{H}_2$  glow-discharge plasma***, *Thin Solid Films*, vol. 457, p. 84, 2004. (Cited on page 78.)
- [86] M. A. Lieberman, ***Spherical shell model of an asymmetric rf discharge***, *J. Appl. Phys.*, vol. 65, p. 4186, 1989. (Cited on pages 79 and 110.)
- [87] M. A. Lieberman and S. E. Savas, ***Bias voltage in finite length, cylindrical and coaxial radio-frequency discharges***, *J. Vac. Sci. Technol. A*, vol. 8, p. 1632, 1990. (Cited on page 79.)
- [88] C. M. O. Mahony, R. Al Wazzan, and W. G. Graham, ***Sheath dynamics observed in a 13.56 MHz-driven plasma***, *Appl. Phys. Lett.*, vol. 71, p. 608, 1997. (Cited on page 87.)
- [89] J. Schulze, B. G. Heil, D. Luggenhölscher *et al.*, ***Electron beams in asymmetric capacitively coupled radio frequency discharges at low pressures***, *J. Phys. D: Appl. Phys.*, vol. 41, p. 042003, 2008. (Cited on page 89.)
- [90] L. Marques, G. Gousset, and L. L. Alves, ***Double Sheaths in RF Discharges***, *IEEE T. Plasma. Sci.*, vol. 33, p. 358, 2005. (Cited on page 120.)

- [91] Z. Donkó, J. Schulze, U. Czarnetzki *et al.*, ***Fundamental investigations of capacitive radio frequency plasmas: simulations and experiments***, *Plasma Phys. Control. Fusion*, vol. 54, p. 124003, 2012. (Cited on page 120.)
- [92] D. Dominé, 2012, private communication. (Cited on pages 125, 129, 135 and 136.)
- [93] T. Gaillard, ***Couches intrinsèques pour cellules photovoltaïques de silicium microcristallin déposées dans un nouveau type de réacteur PECVD***, Oerlikon Solar-Lab, Tech. Rep., 2012. (Cited on page 125.)
- [94] O. Vetterl, F. Finger, R. Carius *et al.*, ***Intrinsic microcrystalline silicon: A new material for photovoltaics***, *Sol. Energy Mater. Sol. Cells*, vol. 62, p. 97, 2000. (Cited on page 129.)
- [95] B. Yan, G. Yue, J. M. Owens *et al.*, ***Light-induced metastability in hydrogenated nanocrystalline silicon solar cells***, *Appl. Phys. Lett.*, vol. 85, p. 1925, 2004. (Cited on page 129.)
- [96] F. Sculati-Meillaud, ***Microcrystalline silicon solar cells: Theory, diagnosis and stability***, Ph.D. thesis, Université de Neuchâtel, 2006. (Cited on page 129.)
- [97] A. Shah, J. Meier, E. Vallat-Sauvain *et al.*, ***Material and solar cell research in microcrystalline silicon***, *Sol. Energy Mater. Sol. Cells*, vol. 78, p. 469, 2003. (Cited on page 129.)
- [98] C. Droz, E. Vallat-Sauvain, J. Bailat *et al.*, ***Relationship between Raman crystallinity and open-circuit voltage in microcrystalline silicon solar cells***, *Sol. Energy Mater. Sol. Cells*, vol. 81, p. 61, 2004. (Cited on page 129.)
- [99] A. H. M. Smets, T. Matsui, and M. Kondo, ***Infrared analysis of the bulk silicon-hydrogen bonds as an optimization tool for high-rate deposition of microcrystalline silicon solar cells***, *Appl. Phys. Lett.*, vol. 92, p. 033506, 2008. (Cited on page 130.)
- [100] A. H. M. Smets, W. M. M. Kessels, and M. C. M. van de Sanden, ***The effect of ion-surface and ion-bulk interactions during hydrogenated amorphous silicon deposition***, *J. Appl. Phys.*, vol. 102, p. 073523, 2007. (Cited on pages 131, 132, 137 and 143.)

- [101] E. A. G. Hamers, W. G. J. H. M. van Sark, J. Bezemer *et al.*, ***Structural properties of a-Si:H related to ion energy distributions in VHF silane deposition plasmas***, *J. Non-Cryst. Solids*, vol. 226, p. 205, 1998. (Cited on pages [131](#) and [132](#).)
- [102] J. Holovsky, ***Fourier Transform Photocurrent Spectroscopy on Non-Crystalline Semiconductors***. InTech, 2011. (Cited on page [131](#).)
- [103] S. Vepřek, F. A. Sarrott, S. Rambert *et al.*, ***Surface hydrogen content and passivation of silicon deposited by plasma induced chemical vapor deposition from silane and the implications for the reaction mechanism***, *J. Vac. Sci. Technol. A*, vol. 7, p. 2614, 1989. (Cited on pages [132](#), [137](#) and [143](#).)
- [104] J. Dutta, U. Kroll, P. Chabloz *et al.*, ***Dependence of intrinsic stress in hydrogenated amorphous silicon on excitation frequency in a plasma-enhanced chemical vapor deposition process***, *J. Appl. Phys.*, vol. 72, p. 3220, 1992. (Cited on pages [132](#), [137](#) and [143](#).)
- [105] H. Keppner, U. Kroll, P. Torres *et al.*, ***Scope of VHF plasma deposition for thin-film silicon solar cells***, in *Photovoltaic Specialists Conference*, p. 669, 1996. (Cited on pages [132](#), [137](#) and [143](#).)
- [106] F. Finger, U. Kroll, V. Viret *et al.*, ***Influences of a high excitation frequency (70 MHz) in the glow discharge technique on the process plasma and the properties of hydrogenated amorphous silicon***, *J. Appl. Phys.*, vol. 71, p. 5665, 1992. (Cited on pages [132](#), [137](#) and [143](#).)
- [107] G. S. Oehrlein, ***Dry Etching Damage of Silicon: A Review***, *Mater. Sci. Eng.*, vol. B4, p. 441, 1989. (Cited on pages [132](#), [137](#) and [143](#).)





# Acknowledgements

My first thanks goes to my supervisors Dr. Christoph Hollenstein and Dr. Alan A. Howling for their insightful supervision and for being always present when guidance was necessary. They both taught me a lot and this thesis would not be what it is without them. Christoph experienced supervision was priceless for keeping this study on tracks and avoiding many dead ends. Alan played a central role in many aspects of this study. He is a bottomless source of knowledge in plasma physics as well as in many other fields and we had many fascinating discussions throughout these years

I want to thank the team at Oerlikon Solar-Lab (Dr. Didier Dominé, Dr. Xiaojie Wang, Tristan Gaillard, Miguel Marmelo, Giovanni Monteduro, and Dr. Ulrich Kroll) for their fruitful collaboration. Didier played a central role in the writing of the chapter on layer deposition and solar cell quality (Ch. 7).

I want to thank the many colleagues at the Centre de Recherche en Physique des Plasmas (CRPP) (David Martinet, Ralph Schnyder, Dr. Pierre Demolon, Dr. Loïc Curchod, Dr. Boris Legradic, Dr. Sylvain Lecoultré and Dr. Philippe Guittienne) for the many discussions during lunches and breaks. I want to also thank Boris and David for putting their own car at risk to improve my driving skills.

Thanks to all other contributors (i.e. Dr. Fabien Coursimault and Tristan Gaillard) for ‘adding their stone’ to this project. I also want to thank the different workshops of the CRPP for all their work done on designing and making/soldering the many pieces used in the diagnostics and experiments throughout this study. This experimental study would not have been possible without their help.

I want to thank my former coworkers at Oerlikon Solar especially Dr. Alban Sublet without which I wouldn’t have had the possibility to do this thesis.

I want to thank my many friends especially James Villalonga, Steve Genoud, Steve Couturier and Lorenza Antognini for all the great moments, the sports and social evenings we shared throughout the years.

I want to thank my parents and family for their important and constant support as

well as for always showing renewed interest for this work and its progress.

Finally, I want to thank Carly Huitema who midwifed this thesis to the world. She has been a constant source of support and encouragement especially throughout the writing.

I wish to acknowledge Oerlikon Solar-Lab and the Commission for Technology and Innovation (CTI) (project numbers 9675.2 and 13271.1) for funding this work.

**Michaël CHESAUX, PhD.,** *michael.chesaux@gmail.com,*

+41 78 883 49 46

Nationality: Swiss and French

Age: 29

- I am a plasma processing physicist who **values teamwork** and **creativity** to solve concrete challenges and develop new products.
- I have **2 years of industry experience** and a **Ph.D.** in collaboration with industry.



## EDUCATION

### Ecole Polytechnique Fédérale de Lausanne (EPFL)

**Ph.D. in physics**

**2009 to 2013**

**Master in physics (M.Sc.),** average grade: 5.3 / 6 (88%)

**2005 to 2007**

**Bachelor in physics (B. Sc.),** average grade: 4.6 / 6 (76%)

**2002 to 2005**

## PROFESSIONAL EXPERIENCE IN R&D

**Applied Ph.D.**

**EPFL partnered with Oerlikon Solar**

**2009 to 2013**

Oerlikon Solar had patented new concept reactor for the deposition of thin film solar cells. They collaborated with the EPFL to develop a prototype reactor based on this concept now in use for the development of solar cells.

- I **developed a prototype reactor.** The project started from simple sketches and involved frequent collaboration with the industrial partner. It ended with a semi-industrial prototype producing low defect density layers.
- I developed diverse **plasma diagnostics** to qualify and improve the reactors properties.

**Application Engineer OERLIKON Solar**

**2007 to 2009**

Oerlikon was racing for word leadership as a thin film solar cell factory supplier. The market was quickly expanding hence the factories needed quick and constant improvement to attract and retain customers.

- I **decreased the production time** of solar cells by 10 % through documentation and improvement of an etching process.
- I **improved troubleshooting procedures** by systematic investigation of reactor failures.
- I **supported customers** by diagnosing and doing on-site repairs on their reactors in both English and German.

## HIGHLIGHT OF TECHNICAL SKILLS

### Plasma source and reactor development

#### Radio Frequency Capacitively Coupled Plasma

- Developed a low ion bombardment plasma source from concept to semi-industrial prototype
- Quantified and mitigated powder produced during deposition
- Improved the homogeneity and etching process in an industrial reactor producing thin film solar cells

#### Direct Current and Plasma Spraying

- Implemented thin a film deposition process in a new type of reactor
- Improved a plasma spraying reactor for coatings using liquid precursors

### Plasma diagnostic development

- Retarding Field Energy Analyser (RFEA) (ion bombardment energy)
- Capacitive probe (plasma potential)
- Langmuir probe (plasma density)
- Optical Emission Spectroscopy (OES) (plasma composition)

### Software skills

- COMSOL (simulation)
- MATLAB (data analysis)
- ORIGIN (graphic and data analysis)
- C++ (programming)

### Process development

#### Thin film coating

- Amorphous and micro-crystalline silicon deposition

#### Material characterisation

- Raman spectroscopy (crystallinity)
- Fourier Transform Infrared spectroscopy (FTIR) (chemical bounds)

#### Development of etching process

- Use of mass spectrometry to investigate the different phases of a etching process
- Developed etching process to reduce the production time of solar cells

## LANGUAGES

- |                    |   |
|--------------------|---|
| ▪ <b>French :</b>  | <b>Mother tongue (C2):</b>  |
| ▪ <b>English :</b> | <b>Fluent (C1):</b><br>Writing a Ph.D. thesis in English                            |
| ▪ <b>German :</b>  | <b>School level (B1):</b><br>I worked for one year in a German speaking environment |

## HOBBIES

- |                     |  |
|---------------------|--|
| <b>Sport:</b>       | Diving, hiking, skiing, cycling and martial arts |
| <b>Creativity:</b>  | Drawing and crafting                             |
| <b>Associative:</b> | Student unions                                   |

## PUBLICATIONS

**M. Chesaux**, A. A. Howling, and C. Hollenstein, *Spurious plasmoid ignition in grid holes of RF plasma reactors detected by change in self-bias*, to be submitted.

**M. Chesaux**, A. A. Howling, D. Dominé, U. Kroll and C. Hollenstein, *Low ion energy RF reactor using an array of plasma through a grounded grid* *J. Vac. Sci. Technol. A*, vol 31, p.021302, 2013.

A. A. Howling, B. Legradic, **M. Chesaux** and C. Hollenstein, *Plasma deposition in an ideal showerhead reactor: a tow-dimensional analytical solution*, *Plasma Sources Sci. Technol.*, vol. 21, p. 015005, 2012.

## PRESENTATIONS

### Oral presentation:

**M. Chesaux**, A. A. Howling, D. Dominé, U. Kroll, C. Hollenstein, *A grid reactor with low ion energy bombardment for large area PECVD of thin film silicon solar cells*, *American Vacuum Society 59th International Symposium and Exhibition*, 2012

### Poster presentation:

**M. Chesaux**, D. Dominé, U. Kroll, A. A. Howling, C. Hollenstein, *A new low ion energy bombardment PECVD reactor for the deposition of large area thin film silicon for solar cell applications*, *International Workshop on Thin-Film Silicon Solar Cell*, 2012